



Calhoun: The NPS Institutional Archive
DSpace Repository

Theses and Dissertations

1. Thesis and Dissertation Collection, all items

2008-09

Design and implementation of an active calibration system for weather radars

Phillips, Jason M.

Monterey California. Naval Postgraduate School

<http://hdl.handle.net/10945/3977>

Downloaded from NPS Archive: Calhoun



Calhoun is the Naval Postgraduate School's public access digital repository for research materials and institutional publications created by the NPS community. Calhoun is named for Professor of Mathematics Guy K. Calhoun, NPS's first appointed -- and published -- scholarly author.

Dudley Knox Library / Naval Postgraduate School
411 Dyer Road / 1 University Circle
Monterey, California USA 93943

<http://www.nps.edu/library>



NAVAL POSTGRADUATE SCHOOL

MONTEREY, CALIFORNIA

THESIS

**DESIGN AND IMPLEMENTATION OF AN ACTIVE
CALIBRATION SYSTEM FOR WEATHER RADARS**

by

Jason M. Phillips

September 2008

Thesis Advisor:
Co-Advisor:

Jeffrey B. Knorr
Terry E. Smith

Approved for public release; distribution is unlimited

THIS PAGE INTENTIONALLY LEFT BLANK

REPORT DOCUMENTATION PAGE			<i>Form Approved OMB No. 0704-0188</i>	
Public reporting burden for this collection of information is estimated to average 1 hour per response, including the time for reviewing instruction, searching existing data sources, gathering and maintaining the data needed, and completing and reviewing the collection of information. Send comments regarding this burden estimate or any other aspect of this collection of information, including suggestions for reducing this burden, to Washington headquarters Services, Directorate for Information Operations and Reports, 1215 Jefferson Davis Highway, Suite 1204, Arlington, VA 22202-4302, and to the Office of Management and Budget, Paperwork Reduction Project (0704-0188) Washington DC 20503.				
1. AGENCY USE ONLY (Leave blank)		2. REPORT DATE September 2008	3. REPORT TYPE AND DATES COVERED Master's Thesis	
4. TITLE AND SUBTITLE Design and Implementation of an Active Calibration System for Weather Radars			5. FUNDING NUMBERS	
6. AUTHOR(S) Jason M. Phillips				
7. PERFORMING ORGANIZATION NAME(S) AND ADDRESS(ES) Naval Postgraduate School Monterey, CA 93943-5000			8. PERFORMING ORGANIZATION REPORT NUMBER	
9. SPONSORING /MONITORING AGENCY NAME(S) AND ADDRESS(ES) N/A			10. SPONSORING/MONITORING AGENCY REPORT NUMBER	
11. SUPPLEMENTARY NOTES The views expressed in this thesis are those of the author and do not reflect the official policy or position of the Department of Defense or the U.S. Government.				
12a. DISTRIBUTION / AVAILABILITY STATEMENT Approved for public release; distribution is unlimited			12b. DISTRIBUTION CODE	
13. ABSTRACT (maximum 200 words) Weather radars permit meteorological quantities such as rainfall rate and wind velocity to be determined. These quantities are calculated from estimates of reflectivity, mean radial velocity and velocity spread. These estimates are derived from modified RF signal parameter measurements. RF scattering and propagation effects are the mechanisms which modify these parameters. Scattering is probabilistic in nature and therefore during measurement estimates of true conditions are formed. Errors in these initial estimations influence the accuracy of all subsequent quantities produced. For meteorological products to be as accurate as possible, the amount of uncertainty in each estimated quantity must be minimized. A well-controlled calibration process is used to reduce the influence of imprecisely known radar system parameters on the uncertainty of the formed estimates. This thesis presents the design and implementation of one such calibration system, an active, external calibrator for use with the MWR-05XP weather radar. Within this thesis, a background of the radar calibration problem, specific research objectives and related works are introduced and discussed. The theory behind the operation of weather radar is also presented and explained. The specific design is described in explicit detail and measured results provided in appendices. Conclusions on the success of the implementation are drawn with recommendations for future work.				
14. SUBJECT TERMS Weather Radar Active Calibrator			15. NUMBER OF PAGES 177	
			16. PRICE CODE	
17. SECURITY CLASSIFICATION OF REPORT Unclassified	18. SECURITY CLASSIFICATION OF THIS PAGE Unclassified	19. SECURITY CLASSIFICATION OF ABSTRACT Unclassified	20. LIMITATION OF ABSTRACT UU	

THIS PAGE INTENTIONALLY LEFT BLANK

Approved for public release; distribution is unlimited

**DESIGN AND IMPLEMENTATION OF AN ACTIVE CALIBRATION SYSTEM
FOR WEATHER RADARS**

Jason M. Phillips
Civilian, United States Department of Defense
B.S.E.E., University of Maryland - College Park, 2002
B.S. Mathematics, University of Maryland - College Park, 2002

Submitted in partial fulfillment of the
requirements for the degrees of

**MASTER OF SCIENCE IN ELECTRICAL ENGINEERING
MASTER OF SCIENCE IN ELECTRONIC WARFARE SYSTEMS
ENGINEERING**

from the

**NAVAL POSTGRADUATE SCHOOL
September 2008**

Author: Jason M. Phillips

Approved by: Jeffrey B. Knorr
Thesis Advisor

Terry E. Smith
Co-Advisor

Jeffrey B. Knorr
Chairman, Department of Electrical and Computer Engineering

Dan C. Boger
Chairman, Department of Information Sciences

THIS PAGE INTENTIONALLY LEFT BLANK

ABSTRACT

Pulsed weather radars can be used to depict meteorological conditions such as rainfall rate and wind velocity. These quantities are calculated from measurements of reflectivity, mean radial velocity and velocity spread using echo signal samples from weather targets. These radar measurements derive from modified radio frequency (RF) echo signal parameters, including amplitude, frequency and phase, returned to the radar from the weather target. RF scattering and propagation effects modify echo signal parameters. Bias and variance in the weather signal parameter estimates naturally influence the accuracy of all subsequent quantities produced. For meteorological products to be as accurate as possible, the amount of uncertainty in each estimated quantity must be minimized. If radar system parameters are not accurately known, the reflectivity estimate will be biased. A well-controlled calibration process is therefore critical to reduce the bias of the reflectivity estimate. This thesis presents the design and implementation of one such calibration system, specifically for use with the MWR-05XP (a Mobile Phased-Array Pulse-Doppler X-band Weather Radar first created at the Naval Postgraduate School in 2005), although the general results are applicable to all radars. The calibration system presented is an active, external calibrator intended to verify end-to-end radar system performance. Within this thesis, a background of the radar calibration problem along with the research objectives for this specific project and related works are introduced and discussed. The theory behind the operation of weather radar (how the three principle quantities are measured and related to signal parameters) is also presented and explained. The density function for precipitation, relation between signal correlation and velocity spread, and fundamentals of weather radar signal parameter estimation are given. The specific design is described in explicit detail and measured results provided in appendices. Conclusions on the success of the implementation are drawn and recommendations for future work are presented.

THIS PAGE INTENTIONALLY LEFT BLANK

TABLE OF CONTENTS

I.	INTRODUCTION.....	1
A.	BACKGROUND	1
B.	RESEARCH OBJECTIVE	1
C.	RELATED WORK	3
D.	ORGANIZATION OF THE THESIS.....	5
II.	BACKGROUND AND SUPPORTING THEORY	7
A.	WEATHER RADAR VS. TRADITIONAL RADAR	7
B.	RADAR RESOLUTION CELL.....	8
C.	SWERLING TARGET TYPES.....	9
D.	SAMPLE CORRELATION.....	10
E.	ESTIMATION OF POWER DENSITY AND REFLECTIVITY (Z).....	12
1.	Antenna Gain and Beam effective Solid Angle	12
2.	Physics of Precipitation	13
a.	<i>Size and Shape</i>	<i>13</i>
b.	<i>Drop Size Distribution (DSD).....</i>	<i>14</i>
c.	<i>Rainfall Rate</i>	<i>14</i>
3.	Weather Radar Range Equation and Estimation of Reflectivity ..	15
F.	RADAR PRINCIPLES AND WEATHER RADAR EQUATION CORRECTION.....	16
G.	ESTIMATION OF VELOCITY.....	19
H.	ESTIMATION OF VELOCITY SPREAD.....	20
I.	CALIBRATION REQUIREMENTS	20
J.	CALIBRATION METHODS AND SELECTED METHOD	21
K.	SUMMARY	22
III.	DESIGN, IMPLEMENTATION AND OPERATION	23
A.	DESIGN	23
B.	HARDWARE IMPLEMENTATION	24
1.	System Description Overview	24
2.	Hardware List	25
3.	Voltage Regulator Circuit	25
4.	RF Components.....	26
5.	Control Hardware.....	26
6.	Hardware Limitations	27
C.	ACS FREQUENCY/DOPPLER CALIBRATION AND SOFTWARE IMPLEMENTATION	28
D.	ADDING VELOCITY SPREAD.....	31
E.	ACS AMPLITUDE/REFLECTIVITY CALIBRATION.....	31
1.	Measurement Premise	32
2.	Measurement Method.....	33
a.	<i>Initial Calculations</i>	<i>34</i>
b.	<i>Anechoic Chamber Measurements</i>	<i>37</i>

IV. CONCLUSION AND FUTURE WORK	47
A. CONCLUSION	47
B. FUTURE WORK	48
APPENDIX A. ACS PICTURES	53
APPENDIX B. DIGITAL PHASE SHIFTER DATA	65
APPENDIX C. SCALAR AND VECTOR NETWORK ANALYZER MEASUREMENT DATA	67
APPENDIX D. PROGRAMMABLE ATTENUATOR DATA	85
APPENDIX E. ANTENNA DATA	87
APPENDIX F. ANTENNA PATTERN DATA	95
A. VNA ANTENNA PATTERN DATA	95
B. ACS ANTENNA PATTERN DATA	101
C. MATLAB PLOTTING FILES	106
D. ABSOLUTE GAIN AND 3 DB BEAMWIDTH FOR X-BAND AND PASTERNAK HORN ANTENNAS (CALCULATIONS AND MEASUREMENTS)	110
E. EXPLANATION OF DATAFILE MEASUREMENTS AND CALCULATIONS	114
F. ANTENNA ISOLATION TEST DATA	116
APPENDIX G. ANECHOIC CHAMBER	119
APPENDIX H. COMPACTRIO	121
A. COMPACTRIO REAL-TIME EMBEDDED CONTROLLER (NI CRIO-9004, 64/512 MEMORY)	121
B. COMPACTRIO RECONFIGURABLE EMBEDDED CHASSIS (NI CRIO-9101, 1M GATE 4-SLOT CHASSIS)	124
C. COMPACTRIO I/O MODULES FOR DIGITAL INPUT AND COUNTER/TIMER (NI 9401, 8 CH 5 V/TTL HIGH SPEED BIDIRECTIONAL DIGITAL I/O MODULE)	126
D. NI DEVELOPER SUITE WITH REAL-TIME AND FPGA SOFTWARE FOR COMPACTRIO	128
APPENDIX I. LABVIEW FOR THE DIGITAL PHASE SHIFTER	129
A. PHASESHIFTERCONTROL	129
B. SLAVECONTROL	130
C. MASTERCONTROL	131
LIST OF REFERENCES	149
INITIAL DISTRIBUTION LIST	151

LIST OF FIGURES

Figure 1.	Illustration of Radar Resolution Cell. [From 1].....	8
Figure 2.	Block Diagram of the ACS.	23
Figure 3.	Diagram of Component Layout inside the ACS Enclosure.	24
Figure 4.	Voltage Regulator Circuit Diagram.	26
Figure 5.	Two Cycles of the Periodic, Linear, Modulating Sawtooth Function.	29
Figure 6.	Graph for Calculating Radar Cross Section of a Sphere. [After 11]	37
Figure 7.	Time vs. Amplitude for Empty Chamber, Sphere and ACS. (ESC_plotTA) ..	39
Figure 8.	Frequency vs. Amplitude for Empty Chamber, Sphere and ACS. (ESC_plotF)	40
Figure 9.	Time vs. Amplitude for Sphere, Zoomed. (S_plotTA=Z)	42
Figure 10.	Time vs. Amplitude for ACS, Zoomed. (C_plotTA=Z)	43
Figure 11.	Frequency vs. Equivalent RCS of the ACS. (RCS_plot).....	44
Figure 12.	Calibrator Front View with RAM (straight on).	53
Figure 13.	Calibrator Front View with RAM (looking down angle).	53
Figure 14.	Calibrator Left Side View (straight on).	53
Figure 15.	Calibrator Left Side View (looking down angle).	54
Figure 16.	Calibrator Left Side View (looking down angle), Zoomed.	55
Figure 17.	Calibrator Left Side View (looking down angle), Zoomed – Top Cover OFF.	56
Figure 18.	Calibrator Top View (straight on), Zoomed – Top Cover OFF.....	57
Figure 19.	Calibrator Inside View (CRIO).....	57
Figure 20.	Calibrator Inside View (Power Supply Circuit).....	58
Figure 21.	Calibrator Inside View (Phase Shifter).	58
Figure 22.	Calibrator Inside View (Power Supply).	59
Figure 23.	Calibrator Right Side View (looking down angle) Zoomed, Top Cover OFF	60
Figure 24.	Calibrator Right Side View (looking from above at external in-line amp).	61
Figure 25.	Calibrator Rear Left Side View (looking down angle).	61
Figure 26.	Right Horn Antenna (close-in view, polarization is horizontal).	62
Figure 27.	12” Sphere (used to calibrate the ACS).	63
Figure 28.	Specifications Sheet for Digital Phase Shifter from G.T. Microwave.....	66
Figure 29.	RF Amplifier Gain Single VNA Plot.....	67
Figure 30.	Digital Phase Shifter Insertion Loss (Left) and Phase Value (Right) Dual VNA Plots. Zero volts applied to all pins. Active Low. All bits “1”. (11111111).	68
Figure 31.	Digital Phase Shifter Insertion Loss (Left) and Phase Value (Right) Dual VNA Plots. Zero volts applied to MSB pin only, five volts others. (10000000).	69
Figure 32.	Digital Phase Shifter Insertion Loss (Left) and Phase Value (Right) Dual VNA Plots. Zero volts applied to second MSB pin only, five volts others. (01000000).	70

Figure 33.	Digital Phase Shifter Insertion Loss (Left) and Phase Value (Right) Dual VNA Plots. Zero volts applied to third MSB pin only, five volts others. (00100000).	71
Figure 34.	Digital Phase Shifter Insertion Loss (Left) and Phase Value (Right) Dual VNA Plots. Zero volts applied to fourth MSB pin only, five volts others. (00010000).	72
Figure 35.	Digital Phase Shifter Insertion Loss (Left) and Phase Value (Right) Dual VNA Plots. Zero volts applied to fifth MSB pin only, five volts others. (00001000).	73
Figure 36.	Digital Phase Shifter Insertion Loss (Left) and Phase Value (Right) Dual VNA Plots. Zero volts applied to sixth MSB pin only, five volts others. (00000100).	74
Figure 37.	Digital Phase Shifter Insertion Loss (Left) and Phase Value (Right) Dual VNA Plots. Zero volts applied to seventh MSB pin only, five volts others. (00000010).	75
Figure 38.	Digital Phase Shifter Insertion Loss (Left) and Phase Value (Right) Dual VNA Plots. Zero volts applied to LSB pin only, five volts others. (00000001).	76
Figure 39.	Digital Phase Shifter Insertion Loss (Left) and Phase Value (Right) Dual VNA Plots. Five volts applied to all pins. (00000000).	77
Figure 40.	Digital Phase Shifter Forward (left) and Reverse (right) Insertion Loss Dual VNA Plots. Demonstration of device's bidirectional property. Losses in the forward and reverse are equal. Five volts applied to all pins. (00000000).	78
Figure 41.	SNA Plot of Scalar Network Analyzer's Straight-Through State. "Calibrated to Zero"	79
Figure 42.	SNA Plot of Cable used with Digital Phase Shifter during SNA testing.	80
Figure 43.	Digital Phase Shifter SNA Plot. Fixed Phase State, no Doppler Shift.	81
Figure 44.	Digital Phase Shifter SNA Plot. Periodic Rotation through Phase States, Doppler Shift.	82
Figure 45.	Digital Phase Shifter Phase Value Single VNA Plot. Zero volts applied to MSB pin only, five volts others. (10000000) 180° Phase Shift.	83
Figure 46.	Digital Phase Shifter Phase Value Single VNA Plot. Zero volts applied to second MSB pin only, five volts others. (01000000) 90° Phase Shift.	84
Figure 47.	Specifications Sheet for Programmable Attenuator from American Microwave.	86
Figure 48.	Pasternack Sectoral Horn Antenna Data Sheet.	88
Figure 49.	Pasternack Sectoral Horn Antenna Outline Drawing.	89
Figure 50.	Pasternack Waveguide to Coaxial Adapter Outline Drawing.	90
Figure 51.	Narda Standard Gain Horn Antenna Datasheet (page 1).	91
Figure 52.	Narda Standard Gain Horn Antenna Datasheet (page 2).	92
Figure 53.	Narda Standard Gain Horn Antenna Datasheet (page 3).	93
Figure 54.	Narda Standard Gain Horn Antenna Datasheet (page 5).	94
Figure 55.	X-band Horn Antenna #1 Pattern at 9370MHz (E plane in red and H plane in blue).	96

Figure 56.	X-band Horn Antenna #2 Pattern at 9370MHz (E plane in red).	96
Figure 57.	X-band Horn Antenna #2 Pattern at 9370MHz (H plane in blue).	97
Figure 58.	X-band Horn Antenna #1 Pattern at 9680MHz (E plane in red and H plane in blue).	97
Figure 59.	X-band Horn Antenna #2 Pattern at 9370MHz (E plane in red and H plane in blue).	98
Figure 60.	X-band Horn Antenna #1 Pattern at 9990MHz (E plane in red and H plane in blue).	98
Figure 61.	X-band Horn Antenna #2 Pattern at 9990MHz (E plane in red and H plane in blue).	99
Figure 62.	Standard Gain Horn Antenna Pattern at 9370MHz (E plane in red and H plane in blue).	99
Figure 63.	Standard Gain Horn Antenna Pattern at 9680MHz (E plane in red and H plane in blue).	100
Figure 64.	Standard Gain Horn Antenna Pattern at 9370MHz (E plane in red and H plane in blue).	100
Figure 65.	Pasternack Horn Antenna #1 Pattern at 9370MHz (E plane in red and H plane in blue).	101
Figure 66.	Pasternack Horn Antenna #2 Pattern at 9370MHz (E plane in red and H plane in blue).	102
Figure 67.	Pasternack Horn Antenna #1 Pattern at 9680MHz (E plane in red and H plane in blue).	102
Figure 68.	Pasternack Horn Antenna #2 Pattern at 9680MHz (E plane in red and H plane in blue).	103
Figure 69.	Pasternack Horn Antenna #1 Pattern at 9990MHz (E plane in red and H plane in blue).	103
Figure 70.	Pasternack Horn Antenna #2 Pattern at 9990MHz (E plane in red and H plane in blue).	104
Figure 71.	Standard Gain Horn Antenna Pattern at 9370MHz (E plane in red and H plane in blue).	104
Figure 72.	Standard Gain Horn Antenna Pattern at 9680MHz (E plane in red and H plane in blue).	105
Figure 73.	Standard Gain Horn Antenna Pattern at 9990MHz (E plane in red and H plane in blue).	105
Figure 74.	Plot of Absolute Gain for X-band Horn Antennas.	111
Figure 75.	Plot of 3dB Beamwidth for X-band Horn Antennas.	112
Figure 76.	Plot of Absolute Gain for Pasternack Horn Antennas.	113
Figure 77.	Plot of 3dB Beamwidth for Pasternack Horn Antennas.	114
Figure 78.	Narda Standard Gain Horn Absolute Gain Plot (zoomed to area of interest and annotated with values of interest).	115
Figure 79.	Anechoic Chamber Diagram.	120
Figure 80.	Figure of CompactRIO Software Architecture from ni.com.	121
Figure 81.	Picture of cRIO-9004 from ni.com.	122
Figure 82.	Datasheet for CompactRIO Real-Time Embedded Controllers from ni.com.	123

Figure 83.	Picture of cRIO-9103 from ni.com.	124
Figure 84.	Datasheet for CompactRIO Reconfigurable Embedded Chassis from ni.com.	125
Figure 85.	Picture of cRIO-9401 from ni.com.	126
Figure 86.	Datasheet for C Series Digital Output and Relay Modules from ni.com.	127
Figure 87.	dataIO_CODE	134
Figure 88.	dataIO_UI	135
Figure 89.	fpgaRX_test_CODE	135
Figure 90.	fpgaRX_test_UI	136
Figure 91.	fpgaTX_test_CODE	136
Figure 92.	fpgaTX_test_UI	136
Figure 93.	KNORR-CAL_project	137
Figure 94.	ManualControl_CODE	138
Figure 95.	ManualControl_UI	139
Figure 96.	MasterControl_CODE	139
Figure 97.	MasterControl_UI	140
Figure 98.	NetworkRX_test_CODE	140
Figure 99.	NetworkRX_test_UI	141
Figure 100.	NetworkTX_test_CODE	141
Figure 101.	PhaseShifterControl6-bit_CODE1	142
Figure 102.	PhaseShifterControl6-bit_CODE2	142
Figure 103.	PhaseShifterControl6-bit_UI	143
Figure 104.	PhaseShifterControl_CODE1	143
Figure 105.	PhaseShifterControl_CODE2	144
Figure 106.	PhaseShifterControl_UI	144
Figure 107.	SlaveControl_CODE0	145
Figure 108.	SlaveControl_CODE1	145
Figure 109.	SlaveControl_CODE2	146
Figure 110.	SlaveControl_UI	146
Figure 111.	tDcalc_CODE	147
Figure 112.	tDcalc_UI	148

LIST OF TABLES

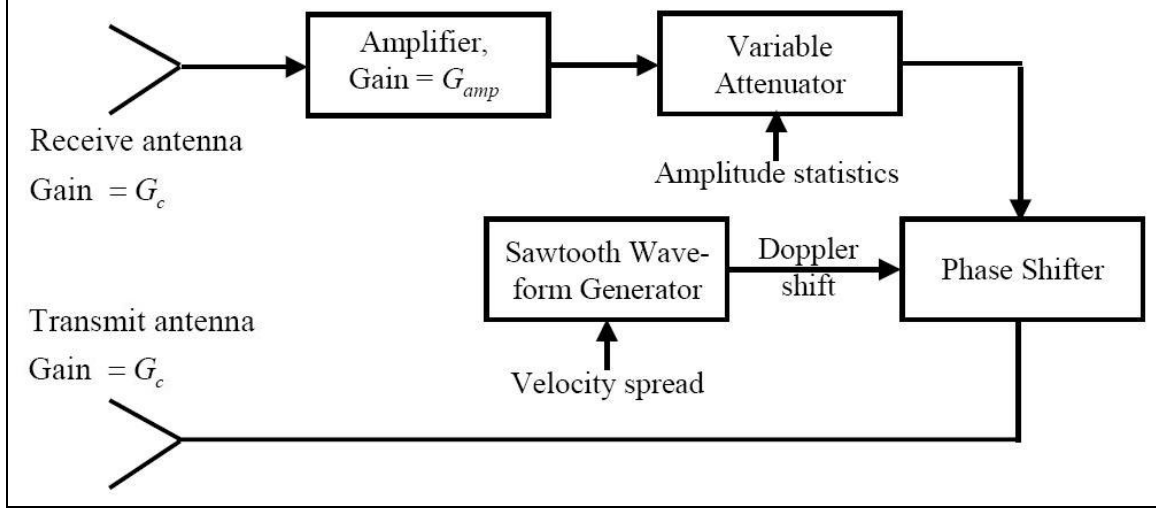
Table 1.	Swerling Target Types and Probability Density Functions.	10
Table 2.	Summary of Constants Used in Estimated Equivalent RCS Calculations.	35
Table 3.	Summary of Estimated Equivalent RCS Calculations.	35
Table 4.	Summary for Calculations of Radar Cross Section of a Sphere.	37
Table 5.	Naming Convention Summary.	38
Table 6.	Power and Logic Connections for Digitally Controlled Phase Shifter.	65
Table 7.	Power and Logic Connections for Programmable Attenuator.	85
Table 8.	Datafile for X-band Horn Antennas.	110
Table 9.	Datafile for Pasternack Horn Antennas.	112
Table 10.	Table Summary of LabVIEW VIs.	133

THIS PAGE INTENTIONALLY LEFT BLANK

EXECUTIVE SUMMARY

Pulsed weather radars can be used to quantify meteorology into amounts such as rainfall rate maps and wind velocity fields. These quantities are calculated from measurements of reflectivity, mean radial velocity and velocity spread using echo signal samples from weather targets. These radar measurements derive from modified radio frequency (RF) echo signal parameters, including amplitude, frequency and phase, returned to the radar from the radar's target. RF scattering and propagation effects are the mechanisms which modify echo signal parameters. Bias and variance in the weather signal parameter estimates naturally influence the accuracy of all subsequent quantities produced. For meteorological products to be as accurate as possible, the amount of uncertainty in each estimated quantity must be minimized. If radar system parameters are not accurately known, the reflectivity estimate will be biased. A well-controlled calibration process is therefore critical to reduce the bias of the reflectivity estimate. This thesis presents the design and implementation of one such calibration system, specifically for use with the MWR-05XP (a Mobile Phased-Array Pulse-Doppler X-band Weather Radar first created at the Naval Postgraduate School in 2005), although the general results are applicable to all radars. The calibration system presented is an active, external calibrator intended to verify end-to-end radar system performance.

The approach is a repeater that will produce a known Radar Cross Section (RCS) via loop gain control and create Doppler velocities and Doppler spread via phase modulation with a sawtooth. Proper control of the sawtooth frequency will also allow introduction of Doppler spread. Although a constant amplitude return would suffice, use of a programmable, constant phase attenuator would also allow control of the amplitude statistics of the return to the radar. Thus, with full control of both amplitude and phase, one could replicate the return for each of the Swerling target types, although it is only precipitation return that is really of interest in our application. A block diagram of the implementation of this proposed Active Calibrator System (ACS) design is presented below.



The reflectivity for a weather radar contains radar system parameters which may not be precisely known. The objective of calibration is to determine the composite of these parameters. The composite of these factors is also known as the radar system calibration constant. In Dr. Jeffrey Knorr's paper, "Weather Radar Equation Correction for Frequency Agile and Phased Array Radars," it has been shown that, for the case where the reference target is on boresight, $\theta = 0$, the measurement is made at the reference frequency, $\lambda = \lambda_0$, and the range is short ($L_a = 1$) the radar system calibration constant can be described as:

$$\left[\frac{P_t G_{rx} G_0^2}{L_s} \right] = \left[\frac{(4\pi)^3 R^4 P_{out}}{\lambda_0^2 \sigma} \right]$$

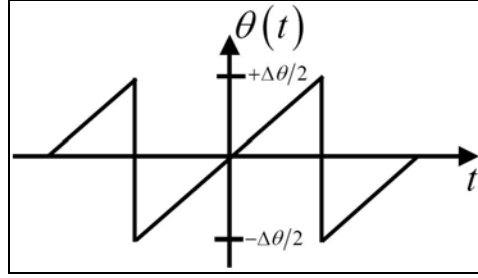
From this equation, it is clear that a measurement of receiver output power and range for a reference target of known cross-section ($\theta = 0$, $\lambda = \lambda_0$, $L_a = 1$) permits the radar system constant on the left side to be determined and the radar calibrated for reflectivity estimation. Phase modulation is required to produce Doppler shift, according to:

$$v(t) = A \cos[\omega_c t + \theta(t)] = A \operatorname{Re} \left[e^{j\omega_c t} e^{j\theta(t)} \right].$$

For $\theta(t)$ periodic where the phase modulated signal has a spectrum given by a sawtooth waveform of amplitude adjusted to produce a phase change that is a multiple of 2π (see waveform pictured below) then,

$$v(t) = A \operatorname{Re} e^{j(f_c + mf_m)t} \text{ where } (\Delta\theta = m2\pi).$$

The signal is translated (Doppler shifted) from frequency f_c to frequency $f_c + mf_m$.

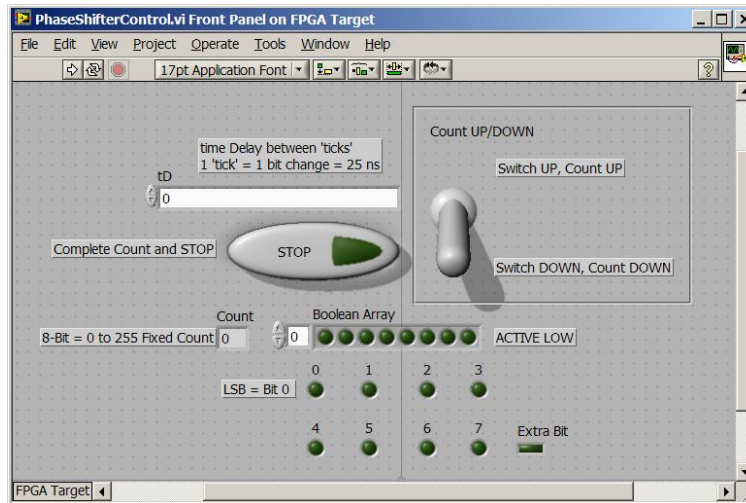


By cycling through 360° (2π) of phase at this periodic rate a known frequency/Doppler shift is produced against which the weather radar can be calibrated. This periodic phase cycling (and thus frequency translation) is implemented in the ACS using a digital phase shifter. Velocity spread can be added to the Doppler shifted signal by varying the frequency of the sawtooth waveform used in the phase modulator. The frequency should be varied in accordance with a Gaussian random variable that has been low pass filtered to produce a signal with the desired correlation time.

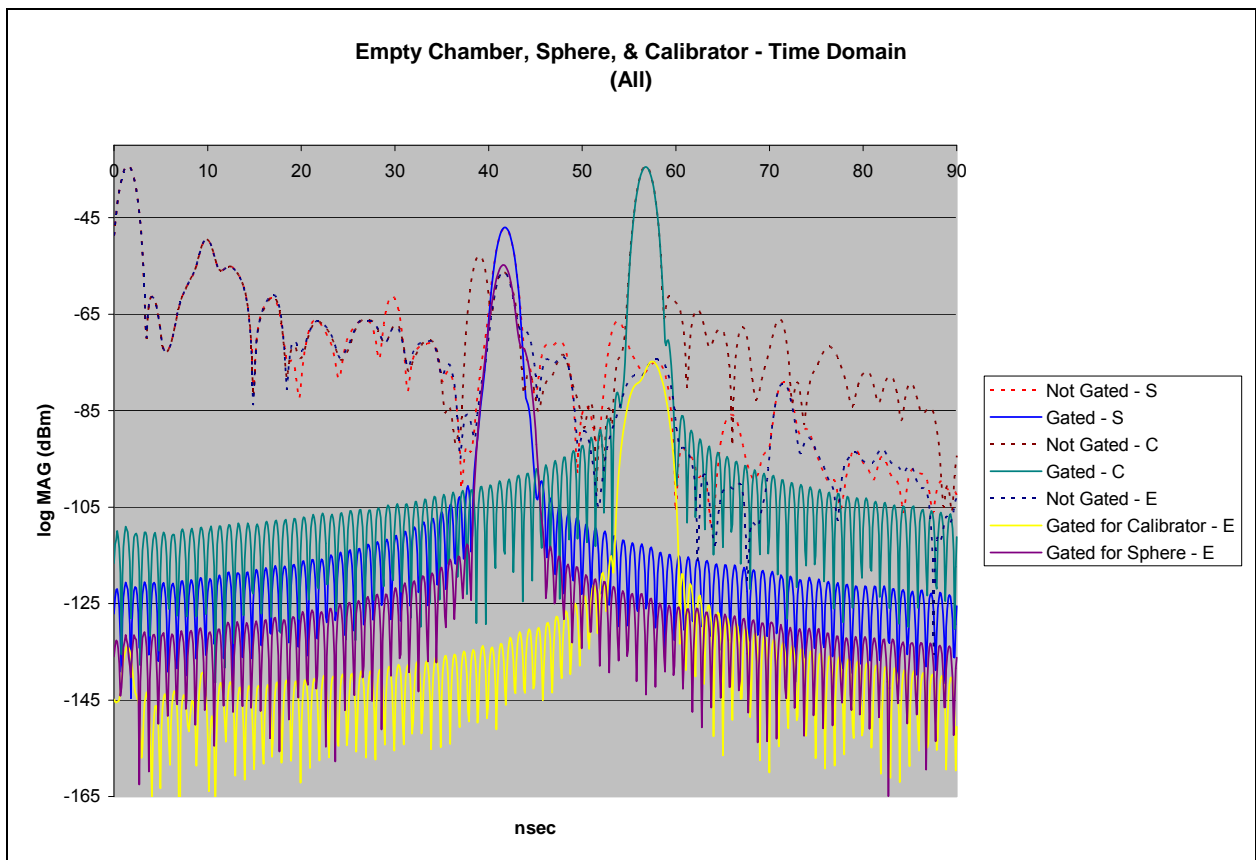
On the basis of these principles, the ACS was constructed (RF box internal configuration digital photograph follows):



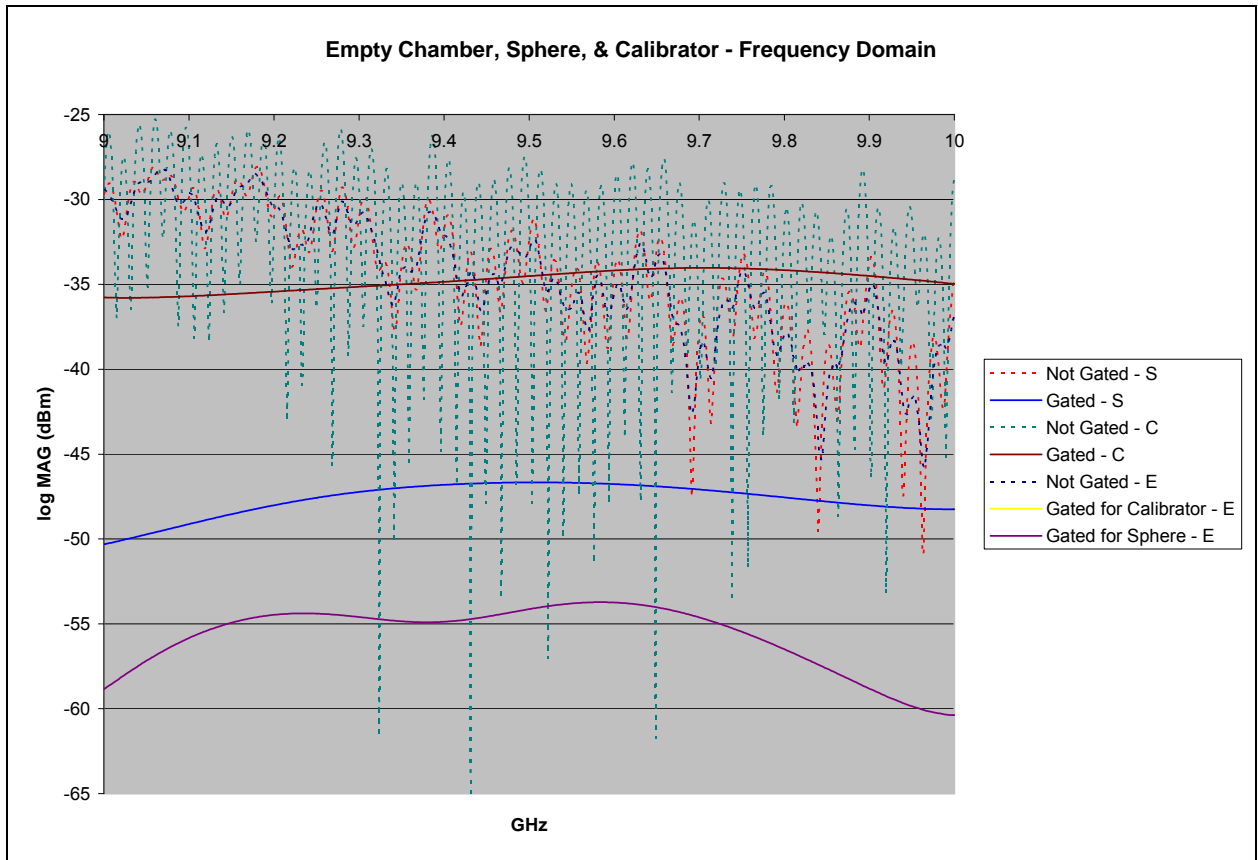
All control of the ACS was achieved through National Instruments LabVIEW (user interface shown below).



After construction, measurements were made to determine the equivalent reflectivity (RCS) of the ACS. The result of those measurements and that entire testing process are presented below.



Time vs. Amplitude for Empty Chamber, Sphere and ACS. (ESC_plotTA)



Frequency vs. Amplitude for Empty Chamber, Sphere and ACS. (ESC_plotF)

The first plot is a composite of all data sets in the time domain, not zoomed (all). The second plot is a composite of all data sets in the frequency domain. All data sets include the measured data for the three targets: an Empty Anechoic Chamber (chamber), the 12" Aluminum Sphere (sphere) and the ACS (calibrator). Timing gates were placed around the sphere's location (42 ns) and calibrator's location (57 ns). These timing gates eliminated undesirable echoes. One such undesirable echo was at <2 ns. This echo corresponds to the coupling between transmit and receive antennas which were placed about 18" apart. There are seven graphed data sets on each plot: the sphere without a time gate and with a time gate centered on its 42 ns return, the calibrator without a time gate and with a time gate centered on its 57 ns return, the empty chamber without a time gate and with a time gate for the calibrator, then with a time gate for the sphere.

For the sphere, the time gate (G2) was centered at 41.8 ns and spanned 39.8 to 43.8 ns. For the calibrator, the time gate (G1) was centered at 56.8 ns and spanned 54.8 to 58.8 ns. The time gates correlate directly to target return distances. The distance

(range) from transmit and receive antennas in the anechoic chamber to the target pedestal inside the chamber is 19 feet (or 38.6 ns in time). The distance is traversed twice (once to the target and then from the target) at the speed of light. The reason the time gate for the sphere was observed at and consequently set at 42 ns is the sphere was suspended from the ceiling of the chamber above and slightly behind the target pedestal inside the anechoic chamber. This added approximately an additional 1.6 feet of distance and 3 ns of time because the hypotenuse rather than the longest leg of the triangle was traversed. The reason the time gate for the calibrator was observed at and consequently set at 57 ns is different than for the sphere. This time gate was approximately 8 ns greater because of the time delay due to transmission line lengths rather than target distance. The 8 ns is almost 8 feet (one-way path), slightly greater than the straight line distance between transmit and receive antennas of the ACS (as expected). See the example calculations below for the mathematical relation between time and distance (two-way path).

$$c = 3.00 \times 10^8 \text{ m/s}$$

$$R = 5.7912 \text{ m (19 feet)}$$

$$\frac{2R}{c} = 38.6 \text{ ns}$$

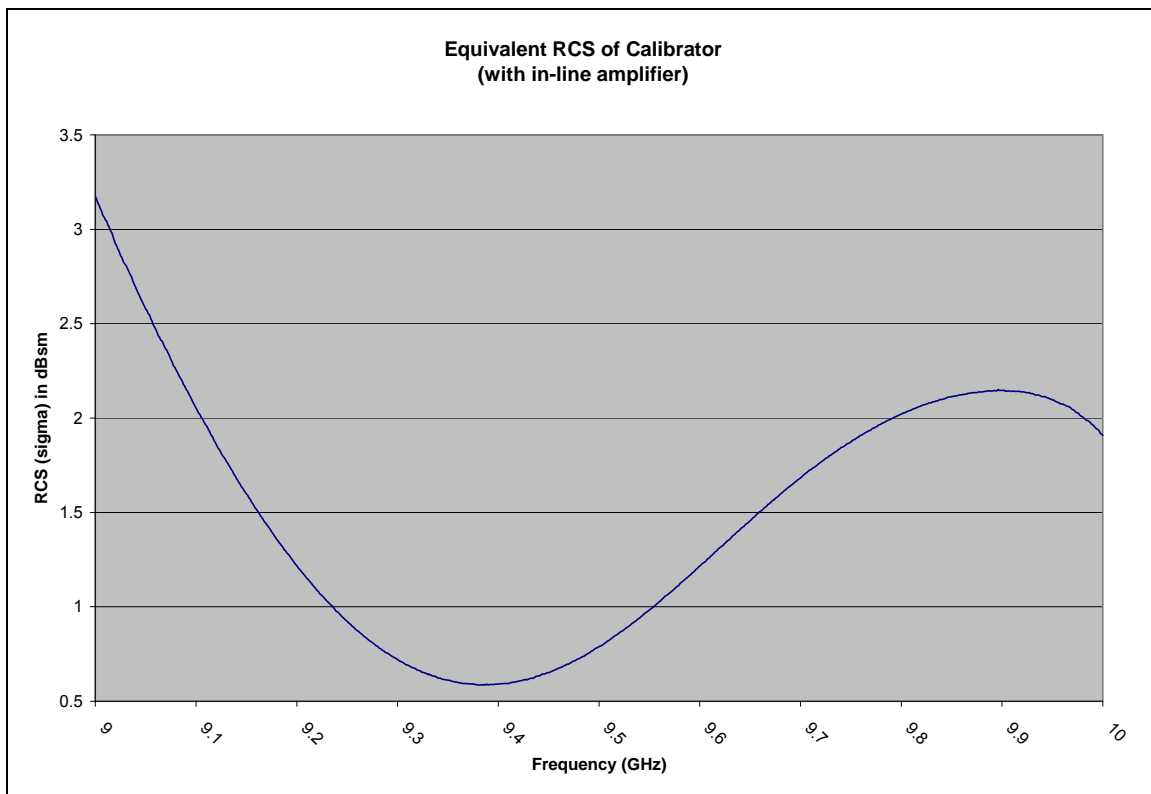
$$t = 41.8 \text{ ns}$$

$$\frac{t \times c}{2} = 6.2700 \text{ m (20.6 feet)}$$

Initially, calculations were made to predict the received power from both the ACS and 12" Sphere. The expected (calculated) value for received power from the ACS was -36.5dBm. The measured value for received power from the ACS was -34.0dBm. The expected (calculated) value for received power from the 12" Sphere was -47.9dBm. The measured value for received power from the 12" Sphere was -46.7dBm. The expected (calculated) values very nearly equaled the measured values.

The next plot is from the data in the frequency domain of both the sphere and calibrator previously presented, now used to calculate the equivalent RCS of the calibrator. Measurements were made from 9-10 GHz. The Vector Network Analyzer used in the test setup as the signal source and receiver in the anechoic chamber recorded the magnitude of the returned amplitude power in logarithmic form (log MAG) in units of

milliwatts (dBm). All measurements are in the frequency domain gated for time (FG). This includes both the sphere (SFG) and calibrator (CFG). The measured values were very close to the expected (calculated) values. The received power for the 12” Aluminum Sphere was calculated to be -47.8679 dBm and observed to be near -47 dBm. The received power for the calibrator was calculated to be -36.5032 dBm and observed to be near -35 dBm. The RCS of the sphere was previously calculated to be -11.3688 dBsm (S-RCS). To calculate the RCS of the calibrator (C-RCS) based on the observed/measured data, the CFG - SFG= Δ (dB) was added to the sphere’s RCS. Over the entire frequency band the C-RCS varied from 0.6 to 3.2 dBsm. Note all these measurements in the chamber included the use of the RF amplifier within the calibrator system. When used with the weather radar, signal levels are great enough and ranges short enough such that an RF amplifier is not needed. Furthermore, calculations are made to make sure the signal return to the radar is in the proper range to prevent receiver saturation.



With these measured values the equivalent RCS of the ACS was observed to range from 0.6 to 3.2 dBsm across the 9-10 GHz RF band. On average (mean), the

equivalent RCS of the ACS was 1.4934 dBsm. The median was 1.5101 dBsm. The high value was 3.1742 dBsm at 9 GHz and the low value was 0.5862 dBsm at 9.38 GHz.

An active calibrator system (ACS) for weather radar was successfully designed and implemented. The ACS was verified to be a functional weather radar active calibration system under laboratory testing. It successfully provided the means (met the requirements) to verify all three of the signal parameters measured (estimated) by a weather radar. These include the zeroth Doppler moment (reflectivity), first Doppler moment (average radial velocity), and second Doppler moment (velocity spread).

ACKNOWLEDGMENTS

I would like to thank the many people who were involved with the completion of both my thesis and Masters Degrees at the Naval Post Graduate School (NPS). Without the assistance of these people, I would not have been able to achieve so much or to get to where I am today. First, I would like to thank Dr. Jeffrey Knorr who acted as my principle advisor throughout the course of my thesis and my two years at NPS. I learned a great deal from Dr. Knorr in and out of the classroom and consider myself fortunate to have been a part of his research. I also credit Bob Broadston for a large part of the success of my thesis. Bob continually shared his experience with me, and always made me feel a part of a working relationship with him. I cannot thank Bob enough for his constant assistance in addressing many of the day to day issues that arose as I completed the research portion of my thesis. I would also like to thank Lt. Colonel Terry Smith. As an active member of the United States Air Force and the Program Officer of the Information Sciences Department, Lt. Col. Smith provided me with an insightful, practical perspective that wholly complemented my meetings with Dr. Knorr. I would like to thank him for the time he committed to advising me during my thesis research and editing my written thesis. Finally, I would also like to acknowledge Dr. David Jenn, an outstanding professor, for his instruction and guidance during my time at NPS.

At NPS, I was given the opportunity to learn at an institution that provides practical skills critical to our nation's defense, but also holds high the value of education beyond mere training. I am extremely honored to have had the privilege to attend one of our nations leading defense institutions while serving my country as a U.S. Federal Government civilian employee. I trust that our nation's leadership will continue to value unique centers of excellence for defense matters, such as the Naval Postgraduate School, and civilian defense programs, such as the one in which I participated.

To all of those individuals from whom I have learned during the course of my formal education, thank you. Both professors and peers were critical to the success achieved during my educational journey. To my family and friends, I will never forget

what you have done for me along the way. While the completion of this thesis and these graduate degrees marks the end of a chapter in my educational journey, I know it certainly is not the end of my education. I look forward to furthering my education while serving my country as I continue my career.

I. INTRODUCTION

A. BACKGROUND

Pulsed weather radars produce estimates of reflectivity, mean radial velocity and velocity spread using echo signal samples from a wide variety of weather targets. From these radar return signals, other meteorological quantities such as rainfall rate and wind field characteristics are also derived. Estimates are derived from the parameters of the modified radio frequency (RF) echo signal (amplitude and frequency/phase) scattered from the target back in the direction of the radar. RF scattering and propagation effects are the mechanisms which modify radar echo signal parameters and it is those modifications that contain the desired weather-related information as a modulation of the carrier wave. Bias and variance in the weather signal parameter estimates naturally influence the accuracy of all subsequent quantities produced, and condition assessments made. For meteorological products to reflect weather conditions as accurately as possible, the uncertainty of each estimate must be minimized, or accurately characterized. If radar system parameter accuracies are not precisely known, the reflectivity estimate will be biased and thus, assessments of true conditions could be either misleading or masked. A well-controlled calibration process is therefore critical to reduce reflectivity bias due to imprecise knowledge of the radar system parameters. There may also be bias associated with the statistical estimation process and its resulting estimator, but poor calibration is the most serious source of error. The variance of the estimate of interest will depend on the number of samples and their correlation.

B. RESEARCH OBJECTIVE

The research objective of this thesis is to design and implement a radar calibration system (calibrator). The calibrator is for specific use with the Naval Postgraduate School's MWR-05XP¹ X-band weather radar, but the general concept is applicable to all

¹ World's first and currently (2007) only Mobile Weather Radar created in 2005 operating at X-band in Pulse-Doppler with a Phased-Array. In acronym, this is the MWR-05XP.

radars. The calibrator presented is an active, external calibrator intended to verify end-to-end radar system performance. An ideal active calibration system produces a radar return with known RCS and Doppler shift permitting the determination of the radar calibration constant. As of 2005, the MWR-05XP operates with a calibration constant determined through the use of radar system parameters that have previously been only approximately known. A known RCS return condition can be obtained when a metal sphere is used to calibrate a radar. This calibration method involves the suspension and isolation of the sphere from great height at long distance² in ideal weather conditions. These pristine conditions are not always available when and where the MWR-05XP is in use. In fact, the MWR-05XP is primarily located at the Center for Interdisciplinary Remotely Piloted Aircraft Studies (CIRPAS) in Marina, CA on the grounds of the municipal airport (a relatively small workspace) where the heights and distances required for calibration are never available. The calibration of the MWR-05XP is done periodically on a large test range at Camp Roberts, CA over 100 miles away. The calibrator research involved in this thesis effort will eliminate the prohibitive burdens (physical conditions and workload) required with flying the sphere while simultaneously allowing more specific calibration parameter determinations along with the inherent advantage of more frequent calibration constant verification. The calibrator also allows the added calibration of Doppler-related quantities (which is not currently possible). The final advantage is the end-to-end method. It uses the entire radar system in normal operating mode. Calibration systems sometimes rely on piecemeal measurements that are combined together for performance estimates, thus leading to larger uncertainties. This system does not.

Research in this effort will implement an existing design of an active calibrator for the MWR-05XP and will not involve the creation of an innovative design configuration. It will neither involve design optimization, nor investigation of alternatives. This calibrator, once implemented, will be used with the MWR-05XP exclusively (i.e. no other radars involved) to determine the radar calibration constant.

² Sphere heights of 0-1000m with ground distance equal to 700m have been used with the MWR-05XP to cover beam elevation angles from 0-55°.

The type of signal used by the calibrator in this process will be of the minimum required complexity, although the performance parameters involved are those that most accurately reflect operational weather characteristics.

The primary hardware involved with this thesis effort will be a digital phase shifter, programmable attenuator, and real-time controller with reconfigurable chassis. The only software involved will be LabVIEW (in the manipulation of the controller hardware) and MATLAB (in the analysis of data and display of results).

C. RELATED WORK

The thesis by Schroder presents a weather radar signal simulator. According to the abstract of the Schroder thesis,

the simulator was developed in MATLAB and implemented several different functionalities allowing for stepped frequency, multiple pulse repetition frequencies (PRFs), pulse compression using a chirp waveform, and variation of both weather and radar input parameters. Post-detection processing capabilities include autocorrelation and Fast Fourier Transform (FFT - for single PRF only); estimation of weather parameters such as reflectivity (Z); average Doppler, radial velocity, and velocity spread; pedagogical plots including a phasor plot of phase change over time and a velocity histogram, instantaneous observed reflectivity and power for each pulse over time.[1]

The output of Schroder's simulator was modified to provide the calibrator controller software with Doppler frequencies and amplitude levels indicative of real-world weather effects for use in the calibration process.

The article by Marshall and Hitschfeld investigates the random fluctuations of the radar echo produced from a random array of scatterers (such as weather scatterers). According to the introduction to this article, "the intent is to establish (theoretically and by analogue computation) the extent of the limitation these fluctuations have on the accuracy of the measurement information obtainable. Additionally, what improvements may be effected by averaging or by modifying the method of pulsing or scanning are

explored.”[2] The Marshall and Hirschfeld theory is used in this research to produce the amplitude levels indicative of real-world weather effects for use in the calibration process.

The report by Pratte and Ice explores external radar calibration methods. According to the executive summary of the Pratte and Ice report, “the targeted radar for this report is the WSR-88D, the weather radar in use (as of 2007) by the U.S. National Weather Service in its national weather radar network. It reviews availability and feasibility of “calibration aids”, equipment and software that will assist in verifying WSR-88D reflectivity measurement and in reducing its uncertainty.”[3] The recommendations of the Pratte and Ice report were used to enhance understanding of the general weather radar calibration problem and its alternative solutions.

The text by Doviak and Zrinc emphasizes the application of Doppler radar for the observations of stormy and clear air. According to the introduction (1.2) to the text, “it presents a comprehensive treatment of the techniques used in extracting meteorological information from weather echoes and relates radar and signal characteristics to meteorological patterns.”[4] The Doviak and Zrinc text served as a classic reference book on radar theory and accepted techniques applied to meteorology.

The paper by Knorr presents a derivation of two correction factors to the classic Probert-Jones weather radar equation for use with frequency agile, phased array weather radars. According to the abstract of this paper, “the result is an extended weather radar equation for use with these advanced weather radars. The two derived factors account for the effect of a changing RF carrier and electronic beaming steering not present in classic weather radars when computing a reflectivity estimate from weather signal data samples.”[5] The Knorr paper, as well as personal discussions with its author (an advisor to this thesis), provided the necessary understanding of the unique calibration requirements of these advanced weather radars from theory to practical application.

Chapter Four of the Federal Meteorological Handbook discusses potential operational uses of the WSR-88D products as well as the structure of certain meteorological phenomena. According to the introduction to Chapter 4 (4.1), “it

provides information on observing and forecasting meteorological phenomena using this radar's products.”[6] Of particular interest in the development of this thesis's research was the discussion in early sections of operationally troublesome radar returns due to such things as ground clutter and sidelobes. The pictorial representations in the Meteorological Handbook were invaluable.

D. ORGANIZATION OF THE THESIS

There are four main chapters and several appendices which comprise this thesis. Chapter I gives a background of the radar calibration problem along with the research objectives for this specific project. Related works are introduced and discussed. An executive summary is also included. Chapter II explains the theory behind the operation of weather radar (how the three principle quantities of reflectivity, velocity and velocity spread are measured and related to signal parameters). The density function for precipitation, relation between signal correlation and velocity spread, and fundamentals of weather radar signal parameter estimation are given. Chapter III describes the specific calibrator design in explicit detail. Measured results are presented and explained in appendices. Chapter IV draws conclusions on the success of the implementation and provides recommendations for future work.

THIS PAGE INTENTIONALLY LEFT BLANK

II. BACKGROUND AND SUPPORTING THEORY

This chapter presents and explains the theory behind the operation of weather radar. The discussion includes how the three principle quantities of reflectivity³, mean radial velocity⁴ and velocity spread⁵ are measured and are related to radar signal parameters. The density function for precipitation, relation between signal correlation and velocity spread, and fundamentals of weather radar signal parameter estimation are given.

Significant portions have been excerpted from Chapter 2 “Weather Radar and Weather/Rain Theory” of Ulf Schroder’s thesis “Development of a Weather Radar Signal Simulator to Examine Sampling Rates and Scanning Schemes.” Both Schroder’s thesis and this thesis are in support of the larger research project/interest of Dr. Jeffrey Knorr (advisor to both theses). Much of the background and supporting theory used in Schroder’s thesis (completed 2005) applies to this thesis (completed 2008) and the larger research project/thrust.

A. WEATHER RADAR VS. TRADITIONAL RADAR

Weather radar samples the scattered RF energy from distributed targets such as precipitation, hail, snow, melting ice, and clear air. This is unlike traditional radar which views these returns as clutter, unwanted echoes that interfere with the observation of the return from a point target of interest. Traditional radar usually implements Doppler filtering to discriminate between slow moving weather clutter and fast moving point targets. In this application, the scattered energy contains descriptive characteristics of the weather condition.

³ Function of the scatterer intensity.

⁴ Function of the mean component of scatterer motion in the radial direction from the radar.

⁵ Function of the variability of Doppler velocity values due to turbulence within and velocity shear across the sampling volume.

B. RADAR RESOLUTION CELL

Weather radar differs from traditional radar in another important way. Traditional radar seeks to encapsulate its target of interest (approximately a point target) entirely within a single radar resolution cell. For weather radar this is neither practical nor informative at either the micro or macro scales. It is impractical to image a single rain drop or an entire storm and even if it were possible the information provided would not be especially useful. Instead, weather radars image a volumetric segment of the meteorological phenomena of interest. This volume is defined by a segment of propagated energy (see Figure 1) covering pulse width, τ . The depth of this segment depends on the pulse width according to:

$$d_v = \frac{c\tau}{2}. \quad (2.1)$$

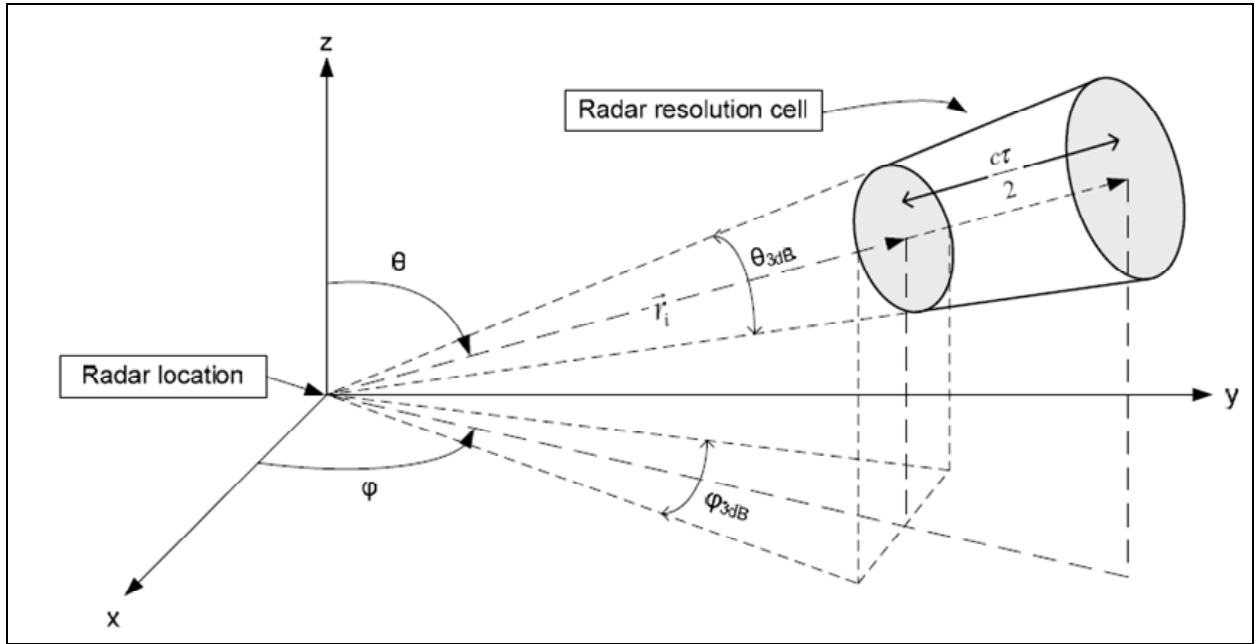


Figure 1. Illustration of Radar Resolution Cell. [From 1]

Schroder's figure above illustrates and later expressions (specifically, reflectivity factor Z) use the volume of the resolution cell. It is uniquely defined here for convenience, as:

$$\Delta V = V_c = \frac{\pi}{4} (R\theta_B)(R\phi_B) \left(\frac{c\tau}{2} \right) \frac{1}{2\ln(2)} \quad (2.2)$$

See Chapter II, Section E, Subsection 1, “Antenna Gain and Beam effective Solid Angle,” for an explanation of the last factor, $\frac{1}{2\ln(2)}$.

C. SWERLING TARGET TYPES

Meteorological conditions produce a radar target return that varies with time. Besides the target itself, fluctuations in the target’s return may also be caused by variations in the medium between the target and the radar (atmospheric and meteorological conditions not the intended target), radar system instabilities (platform motion and equipment instabilities), target aspect changes, and many other variables. In order to analyze all of this variation, the target is modeled as an overall system. For systems analysis purposes, only the ‘gross’ behavior of a target needs to be known, not every detail of all the complicated physics involved in the complex scattering situation. Therefore, fluctuations caused by all of these many sources (exclusive of those caused simply by a change in range) are usually grouped together and represented by a single quantity for a specific target type.

The following excerpt was relayed from the radar text by Skolnik, although nearly every radar text contains some explanation of Swerling target types. Let σ be a random variable with a probability density function (PDF) that depends on the factors associated with target fluctuations other than a change in range and the overbar represents the average value of the random variable. Two PDFs are commonly used:

$$p(\sigma) = \frac{1}{\sigma} e^{-\sigma/\bar{\sigma}}, \text{ PDF \#1} \quad (2.3)$$

and

$$p(\sigma) = \frac{4\sigma}{\bar{\sigma}^2} e^{-2\sigma/\bar{\sigma}}, \text{ PDF \#2} \quad (2.4)$$

These two PDFs approximate the nature of the scattering of RF energy from many targets. There are targets which consist of many independent scattering elements of

which no single one (or few) dominates (PDF #1) and targets which have one main scattering element that dominates in the presence of smaller independent scattering sources (PDF #2). These two PDFs along with the rate at which the fluctuations take place allow the definition of four types of radar targets, also known as Swerling target types. Swerling target types I and II are associated with PDF #1 and types III and IV with PDF #2. The rate of the fluctuations in this scattering is the other differentiating factor which further defines the Swerling target type. There are targets with slow fluctuations (scan-to-scan) and targets with rapid fluctuations (pulse-to-pulse). Swerling target types I and III are of the former and types II and IV of the latter.

Swerling Target Types and Probability Density Functions		
	PDF #1	PDF #2
Slow Fluctuations (scan-to-scan)	Type I	Type III
Rapid Fluctuations (pulse-to-pulse)	Type II	Type IV

Table 1. Swerling Target Types and Probability Density Functions.

As a weather radar, the MWR-05XP targets Swerling types I and II. The calibrator described in this thesis was consequently developed for those same Swerling types, but the general process of the design and implementation of a radar calibrator can be applied to any radar and Swerling target not just weather radars and Swerling types I and II.

D. SAMPLE CORRELATION

To paraphrase Schroder, the power level of scattered RF energy from distributed targets varies over time. An estimate of the average power level is achieved by averaging power over a number samples. The variance of a reflectivity estimate can be improved simply by averaging more samples. However, these samples may not be independent of one another. Independence signifies a sufficient level of change in the distribution of the target within the volume being imaged. For this ‘sufficient’ level of change to have

occurred there exists a minimum required period of time. This minimum time period guarantees samples are not correlated from one observation period to the next.

Schroder explains, "The power spectral density of a meteorological signal is approximately Gaussian and can be written as

$$S(f) = S_0 e^{-\left\{ \frac{(f-\bar{f})^2}{2\sigma_f^2} \right\}} \quad (2.5)$$

where f is the Doppler frequency and σ_f^2 is the Doppler spectrum variance. Taking the Fourier transform of Equation (2.5) and normalizing results in the correlation coefficient

$$\rho(t) e^{-\left(\frac{t^2}{2\sigma_t^2} \right)} \quad (2.6)$$

where σ_t^2 is the time spectrum variance and is related to σ_f^2 by

$$\sigma_t = \frac{1}{2\pi\sigma_f} \quad (2.7)$$

and

$$\sigma_f = \frac{2\sigma_v}{\lambda}. \quad (2.8)$$

By using the correlation coefficient a measure of minimum difference in time can be estimated ensuring dependent or independent samples. Nathanson claims that for independent sampling $\rho(\tau) < 0.02$ is required whereas $\rho(\tau) > 0.15$ will ensure dependence. Doviak and Zrnić set a correlation threshold for coherence at $\rho^2(\tau) \geq e^{-1}$ which corresponds to a value of $\rho(\tau) \geq 0.6$. Using this threshold renders

$$T_s \leq 0.25 \frac{\lambda}{\pi\sigma_v} \quad (2.9)$$

For highly correlated samples."

A level of 'sufficient' change has occurred within an observation period for a sample so that any subsequent samples may be deemed independent if:

$$T_s > 0.70 \frac{\lambda}{\pi\sigma_v} \quad (2.10)$$

where T_s is the sample time period and σ_v is the RMS velocity spread.

E. ESTIMATION OF POWER DENSITY AND REFLECTIVITY (Z)

1. Antenna Gain and Beam effective Solid Angle

Antenna gain varies depending on azimuth and elevation angles for directive antennas. For a point target, antenna gain is constant only for a fixed azimuth and elevation angle defined between the radar and a point in space at a specific time. For a volumetric target, antenna gain varies across a range of azimuth and elevation angles defined between the radar and a volume of space at a specific time. The antenna pattern function, $f(\theta, \phi)$, integrated over the solid angle corresponding to the radar resolution cell is used to estimate a value of antenna gain for volumetric targets.

From Schroder (and Probert-Jones as the original source), “The magnitude of the antenna pattern function is first squared to yield a power relation and squared again to agree with the two way propagation of radar.

$$\int_{4\pi} |f(\theta, \phi)|^4 d\Omega \quad (2.11)$$

The Gaussian Pattern Model is the antenna pattern function that will be used. It provides a good approximation of the main beam between the half power points. Extending it in both azimuth and elevation provides

$$|f(\theta, \phi)|^2 = e^{-\left[\frac{\theta^2}{\gamma^2} + \frac{\phi^2}{\delta^2}\right]}, \quad |\theta| \leq \frac{1}{2}\theta_1, \quad |\phi| \leq \frac{1}{2}\phi_1 \quad (2.12)$$

where $\gamma^2 = \frac{\theta_1^2}{4 \ln 2}$ and $\delta^2 = \frac{\phi_1^2}{4 \ln 2}$, and θ_1, ϕ_1 are the half power beam widths in the orthogonal planes.

Performing integration over the solid angle gives

$$\int_{4\pi} |f(\theta, \phi)|^4 d\Omega = \int_{-\infty}^{+\infty} \int_{-\infty}^{+\infty} e^{-\left[\frac{2\theta^2}{\gamma^2} + \frac{2\phi^2}{\delta^2}\right]} d\theta d\phi = \frac{\pi\theta_1\phi_1}{8 \ln 2} (1 - \xi) \quad (2.13)$$

where $\xi < 0.034$ and represents the contributions from the sidelobes. In a further approximation, at its maximum value the $(1 - \xi)$ term contributes a negligible 0.15 dB and therefore can be ignored.”

The final form of the expression used to approximate beam solid angle for volumetric targets is

$$\int_{4\pi} |f(\theta, \phi)|^4 d\Omega = \frac{\pi \theta_1 \phi_1}{8 \ln 2}. \quad (2.14)$$

See also the Probert-Jones paper[7]. The equation above gives beam solid angle contributing to the volume return. Note this result is based on a Gaussian approximation to the beam pattern. As Dr. Knorr shows in his paper, integration of an actual antenna pattern will generally result in a correction which may not be negligible.

2. Physics of Precipitation

The following presents some basics in precipitation physics relevant to developing a physical understanding of precipitation, specifically rain the primary target of weather radar. The following three sections have been selectively chosen from a larger discussion of the physics of precipitation by Schroder. Each of the three sections’ text has been paraphrased and equations reproduced verbatim.

a. Size and Shape

Raindrop size determines the terminal velocity at which the drop falls and the shape of the drop. Small drops, with a diameter $D < 0.35$ mm, are spherical. Medium size drops, with diameters $0.35 \text{ mm} < D < 4$ mm, have progressively flattened bases and are approximated as spheroids. Large drops, $D > 4$ mm, do not last very long and tend to break apart upon collision. The largest drops, $D > 10$ mm, are unstable and break apart without collision.

b. Drop Size Distribution (DSD)

Radar cross section (RCS) density, $\bar{\eta}$, is the average RCS density per unit volume, as previously mentioned, and for independent scattering is the sum of the RCS of all scatters in the return volume divided by that volume. The DSD represents the diameter density (mm/m³) of drops for all diameters. The Marshall-Palmer DSD provides a general model:

$$\begin{aligned} N(D) &= N_0 e^{-\Lambda D} \\ \Lambda &= 4.1 R^{-0.21} \text{mm}^{-1} \\ N_0 &= 8 \times 10^3 \text{m}^{-3} \text{mm}^{-1} \end{aligned} \quad (2.15)$$

Applying truncation with a maximum drop diameter of D_{\max} yields

$$N(D) = \begin{cases} N_0 e^{-\Lambda D}, & D < D_{\max} \\ 0, & D_{\max} < D \end{cases}. \quad (2.16)$$

c. Rainfall Rate

Rainfall rate determines the depth of accumulated water per unit time. It can be derived from water content and fall speeds. A cloud's water density is

$$M = \frac{\pi}{6} \rho_w \int_0^{\infty} D^3 N(D) dD \quad (2.17)$$

where ρ_w is the water density of a rain drop.

Turning this into rainfall rate

$$R = \frac{\pi}{6} \int_0^{\infty} D^3 N(D) v(D) dD. \quad (2.18)$$

Rainfall rate is estimated from reflectivity using any one of a number of slightly different models, $Z = Ar^b$. $Z = 300r^{1.4}$, for example, is the current WSR-88D default model. The best rainfall model depends upon the type of storm or equivalently, drop size distribution. Dual polarization radars provide more information about drop size and thus rainfall rate. Latest results from JPOL experiment (dual polarization WSR-88D at NSSL) are given in Ryzhkov[8].

3. Weather Radar Range Equation and Estimation of Reflectivity

Again, following Schroder, the basic form of the radar range equation (neglecting minor losses):

$$P_r = \frac{P_t G_t G_r \sigma \lambda^2}{(4\pi)^3 R^4} \quad (2.19)$$

“In the basic form of the weather radar equation radar cross section (RCS), σ , is replaced by RCS density, $\bar{\eta}$, which is the expected RCS density per unit volume. Since the target is a volume target, the expected return needs to be integrated over the whole volume, which can be divided into the solid angle and depth of the return. Letting the power level at the target be

$$P_{target} = \frac{P_t G_t}{4\pi R^2} dA = \frac{P_t G_t}{4\pi} d\Omega \quad (2.20)$$

and integrating the return power over the return volume renders

$$\bar{P}_r = \int dP_r = \frac{P_t G_t G_r \lambda^2}{(4\pi)^3} \int_R^{R+\frac{c\tau}{2}} \frac{dR}{R^2} \bar{\eta} \int_{\Omega} |f(\theta, \phi)|^4 d\Omega = \frac{P_t G_t G_r \lambda^2}{1024\pi^2} \frac{c\tau}{R^2} \frac{\theta_1 \phi_1}{\ln 2} \bar{\eta} \quad (2.21)$$

recognizing that $R \approx \frac{c\tau}{2}$.

Radar meteorologists use the reflectivity factor, Z , instead of RCS density where

$$\bar{\eta} = \frac{\pi^5}{\lambda^4} |K_w|^2 Z \quad (2.22)$$

and

$$Z \equiv \frac{1}{V} \sum_{i \in V} D_i^6. \quad (2.23)$$

Substituting Equation (2.22) into Equation (2.21) and solving for Z yields the reflectivity estimator

$$\hat{Z} = \bar{P}_r \frac{1024\pi^2 R^2 \ln 2}{P_t G_t G_r \lambda^2 c \tau \theta_1 \phi_1} \frac{\lambda^4}{\pi^5 |K_w|^2} = \bar{P}_r \frac{1024 R^2 \ln 2 \lambda^2}{P_t G_t G_r c \tau \theta_1 \phi_1 \pi^3 |K_w|^2}. \quad (2.24)$$

For an assumed continuous distribution of drops sizes with diameter density $N(D)$ Equation (2.23) becomes

$$Z = \int_0^{D_{\max}} D^6 N(D) dD. \quad (2.25)$$

Solving the integral form for an assumed Marshall-Palmer Drop Size Distribution (DSD) Equation (2.15), yields

$$Z = \int_0^{\infty} D^6 N(D) dD = \frac{6! N_0}{(4.1R^{-0.21})^7} \quad (2.26)$$

Drops do not exist in sizes ranging up to infinite diameter, but are likely to be limited by a maximum diameter. Doviak and Zrnić state that Equation (2.26) overestimates Z and suggest a truncated DSD with $D = D_{\max}$. In this case,

$$Z = \frac{N_0}{(4.1R^{-0.21})^7} \gamma(7, a) \quad (2.27)$$

where $a = \Lambda D_{\max}$ and $\gamma(7, a)$ is the incomplete Gamma function. Equations (2.26) and (2.27) provide an analytical means for computing Z .

F. RADAR PRINCIPLES AND WEATHER RADAR EQUATION CORRECTION

The basic results for phased array weather radar are presented from Knorr's paper. This paper addresses issues unique to frequency hopping, phased array weather radars and quantifies the need for a target of known radar cross section (RCS).

“The first term in the equation below indicates those radar system parameters which may not be precisely known.

$$\left[\frac{P_t G_{rx} G_0^2}{L_s} \right] \left[\frac{(\lambda_0/\lambda)^4 (\cos^2 \theta) \lambda^2 \sigma}{(4\pi)^3 R^4 L_a} \right] = P_{out} \quad (2.28)$$

where

λ_0 = reference⁶ wavelength (m)

⁶ The choice of reference wavelength within the operating band of the radar is arbitrary.

L_s = radar system losses (ratio)
 L_a = atmospheric propagation loss (ratio)
 P_{out} = output power (W)
 R = range to target (m)
 P_t = transmit power
 G_{rx} = receiver gain
 G_0 = gain at the reference frequency, f_0
 λ = operating wavelength (m)
 θ = angle of the antenna beam with respect to boresight or the normal to the array face
 σ = target radar cross section (RCS) (m^2)

The objective of calibration is to determine the composite of these factors with a single measurement. To simplify this process, several conditions can be selected. These include: calibration on boresight with the antennas of the active calibrator system (ACS) and the radar ($\theta = 0$), calibration at the reference RF center frequency ($\lambda = \lambda_0$), and calibration at a range that is short enough that atmospheric losses can be ignored ($L_a = 1$). Then, the equation simplifies and rearranges to:

$$\left[\frac{P_t G_{rx} G_0^2}{L_s} \right] = \left[\frac{(4\pi)^3 R^4 P_{out}}{\lambda_0^2 \sigma} \right] \quad (2.29)$$

With this relationship, a measure of the radar receiver's output power and range for a reference target of known cross-section (the ACS's equivalent reflectivity) will determine the radar system constant (left hand side of the equation)."

For frequency agile, phased array weather radars, the equation for reflectivity takes the form

$$Z = \left[\frac{1024 \ln 2 \lambda_0^4}{\pi^3 (c\tau) |K|^2 \lambda_0^2} \right] \left[\frac{1}{(\theta_{B0}^{br} \phi_{B0}^{br})} \right] \left[\frac{L_s}{P_t G_{rx} G_0^2} \right] \left[\frac{L_a \overline{P_{out}}}{(f/f_0)^4 \cos \theta} \right] (R^2) \quad (2.30)$$

where

Z = reflectivity (mm^6/m^3)
 λ_0 = reference wavelength (m)
 L_s = radar system losses (ratio)
 L_a = atmospheric propagation loss (ratio)
 $\overline{P_{out}}$ = average output power (W)
 R = range to target (m)
 c = speed of light in a vacuum = 3×10^8 m/s
 τ = pulsewidth (s)

$$|K|^2 = \left| \left(\varepsilon_r - 1 \right) / \left(\varepsilon_r + 2 \right) \right|^2 \approx 0.93 \text{ (H}_2\text{O)}$$

ε_r = hydrometeor relative permittivity

θ_{B0}^{br} and ϕ_{B0}^{br} are the broadside 3 dB principal plane beamwidths at the reference frequency

P_t = transmit power

G_{rx} = receiver gain

G_θ = gain at the reference frequency, f_θ

f = operating frequency (Hz)

f_θ = reference⁷ frequency (Hz)

θ = angle of the antenna beam with respect to boresight or the normal to the array face

Note that the units of Z are given correctly (mm^6/m^3) by the first two terms of Equation (2.30) if range is in millimeters, λ_0 in the numerator of the first term is in millimeters and the quantities in the denominator of the first term are in meters.

This is the corrected form of the classical Probert-Jones classical weather radar equation as derived by Dr. Jeffrey Knorr in his paper, “Weather Radar Equation Correction for Frequency Agile and Phased Array Radars.”

The third term contains radar system parameters which may not be precisely known. The objective of calibration is to determine the composite effect of these factors. The composite of these factors is also known as the radar system calibration constant. In Dr. Knorr’s paper it has been shown that, for the case where the reference target is on boresight, $\theta = 0$, the measurement is made at the reference frequency, $\lambda = \lambda_\theta$, and the range is short ($L_a = 1$)

$$\left[\frac{P_t G_{rx} G_\theta^2}{L_s} \right] = \left[\frac{(4\pi)^3 R^4 P_{out}}{\lambda_0^2 \sigma} \right]. \quad (2.31)$$

From Equation (2.31), it is clear that a measurement of receiver output power and range for a reference target of known cross-section ($\theta = 0$, $\lambda = \lambda_\theta$, $L_a = 1$) permits the radar system constant on the left side to be determined and the radar calibrated for reflectivity estimation.

⁷ The choice of reference frequency within the operating band of the radar is arbitrary.

G. ESTIMATION OF VELOCITY

According to Schroder, “Pulsed radar can, by measuring the phase change between consecutive pulses, estimate radial velocity. The effect, called Doppler, is the frequency change that occurs due to the relative movement of a target with respect to the radar. Considering a two-way propagation path renders a total phase change of

$$\phi = 2\pi \frac{2R}{\lambda} \quad (2.32)$$

In terms of angular frequency the result is

$$\varpi = \frac{d\phi}{dt} = \frac{4\pi}{\lambda} \frac{dR}{dt} = \frac{4\pi v_r}{\lambda} = 2\pi f_d \quad (2.33)$$

where v_r is the radial velocity and f_d is the Doppler frequency.

From a pulse pair, using a coherent detector, the phase change can be extracted using

$$\begin{aligned} V_n &= I_n + jQ_n = A_n e^{j\phi_n} \\ \arg\{V_n\} &= \phi_n \\ V_{n+1}V_n^* &= A_{n+1}A_n e^{j(\phi_{n+1}-\phi_n)} \\ \arg\{V_{n+1}V_n^*\} &= \phi_{n+1} - \phi_n = \delta\phi \end{aligned} \quad (2.34)$$

leading to the single pulse pair velocity estimate

$$\hat{v}_r = \frac{\lambda \delta\phi}{4\pi \delta t} = \frac{\lambda}{4\pi T_p} \arg\{V_{n+1}V_n^*\} = \frac{\lambda f_p}{4\pi} \arg\{V_{n+1}V_n^*\} \quad (2.35)$$

where T_p is time between pulses and f_p is pulse repetition frequency.”

Also from Schroder, coherence between pulse pairs is required to measure phase change over time for a volumetric target to minimize phase change from effects other than radial movement. The variance of a velocity estimate can be improved simply by averaging more samples. Building on the single pulse pair velocity estimate Equation (2.35), the multiple pulse pair estimator becomes:

$$\hat{v} = \frac{1}{N-1} \sum_{n=1}^{N-1} v_{n+1} = \frac{1}{N-1} \frac{\lambda f_p}{4\pi} \sum_{n=1}^{N-1} \arg\{V_{n+1}V_n^*\}. \quad (2.36)$$

H. ESTIMATION OF VELOCITY SPREAD

Turbulence, wind shear, and differences in fall speed due to drop size are but a few of the many directly influencing factors on the spread in radial velocity of precipitation. There are even indirect factors (motion of the radar antenna) which impart an apparent spread in velocity. The net effect of these factors is the width of the spread in the velocity spectrum and the time for de-correlation between samples.

Schroder explains, “An estimate of the velocity spread can be computed using the velocity samples obtained from a pulse pair comparison between single pulse pair velocity estimates Equation (2.35). The estimator for sample variance is given by

$$\sigma_v^2 = \frac{\sum_{i=1}^N (\bar{v}_i - \bar{v})^2}{N} \quad (2.37)$$

and the estimator for standard deviation is”

$$\sigma_v = \sqrt{\sigma_v^2}. \quad (2.38)$$

I. CALIBRATION REQUIREMENTS

Factors exist both internally (hardware and software) and externally (environmental and remote sensing effects) that influence a radar’s measurements apart from the target return that is trying to be quantified. The calibration process is used to reduce the influence of these factors on the composite measurement. Internal calibrators minimize system variations by separating the instrument from variable external influences (such as through the use of known reference signals generated internally to test internalized system components). External calibrators, however, operate completely outside (and independent of) the instrument under test. By operating completely outside, external calibrators incorporate those elements in the calibration process that describes external influences that would effect the instrument’s measurements, but are not considered with an internal calibration method. By operating independently, external calibrators are able to calibrate for the same factors targeted by internal calibrators without the calibrator being influenced in its calibration by the instrument under test. With these two additional traits, external calibrators can verify whole-system calibration.

The result is a true “end-to-end” calibration of the specific radar configuration for the specific external measurements that are about to be acquired.

Because these internally and externally influencing factors are so many and so varied they cannot be individually quantified in theoretically expressions. Instead, these combined effect factors are often denoted by, in terms of Pratte, “the so-called “radar constant” C. In any given implementation, the radar constant C can contain slowly varying quantities, such as receiver conversion gain, system and site losses (to include propagation path loss caused by the atmosphere), and “hidden” assumptions. In WSR-88D software jargon the radar constant derived from the engineering calibration is called “SYSCAL” (Sirmans 1992), and temporal variations obtained by the internal, electronic calibration-maintenance function software is called “delta SYSCAL” or “CAL#”.”

J. CALIBRATION METHODS AND SELECTED METHOD

A summary of alternative calibration methods was obtained from Pratte. A list of these methods follows:

1. Traceability
2. Solar and Celestial Radiative Flux Transfer Methods
3. Radar Calibration Targets
4. Lunar Reflectivity
5. Transponder Methods
6. Elevated Ground-range Methods
7. Near-Field Measurements
8. Reflectivity Comparison Methods
9. Rain gauge Comparison Methods
10. Dual Polarization Consistency Methods

Compared to other calibration methods, use of an external active calibration system is the most reliable, independent and thorough means of calibration. For this reason, this type of system was chosen for implementation.

The approach is a repeater that will produce a known RCS via loop gain control and add Doppler return information via phase modulation with a controlled sawtooth. Proper control of the sawtooth frequency introduces Doppler spread, an important measurement quantity in the weather radar. This approach assumes a smooth profile in Doppler return as a function of the varying sawtooth. A calibration sphere is selected to

enable that smooth response profile (see Figure 6). Although a constant amplitude return would seemingly suffice, use of a programmable, constant phase attenuator would also allow software control of the amplitude statistics of the return to the radar. Thus, with full control of both amplitude and phase, one could replicate the return for each of the Swerling target types, although it is only the precipitation return that is really of primary interest in our application.

K. SUMMARY

This chapter has lead up to the formulations of the radar equation for a point target and for a volume target which show that the radar calibration constant can be determined if, having a target of known RCS, the echo power from that target is measured. The objective of this thesis's research is to determine if an active calibrator can be built which will produce the desired known RCS over a response range of interest for weather returns. Introducing a known Doppler shift and known RMS frequency spread allows one to compare the radar estimates of those parameters with the values set for the calibrator. The Doppler shift also addresses problems associated with use of the calibrator in an environment where there is fixed clutter return.

III. DESIGN, IMPLEMENTATION AND OPERATION

A. DESIGN

This study implemented an existing design (see Figure 2) of an active calibrator system (ACS) for the MWR-05XP. It did not involve the creation of such a design nor did it involve the investigation of alternatives to or optimization of this design.

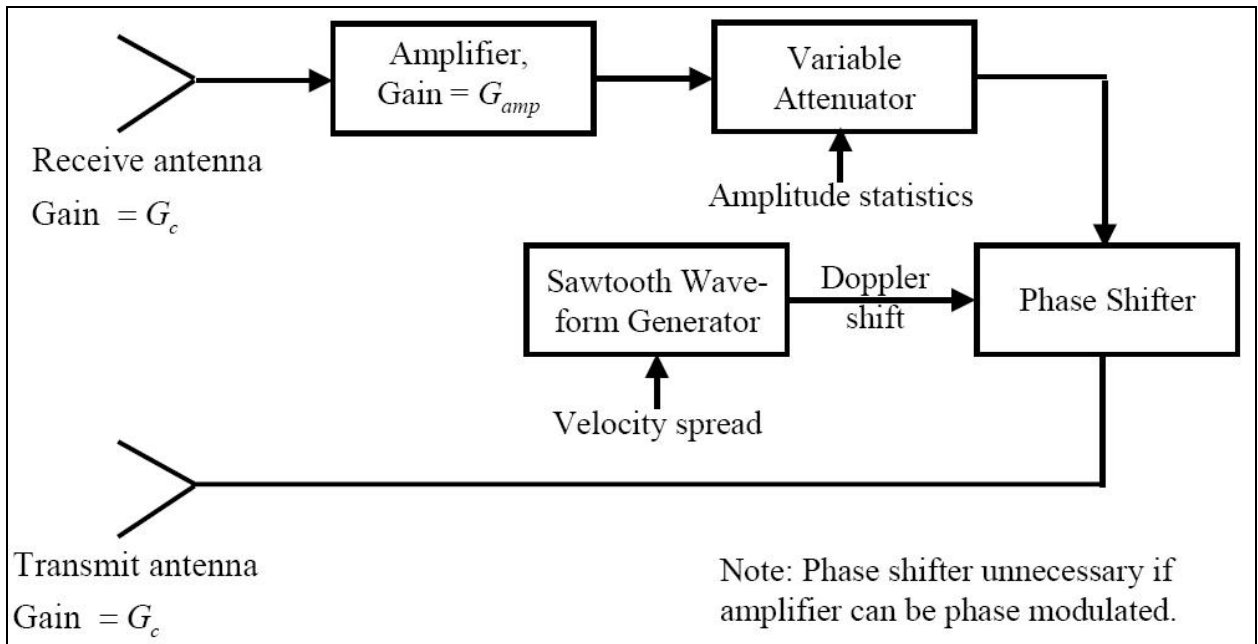


Figure 2. Block Diagram of the ACS.

See Figure 3 for a layout of the actual components used. These components comprise the internals of the Active Calibrator System or ACS that was implemented in this study.

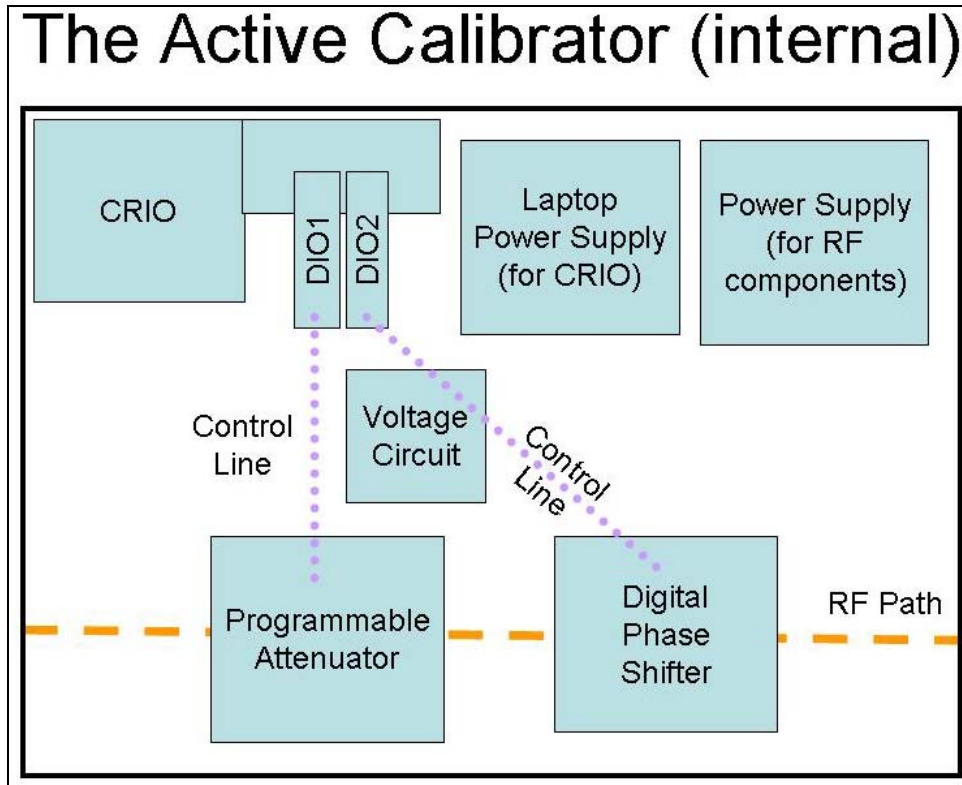


Figure 3. Diagram of Component Layout inside the ACS Enclosure.

B. HARDWARE IMPLEMENTATION

1. System Description Overview

See ACS Pictures Appendix.

The active calibrator system (ACS) is comprised of two Pasternack sectoral horn antennas mounted on either end of a 6 ft long 1"x4" piece of lumber. To this piece of lumber, another piece of lumber of the same dimensions is attached to create an "L" bracket. Midway between the two antennas is centered the ACS enclosure, an aluminum box (17"x13"x5"), to house the power supplies, control computer, and RF components (programmable attenuator, digital phase shifter, etc.). On the face of this enclosure, parallel to the antennas' mainbeams, is attached a second piece of lumber (cut to the length of the enclosure face) to present a flush, all wood box exterior. Along this exterior and running the entire length of the "L" bracket between the two antennas, X-band Radar

Absorbent Material (RAM) is attached. Although this RAM has its greatest RF absorbency at 9.4 GHz, it provides sufficient RF absorbency across the entire RF range of interest, 9-10 GHz, to reduce undesired RF returns greater in power than the transmitted power of the ACS's transmit antenna output. This RAM is sectioned into three pieces (two 24"x10"x2" and one 19"x9"x2"). Each piece is attached via removable Velcro to aid in transport and storage. The antennas are mounted and oriented to transmit and receive horizontally polarized signals. They are connected to the enclosure via 3 ft RF cables. All of the ACS's components apart from the antennas are contained inside the enclosure.

2. Hardware List

External Hardware (Quantity/Description/Dimensions, if applicable)

- (1) Aluminum box(enclosure) (17"x13"x5")
- (3) Pieces Emerson & Cuming AN77 RAM (two, left and right side, 24"x10"x2" and one, center, 19"x9"x2")
- (3) Pieces lumber (1"x4", two 6 ft long and one 19" long)
- (2) Pasternack Sectoral Horn Antennas
- (2) Pasternack semi-flexible RF Cables (3 ft)
- (1) Ethernet (RJ-45) Cable
- (1) Dell Precision M65 with 2.33 GHz Core 2 Duo Processor, 2GB 667 MHz RAM, 80 GB HDD Laptop and Dell 90W-AC Power Supply
- (1) AC Power Cable
- Miscellaneous Mounting Hardware (nuts, screws, washers, bolts, etc.)

Internal Hardware (Quantity/Description)

- (1) Laptop Power Supply (24V CUI EA1050B-240)
- (1) Condor DC Power Supply (GLC-50A)
- (2) 25-pin-to-15-pin Control/Power Cables
- (1) Voltage Regulator Circuit
- (1) National Instruments Control Computer (CompactRIO Model Line to include: (1) real-time controller, (1) reconfigurable embedded chassis, and (2) I/O modules)

3. Voltage Regulator Circuit

A voltage regulator circuit was required to convert the DC power supplied by the Condor power supply (-15VDC, +15VDC, and +5VDC) to the additional voltages (-5VDC and +12VDC) required by the RF components.

Voltage Regulator Circuit Hardware List (Quantity/Description)

(2) 0.01 uF Capacitors

(1) 33 ohm Resistor

(1) 7905C (provides -5VDC from -15VDC input)

(1) 7812CT (provides +12VDC from +15VDC input)

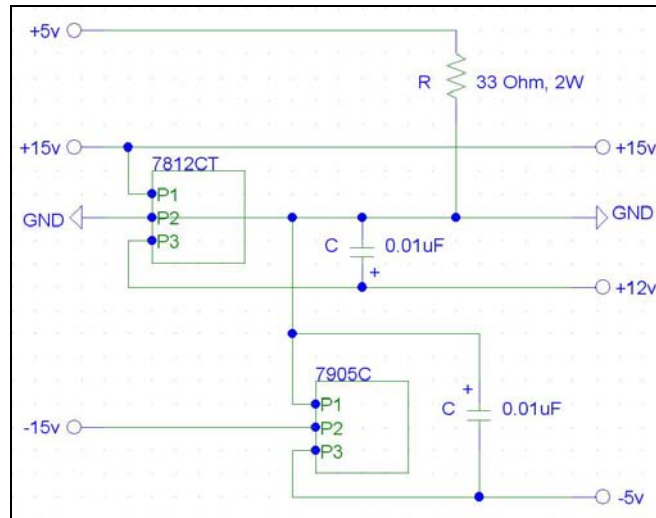


Figure 4. Voltage Regulator Circuit Diagram.

4. RF Components

See Appendix on Digital Phase Shifter.

See Appendix on Programmable Attenuator.

See Appendix on Antennas. Appendix describes antenna specifications.

See Appendix on Antenna Testing. Appendix describes antenna patterns, gain and beamwidth calculations, and isolation.

5. Control Hardware

Control of the ACS is achieved through the use of the National Instruments (NI) Compact Reconfigurable Input/Output (CompactRIO) product line. From the ni.com/compactrio website, “The National Instruments CompactRIO programmable automation controller (PAC) is a low-cost reconfigurable control and acquisition system designed for applications that require high performance and reliability. The system

combines an open embedded architecture with small size, extreme ruggedness, and hot-swappable industrial I/O modules. NI CompactRIO is powered by reconfigurable I/O (RIO) FPGA technology.” Again from the ni.com/pac website, “PACs combine programmable logic controller (PLC) ruggedness with PC functionality under an open, flexible software architecture.”

The CompactRIO products used by the ACS include: a real-time controller, a reconfigurable embedded chassis, and two I/O modules for digital input. Software development was done on a Windows PC laptop with NI’s Developer Suite with Real-time deployment and FPGA deployment options installed. Through this developer suite and these options, all software development was done in the NI LabVIEWTM visual programming language. For items not run on either the laptop’s Windows O/S or the real-time controller’s real-time O/S, LabVIEW was auto-compiled into the VHSIC Hardware Description Language (VHDL) and run on the reconfigurable embedded chassis. This process was seamless to the developer and no specific knowledge of VHDL was required. These items included all of the software control required to manipulate the phase shifter and programmable attenuator on a time scale at or near its fastest possible switching speed. A normal O/S or real-time O/S is incapable of this speed of control requiring the use of Field Programmable Gate Arrays (FPGAs).

See Appendix on CompactRIO.

6. Hardware Limitations

There are a few hardware limitations associated with the ACS. These limitations affect the maximum possible Doppler shift and therefore radial velocity and velocity spread that can be practically generated. Limited factors are dictated by the switching speed of the programmable attenuator (300 ns) and phase shifter (500 ns), the CRIO FPGA clock (25ns), and the response time of the digital I/O module (100 ns). Obviously, the switching speeds of the programmable attenuator and phase shifter are the true limiting factors as the CRIO components are more than capable of switching states at or faster than the fastest switching speeds of both RF components.

See the example calculation of the effect of the phase shifter's fastest possible switching speed.

$$\begin{aligned}\frac{1}{2^8 \times (500 \times 10^{-9})} &= 7812.5 \text{ Hz Doppler Frequency Shift} \\ 7812.5 \times \frac{299792458}{2 \times 999000000} &= 117.2 \text{ m/s Radial Velocity} \\ 117.2 \times 2.23693629 &= 262.2 \text{ mph Radial Velocity}\end{aligned}$$

This limitation actually falls below what is physically possible (or what has been observed) and, therefore, could potentially limit ACS applicability in a few applications. The fastest wind speed ever recorded on Earth was 318 mph in one of the tornadoes that hit the suburbs of Oklahoma City on 3 May 1999.⁸ However, the fastest recorded wind speed not associated with a tornado was measured at 230 mph in 1934.⁹

C. ACS FREQUENCY/DOPPLER CALIBRATION AND SOFTWARE IMPLEMENTATION

In order to calibrate the weather radar's ability to measure radial velocity and velocity spread, the ACS must be able to produce a known Doppler shift and Doppler spread. By comparing the known quantity to the measured quantity and adjusting for any discrepancy, the calibration can be completed and the weather radar's accuracy assured. This section describes how the ACS achieves this.

The active calibrator's loop gain determines equivalent reflectivity, Z_{eq} .¹⁰ Phase modulation is required to produce Doppler shift, according to:

$$v(t) = A \cos[\omega_c t + \theta(t)] = A \operatorname{Re}[e^{j\omega_c t} e^{j\theta(t)}]. \quad (3.1)$$

Following the derivations in Tan's thesis [9] and the paper by Cummings [10], for $\theta(t)$ periodic,

⁸ National Weather Service Forecast Office, "Frequently Asked Questions about the May 3, 1999 Bridge Creek/OKC Area Tornado," retrieved 2008-09-21 from <http://www.srh.noaa.gov/oun/storms/19990503/may3faqs.php>

⁹ University Corporation for Atmospheric Research (UCAR), "Windows to the Universe/Wind," retrieved 2008-09-21 from <http://www.windows.ucar.edu/tour/link=/earth/Atmosphere/wind.html>

¹⁰ See section on "ACS Amplitude/Reflectivity Calibration" (next section) for a discussion on the determination of equivalent reflectivity.

$$e^{j\theta(t)} = \frac{1}{T} \sum_{-\infty}^{+\infty} c_n e^{j\omega_n t} \text{ where } c_n = \int_{-\frac{T}{2}}^{\frac{T}{2}} e^{j\theta(t)} e^{-jn\omega_m t} dt . \quad (3.2)$$

Thus,

$$v(t) = A \operatorname{Re} \left[\frac{1}{T} \sum_{-\infty}^{+\infty} c_n e^{j(n\omega_m + \omega_c)t} \right] \quad (3.3)$$

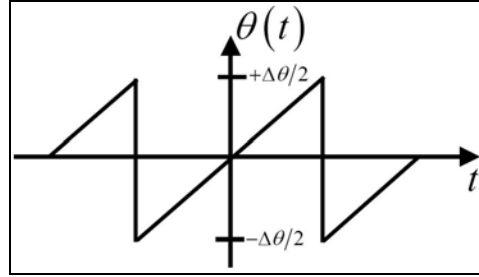


Figure 5. Two Cycles of the Periodic, Linear, Modulating Sawtooth Function.

$$\theta(t) = \frac{\Delta\theta}{T} t \text{ for } \left(-\frac{T}{2} \leq t \leq +\frac{T}{2} \right) \quad (3.4)$$

$$c_n = T \frac{\sin(\Delta\theta/2 - n\pi)}{(\Delta\theta/2 - n\pi)} .$$

In general, the phase modulated signal has a general signal given by

$$v(t) = A \operatorname{Re} \sum_{-\infty}^{+\infty} \frac{\sin(\Delta\theta/2 - n\pi)}{(\Delta\theta/2 - n\pi)} e^{j(f_c + n f_m)t} . \quad (3.5)$$

If the amplitude of the sawtooth is adjusted to produce a phase change that is a multiple of 2π then

$$\Delta\theta = m2\pi \text{ for } (m \in I)$$

$$\frac{c_n}{T} = \begin{cases} 1 & \text{for } n = m \\ 0 & \text{for } n \neq m \end{cases} . \quad (3.6)$$

Therefore,

$$v(t) = A \operatorname{Re} e^{j(f_c + m f_m)t} \text{ where } (\Delta\theta = m2\pi) . \quad (3.7)$$

The real part of the complex exponential expression is cosine with argument indicating the translation (Doppler shift) from frequency f_c to frequency $f_c + mf_m$. In other words, each spectral line is separated by the modulating frequency and lines exist symmetrically above and below the carrier.

By cycling through 360° (2π) of phase at this periodic rate a known frequency/Doppler shift is produced against which the weather radar can be calibrated. This periodic phase cycling (and thus frequency translation) is implemented in the ACS using a digital phase shifter. However, there are imperfections associated with this method. Imperfect implementation results in spurious sidebands due to finite sawtooth flyback time, incorrect sawtooth amplitude, the digital staircase approximation to linear phase shift, phase error, and finite phase shifter switching time.[10]

Again, following the derivations in the thesis by Tan [8], for a digital phase shifter using $N=2^B$ steps,

$$v(t) = A \sum_{K=-\infty}^{+\infty} \frac{(-1)^m}{mN+1} \frac{\sin(\pi/N)}{(\pi/N)} \cos(\omega_c + K\omega_m)t \quad (3.8)$$

where $K = mN+1$ and m is an integer. The frequencies of the non-zero spectral components are given by $f = f_c + Kf_m$ or $f = f_c + (mN+1)f_m$. The amplitude of the K^{th} sideband relative to the input carrier is given by

$$\frac{P_K}{P_0} = \frac{|C_K|^2 A^2 / 2}{A^2 / 2} = |C_K|^2. \quad (3.9)$$

The first sideband in the spectrum of the translated signal is

$$v_1(t) = \frac{\sin(\pi/N)}{(\pi/N)} A \cos(\omega_c + K\omega_m)t. \quad (3.10)$$

The translation loss is defined as

$$TL_{dB} = -20 \log \left[\frac{\sin(\pi/N)}{(\pi/N)} \right] = -20 \log \left[\frac{\sin(\pi/2^B)}{(\pi/2^B)} \right]. \quad (3.11)$$

This loss rapidly approaches 0 dB as the number of bits of phase shift increase. If $B=4$ bits, for example, $TL_{dB}=0.06$ dB.

The amplitudes of the undesired sidebands are also of interest. The undesired sideband with the highest amplitude is $K = -N + 1$. Relative to the desired sideband, $K=1$, the suppression ratio is

$$SR_b = 20 \log(N - 1) = 20 \log(2^B - 1). \quad (3.12)$$

The suppression ratio also improves rapidly as the number of bits is increased. If $N=4$, for example, $SR_{dB} = 23.5$ dB.

See Appendix I on LabVIEW for the Digital Phase Shifter which gives further explanation of how the phase shifter is controlled by the CompactRIO to produce the 2π periodic phase cycling.

In conclusion, one of the primary advantages of the ACS is its ability to introduce Doppler shift. This permits the calibrator signal to be extracted from mainbeam ground clutter at elevation angles near zero and from sidelobe clutter at higher elevation angles. In most cases, convenience will dictate that the ACS be operated near the ground.

D. ADDING VELOCITY SPREAD

Velocity spread can be added to the Doppler shifted signal by varying the frequency of the sawtooth waveform used in the phase modulator. The frequency should be varied in accordance with a Gaussian random variable that has been low pass filtered to produce a modulating signal with the desired correlation time. This functionality was not fully implemented in the ACS at the conclusion of this study. See Chapter IV on Future Work.

E. ACS AMPLITUDE/REFLECTIVITY CALIBRATION

In order to calibrate the weather radar's ability to measure reflectivity, the ACS must be able to reliably simulate a known reflectivity. This is accomplished by receiving the incident radar signal and retransmitting a signal of known power relative to the incident signal. From a measurement of the echo signal power received by the radar and knowledge of the ACS loop gain, the calibration can be completed and the weather

radar's absolute accuracy in amplitude assured. This section describes how the ACS is calibrated so it can in turn be used to calibrate a weather radar.

1. Measurement Premise

The ACS needs to produce a power density equivalent to that scattered by a target of known RCS. This power will be the effective radiated power (or ERP) of the ACS. The ERP of the ACS will be a function of (depend on) the ERP of the radar. This is because the ACS does not produce an ERP from an independent/internal power source, but rather as acts a repeater (and modifier) of the power received from the radar.

The power received from the radar will depend on the ERP of the radar and the losses involved between the ACS and the radar. At this radar frequency, the losses between the ACS and the radar will primarily depend on the distance between the ACS and the radar (spreading loss or free space loss only, unless a ground reflection is present as will be the case for elevation angles near zero) and atmospheric attenuation (propagation loss), but also losses internal to the radar (system losses which cannot be precisely known). Those losses which depend on distance will affect the reflectivity observed by the radar due to the calibrator twice – first, as the ERP of the radar is affected on its way to becoming the received power of the calibrator and, second, as the ERP of the calibrator is affected on its return to becoming the received power of the radar. While the spreading loss is well known ($L = \left(\frac{4\pi R}{\lambda}\right)^2$) and can be accurately calculated, the propagation loss is less well known (as it depends on many time variant factors) and is more difficult to accurately calculate. In order to isolate this uncertainty at any given time, the equivalent reflectivity of the ACS can be compared to a known reflectivity at equal distances and with the propagation losses minimized as much as possible (as in an anechoic chamber). By comparing these two values, the equivalent reflectivity of the ACS can be measured. Under these settings the losses internal to the radar can be isolated (the system losses which cannot be precisely known will be calibrated out).

An equation for the ERP of the ACS and thereby the equivalent reflectivity of the ACS can be defined as a function of the received power of the ACS (from the radar) and the loop gain (system gain and losses) of the ACS. These include the gain of both antennas (transmit and receive), cable losses, phase shifter losses, programmable attenuator losses, isolator losses, amplifier gain, and other RF components' losses (only the amplifier provides gain). On the whole, the ACS's ERP and therefore its equivalent reflectivity can be controlled (varied) by the programmable attenuator (variable gain/loss). However, this is only effective as long as the net gain/loss of all of the ACS's RF components (fixed gain/loss) in total exceed the reflectivity of the ACS due to its exposed surface area.

The equivalent reflectivity due to the ACS's transmit antenna is in direct competition with the actual reflectivity due to the ACS's surface area. Both depend on the radar ERP, but the equivalent reflectivity further depends on the ACS's loop gain acting to re-radiate the radar's power while the actual reflectivity depends on the exposed surface area of the ACS (to include all sides facing the radar) acting to reflect the radar's power. If the controlled power does not exceed this value, variable amplitude calibration (as will be needed for amplitude statistics) will not be possible. Instead, only a single reflectivity (the actual reflectivity) of the ACS will ever be observed by the radar. This is the same principle used in passive calibration systems (such as the balloon and sphere) where a controlled Doppler calibration is not possible. Radar Absorbent Material (RAM) was used to reduce the actual reflectivity to levels below the equivalent reflectivity. See Chapter III, Section B, Subsection 1 for further details on RAM use.

2. Measurement Method

What follows is the method used to calibrate out these unknown system losses for accurate reflectivity measurements (estimates) by the weather radar based on the equivalent RCS of the ACS. See Chapter II, Section F, on "Radar Principles and Weather Radar Equation Correction" for background and supporting theory directly applicable to this process and these calculations. The following development shows how the equivalent RCS of the ACS was experimentally determined through anechoic

chamber measurements and subsequent calculations to satisfy a most fundamental radar calibration requirement – namely, that the ACS’s equivalent RCS must be known [5].

As mentioned before, the value of the equivalent reflectivity (or more accurately equivalent radar cross section or RCS) of the ACS can be measured and calculated in comparison to a known reflectivity (or RCS) of another target. In this study, an aluminum sphere was used and measurements made inside an anechoic chamber at a fixed, known distance to serve as the known reflectivity. A 12” diameter aluminum sphere was chosen out of three diameters available based on the initial calculations and estimates performed below.

a. Initial Calculations

Prior to making measurements in the anechoic chamber theoretical calculations were made using approximately known or individually measured values of the required quantities. The signal source in the anechoic chamber was a vector network analyzer (VNA). The VNA replaces the radar as the signal source when calibrating the ACS in the anechoic chamber.

Below is a list of constants, either measured or known, to include:

R , the measured one-way distance from the transmit and receive antennas to the ACS inside the anechoic chamber. (measured)

f , the radio center frequency. (known, selected on vector network analyzer or VNA)

c , the speed of light. (known)

λ , the wavelength. (calculated)

P_t , the VNA transmit power a.k.a. the power input to the anechoic transmit antenna from the VNA to include all losses from the output of the VNA to the antenna (cabling, etc.). (known, selected on VNA)

$G_t=G_r$, the gain of the VNA antenna – one in the same - a.k.a. the anechoic transmit and receive antennas - both the same. (measured, See Appendices on Antennas.)

$EIRP$, the radar’s Effective Isotropic Radiated Power. The product of the transmit power and antenna gain. (calculated)

G_c , the calibrator’s antenna gain. Both antennas on the calibrator are the same. (measured, See Appendices E and F on Antennas.)

G_{amp} , the calibrator’s loop gain to include all system losses (cabling, phase shifter while not phase shifting, connectors, etc.) – i.e. net gain. The actual gain of the amplifier used in the calibrator is +35 dB with -20 dB of system losses for +15 dB net. (calculated via measured values: amplifier gain and system losses)

FSL , the Free Space Loss or Spreading Loss associated with the distance R . (calculated)

CI , the calibrator's input signal power as measured into the system at the receive antenna's output port. (calculated)

RI , the VNA input signal power as measured into the system at the receive antenna's output port. (calculated)

$$f = 9.50 \times 10^9 \text{ Hz}$$

$$c = 3.00 \times 10^8 \text{ m/s}$$

$$\lambda = \frac{c}{f} = 3.16 \times 10^{-2} \text{ m}$$

$$P_t = 25 \text{ dBm} = 316.2278 \text{ mW}$$

$$G_t = G_r = 16 \text{ dBm} = 39.8107 \text{ ratio}$$

$$EIRP = P_t G_t = 41 \text{ dBm} = 12589.2541 \text{ mW}$$

$$G_c = 13 \text{ dBm} = 19.9526 \text{ ratio}$$

$$G_{amp} = 15 \text{ dBm} = 31.6228 \text{ ratio}$$

$$R = 5.7912 \text{ m (19 feet)}$$

$$FSL = \left[\frac{\lambda}{4\pi R} \right]^2 = 1.8830 \times 10^{-7} \text{ ratio} = -67.2516 \text{ dB}$$

$$CI = EIRP \times FSL \times G_c = 4.7298 \times 10^{-2} \text{ mW} = -13.2516 \text{ dBm}$$

$$RI = CI \times G_{amp} \times G_c \times FSL \times G_r = 2.2371 \times 10^{-4} \text{ mW} = -36.2032 \text{ dBm}$$

Constants									
Quantity:	Range	Frequency	Speed of Light	Wavelength	Radar Transmit Power	Radar Antenna Gain	Radar EIRP	Calibrator Antenna Gain	Calibrator Amplifier Gain
Symbol:	R	f	c	$\lambda = c/f$	P_t	$G_t = G_r$	$EIRP = P_t \times G_t$	G_c	G_{amp}
Units:	ft	Hz	m/s	m	dBm	dB	dBm	dB	dB
Value:	19	9.50E+09	3.00E+08	3.16E-02	25	16	41	13	15
Alt. Units:	m				mW	ratio	mW	ratio	ratio
Alt. Value:	5.79				316.23	39.81	12589.25	19.95	31.62

Table 2. Summary of Constants Used in Estimated Equivalent RCS Calculations.

Calculations					
Quantity:	Free Space Loss		Calibrator Input		Radar Input
Symbol/Equation:	$FSL = [\lambda / (4 \times \pi \times R)]^2$		$CI = EIRP \times FSL \times G_c$		$RI = CI \times G_{amp} \times G_c \times FSL \times G_r$
Units:	ratio	dB	mW	dBm	mW dBm
Value:	1.88E-07	-67.25	4.73E-02	-13.25	2.24E-04 -36.50

Table 3. Summary of Estimated Equivalent RCS Calculations.

-36dBm is approximately the value of VNA input signal power expected when measuring the ACS inside the anechoic chamber. This will be the total returned power from the ACS due to the relayed power and not the reflected power. The reflected

power is much smaller (no return was detected with the ACS in the anechoic chamber and RAM attached) and has been minimized by the use of X-band Radar Absorbent Material (RAM). Again, see Chapter III, Section B, Subsection 1 for further details on RAM use.

The power received from the ACS must be compared to the received power from a target of a known RCS to calculate an equivalent RCS for the ACS. The known RCS that was used was that of a polished aluminum sphere. Three spheres were available, a 3", a 6" and a 12" diameter sphere. The expected received power was calculated for all three. The relation for the monostatic RCS of a sphere in the optical region (frequency region) was used. The power had to be great enough to be detected by the VNA, but not so great as to cause saturation. The best suitable candidate from the three available was found to be the 12" diameter sphere because of its larger (but not too large, i.e. saturating) return amplitude. See example calculation below.

$$a = 6 \text{ in} = 0.1524 \text{ m}$$

$$\beta a = \frac{2\pi a}{\lambda} = 30.3 \Rightarrow \text{Optical Region (See Figure 6.)}$$

$$\frac{\sigma}{\pi a^2} = 1 \text{ for Optical Region (See Figure 6.)}$$

$$\sigma = \pi a^2 = 7.2966 \times 10^2 \text{ sm} = -11.3688 \text{ dBsm}$$

$$\text{Received Power} = 1.6338 \times 10^5 \text{ mW} = -47.8679 \text{ dBm}$$

Following the example, for a 3" diameter sphere -59.909 dBm and for a 6" diameter sphere -53.889 dBm.

Monostatic RCS of a sphere, $\beta = 2\pi / \lambda (=k)$, a = radius, illustrates the three frequency regions: (1) Rayleigh, (2) Mie, and (3) optical

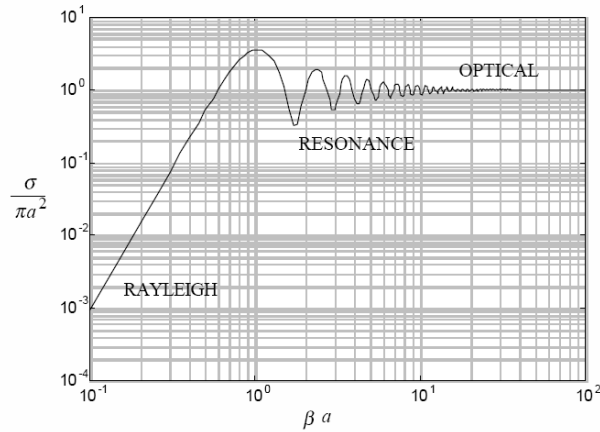


Figure 6. Graph for Calculating Radar Cross Section of a Sphere. [After 11]

Sphere Calculations									
Quantity:	Sphere (Diameter)	Radius	Radius	OPTICAL	OPTICAL	RCS	RCS	Received Power	Received Power
Symbol:	-	a	a	$\beta a = 2\pi a / \lambda$	$\sigma / \pi a^2$	$\sigma = \pi a^2$	$\sigma = \pi a^2$	mW	dBm
Units:	-	in	m	-	-	m ²	dBsm	mW	dBm
Value:	3"	1.5	3.81E-02	7.58	1	4.56E-03	-23.41	1.02E-06	-59.91
Value:	6"	3	7.62E-02	15.16	1	1.82E-02	-17.39	4.08E-06	-53.89
Value:	12"	6	1.52E-01	30.32	1	7.30E-02	-11.37	1.63E-05	-47.87

Table 4. Summary for Calculations of Radar Cross Section of a Sphere.

b. Anechoic Chamber Measurements

Measurements were made in an anechoic chamber with the Vector Network Analyzer system. Three different series of measurements were made. One with the chamber empty (E), one with the sphere in the chamber (S), and one with the calibrator in the chamber (C). Measurements were made and represented both in the time domain (T) and frequency domain (F).¹¹ To eliminate any possible interference from reflections (echoes) in the chamber due to less than ideal performance from the anechoic chamber (there were design compromises made in the chamber at the time of

¹¹ The basic measurement is a swept frequency (frequency domain) measurement. The time domain response is then obtained via FFT. Time domain resolution is determined by frequency domain bandwidth. A 1 GHz BW should give about 1 ft. resolution. See reference [10]. It provides further explanation of this information.

construction due to space limitations) time based gating was used to eliminate undesired signals. Measurements were made both with this time based gating (G) and without (N). In the time domain, data sets and plots were often zoomed to the time/distance of interest (when/where the calibrator's return was expected). These are annotated zoomed (Z) or not (A, for all). When not zoomed, they include all data starting from time zero. Table 5 summarizes the abbreviations, just discussed, that are used when referring to the various anechoic chamber measurement data sets. In all cases, a total 90 ns time base was used (RCS90).

S=sphere	T=time domain	G=gated	A=all (0 sec to zoomed)	G1=54.8-58.8 ns
E=empty chamber	F=frequency domain	N=not gated	Z=zoomed (around time gate)	G2=39.8-43.8 ns
C=calibrator			NOTE: does not apply to F, always 9-10 GHz	

Table 5. Naming Convention Summary.

Figure 7 is a composite of all data sets in the time domain, not zoomed (all). Figure 8 is a composite of all data sets in the frequency domain. All data sets include the measured data for the three targets: an Empty Anechoic Chamber (chamber), the 12" Aluminum Sphere (sphere) and the ACS (calibrator). Timing gates were placed around the sphere's location (42 ns) and calibrator's location (57 ns). These timing gates eliminated undesirable echoes. One such undesirable echo was at <2 ns. This echo corresponds to the coupling between transmit and receive antennas which were placed about 18" apart. There are seven graphed data sets on each plot: (1 and 2) the sphere without a time gate and with a time gate centered on its 42 ns return, (3 and 4) the calibrator without a time gate and with a time gate centered on its 57 ns return, (5 and 6) the empty chamber without a time gate and with a time gate for the calibrator, then (7) with a time gate for the sphere.

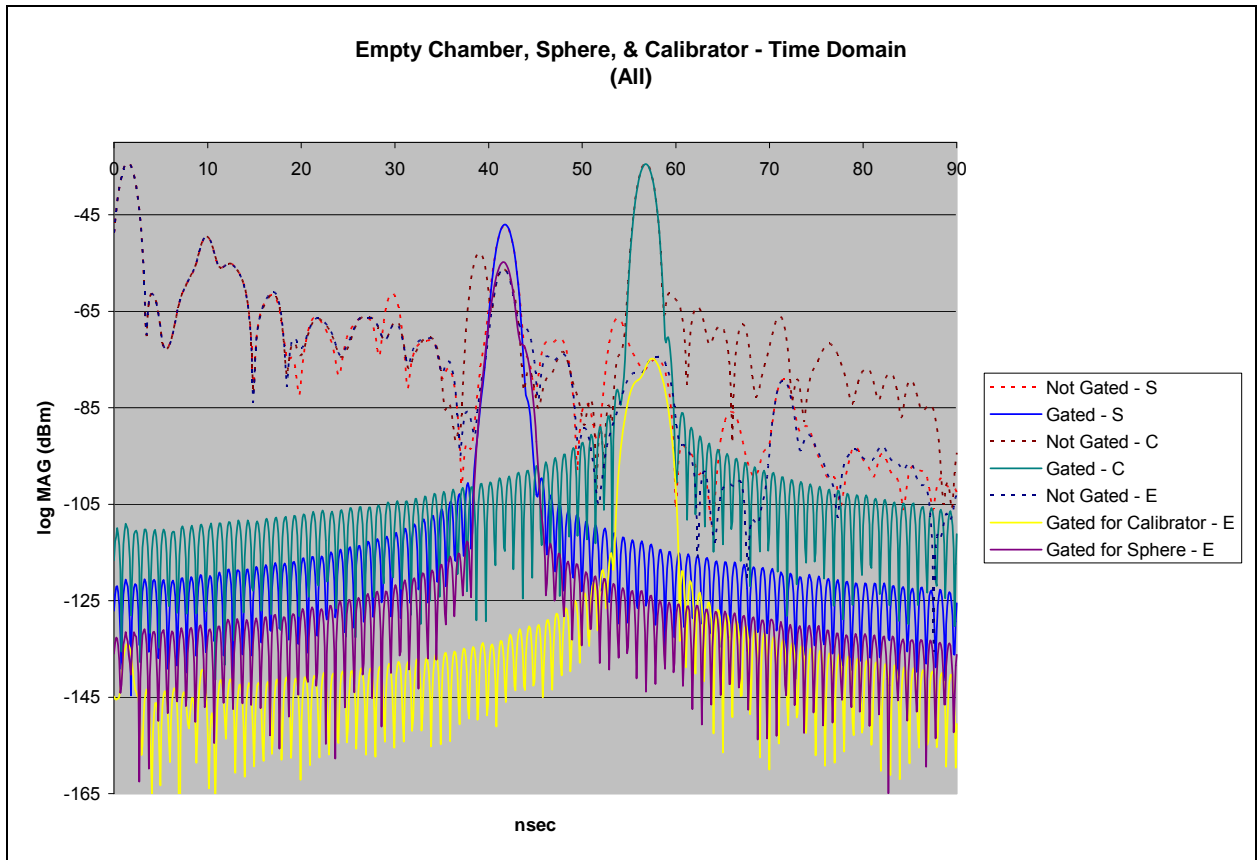


Figure 7. Time vs. Amplitude for Empty Chamber, Sphere and ACS.
(ESC_plotTA)

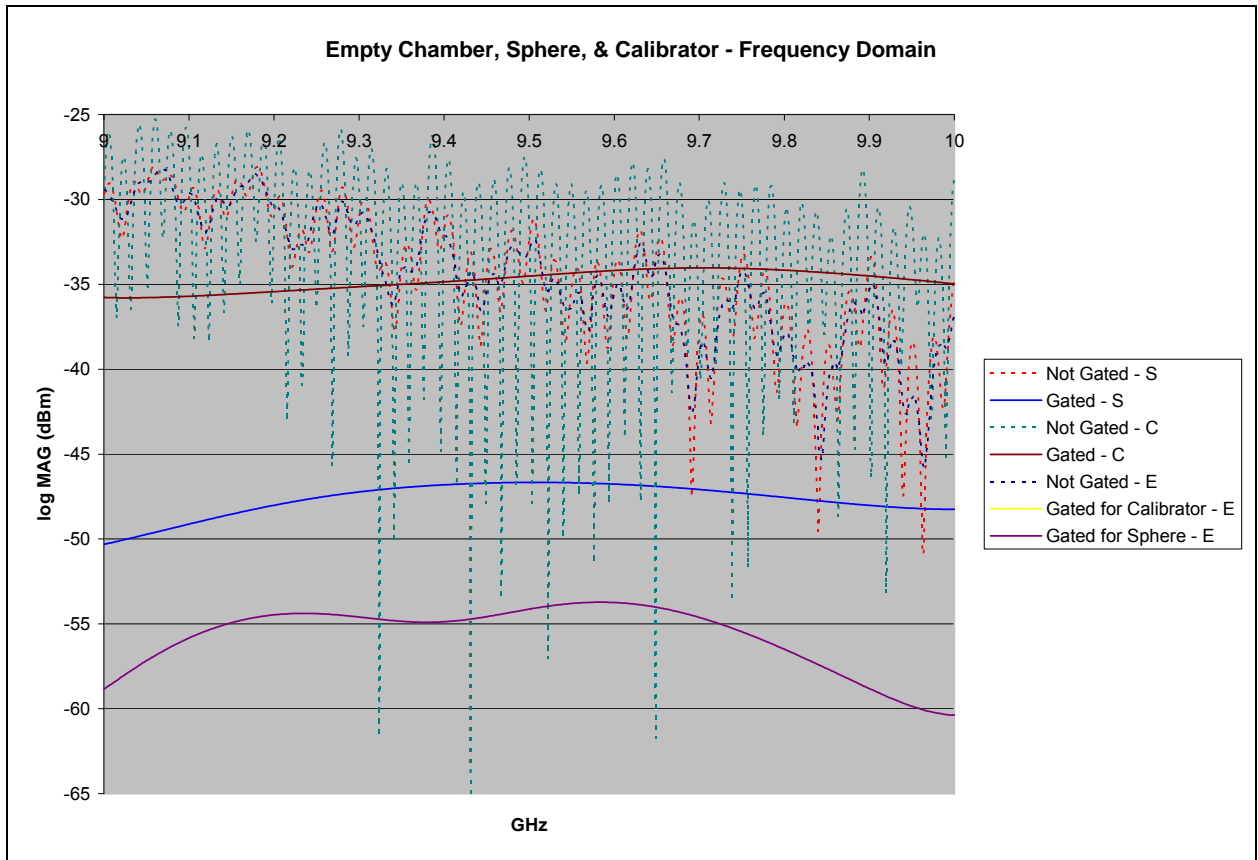


Figure 8. Frequency vs. Amplitude for Empty Chamber, Sphere and ACS.
(ESC_plotF)

Figure 9 and Figure 10 are data sets in the time domain of the sphere and the calibrator only, respectively. Each plot is of the respective target only and zoomed to very near the time gate size of each target. For the sphere, the time gate (G2) was centered at 41.8 ns and spanned 39.8 to 43.8 ns. For the calibrator, the time gate (G1) was centered at 56.8 ns and spanned 54.8 to 58.8 ns. The time gates correlate directly to target return distances. As mentioned before, the distance (range) from the transmit and receive antennas in the anechoic chamber to the target pedestal inside the chamber is 19 feet. 19 feet is 38.6 ns in time. The distance is traversed twice (once to the target and then from the target) at the speed of light. The reason the time gate for the sphere was observed at and consequently set at 42 ns is the sphere was suspended from the ceiling of the chamber above and slightly behind the target pedestal inside the anechoic chamber. This added approximately an additional 1.6 feet of distance and 3 ns of time because the

range hypotenuse of the distance (height geometry is involved) rather than the longest leg alone. The reason the time gate for the calibrator was observed at and consequently set at 57 ns is different than for the sphere. This time gate was approximately 8 ns greater because of the time delay due to transmission line lengths rather than target distance. The 8 ns is equivalent to 8 feet (one-way path), slightly greater than the straight line distance between the transmit and receive antennas of the ACS (as expected). See the example calculations below for the mathematical relation between time and distance (two-way path).

$$c = 3.00 \times 10^8 \text{ m/s}$$

$$R = 5.7912 \text{ m (19 feet)}$$

$$\frac{2R}{c} = 38.6 \text{ ns}$$

$$t = 41.8 \text{ ns}$$

$$\frac{t \times c}{2} = 6.2700 \text{ m (20.6 feet)}$$

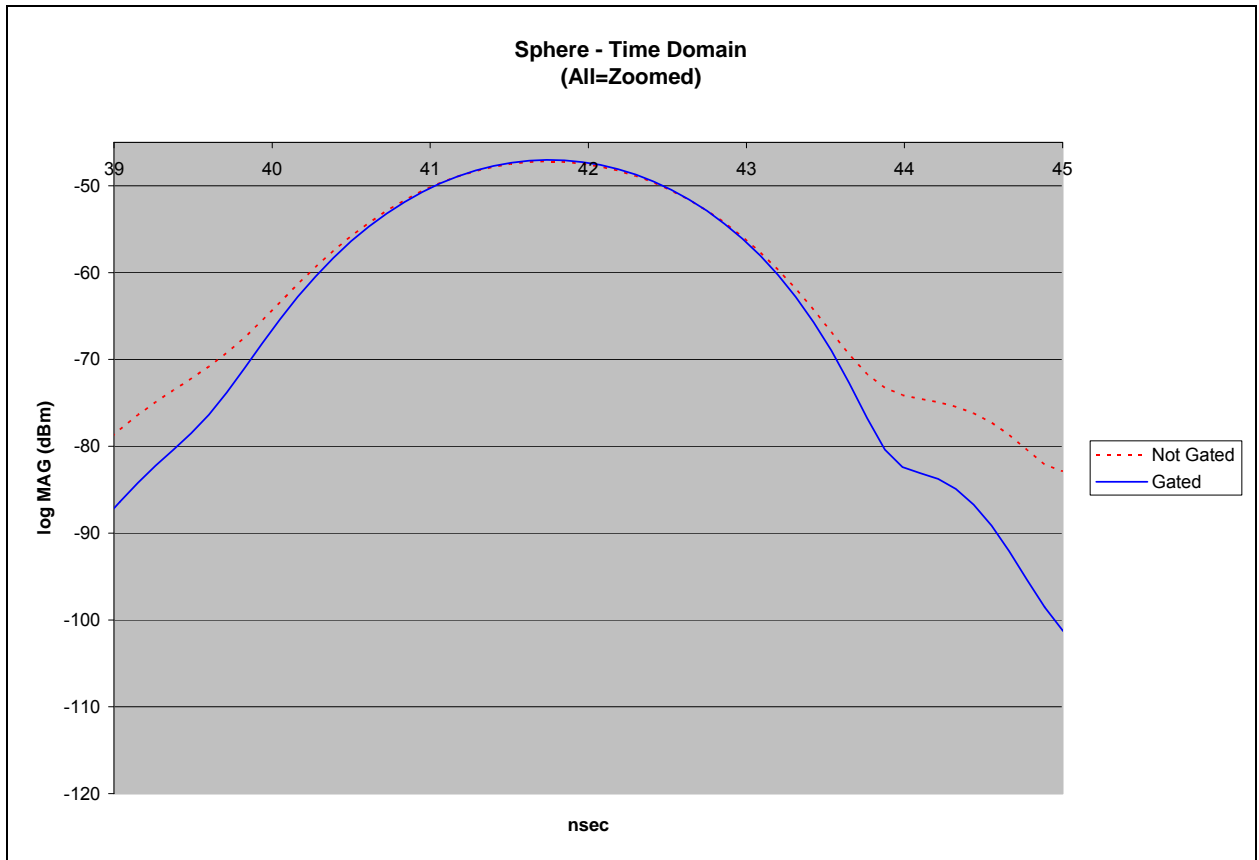


Figure 9. Time vs. Amplitude for Sphere, Zoomed. (S_plotTA=Z)

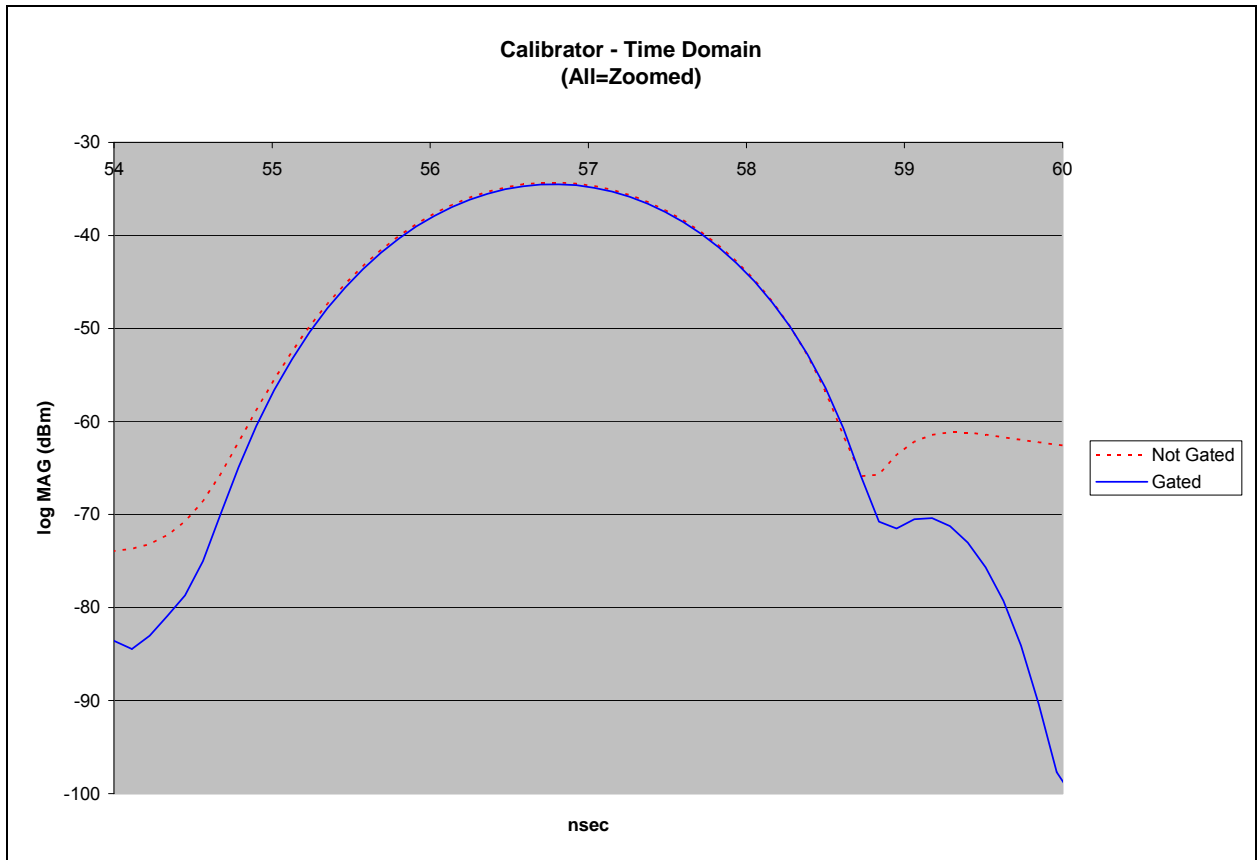


Figure 10. Time vs. Amplitude for ACS, Zoomed. (C_plotTA=Z)

The expected (calculated) value for received power from the ACS was -36.5 dBm. The measured value for received power from the ACS was -34.8 dBm. The expected (calculated) value for received power from the 12" Sphere was -47.9 dBm. The measured value for received power from the 12" Sphere was -46.7 dBm. All expected (calculated) values very nearly equaled the measured values.

Figure 11 is from the data in the frequency domain of both the sphere and calibrator previously presented, now used to calculate the equivalent RCS of the calibrator. Measurements were made from 9-10 GHz. The VNA recorded the magnitude of the returned amplitude power in logarithmic form (log MAG) in units of milliwatts (dBm). All measurements are in the frequency domain gated for time (FG). This includes both the sphere (SFG) and calibrator (CFG). As can be seen, the measured values were very close to the expected (calculated) values. The received power for the

12” Aluminum Sphere was calculated to be -47.87 dBm and observed to be near -47 dBm. The received power for the calibrator was calculated to be -36.50 dBm and observed to be near -35 dBm. The RCS of the sphere was previously calculated to be -11.37 dBsm (S-RCS). To calculate the RCS of the calibrator (C-RCS) based on the observed/measured data, the CFG - SFG= Δ (dB) was added to the sphere’s RCS. Over the entire frequency band the C-RCS varied from 0.6 to 3.2 dBsm. Note all these measurements in the chamber included the use of the RF amplifier within the calibrator system. When used with the weather radar, signal levels are great enough and ranges short enough such that an RF amplifier is not needed. Furthermore, calculations are made to make sure the signal return to the radar is in the proper range to prevent receiver saturation.

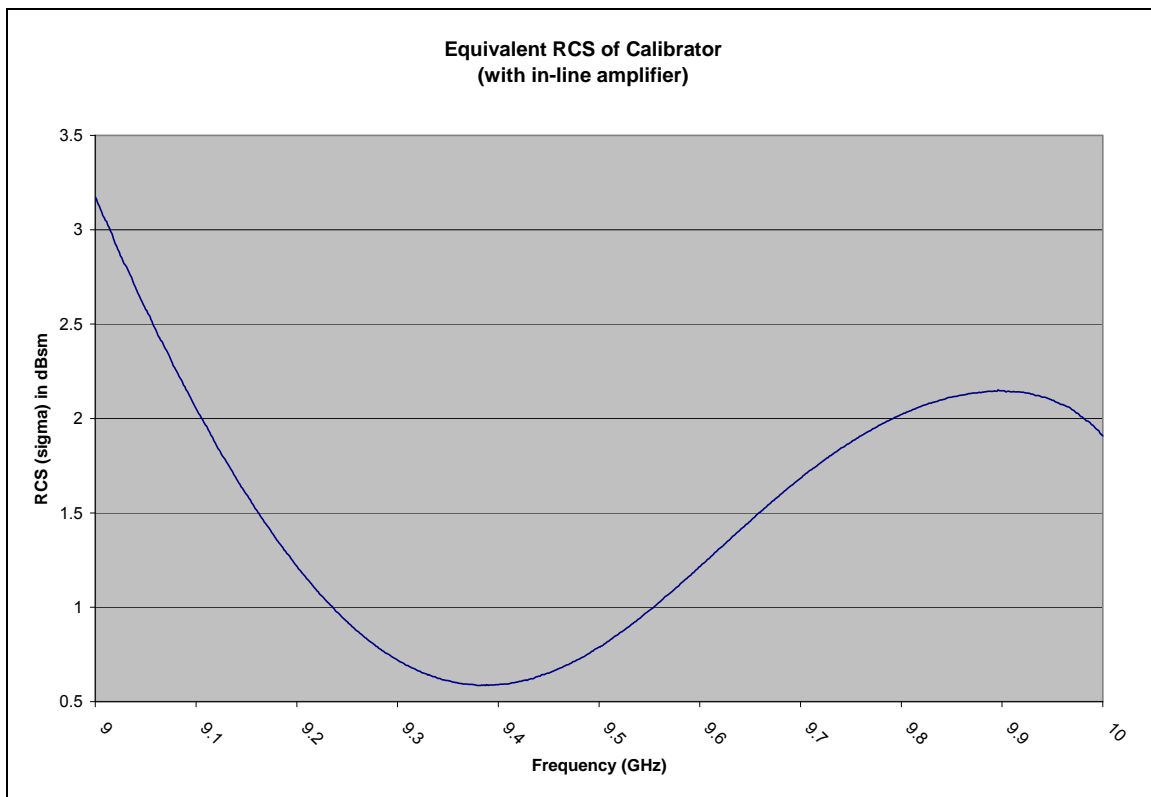


Figure 11. Frequency vs. Equivalent RCS of the ACS. (RCS_plot)

With these measured values the equivalent RCS of the ACS was observed to range from 0.6 to 3.2 dBsm across the 9-10 GHz RF band. On average (mean), the

equivalent RCS of the ACS was 1.4934 dBsm. The median was 1.5101 dBsm. The high value was 3.1742 dBsm at 9 GHz and the low value was 0.5862 dBsm at 9.38 GHz.

In summary, the basic radar measurement is echo signal power (for each signal sample). From the samples, average power is estimated. Reflectivity follows directly from substitution of average power in the weather radar equation. The ACS provides a method of collectively determining the imprecisely known radar system parameters appearing in the weather radar equation. Amplitude statistics from the Weather Signal Simulator, like Doppler statistics, are a planned addition once the programmable attenuator arrives and is installed. See Chapter IV on Future Work for other planned additions.

THIS PAGE INTENTIONALLY LEFT BLANK

IV. CONCLUSION AND FUTURE WORK

A. CONCLUSION

An active calibration system (ACS) for weather radar was successfully designed and implemented. The ACS was verified to be a functional weather radar active calibration system under laboratory testing. It successfully provided the means (met the requirements) to verify all three of the signal parameters measured (estimated) by a weather radar. These include the zeroth Doppler moment (reflectivity), first Doppler moment (average radial velocity), and second Doppler moment (velocity spread).

The cross-section (σ , or equivalent RCS) of the ACS and therefore the means to measure and calculate the radar calibration constant (for reflectivity according to Equation (2.31)) was successfully determined. The underlying data to calculate the cross-section was measured and based on subsequent calculations determined to vary from 0.6 to 3.2 dBsm across the frequency band of interest.

A constant Doppler shift (radial velocity) created by the ACS was observed and verified by the visual inspection of several independent human operators using a spectrum analyzer. The ACS successfully produced a known, operator selected radial velocity. While it was not possible to observe a variable Doppler shift (velocity spread) in exactly the same manner because of time scale limitations, the method to produce a variable Doppler shift was manually verified in a similar manner. The ACS produced an observable constant Doppler shift when provided a variable Doppler data file containing several entries of the same Doppler shift rather than several entries each of a different Doppler shift. If the control software read and executed each Doppler shift entry (regardless of whether they were all the same) and produced the corresponding Doppler shift (which could be observed), there is no reason to believe the control software would not read and execute each Doppler shift entry (when they are different) to potentially produce the corresponding varying Doppler shifts that are desired in the same manner as was demonstrated for the test fixture. Based on this, the ACS was deemed to have successfully produced a known velocity spread.

When tested with the MWR-05XP weather radar this should be sufficient to remove system bias from the reflectivity estimate and to check the accuracy of mean radial velocity and velocity spread estimates.

B. FUTURE WORK

The first item for future work is to field test the active calibrator system (ACS) with the MWR-05XP. It should be tested to see if the constant Doppler generated by the ACS is observed by the MWR-05XP. Then, a variable Doppler should be generated by the ACS and to see if the MWR-05XP observes a Doppler spread. It should also be tested to see if the equivalent RCS/Reflectivity measured is observed as expected and then compared to the radar calibration constants obtained from the balloon and sphere calibration system.

The active calibrator system was not entirely fabricated when this thesis research was concluded. The programmable attenuator had not yet been received. Once received, the programmable attenuator will need to be installed. New RF cables will have to be fabricated to route the RF path sequentially through the phase shifter and programmable attenuator. A control/power cable will have to be fabricated to link the CRIO's DIO module and the DC power supply voltages from the voltage regulator circuit with the programmable attenuator. This cable will be the same type (25-pin to 15-pin) as the one used for the same purposes by the phase shifter differing only by pin assignments. The parts to fabricate this cable have already been procured and received.

The control software for the programmable attenuator has, for the most part, already been written. The control software to independently control the programmable attenuator is the same as for the phase shifter. It need only be duplicated with minor modifications (e.g. filename for Reflectivity values vs. filename for Doppler values, MATLAB script to convert Reflectivity to amplitude shifts vs. Doppler values to phase shifts, etc.). All of the LabVIEW code could be duplicated with minor modifications and run separately to control the programmable attenuator in the same manner as the phase shifter (both 8-bit). In its current state, the ACS can calibrate the MWR-05XP for a single constant amplitude return (Reflectivity) and multiple variable Doppler values.

With the addition of duplicate control code and the addition of the programmable attenuator, the ACS can be configured to calibrate the MWR-05XP for multiple variable amplitude returns to simulate the changes in pulse amplitude that would be observed. However, controlling these values independently (one and then the other) does not allow a calibrator to simulate “real world” weather conditions. In order to calibrate the radar with “real world” weather conditions amplitude and phase values must be controlled simultaneously and dependently. To do this, the control code for both the programmable attenuator and phase shifter must be timed together. This can be achieved by controlling the programmable attenuator and phase shifter from within the same control code. This is slightly less straight forward than the minor modifications for independent control of the two devices. However, it is possible and desirable. The existing phase shifter control code would have to be modified to contain duplicate control subroutines for the programmable attenuator from within its own control code. The difference would primarily be the additional use of nested loops and sequence frames from with the same control code (LabVIEW VI). With implementation of this simultaneous dependent control “real world” weather signal statistics could be simulated by the phase and amplitude variation of the ACS.

Testing of these “real world” weather patterns with the MWR-05XP is the final objective. However, the ACS could and should be tested incrementally with the MWR-05XP at various times as new features are implemented. It is suggested that the MWR-05XP and ACS be tested together first, “as-is” (with the phase shifter installed only), then after the addition of the programmable attenuator and added ability to control both the phase shifter and programmable attenuator simultaneously. Final testing would occur after all features are fully implemented and integrated into the ACS (to include output of amplitude and Doppler statistics of “real world” weather patterns from the Weather Signal Simulator).

In summary outline, Future Work should include:

1. A test of the ACS with the MWR-05XP in its current state (at the close of this thesis research).

- a. To include observations of the first and second Doppler moments, wind speed and wind shear a.k.a. radial velocity and velocity spread a.k.a. a constant Doppler and a variable Doppler.
 - b. To include an observation of the zeroth Doppler moment, a.k.a. reflectivity (to include use of the radar calibration constant) or a single, constant amplitude return (corresponding to the equivalent RCS of the ACS).
 - c. To include a comparison of the observation made in (b.) to the observation made with a balloon and sphere calibration system.
2. Incorporation of the phase invariant programmable attenuator, both the hardware and independent software control (i.e. not affecting the digital phase shifter's software control).
3. Creation of dependent software control of both the programmable attenuator and phase shifter (i.e. control of phase and amplitude simultaneously).
4. A test of the ACS with the MWR-05XP in its advanced state (at the close of Future Work (2.) and (3.)).
 - a. To include observations of the zeroth Doppler moment, reflectivities (to include use of the radar calibration constants) or multiple, variable amplitude returns (corresponding to several equivalent RCSs of the ACS).
 - b. To include observations of all three Doppler moments simultaneously (simultaneous phase and amplitude).
5. Modification of the Weather Signal Simulator to interact directly with the ACS control software to output "real world" weather patterns for the MWR-05XP (within hardware and software limitations, both for the MWR-05XP and ACS – e.g. ambiguous velocities due to PRF and switching speed of ACS hardware).

6. A test of the ACS with the MWR-05XP in its final state (at the close of Future Work (5.)). Are “real world” weather signal statistics observed?

In closing, it should also be noted that if the ACS is used at ground level (the most likely case), a ground reflection will occur. The signal received by the radar will then be determined by the amplitudes and relative phase between the direct (line-of-sight) and ground reflected signal components as influenced by the ground characteristics. The two-way propagation gain is 12 dB if the ground reflected signal is equal in amplitude and in phase with the direct signal. This effect has been observed in measurements made with another calibration system subsequent to the completion of the research work described here. Compensating for this effect complicates the calibration procedure and will require that the ACS antenna be moved through a sequence of heights above ground to determine locations where the direct and ground reflected signals are in phase and 180 degrees out of phase. Signal measurements at these two locations will permit determination of the propagation gain for the case where the direct and ground reflected signals are in phase.

THIS PAGE INTENTIONALLY LEFT BLANK

APPENDIX A. ACS PICTURES



Figure 12. Calibrator Front View with RAM (straight on).



Figure 13. Calibrator Front View with RAM (looking down angle).

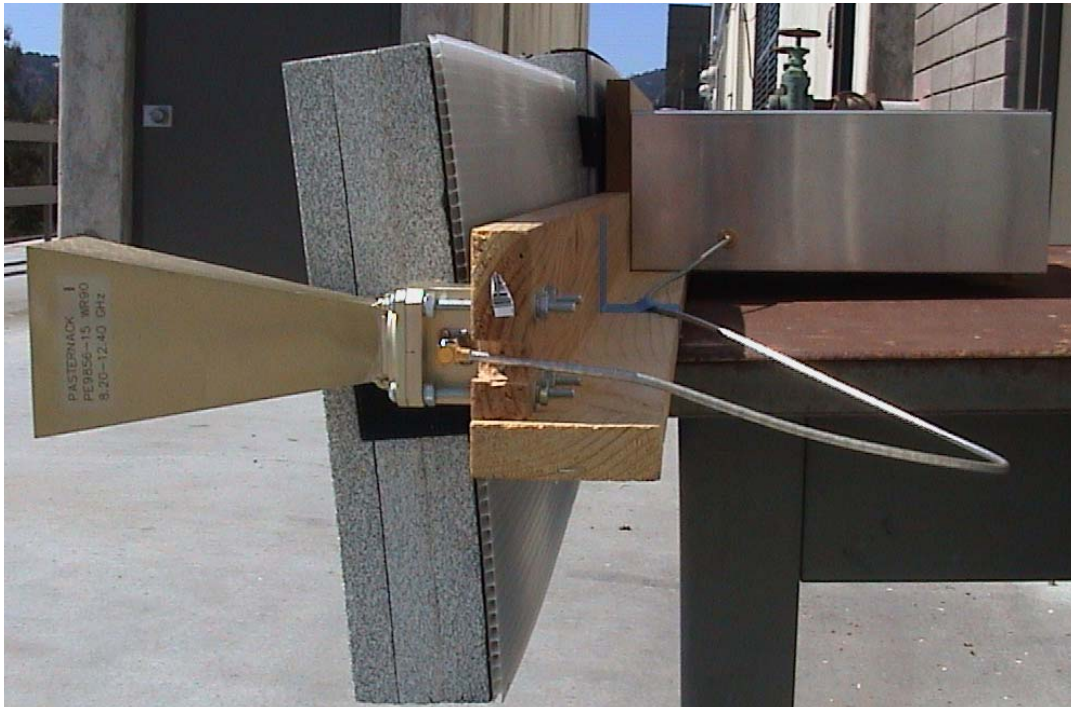


Figure 14. Calibrator Left Side View (straight on).

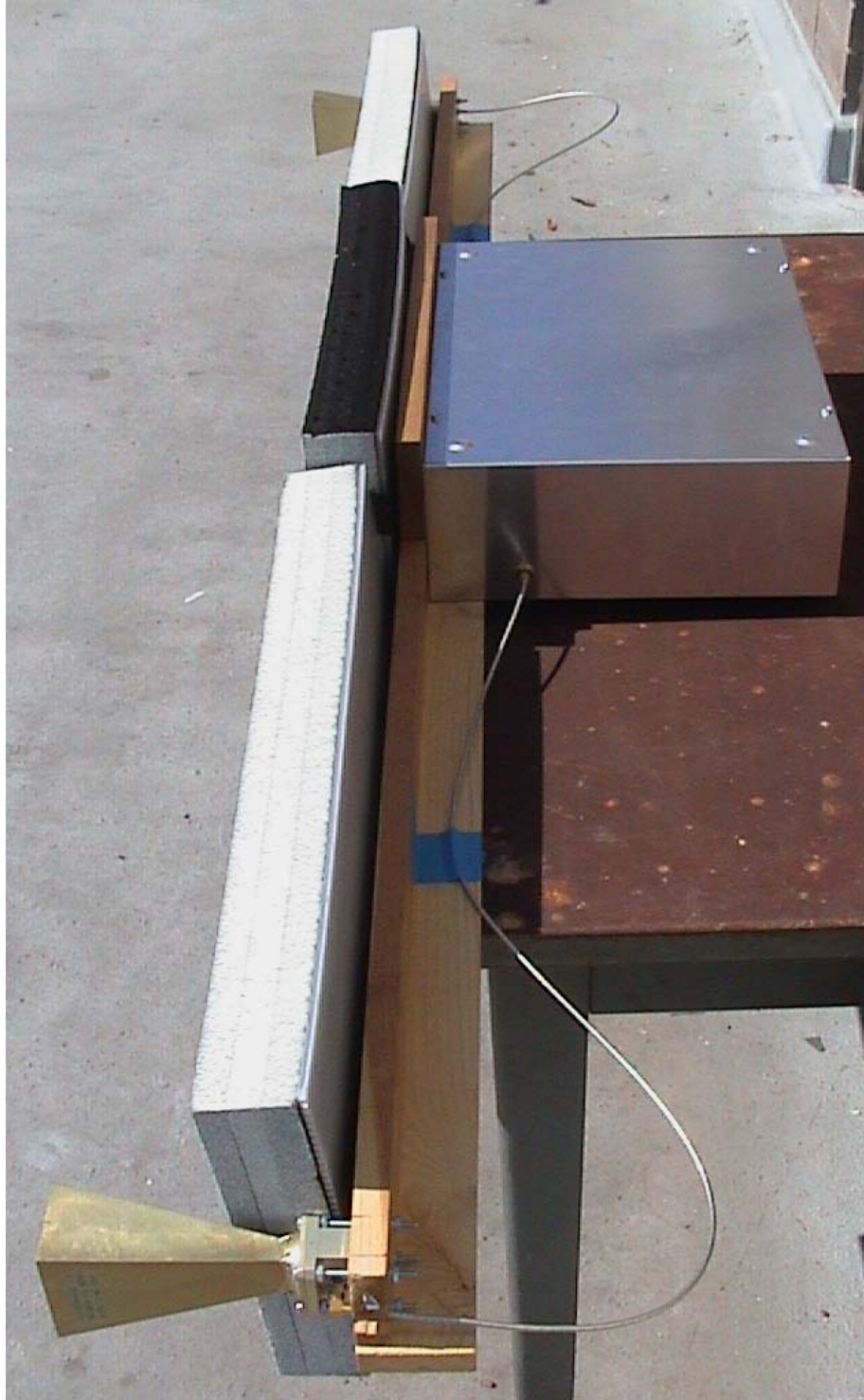


Figure 15. Calibrator Left Side View (looking down angle).

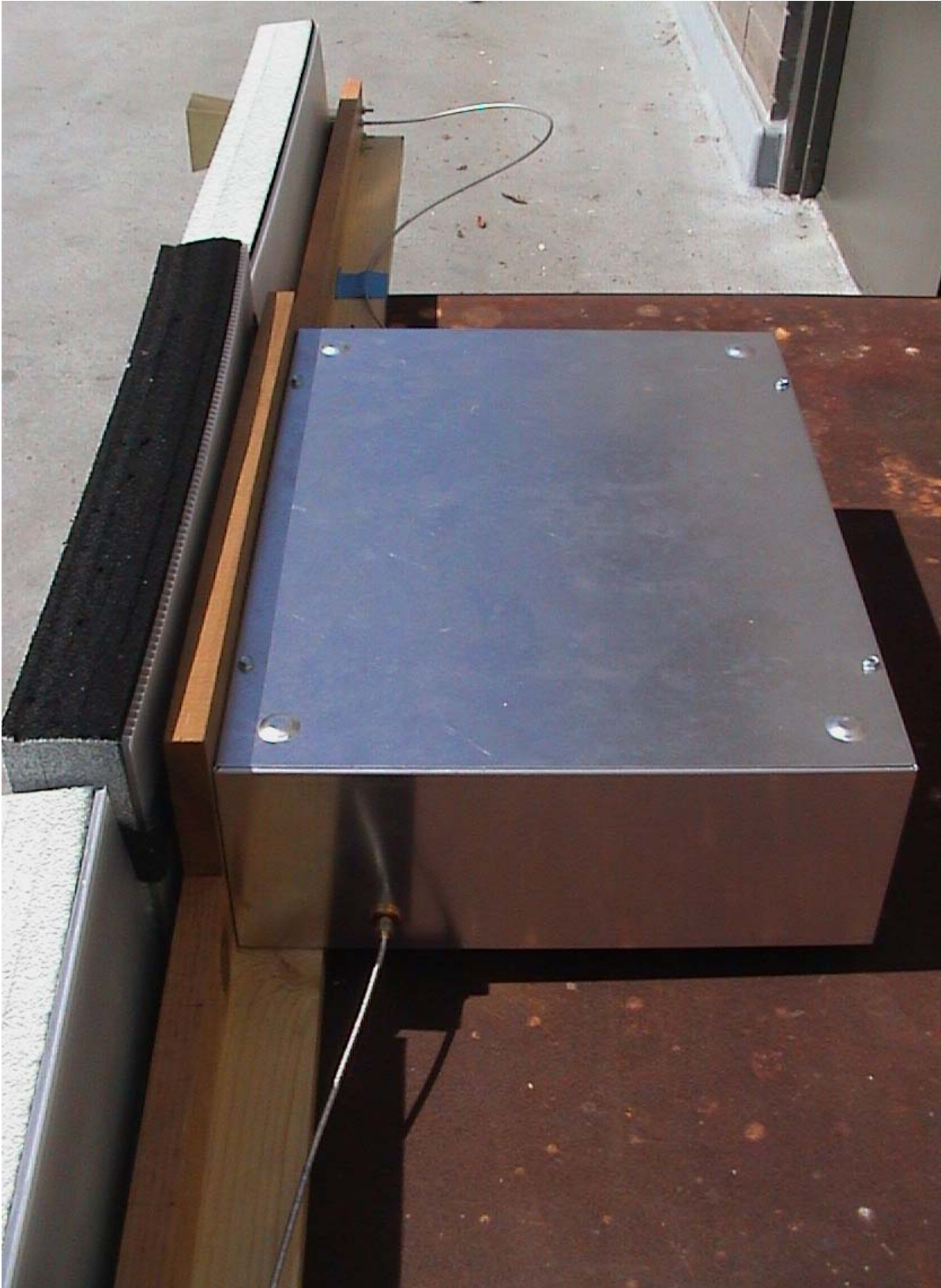


Figure 16. Calibrator Left Side View (looking down angle), Zoomed.

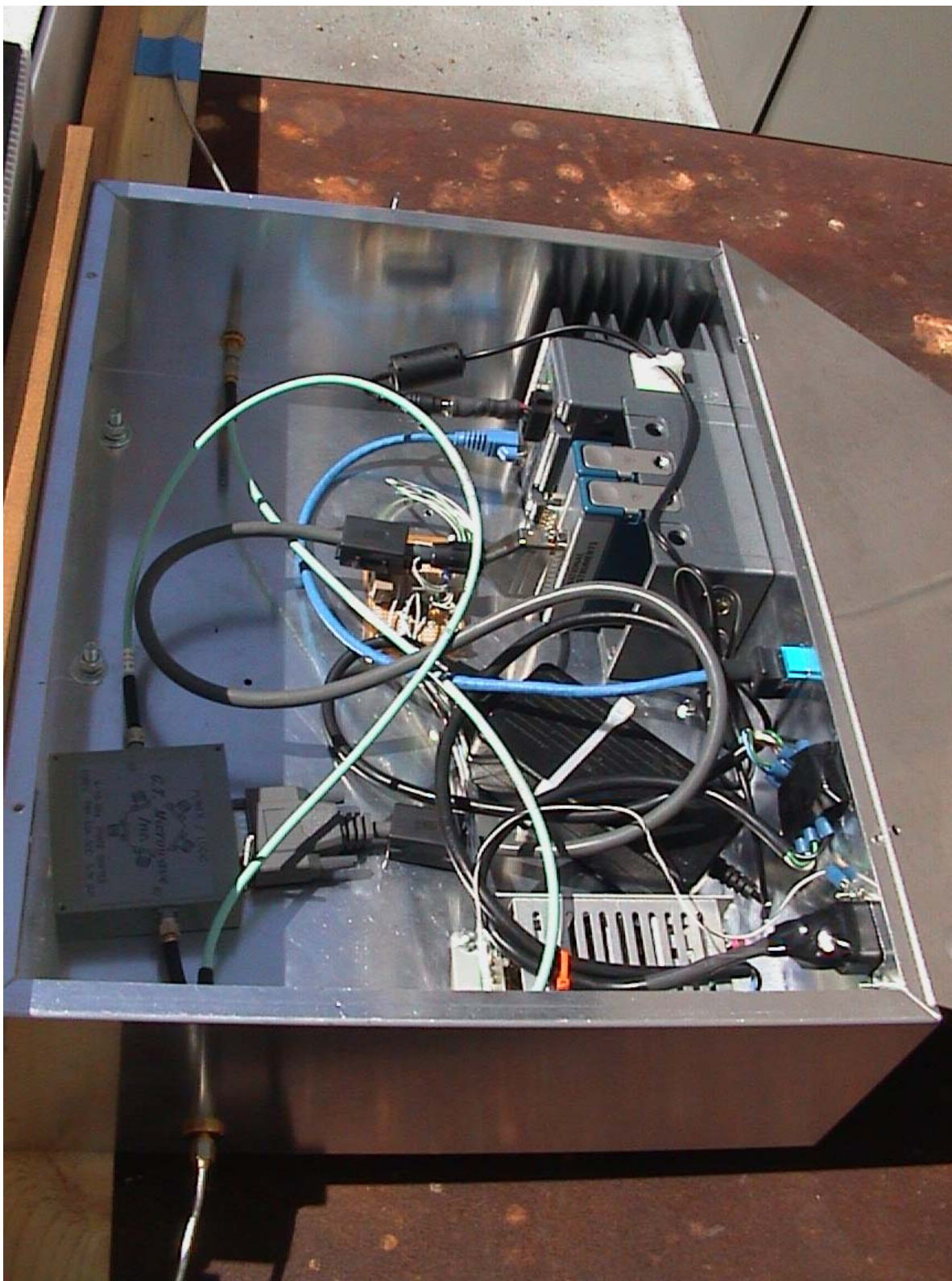


Figure 17. Calibrator Left Side View (looking down angle), Zoomed – Top Cover OFF.

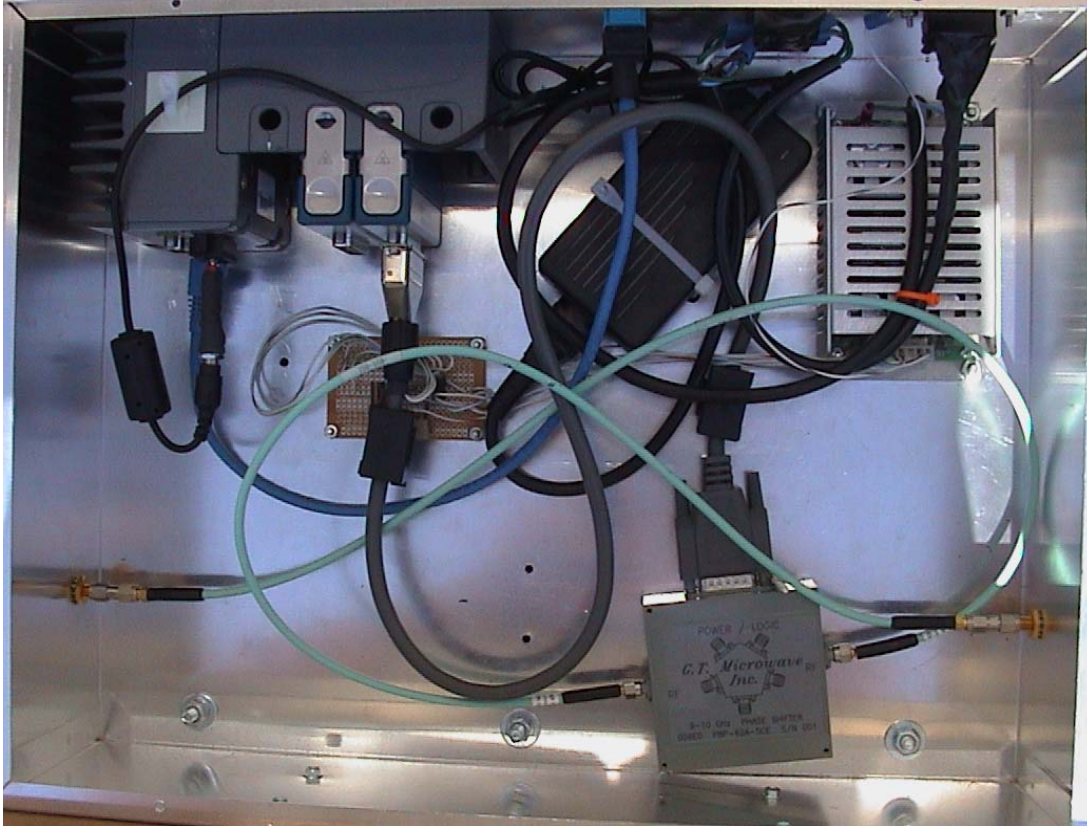


Figure 18. Calibrator Top View (straight on), Zoomed – Top Cover OFF.



Figure 19. Calibrator Inside View (CRIO).

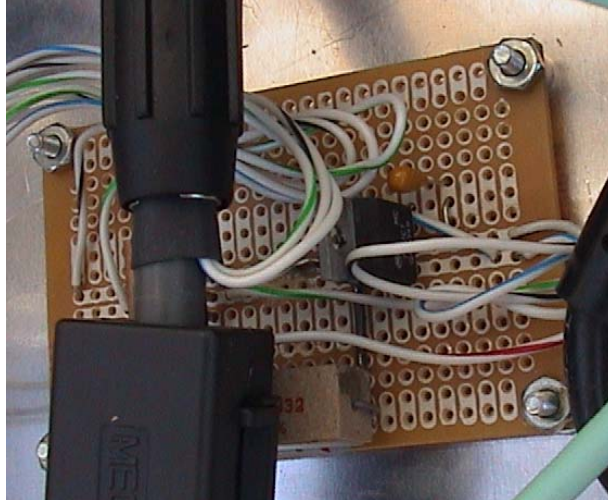


Figure 20. Calibrator Inside View (Power Supply Circuit).

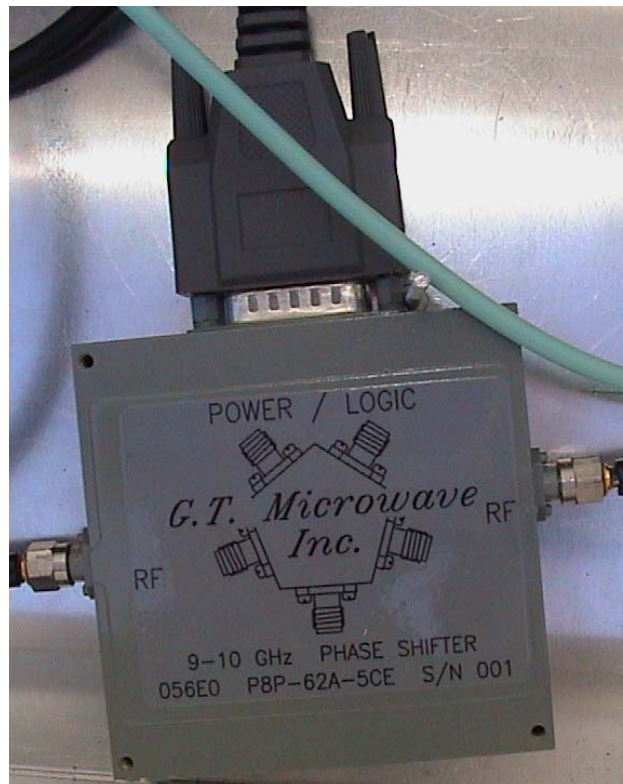


Figure 21. Calibrator Inside View (Phase Shifter).

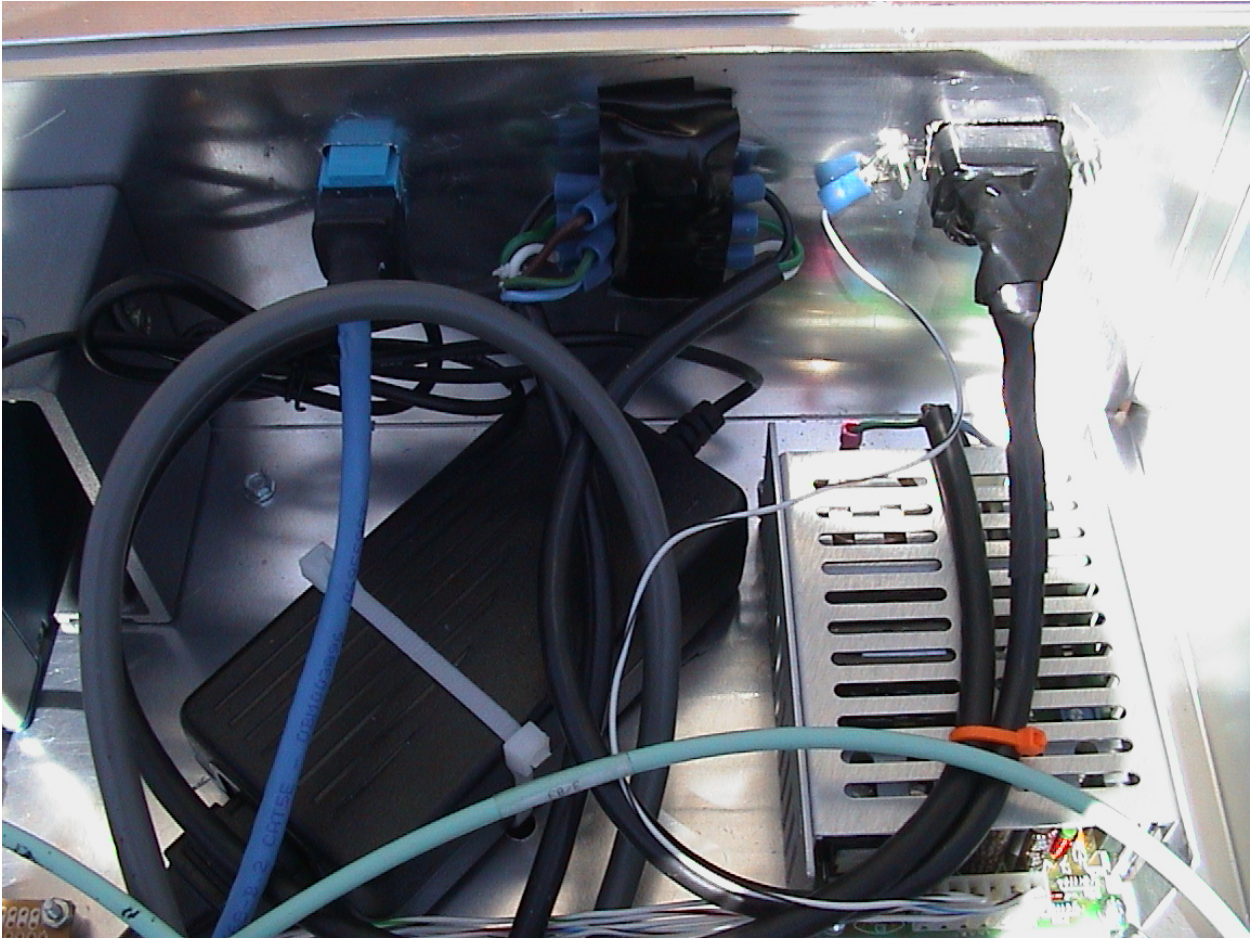


Figure 22. Calibrator Inside View (Power Supply).



Figure 23. Calibrator Right Side View (looking down angle) Zoomed, Top Cover OFF

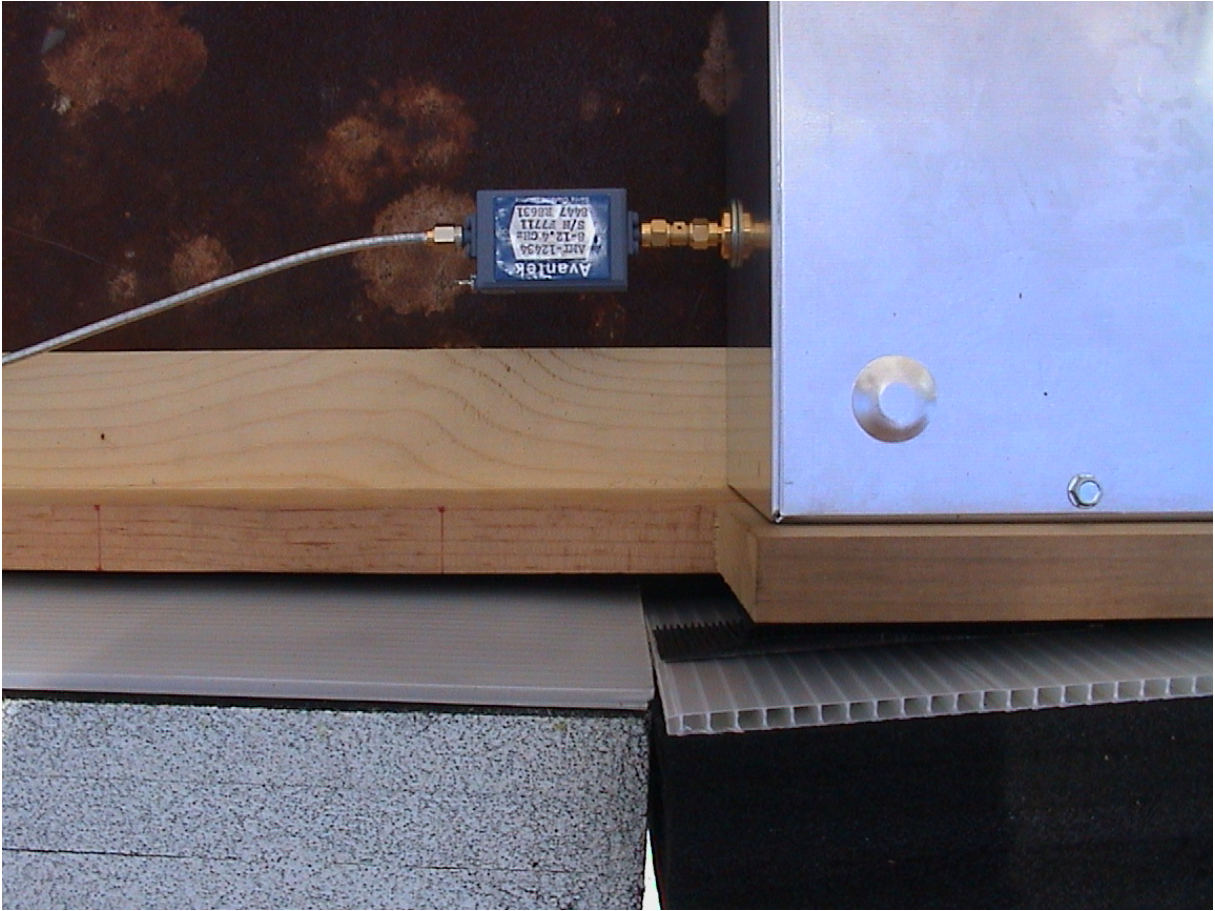


Figure 24. Calibrator Right Side View (looking from above at external in-line amp).



Figure 25. Calibrator Rear Left Side View (looking down angle).

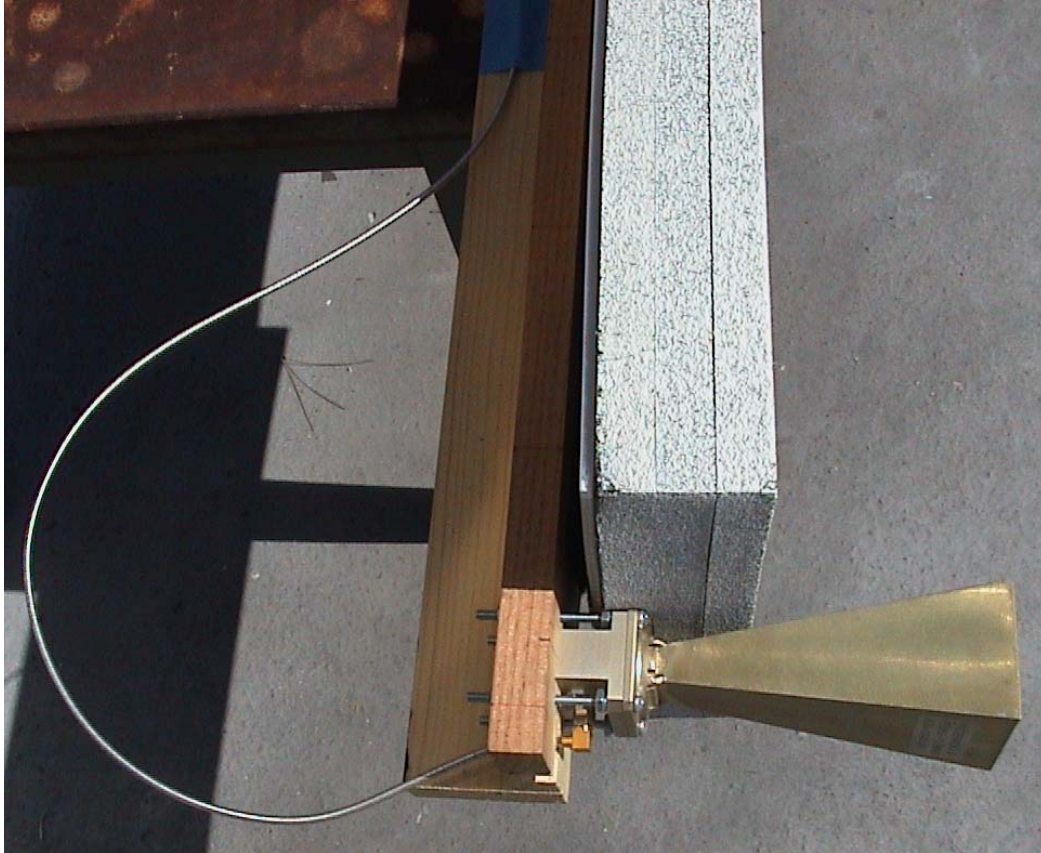


Figure 26. Right Horn Antenna (close-in view, polarization is horizontal).

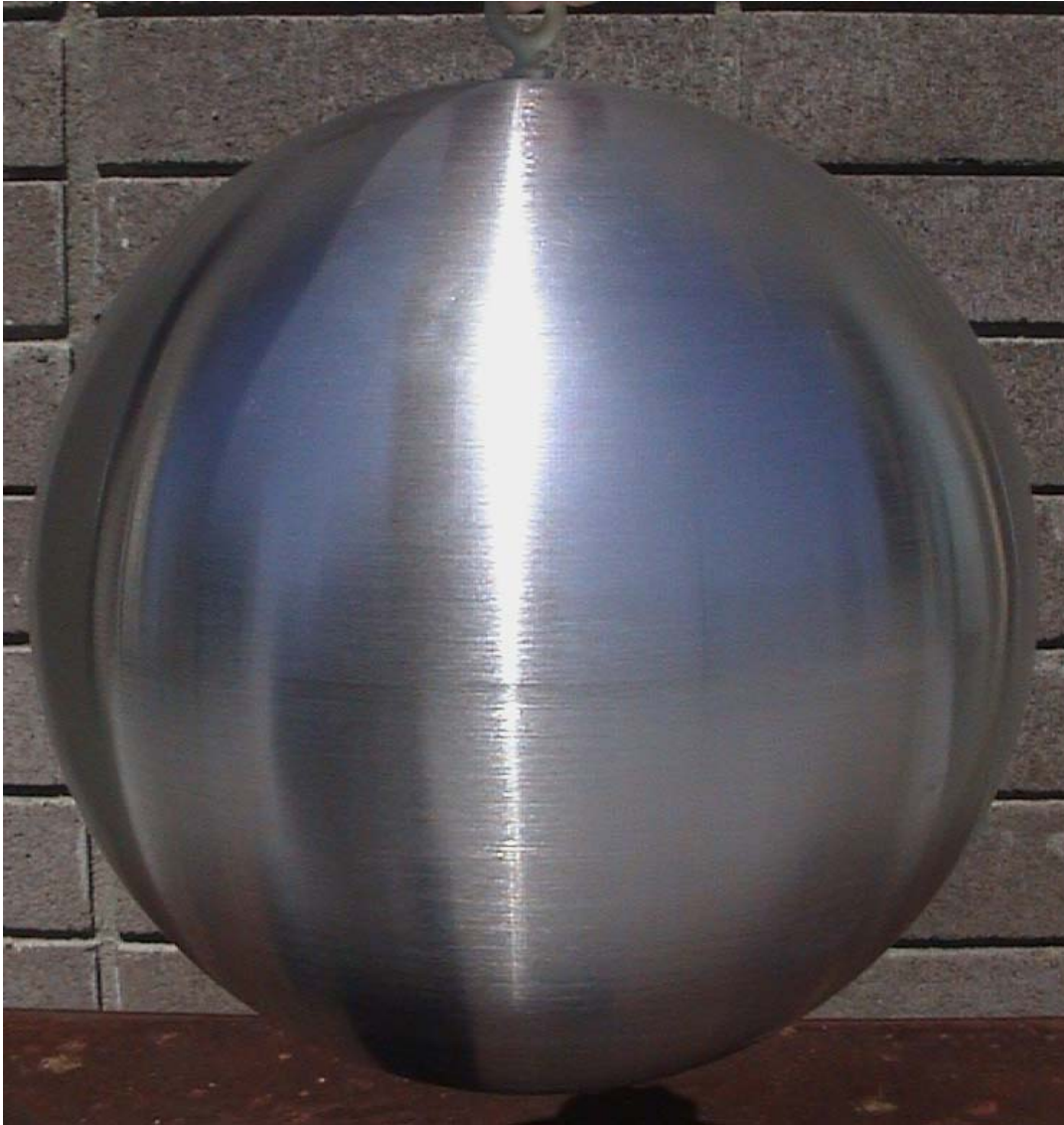


Figure 27. 12" Sphere (used to calibrate the ACS).

THIS PAGE INTENTIONALLY LEFT BLANK

APPENDIX B. DIGITAL PHASE SHIFTER DATA

Digitally Controlled Phase Shifter
Manufacturer: G.T. Microwave, Inc.
Model Number: P8P-68N-5

Electrical Specifications for Digitally Controlled 360° Phase Shifters:

Frequency Range (GHz): 6.0-18.0

Phase Error Vs Freq. Max: +/- 10.0°

Amplitude Balance Max: +/- 1.50 dB

Insertion Loss Max: 12.0 dB

V.S.W.R. Max: 1.90:1

Switching Speed nSec Max: 500

RF Input Power dBm CW: +15

RF Input Power dBm Max: +20

Power/Logic Connections:

No. of BITS	LOGIC PIN ASSIGNMENTS	+15V PIN	-15V PIN	GND PIN
8	L.S.B. @ 1 to M.S.B. @ 8	13	14	15

Table 6. Power and Logic Connections for Digitally Controlled Phase Shifter.

DIGITALLY CONTROLLED PHASE SHIFTERS

G.T. Microwave Features:

Frequency Ranges: From 500 MHz to 24 GHz any optimized bandwidth is available.

TTL Compatible Logic: G.T.M.I.'s binary logic Digital to Analog Converter with 8 inputs; Logic '1'/BIT = 256 discrete phase shifts with a 1.4° Resolution (L.S.B.) or all Logic '0' = 0° Reference state. Any resolution up to 12 Bits is available.

Optional Models: Analog Voltage controlled or Switched Line Digital phase shifters are available, please consult factory.

High Speed Switching: Phase Shifters listed are measured from any set value to any value.

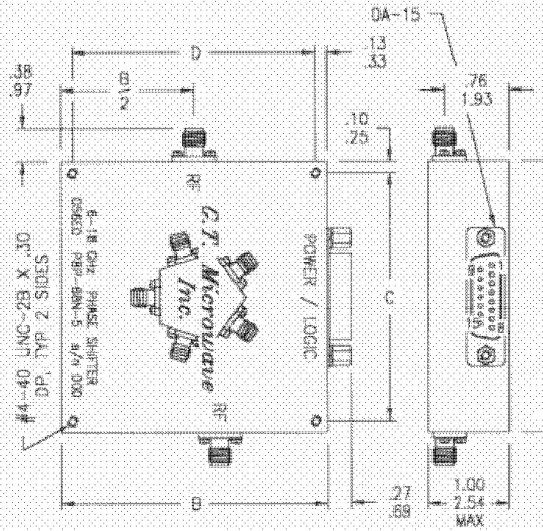
Low DC Power Consumption: Phase Shifters require $\pm 15\text{VDC}$, $\pm 1\%$ @ $+100/-250\text{mA}$.

Stable Phase Shifts: Variation vs Temperature from -55° to 85°C is typically $\pm 0.2^\circ/\text{C}$ from set value. Temperature Compensated models are available upon request.

High RF Power Handling: For power levels greater than listed, please consult factory.

Standard Interfaces: RF port connectors are 'SMA', female per MIL-C-39012.

Life Time Integrity: G.T.M.I.'s phase shifters are designed to meet MIL-E-16400, Range 1 and MIL-E-5400, Class 2 environments operating within the -55° to $+85^\circ\text{C}$ temperature range.



FOR SIZES SEE PAGE 7

DIMENSIONS ARE EXPRESSED IN CM TOLERANCES $\pm .02$ $\pm .010$ $\pm .05$ $\pm .025$

POWER/LOGIC Connections

No. of BITS	LOGIC PIN ASSIGNMENTS	+15V PIN	-15V PIN	GND PIN
8	L.S.B. @ 1 to M.S.B. @ 8	13	14	15

ALL UN-USED PINS HAVE NO INTERNAL CONNECTIONS

Electrical Specifications for DIGITALLY CONTROLLED 360° PHASE SHIFTERS

G.T.M.I.'s MODEL NUMBER	FREQUENCY RANGE GHz	PHASE ERROR Vs FREQ. MAX	AMPLITUDE BALANCE MAX	INSERTION LOSS MAX	V.S.W.R. MAX	SWITCHING SPEED nSEC MAX	RF INPUT POWER dBm CW MAX	OUTLINE SIZE
PSP-38N-5	0.5-2.0	$\pm 10.0^\circ$	± 1.50 dB	13.0 dB	1.70:1	500	+15 -20	1
PSP-38N-5	1.0-3.0			11.0 dB	1.80:1			2
PSP-48N-5	2.0-6.0			12.0 dB	1.90:1			3
PSP-68N-5	6.0-18.0	$\pm 22.0^\circ$	± 2.00 dB	15.0 dB	2.20:1			4
PSP-84N-5	18.0-24.0			16.0 dB	2.20:1			
PSP-69N-5	2.0-18.0							

For substantial improvement in performance, ask for OPTIMIZED NARROWBAND models

Figure 28. Specifications Sheet for Digital Phase Shifter from G.T. Microwave.

RF Measurements on Digital Phase Shifter: See Appendix on Scalar and Vector Network Analyzer Measurements.

**APPENDIX C. SCALAR AND VECTOR NETWORK ANALYZER
MEASUREMENT DATA**

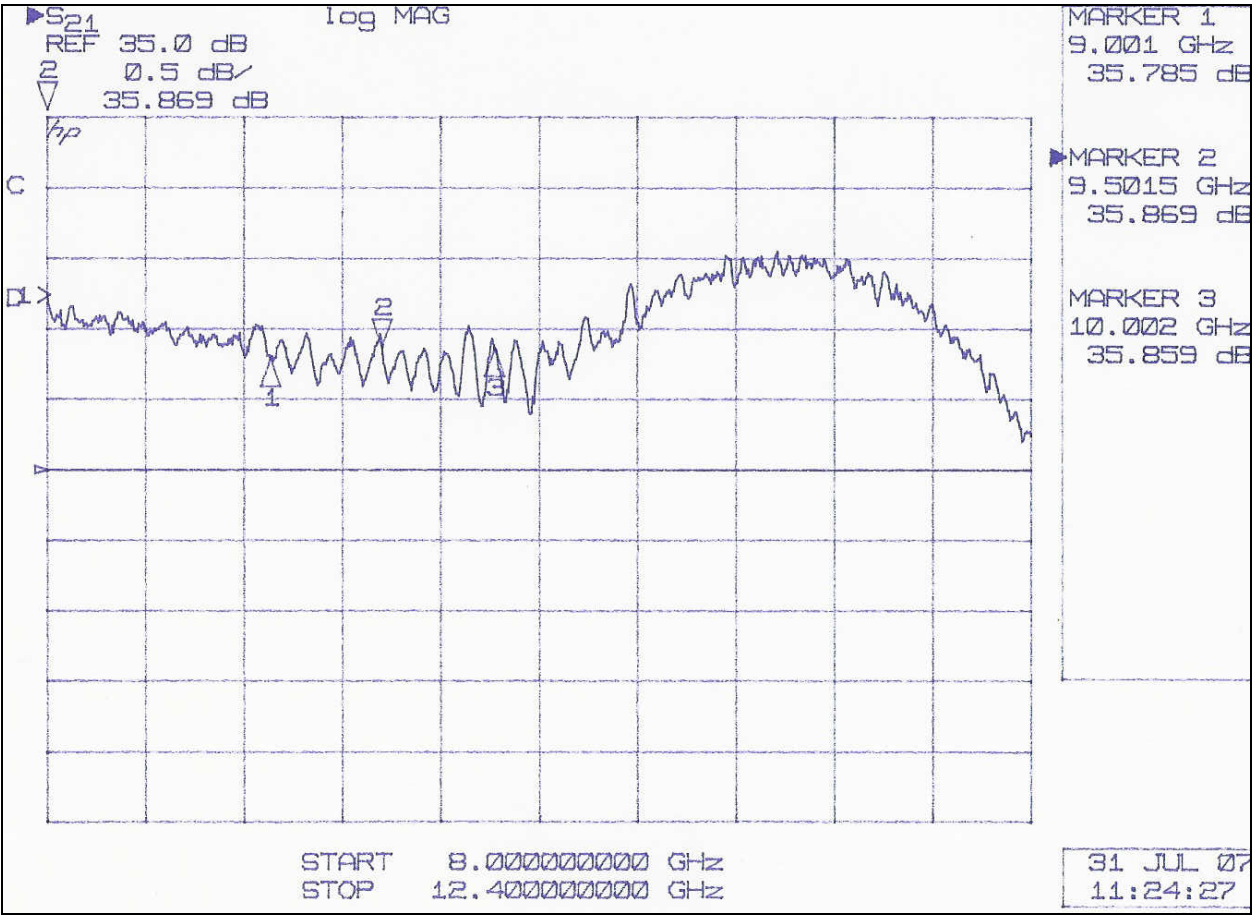


Figure 29. RF Amplifier Gain Single VNA Plot.

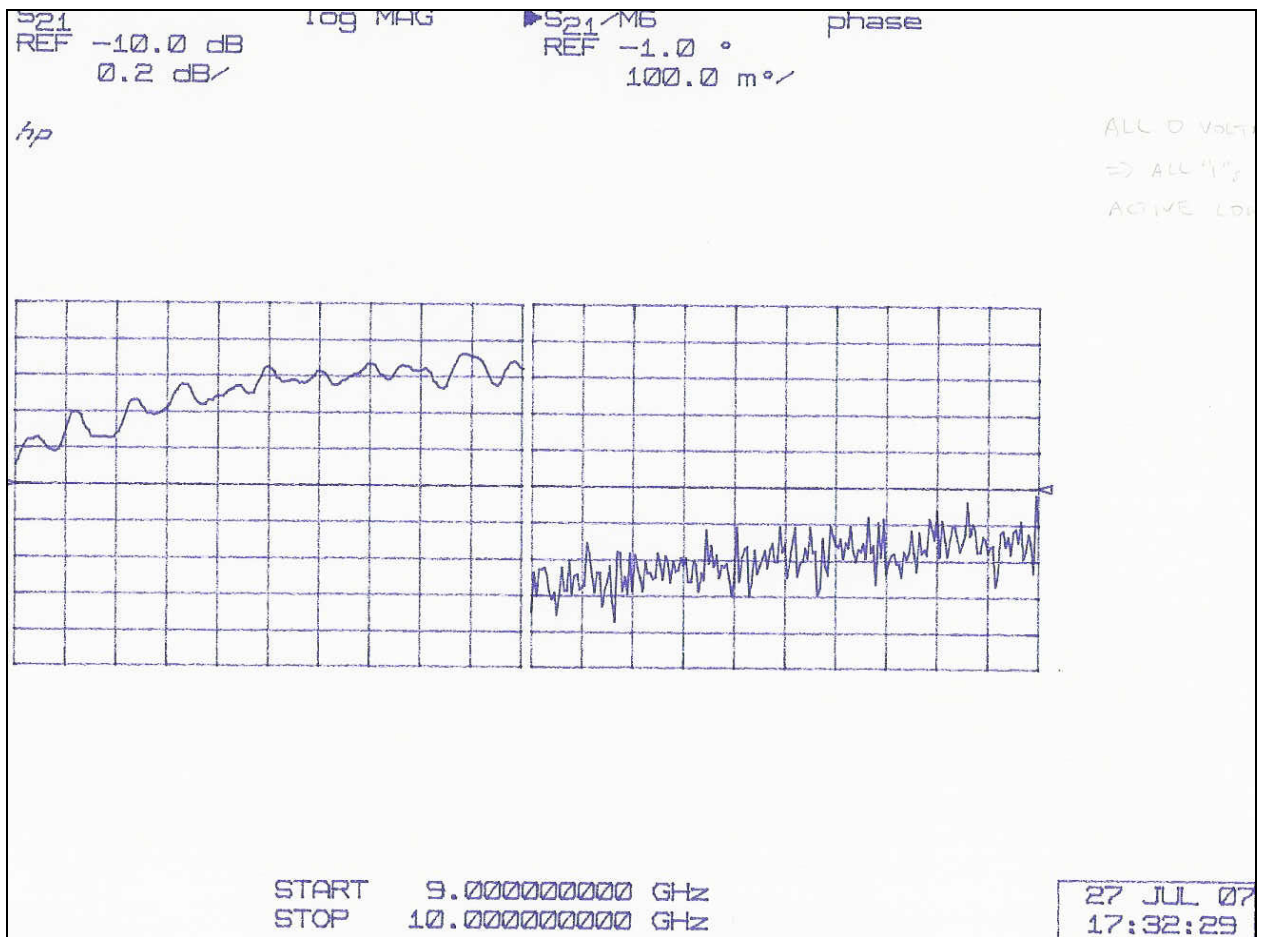


Figure 30. Digital Phase Shifter Insertion Loss (Left) and Phase Value (Right) Dual VNA Plots. Zero volts applied to all pins. Active Low. All bits "1". (11111111).

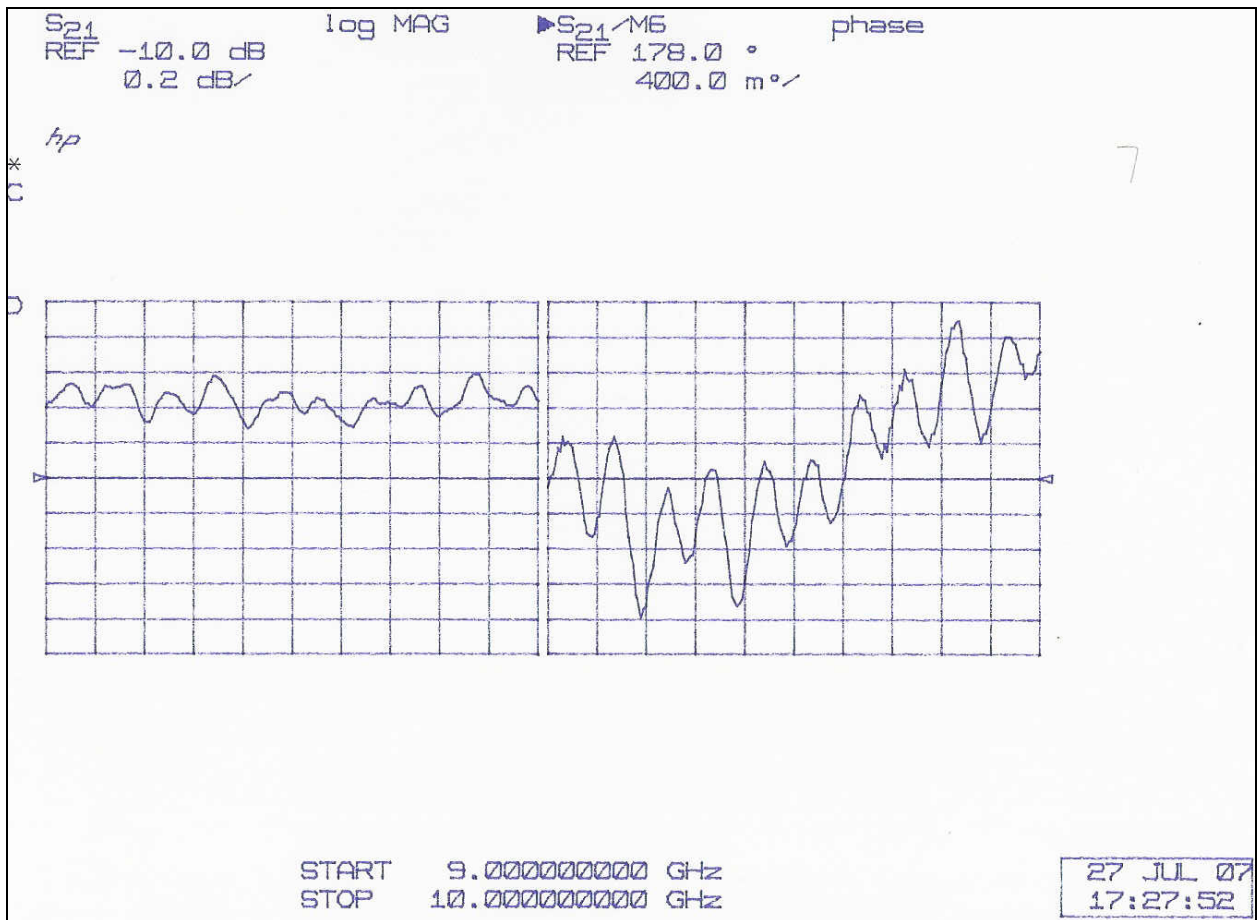


Figure 31. Digital Phase Shifter Insertion Loss (Left) and Phase Value (Right) Dual VNA Plots. Zero volts applied to MSB pin only, five volts others. (10000000).

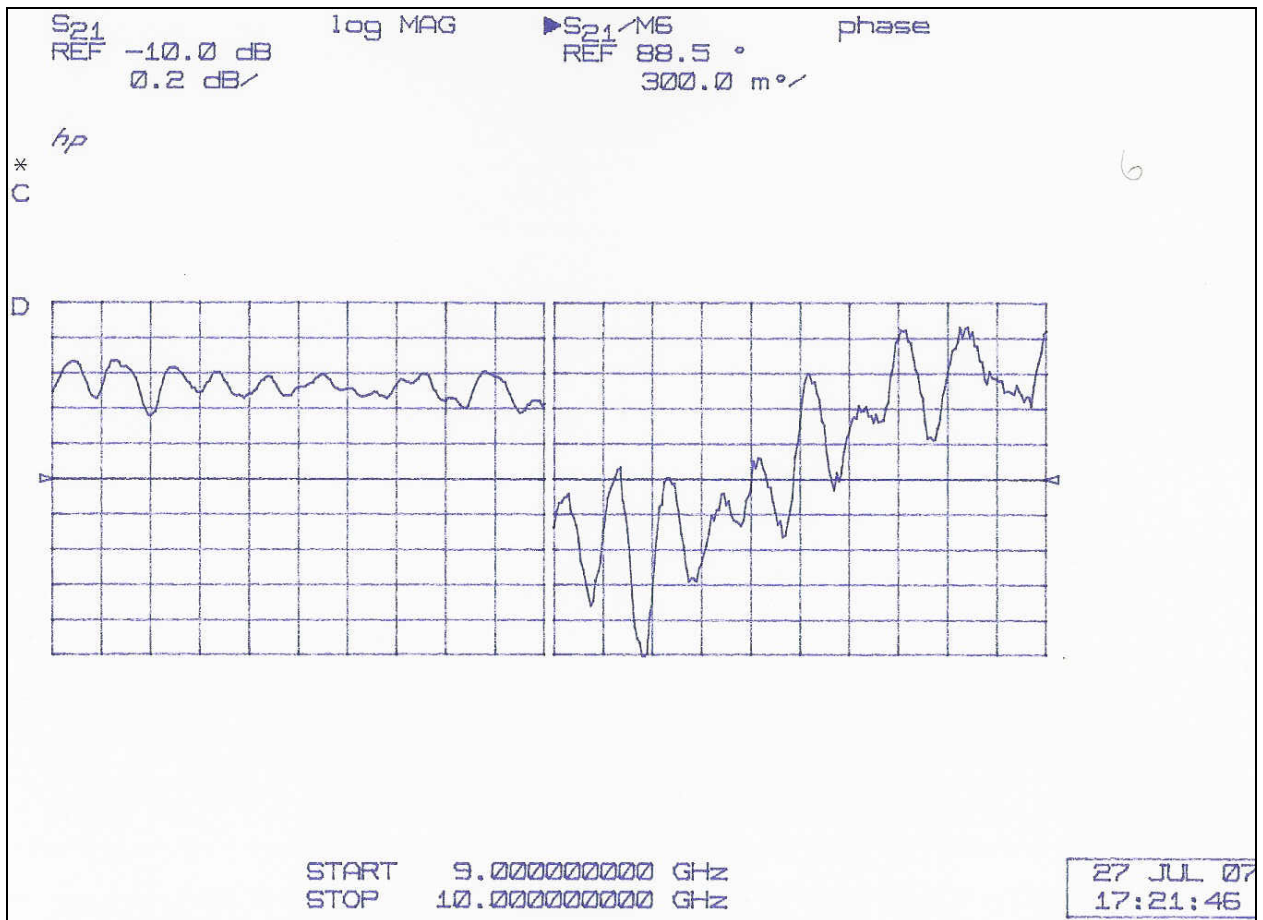


Figure 32. Digital Phase Shifter Insertion Loss (Left) and Phase Value (Right) Dual VNA Plots. Zero volts applied to second MSB pin only, five volts others. (01000000).

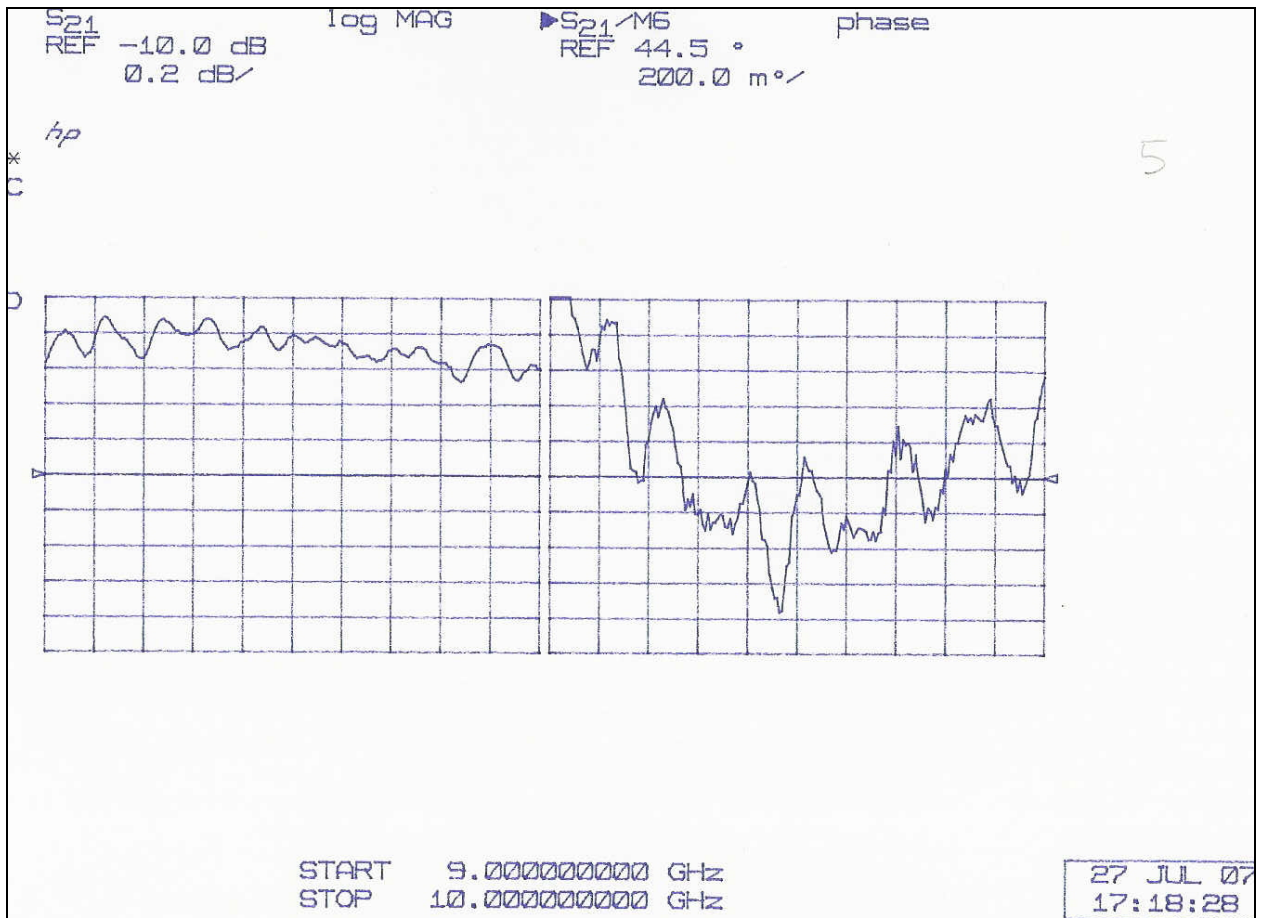


Figure 33. Digital Phase Shifter Insertion Loss (Left) and Phase Value (Right) Dual VNA Plots. Zero volts applied to third MSB pin only, five volts others. (00100000).

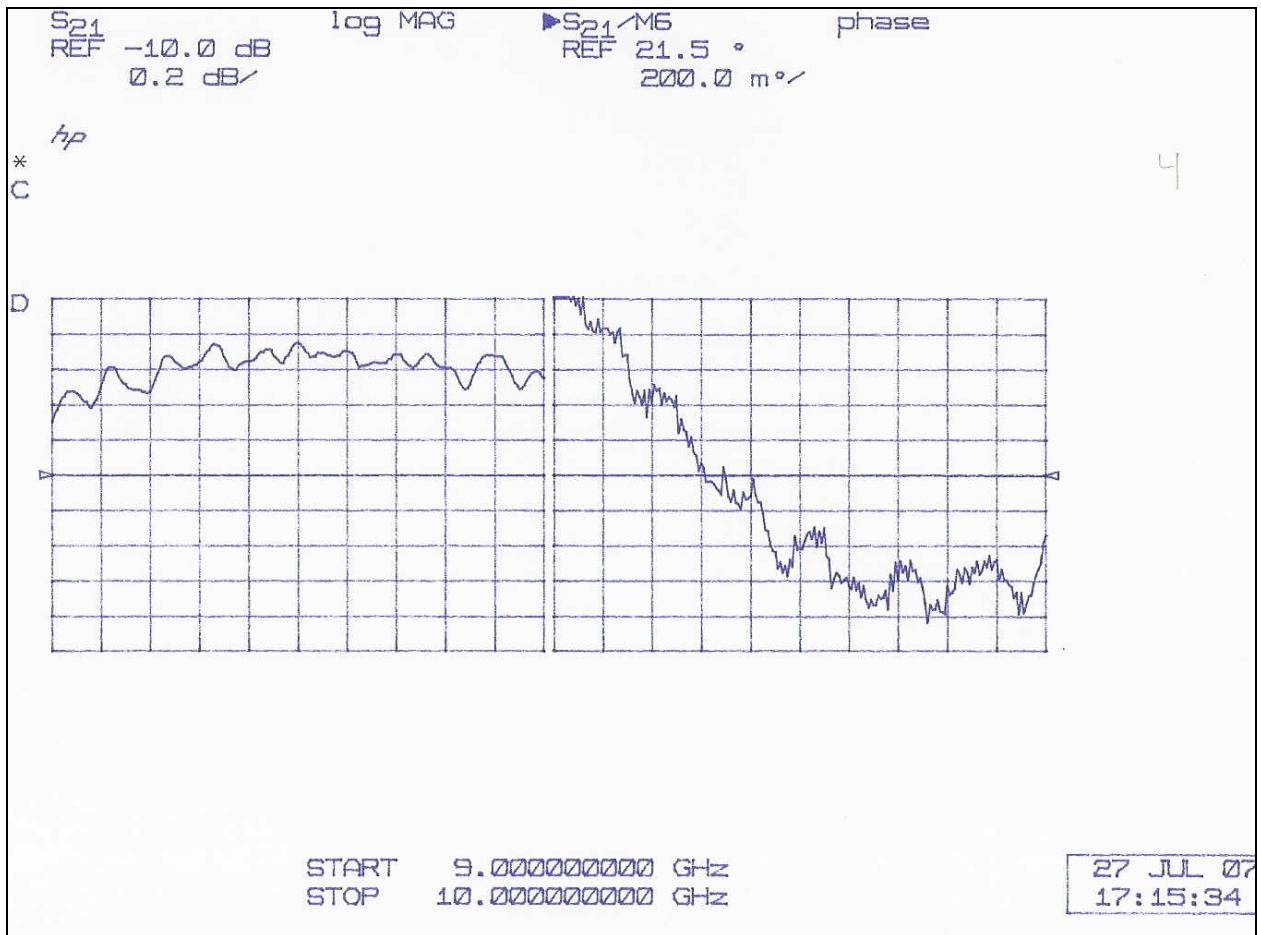


Figure 34. Digital Phase Shifter Insertion Loss (Left) and Phase Value (Right) Dual VNA Plots. Zero volts applied to fourth MSB pin only, five volts others. (00010000).

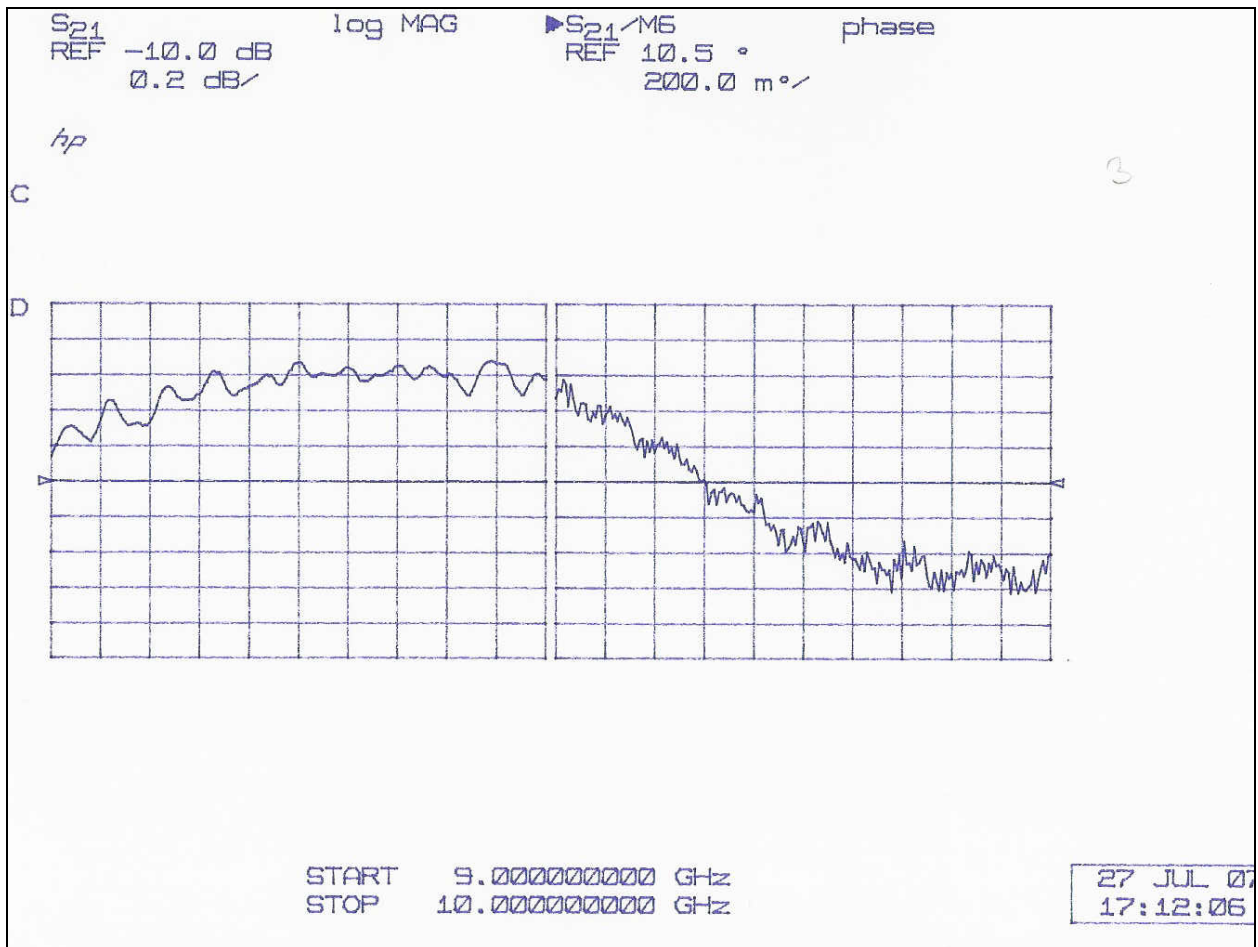


Figure 35. Digital Phase Shifter Insertion Loss (Left) and Phase Value (Right) Dual VNA Plots. Zero volts applied to fifth MSB pin only, five volts others. (00001000).

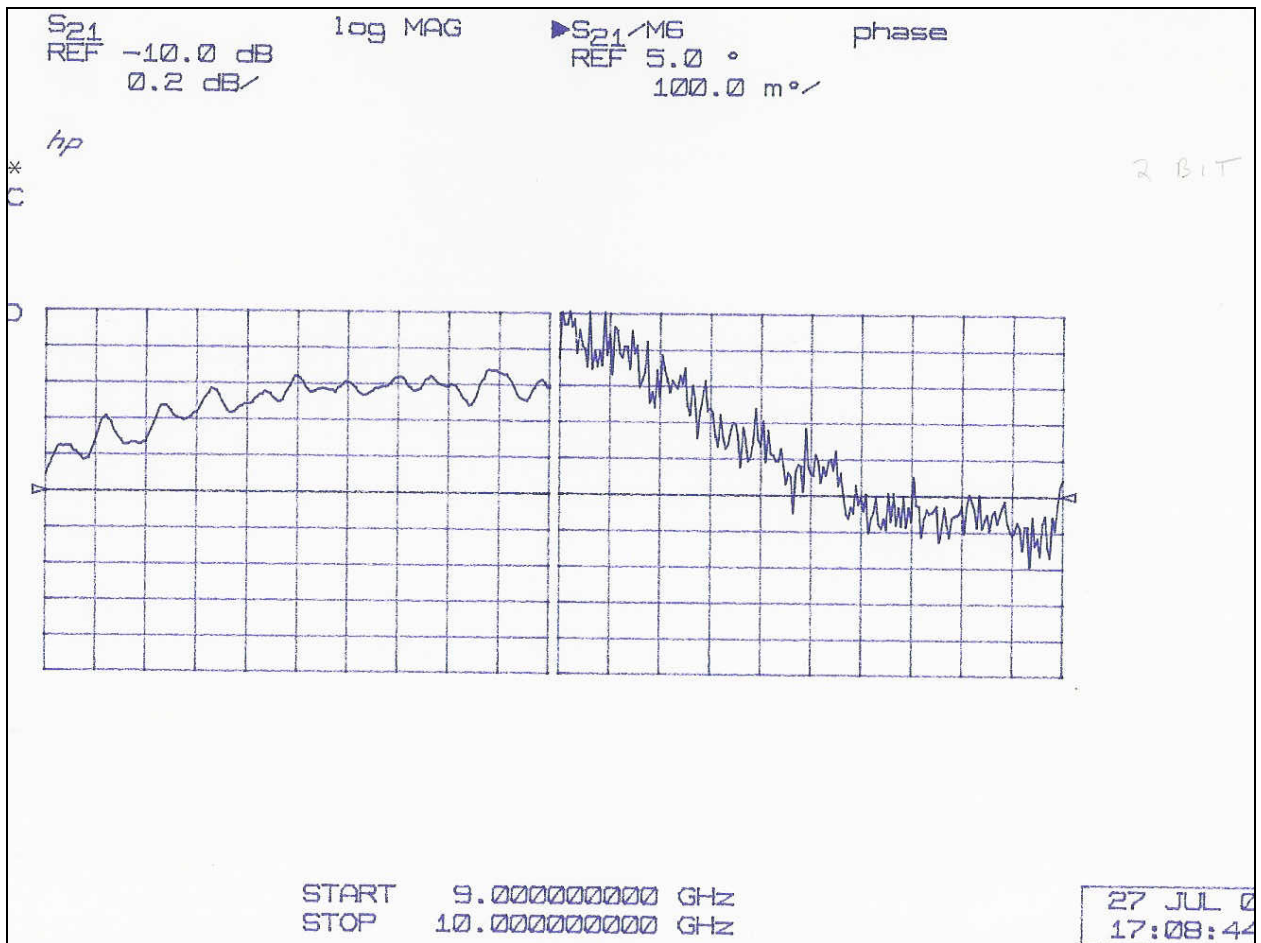


Figure 36. Digital Phase Shifter Insertion Loss (Left) and Phase Value (Right) Dual VNA Plots. Zero volts applied to sixth MSB pin only, five volts others. (00000100).

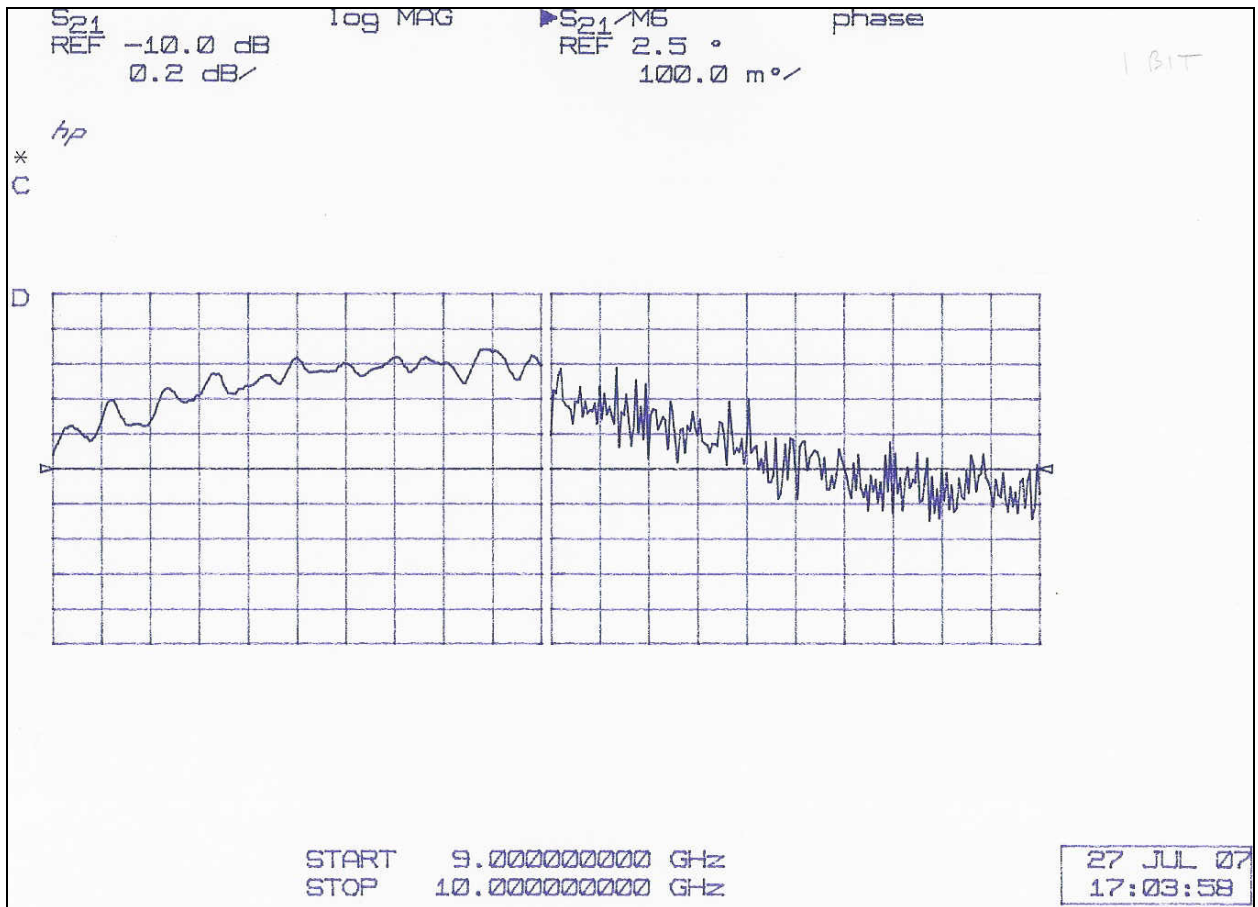


Figure 37. Digital Phase Shifter Insertion Loss (Left) and Phase Value (Right) Dual VNA Plots. Zero volts applied to seventh MSB pin only, five volts others. (00000010).

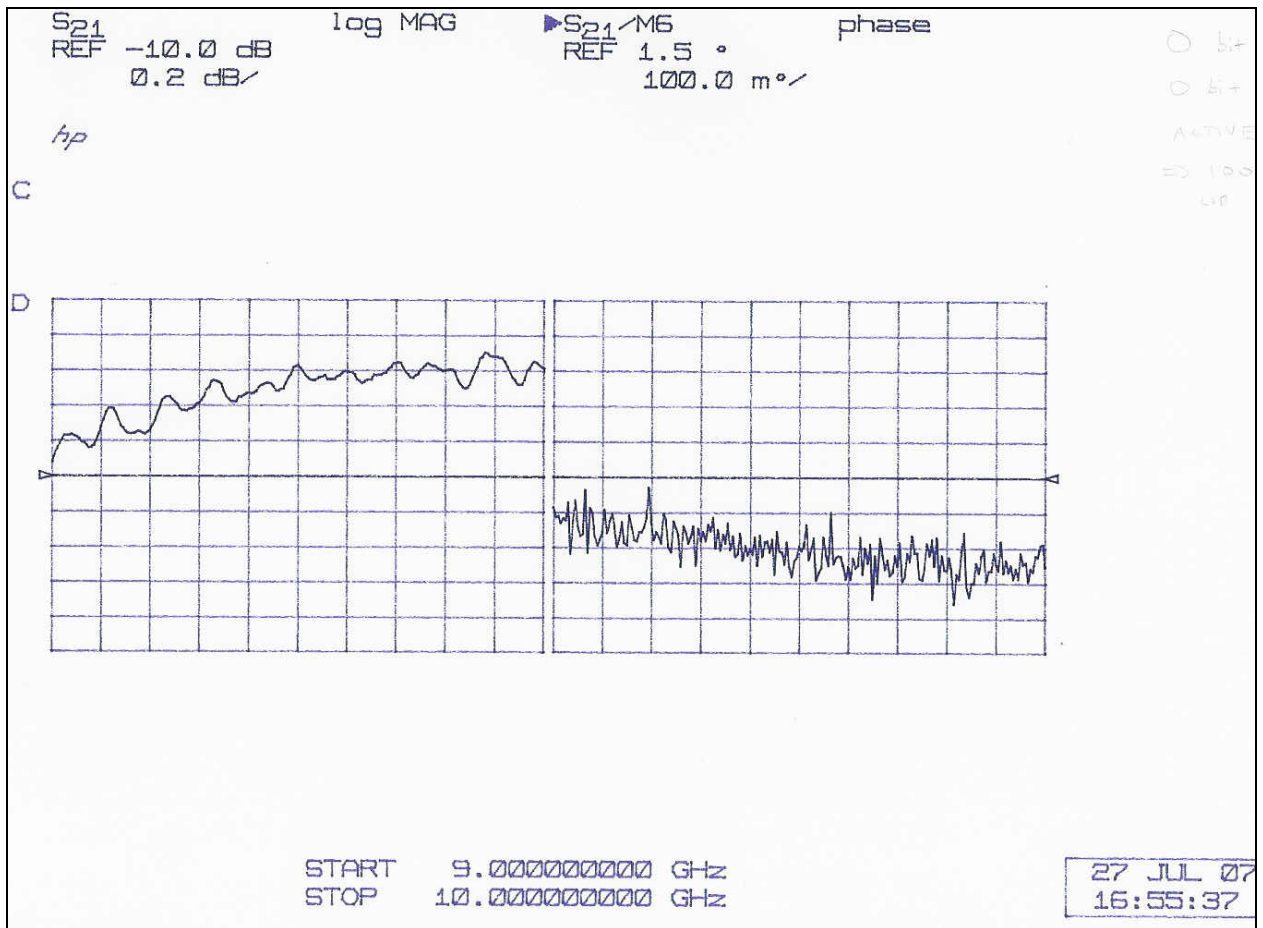


Figure 38. Digital Phase Shifter Insertion Loss (Left) and Phase Value (Right) Dual VNA Plots. Zero volts applied to LSB pin only, five volts others. (00000001).

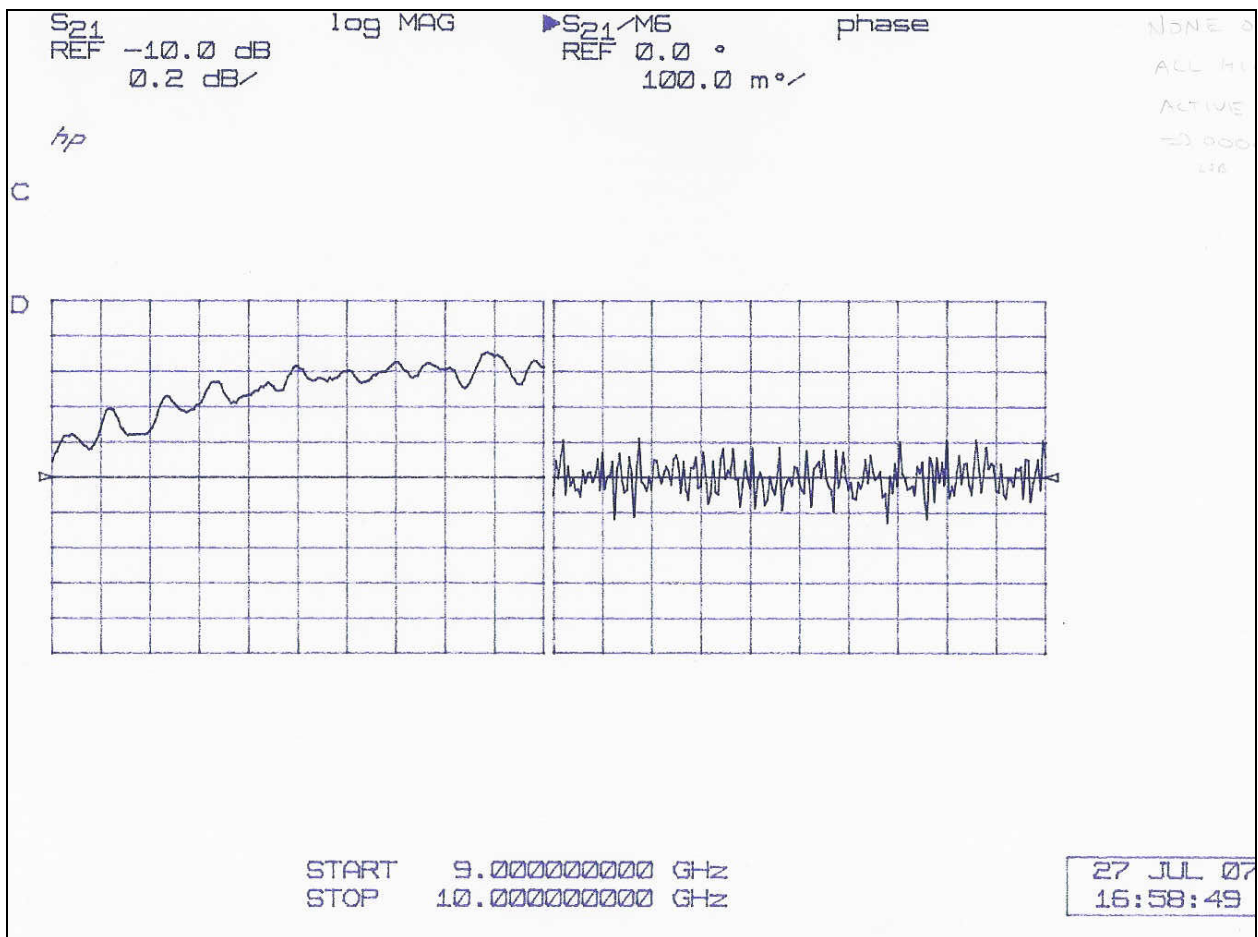


Figure 39. Digital Phase Shifter Insertion Loss (Left) and Phase Value (Right) Dual VNA Plots. Five volts applied to all pins. (00000000).

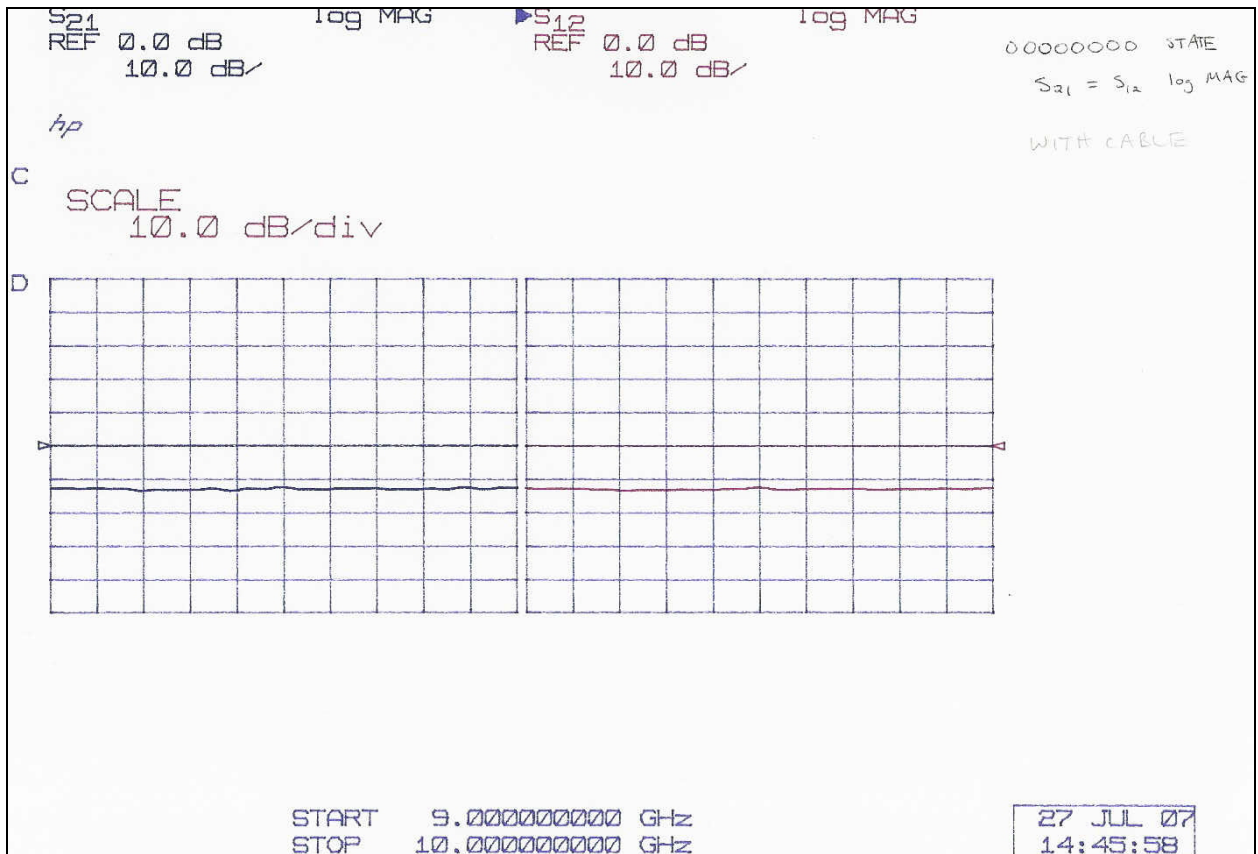


Figure 40. Digital Phase Shifter Forward (left) and Reverse (right) Insertion Loss Dual VNA Plots. Demonstration of device's bidirectional property. Losses in the forward and reverse are equal. Five volts applied to all pins. (00000000).

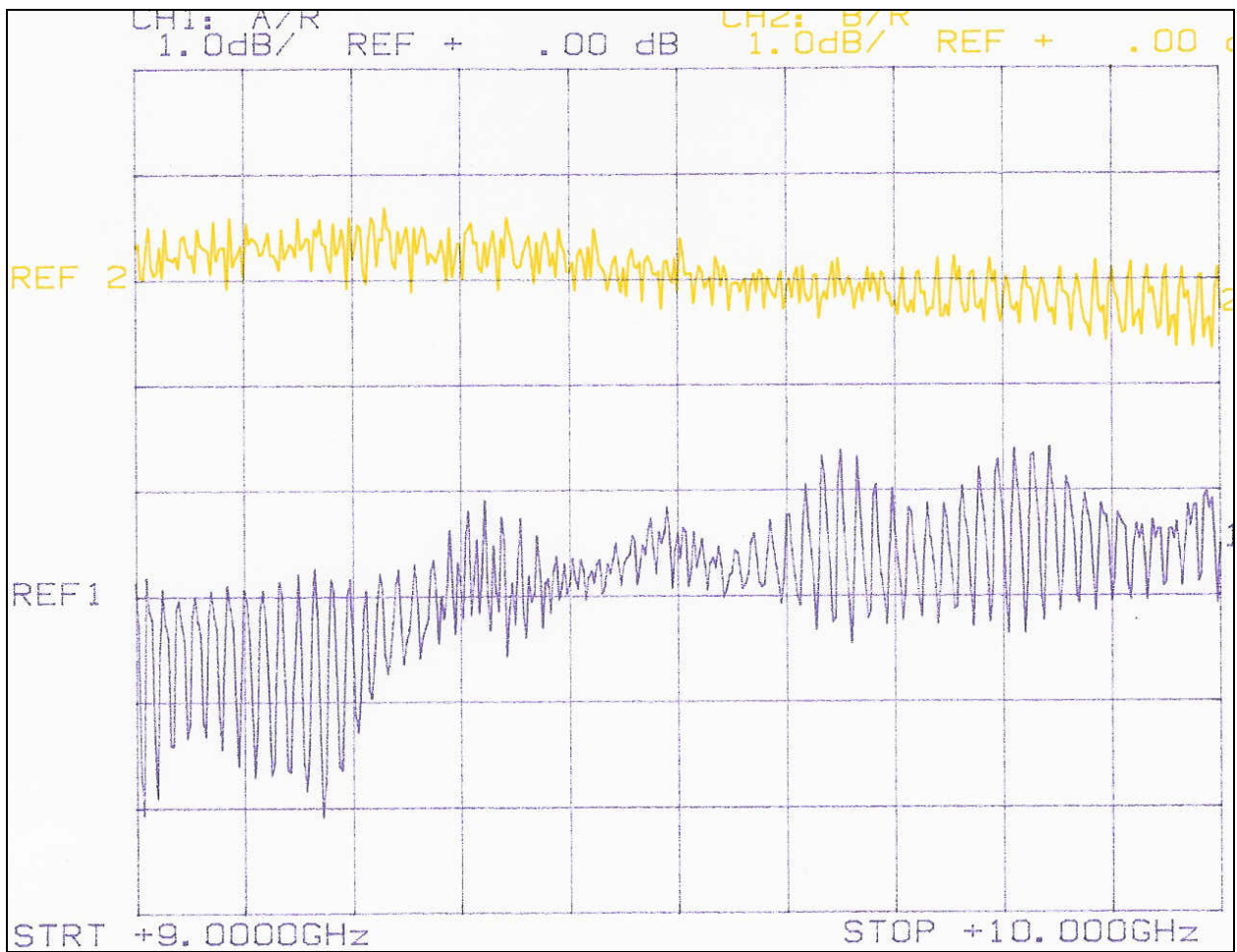


Figure 41. SNA Plot of Scalar Network Analyzer's Straight-Through State.
"Calibrated to Zero".

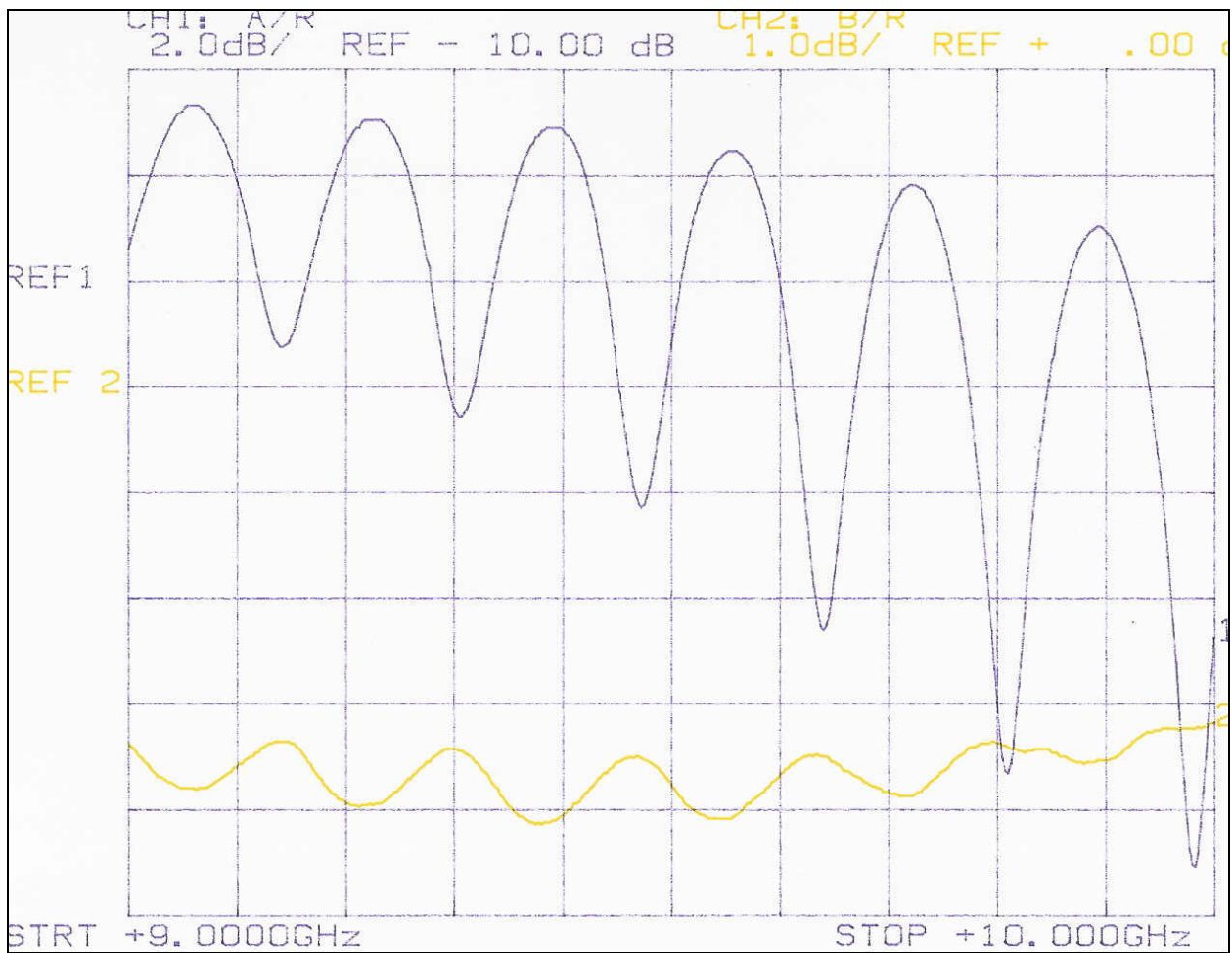


Figure 42. SNA Plot of Cable used with Digital Phase Shifter during SNA testing.

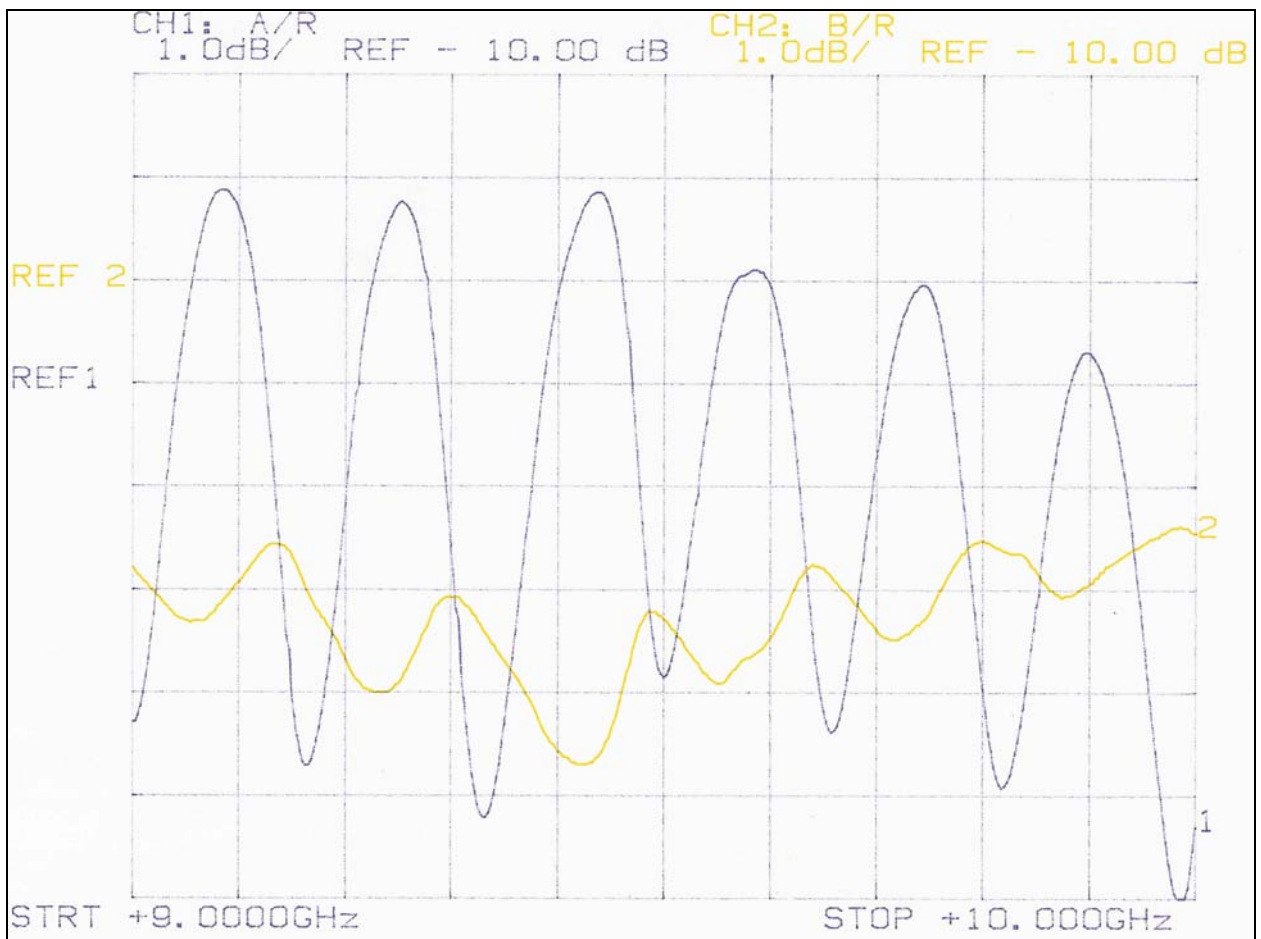


Figure 43. Digital Phase Shifter SNA Plot. Fixed Phase State, no Doppler Shift.

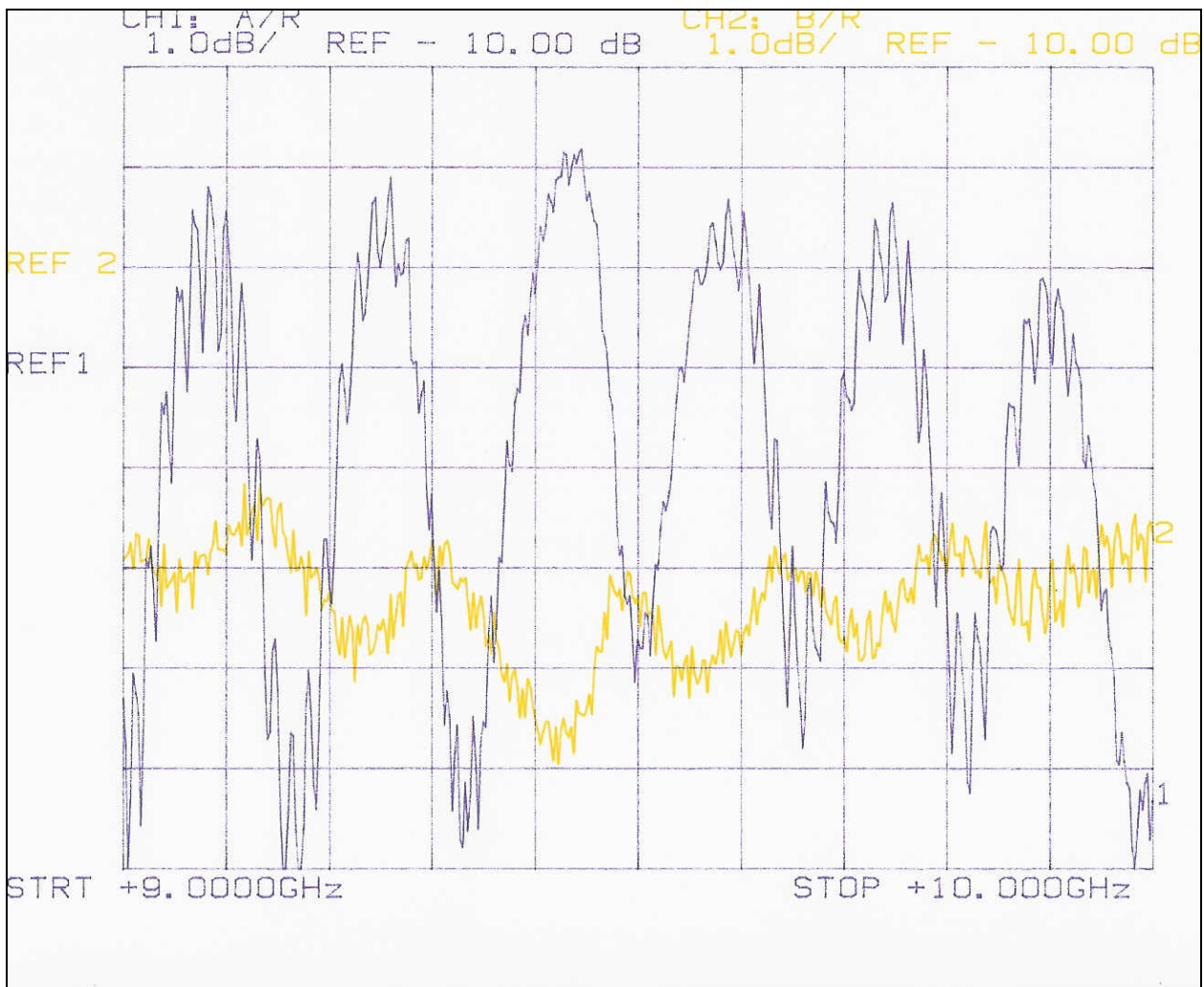


Figure 44. Digital Phase Shifter SNA Plot. Periodic Rotation through Phase States, Doppler Shift.

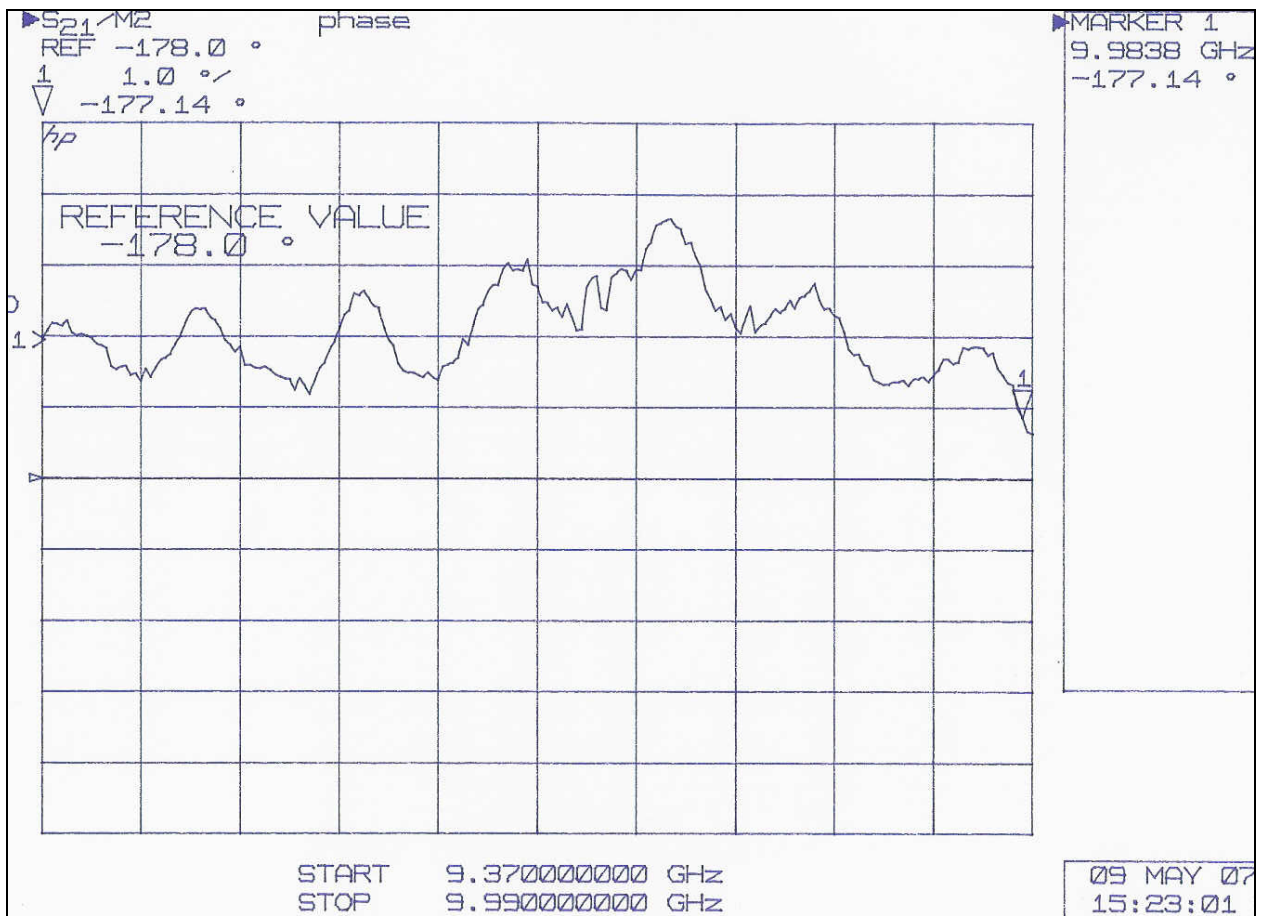


Figure 45. Digital Phase Shifter Phase Value Single VNA Plot. Zero volts applied to MSB pin only, five volts others. (10000000) 180° Phase Shift.

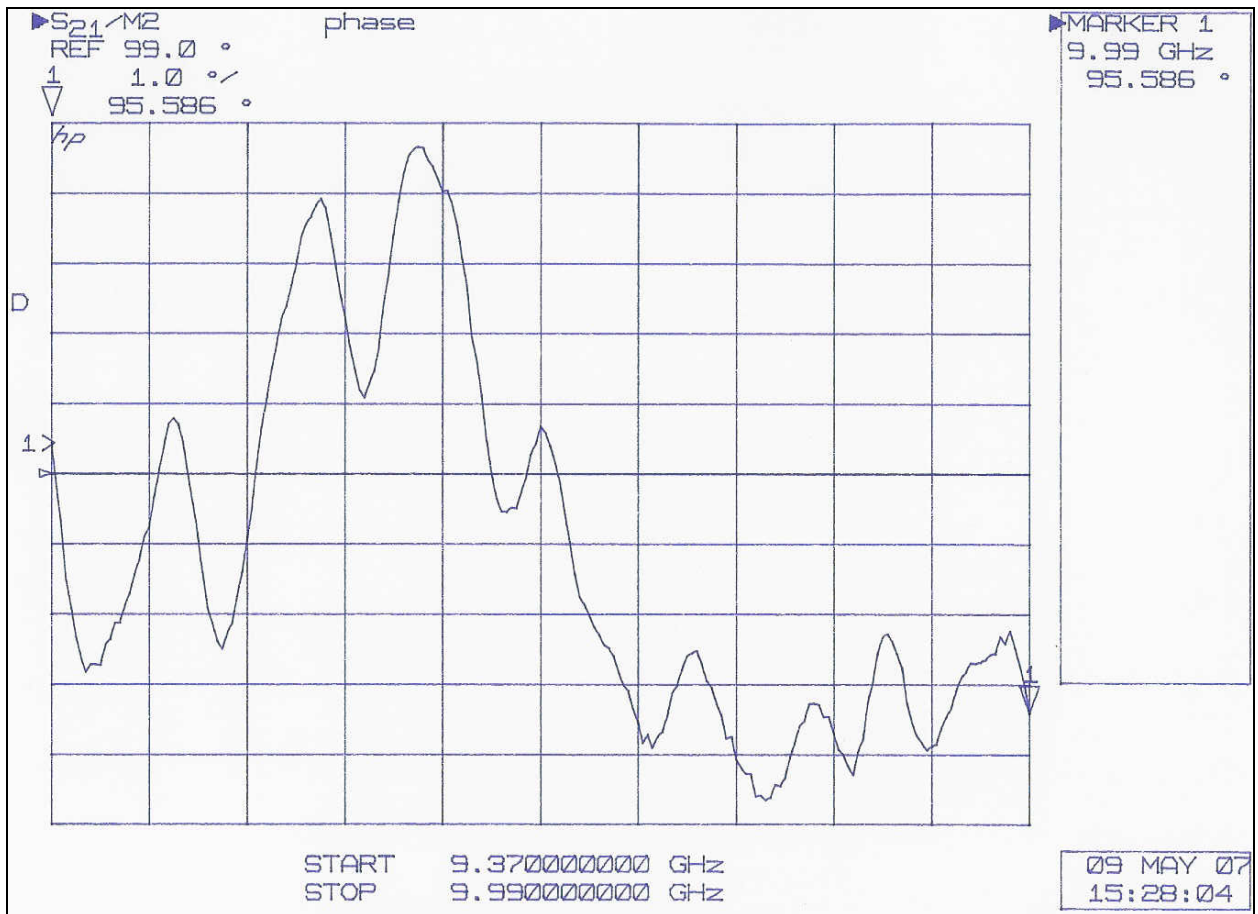


Figure 46. Digital Phase Shifter Phase Value Single VNA Plot. Zero volts applied to second MSB pin only, five volts others. (01000000) 90° Phase Shift.

APPENDIX D. PROGRAMMABLE ATTENUATOR DATA

Phase Invariant Programmable Attenuator
Manufacturer: American Microwave Corporation
Model Number: PI-DVAN-8012-8

Electrical Specifications:

Frequency: 8 GHz to 12 GHz

Range/Resolution: 60 dB/0.25 dB

Insertion Loss: 4.0 dB Typical

Switching speed: 300 ns Maximum

Maximum Power (No Damage): +27 dBm (operating +10 dBm)

Phase Variation/Shift: 0 to 20 dB : +/-5°

20 to 40 dB : +/-10°

40 to 60 dB : +/-20°

Power/Logic Connections:

No. of BITS	LOGIC PIN ASSIGNMENTS	+15V PIN	-15V PIN	GND PIN
8	L.S.B. @ 5 to M.S.B. @ 12	13	14	4

Table 7. Power and Logic Connections for Programmable Attenuator.

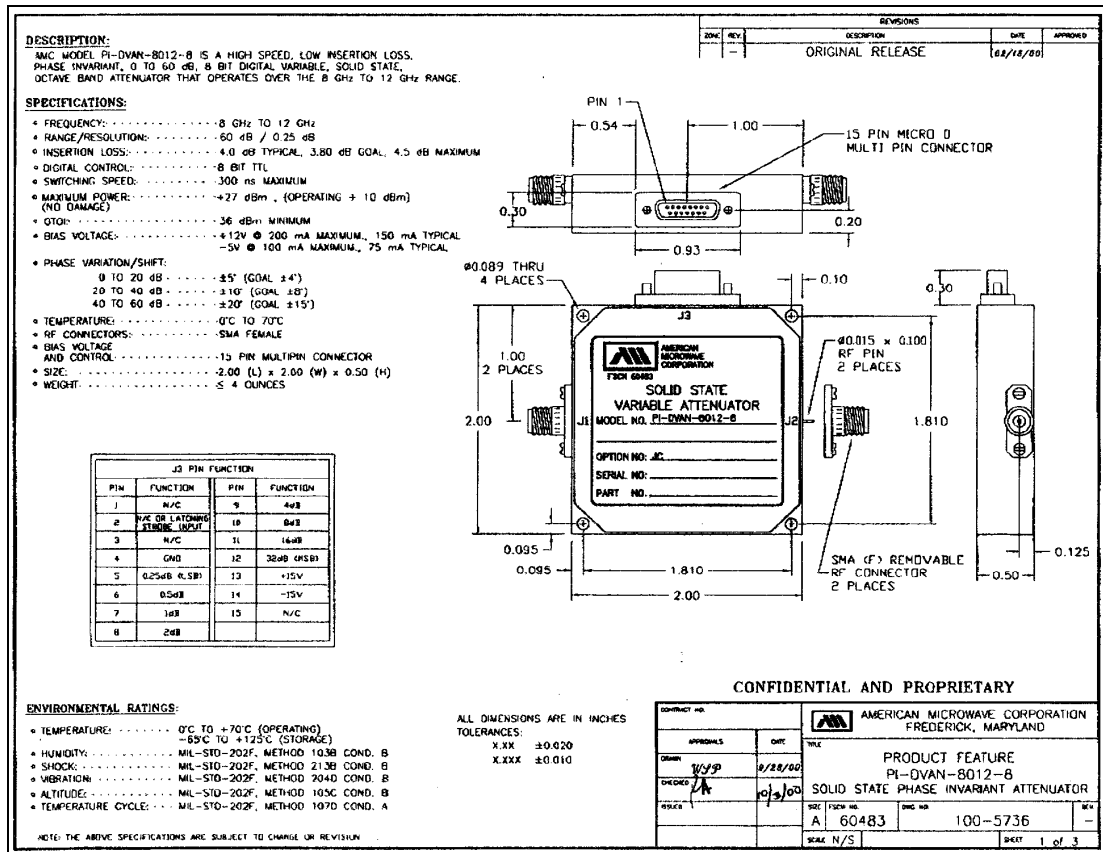


Figure 47. Specifications Sheet for Programmable Attenuator from American Microwave.

APPENDIX E. ANTENNA DATA

Antenna List:

- (2) Pasternack Sectoral Horn Antennas (used as part of ACS)
- (2) Unknown X-band Quad-Ridge Dual-Pol Horn Antennas (used as part of anechoic chamber ACS testing)
- (1) Narda Standard Gain Horn Antenna (used as part of anechoic chamber antenna testing)

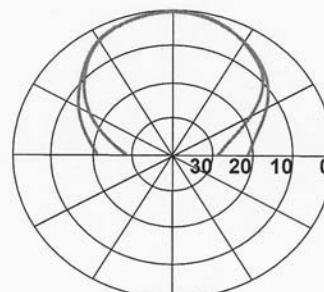


PASTERNAK ENTERPRISES, INC.
PO Box 16759, Irvine, Ca 92623

Toll Free: (866) 726-8375
Direct: +1 (949) 261-1920
FAX: +1 (949) 261-7451
Email: techsupport@pasternack.com

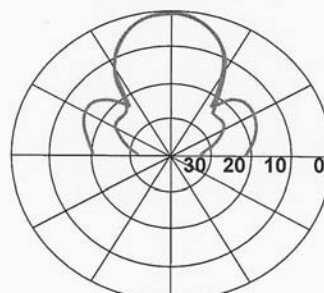
PE9850 thru PE9864 Standard Gain Horns

Standard Gain Horns					
P/N	Size	Frequency (GHz)	Gain (dB)	3 dB Width	
				E-Plane	H-Plane
PE9850-10	WR28	26.5 - 40.0	10	54.2°	54.4°
PE9850-15	WR28	26.5 - 40.0	15	32.1°	31.3°
PE9850-20	WR28	26.5 - 40.0	20	16.7°	18.3°
PE9851-10	WR34	22.0 - 33.0	10	54.1°	53.2°
PE9851-15	WR34	22.0 - 33.0	15	23.1°	40.8°
PE9851-20	WR34	22.0 - 33.0	20	17.0°	17.4°
PE9852-10	WR42	18.0 - 26.5	10	58.0°	57.0°
PE9852-15	WR42	18.0 - 26.5	15	31.3°	31.5°
PE9852-20	WR42	18.0 - 26.5	20	17.5°	17.8°
PE9853-10	WR51	15.0 - 22.0	10	55.1°	54.2°
PE9853-15	WR51	15.0 - 22.0	15	32.0°	31.8°
PE9853-20	WR51	15.0 - 22.0	20	16.9°	18.0°
PE9854-10	WR62	12.4 - 18.0	10	55.3°	50.9°
PE9854-15	WR62	12.4 - 18.0	15	30.1°	31.2°
PE9854-20	WR62	12.4 - 18.0	20	18.8°	18.9°
PE9855-10	WR75	10.0 - 15.0	10	50.2°	49.2°
PE9855-15	WR75	10.0 - 15.0	15	35.4°	28.5°
PE9855-20	WR75	10.0 - 15.0	20	16.3°	17.2°
PE9856-10	WR90	8.20 - 12.4	10	48.5°	47.4°
PE9856-15	WR90	8.20 - 12.4	15	29.3°	29.0°
PE9856-20	WR90	8.20 - 12.4	20	16.1°	16.5°
PE9857-10	WR102	7.00 - 11.0	10	55.5°	54.1°
PE9857-15	WR102	7.00 - 11.0	15	29.6°	29.3°
PE9857-20	WR102	7.00 - 11.0	20	17.0°	16.7°
PE9858-10	WR112	7.05 - 10.0	10	56.8°	55.2°
PE9858-15	WR112	7.05 - 10.0	15	32.4°	32.0°
PE9858-20	WR112	7.05 - 10.0	20	19.3°	19.3°
PE9859-10	WR137	5.85 - 8.20	10	55.1°	54.2°
PE9859-15	WR137	5.85 - 8.20	15	33.7°	33.2°
PE9859-20	WR137	5.85 - 8.20	20	18.7°	18.8°
PE9860-10	WR159	4.09 - 7.05	10	59.8°	48.3°
PE9860-15	WR159	4.09 - 7.05	15	31.3°	30.8°
PE9860-20	WR159	4.09 - 7.05	20	14.3°	16.9°
PE9861-10	WR187	3.95 - 5.85	10	55.0°	54.1°
PE9861-15	WR187	3.95 - 5.85	15	33.8°	33.3°
PE9861-20	WR187	3.95 - 5.85	20	18.9°	19.2°
PE9862-10	WR229	3.30 - 4.90	10	58.6°	51.9°
PE9862-15	WR229	3.30 - 4.90	15	32.7°	32.4°
PE9862-20	WR229	3.30 - 4.90	20	17.1°	16.7°
PE9863-10	WR284	2.60 - 3.95	10	50.8°	54.1°
PE9863-15	WR284	2.60 - 3.95	15	31.0°	30.6°
PE9863-20	WR284	2.60 - 3.95	20	17.2°	16.5°
PE9864-10	WR430	1.70 - 2.60	10	64.8°	45.4°
PE9864-15	WR430	1.70 - 2.60	15	33.1°	32.0°
PE9864-20	WR430	1.70 - 2.60	20	17.3°	17.4°



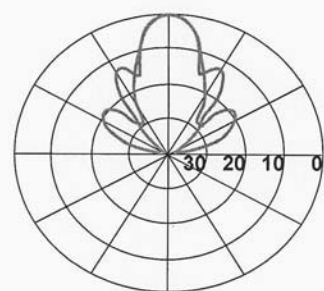
— Typical E-Plane Pattern
— Typical H-Plane Pattern

Typical 10dB Gain



— Typical E-Plane Pattern
— Typical H-Plane Pattern

Typical 15dB Gain



— Typical E-Plane Pattern
— Typical H-Plane Pattern

Typical 20dB Gain

Gain and beamwidth data are typical.
Additional data, such as calibration data, is provided for an additional fee.

Figure 48. Pasternack Sectoral Horn Antenna Data Sheet.

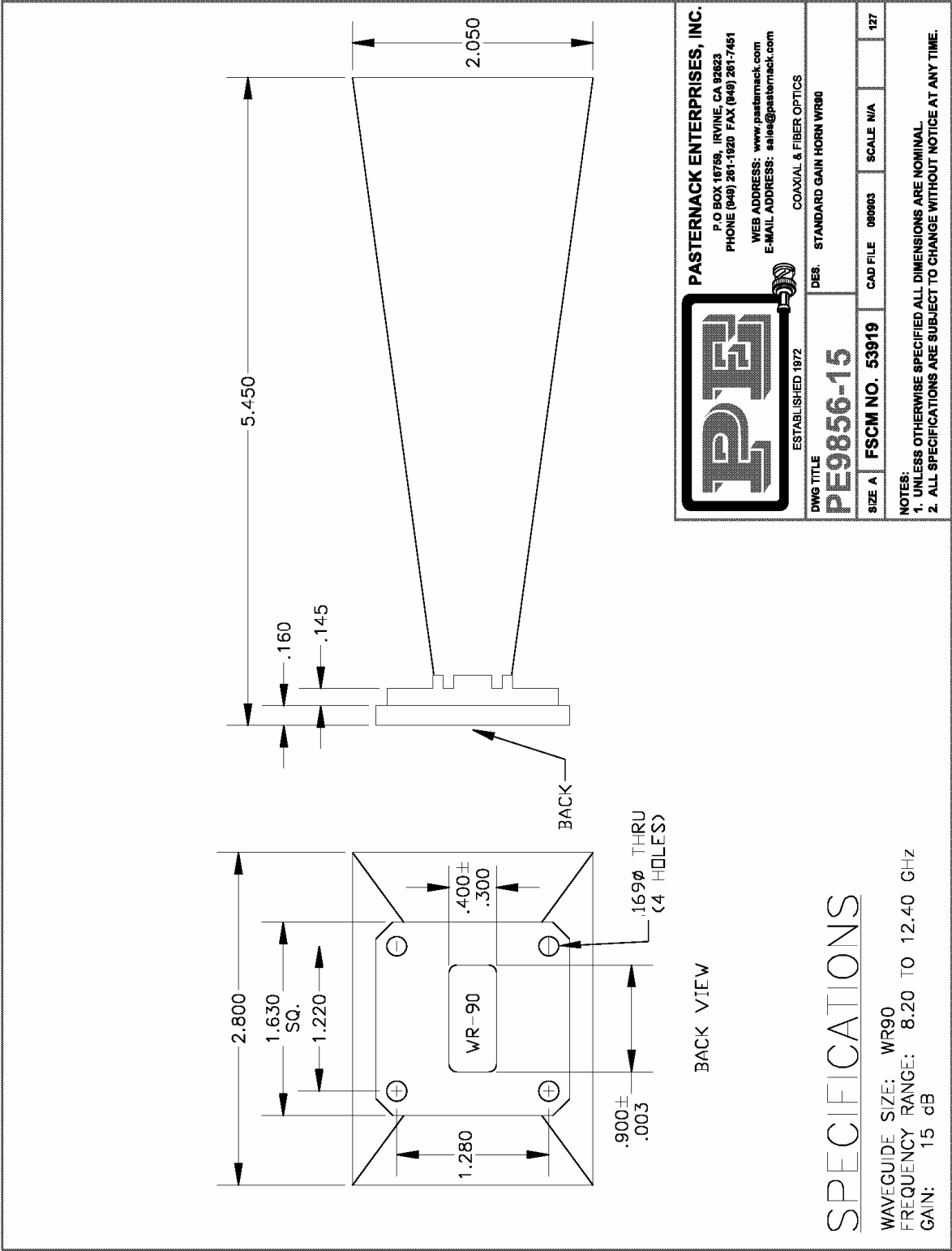


Figure 49. Pasternack Sectoral Horn Antenna Outline Drawing.

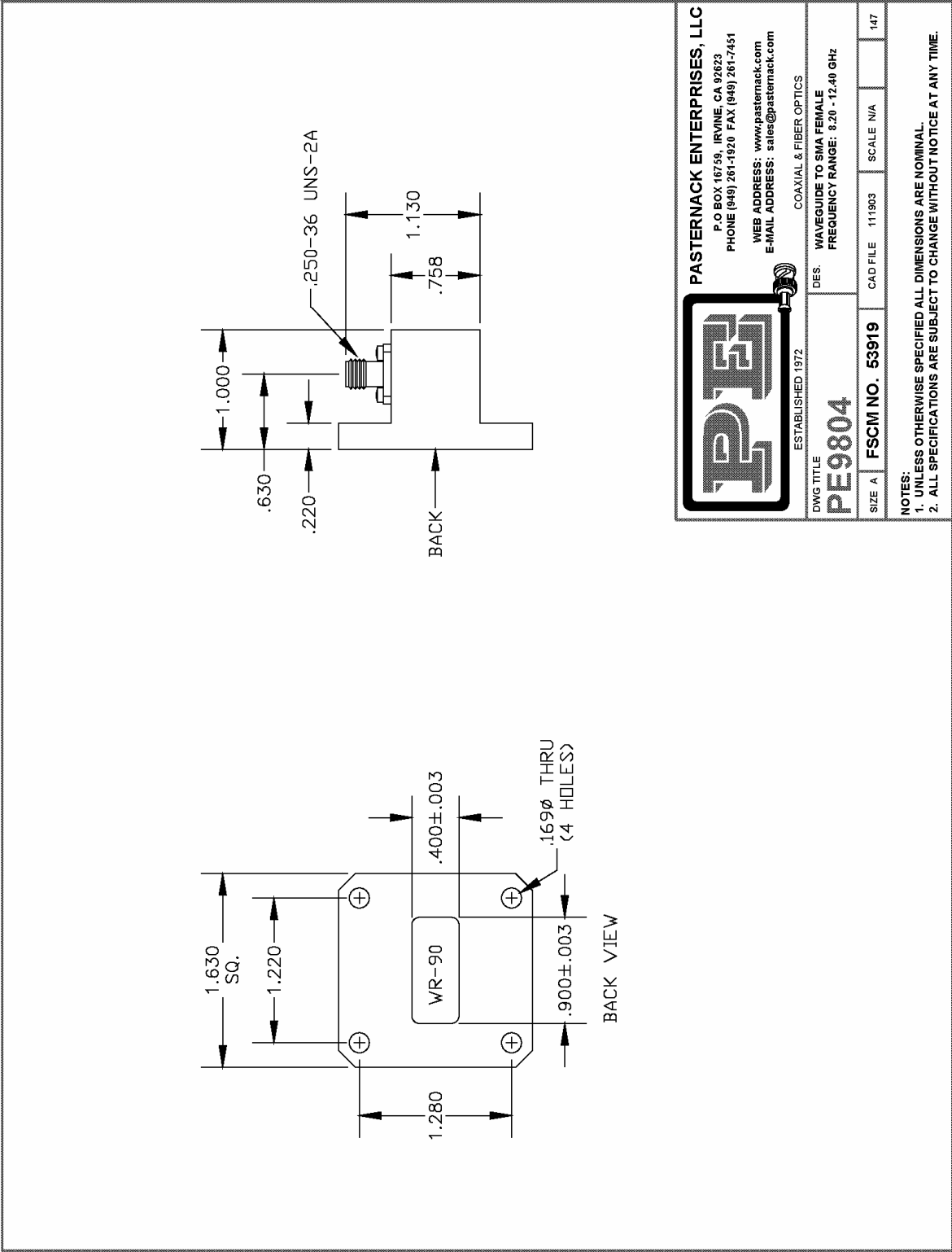


Figure 50. Pasternack Waveguide to Coaxial Adapter Outline Drawing.

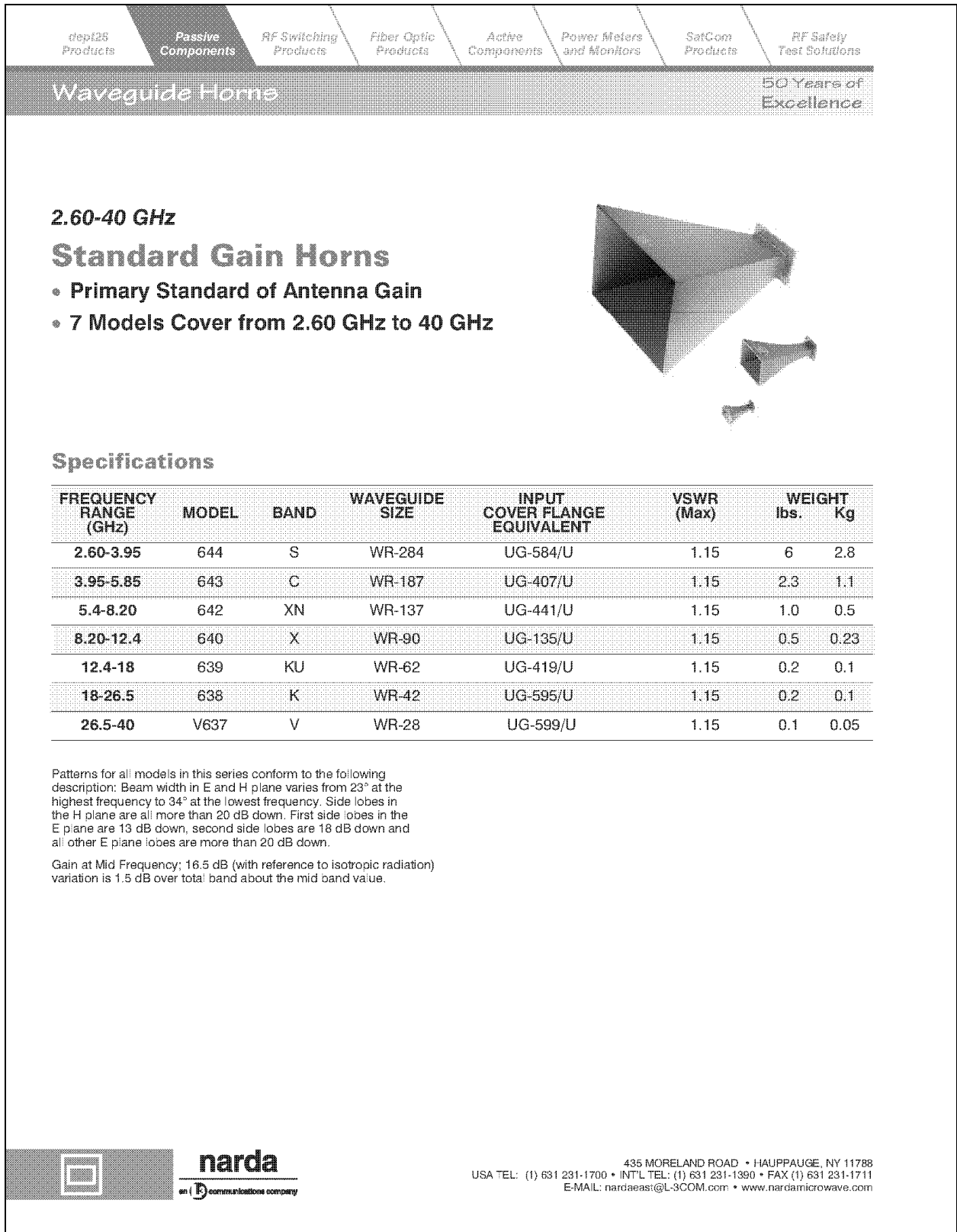
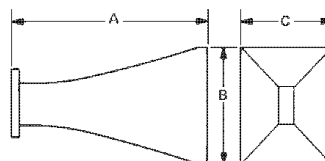


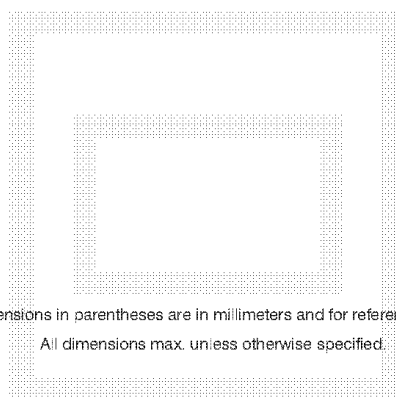
Figure 51. Narda Standard Gain Horn Antenna Datasheet (page 1).

Outline Drawing

Standard Gain Horn



MODEL	A MAX	B MAX	C MAX
V637	1.76 (44.7)	1.06 (26.9)	.82 (20.8)
638	2.57 (65.2)	1.51 (38.3)	1.16 (29.4)
639	3.48 (88.3)	2.20 (55.8)	1.73 (43.9)
640	5.06 (128.5)	3.09 (78.4)	3.34 (84.9)
642	7.76 (197.1)	4.67 (118.6)	3.53 (89.6)
643	10.47 (265.9)	6.34 (161.0)	4.80 (121.9)
644	15.62 (401.8)	9.52 (241.8)	7.16 (181.8)



Dimensions in parentheses are in millimeters and for reference only.

All dimensions max. unless otherwise specified.

435 MORELAND ROAD • HAUPPAUGE, NY 11788
 USA TEL: (1) 631 231-1700 • INTL TEL: (1) 631 231-1390 • FAX (1) 631 231-1711
 E-MAIL: nardaeast@L-3COM.com • www.nardamicrowave.com

narda
 an L-3 communications company



Figure 52. Narda Standard Gain Horn Antenna Datasheet (page 2).

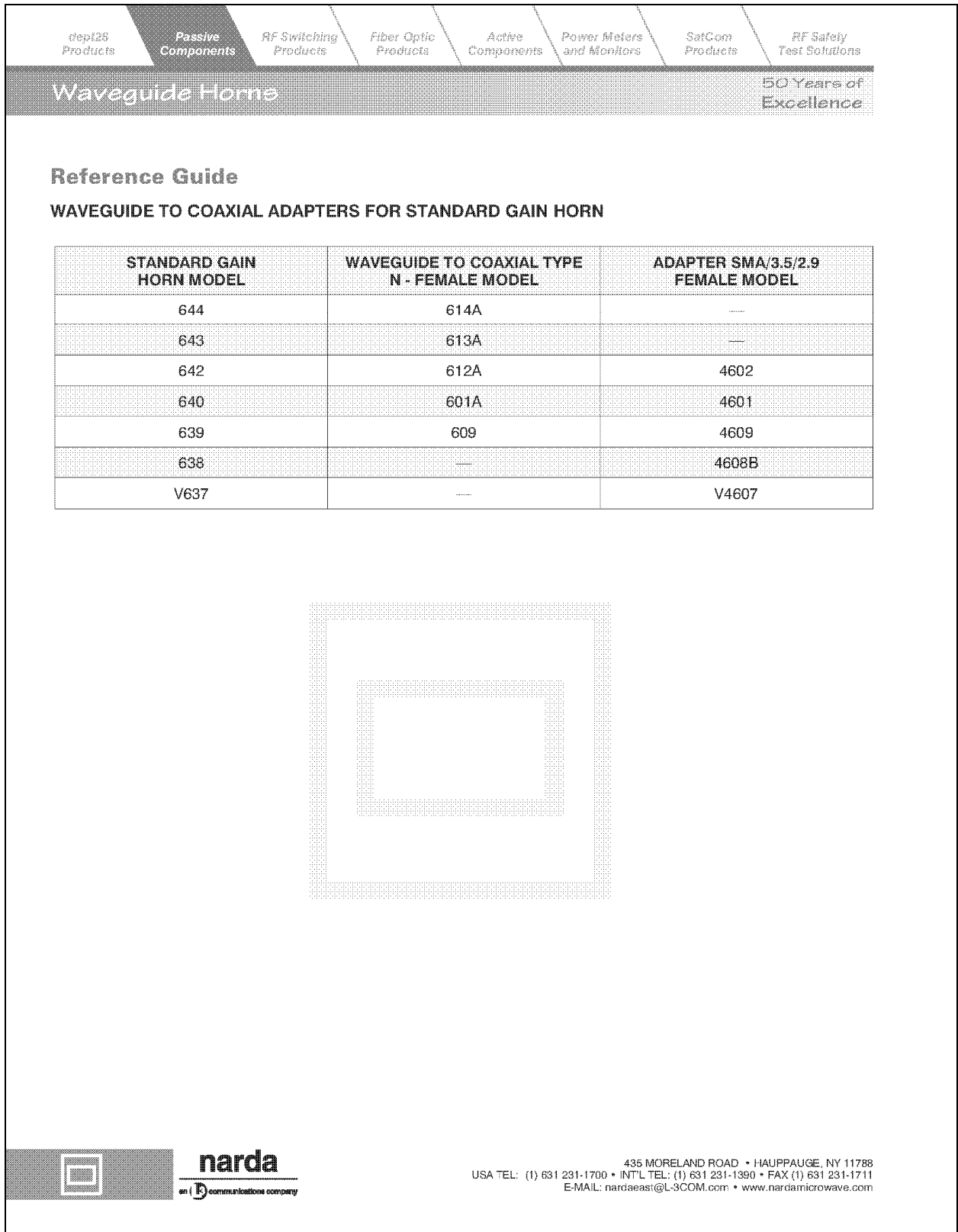


Figure 53. Narda Standard Gain Horn Antenna Datasheet (page 3).

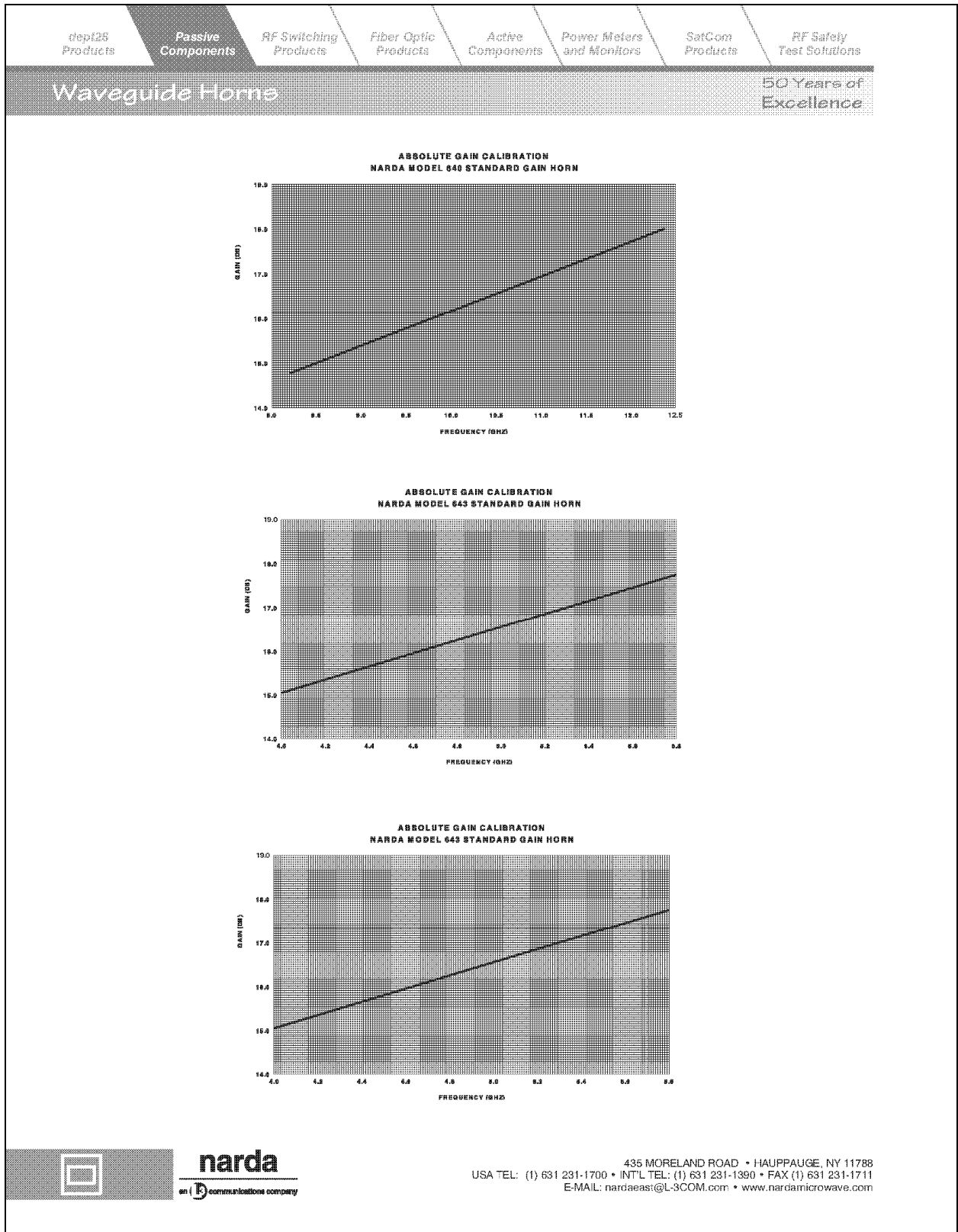


Figure 54. Narda Standard Gain Horn Antenna Datasheet (page 5).

APPENDIX F. ANTENNA PATTERN DATA

A total of five antennas were used in testing. One Narda standard gain horn antenna was used during antenna testing (patterns) only. Two X-band horn antennas were used during antenna testing (patterns), then used during ACS testing (as the transmit and receive antennas of the radar/VNA). Two Pasternack horn antennas were used during antenna testing (patterns), then used during ACS testing (as the transmit and receive antennas of the ACS). Measurements were made at three frequencies: 9370, 9680, and 9990 MHz (low, mid, and high frequency points on the MWR-05XP weather radar's RF band). E-plane and H-plane patterns were measured. To measure both planes, the antenna under test was first rotated 360° in azimuth with the radiator oriented for horizontal polarization (E-plane), then rolled 90° and the process repeated with the radiator now oriented for vertical polarization (H-plane). In total, two plane patterns were measured for five antennas at three frequencies to create thirty data sets.

A. VNA ANTENNA PATTERN DATA

In all plots, solid line is for X-band Horn Antenna #1 (“xbh”) and dotted line is for X-band Horn Antenna #2 (“ybh”). The last three plots are solid line for the Standard Gain Horn (“sgh”) which are included to provide a gain reference.

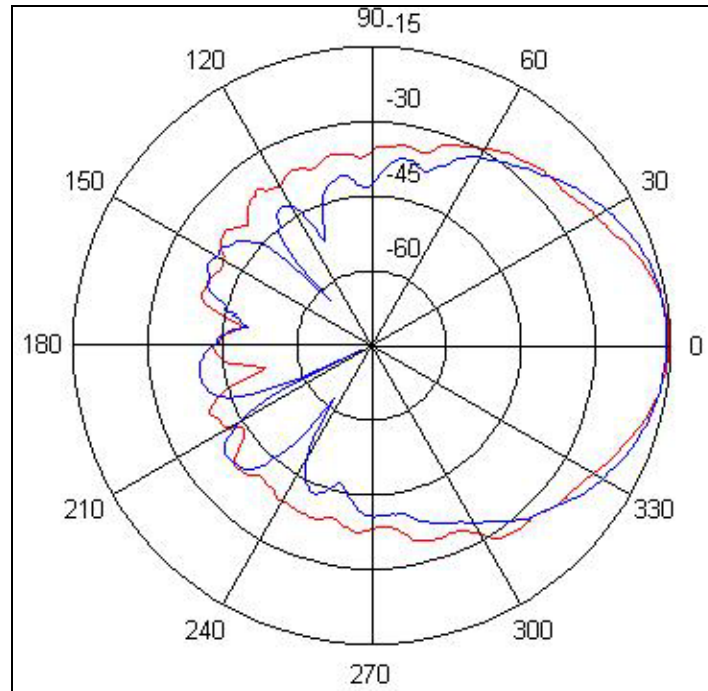


Figure 55. X-band Horn Antenna #1 Pattern at 9370MHz (E plane in red and H plane in blue).

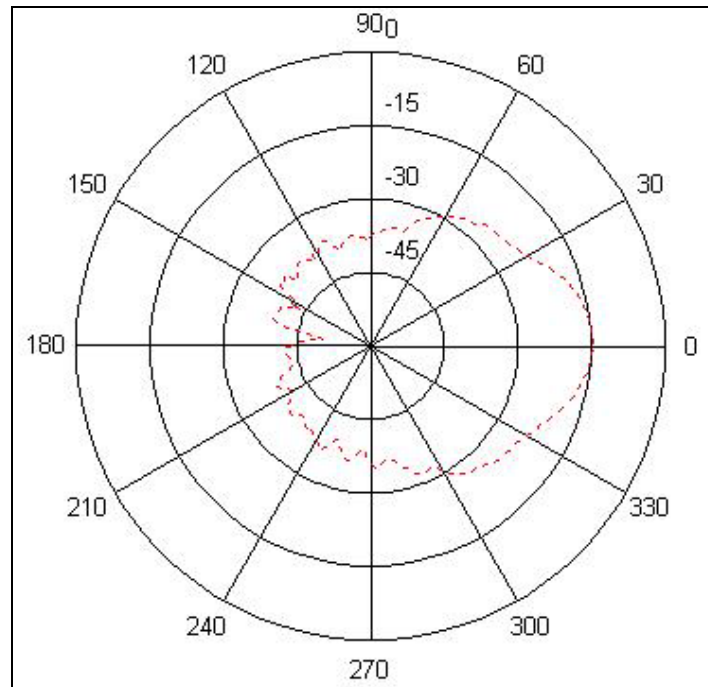


Figure 56. X-band Horn Antenna #2 Pattern at 9370MHz (E plane in red).¹²

¹² Note because the measured values slightly exceeded -15 dB the gain values have been normalized to 0 rather than -15.

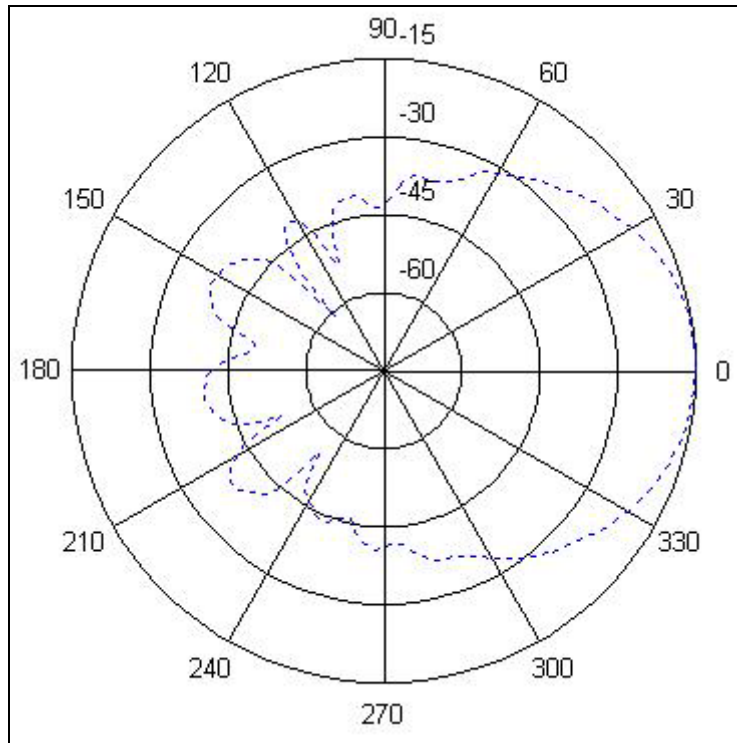


Figure 57. X-band Horn Antenna #2 Pattern at 9370MHz (H plane in blue).

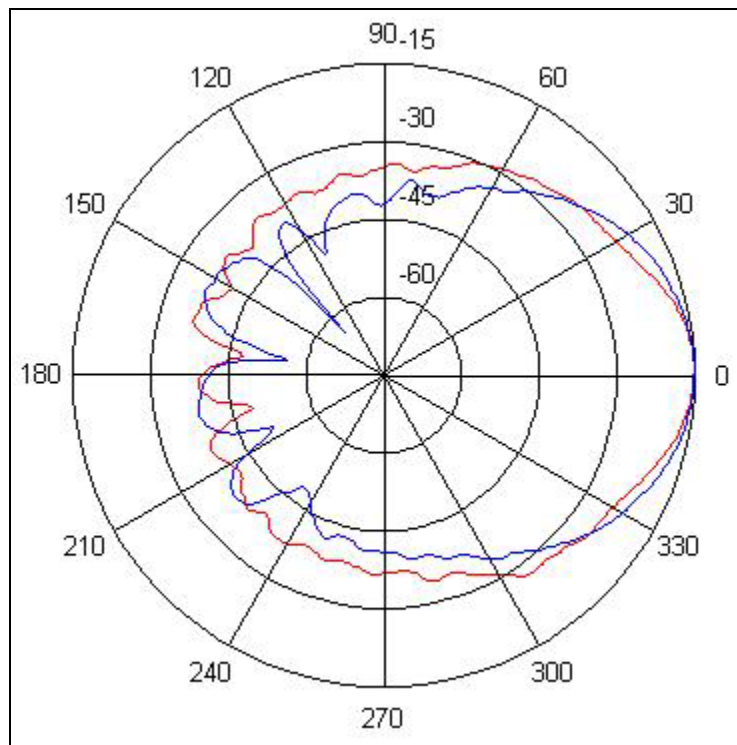


Figure 58. X-band Horn Antenna #1 Pattern at 9680MHz (E plane in red and H plane in blue).

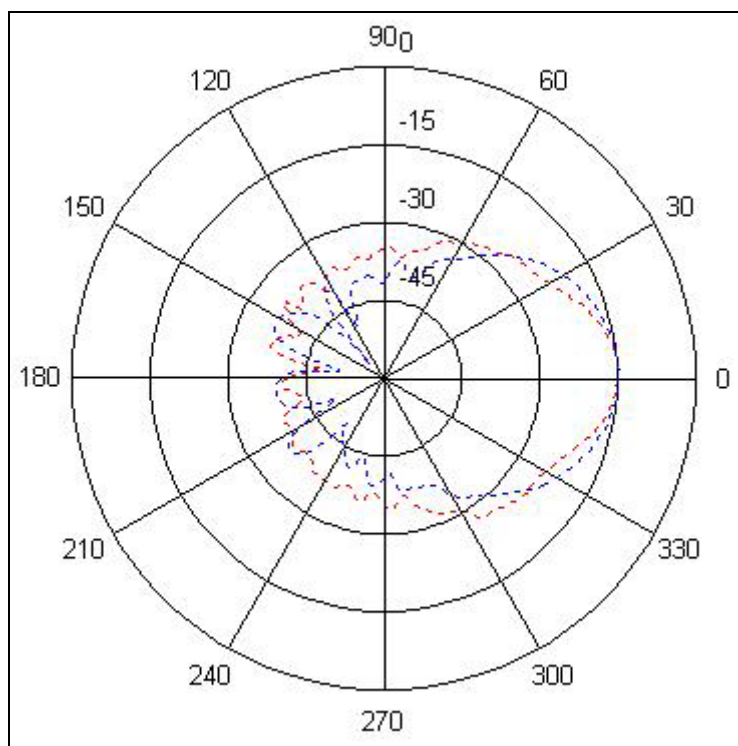


Figure 59. X-band Horn Antenna #2 Pattern at 9370MHz (E plane in red and H plane in blue).

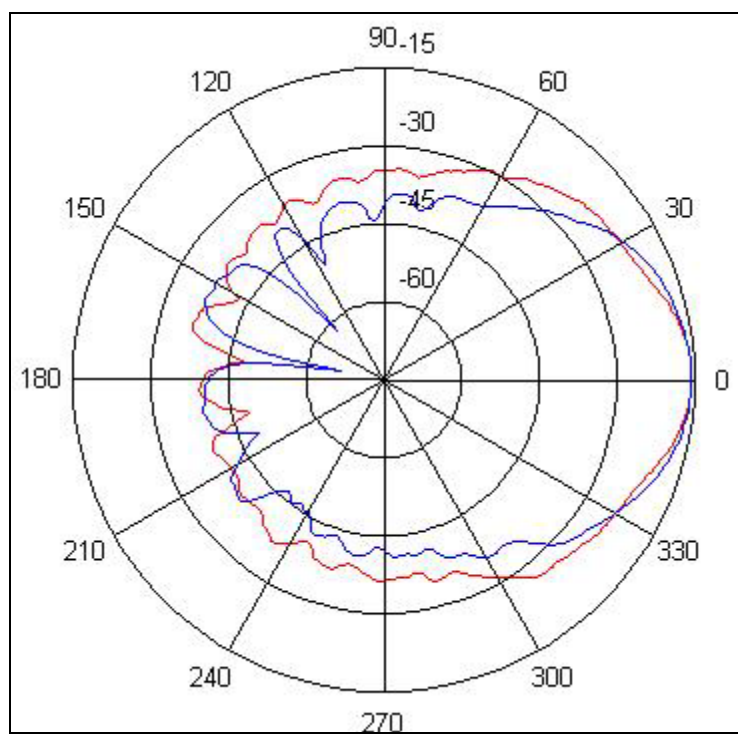


Figure 60. X-band Horn Antenna #1 Pattern at 9990MHz (E plane in red and H plane in blue).

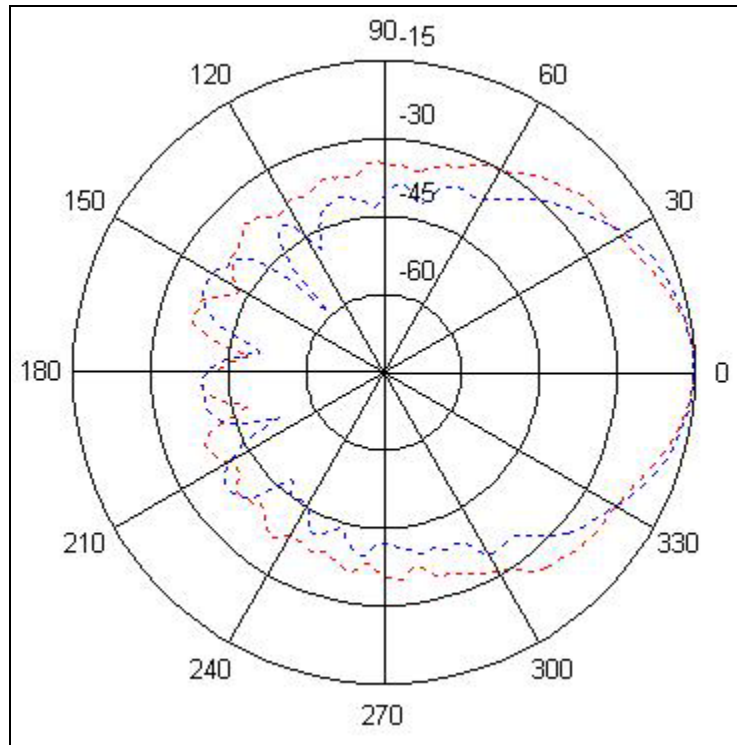


Figure 61. X-band Horn Antenna #2 Pattern at 9990MHz (E plane in red and H plane in blue).

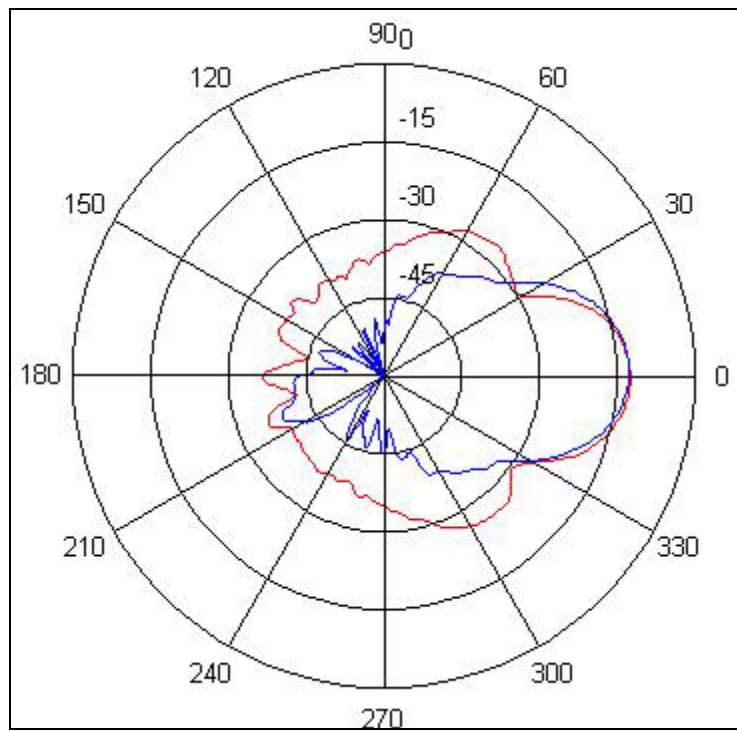


Figure 62. Standard Gain Horn Antenna Pattern at 9370MHz (E plane in red and H plane in blue).

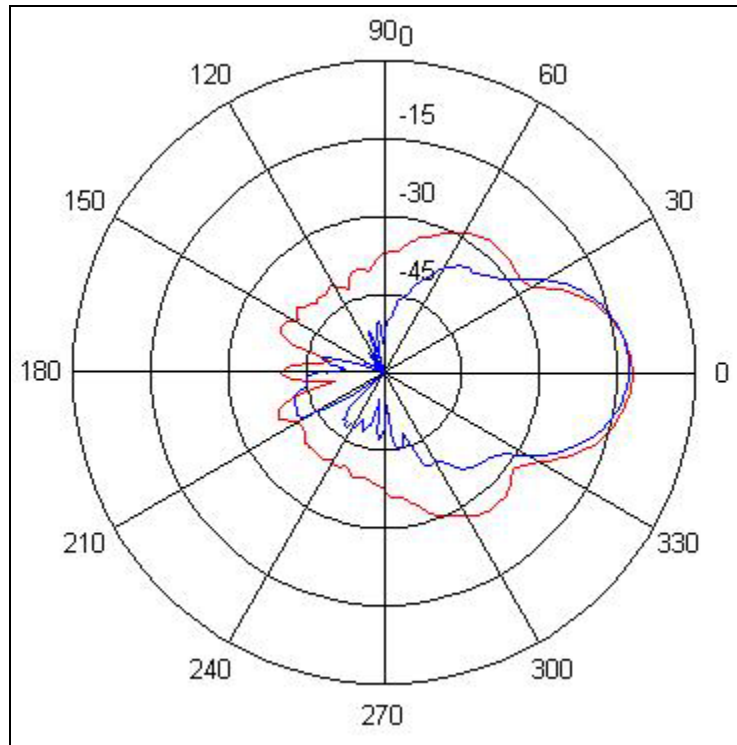


Figure 63. Standard Gain Horn Antenna Pattern at 9680MHz (E plane in red and H plane in blue).

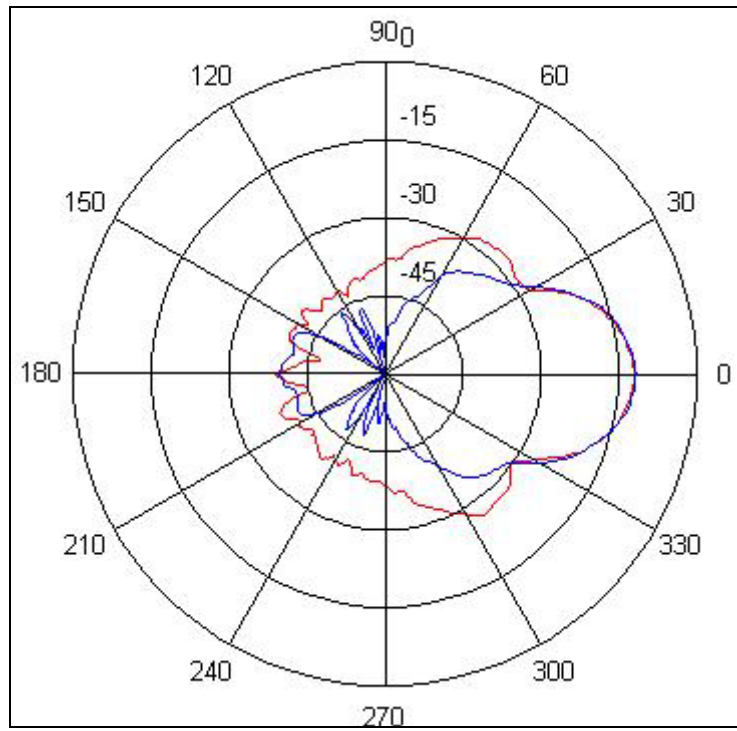


Figure 64. Standard Gain Horn Antenna Pattern at 9370MHz (E plane in red and H plane in blue).

B. ACS ANTENNA PATTERN DATA

In all plots, solid line is for Pasternack Horn Antenna #1 (a.k.a. “xpe”) and dotted line is for Pasternack Horn Antenna #2 (a.k.a. “ype”). The last three plots are solid line for the Standard Gain Horn (a.k.a. “sgh”). The pattern plots for the Standard Gain Horn have been included to provide a gain reference and in all three plots the gain has been adjusted to account for the use of a 6.5 dB attenuator. Also, note all data have been shifted -90° to boresight the patterns at 0° . This was done to make these patterns look like the other patterns previously presented. Additionally, in all plots the E-plane pattern is in red and H-plane pattern is in blue.

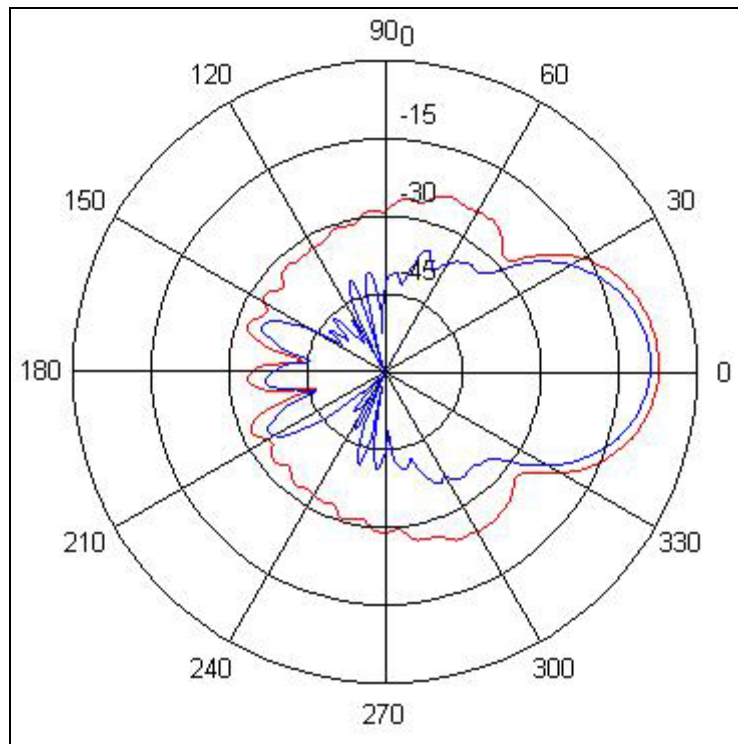


Figure 65. Pasternack Horn Antenna #1 Pattern at 9370MHz (E plane in red and H plane in blue).

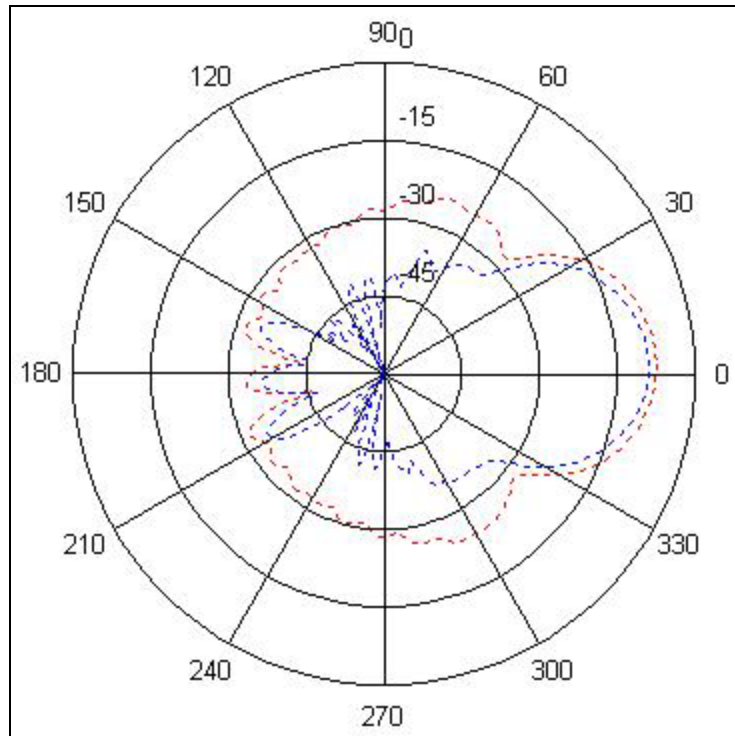


Figure 66. Pasternack Horn Antenna #2 Pattern at 9370MHz (E plane in red and H plane in blue).

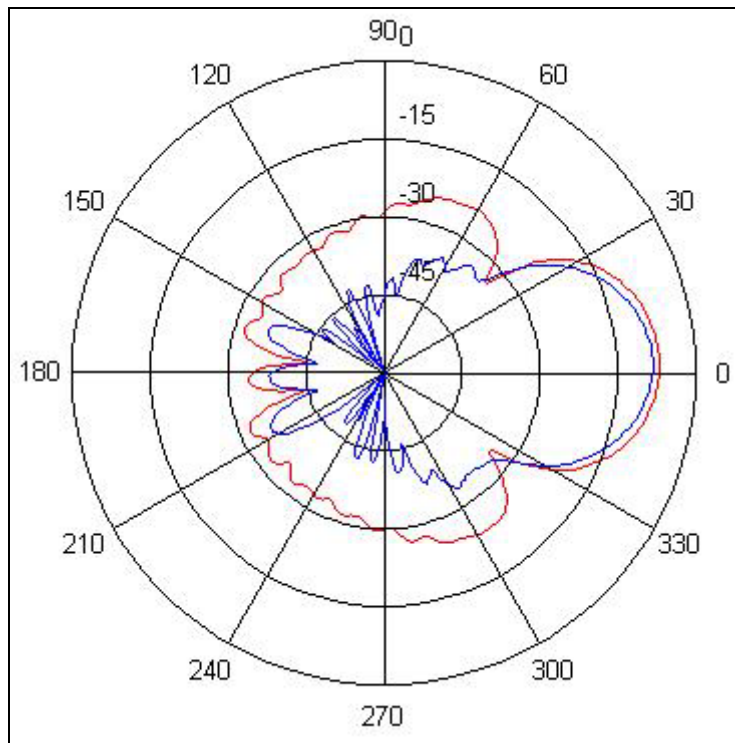


Figure 67. Pasternack Horn Antenna #1 Pattern at 9680MHz (E plane in red and H plane in blue).

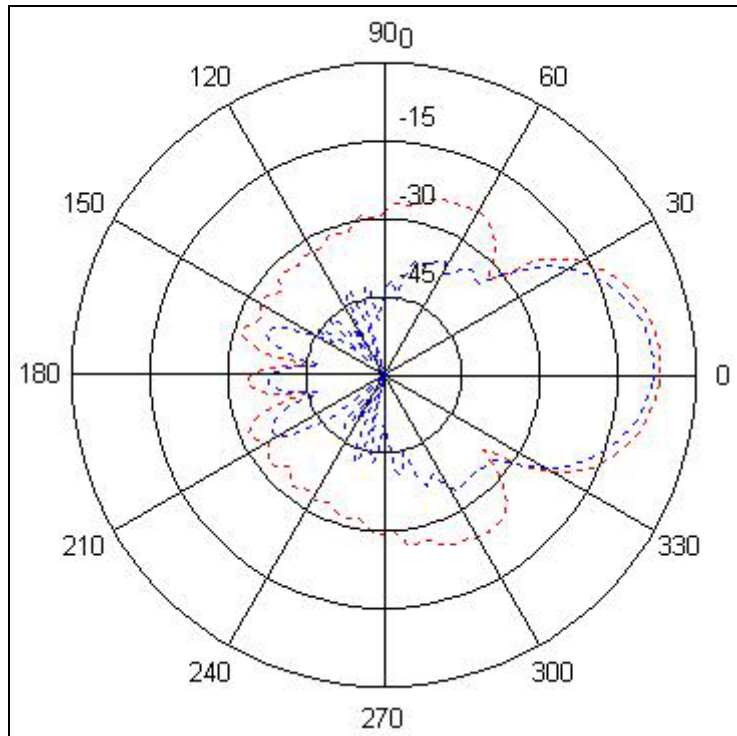


Figure 68. Pasternack Horn Antenna #2 Pattern at 9680MHz (E plane in red and H plane in blue).

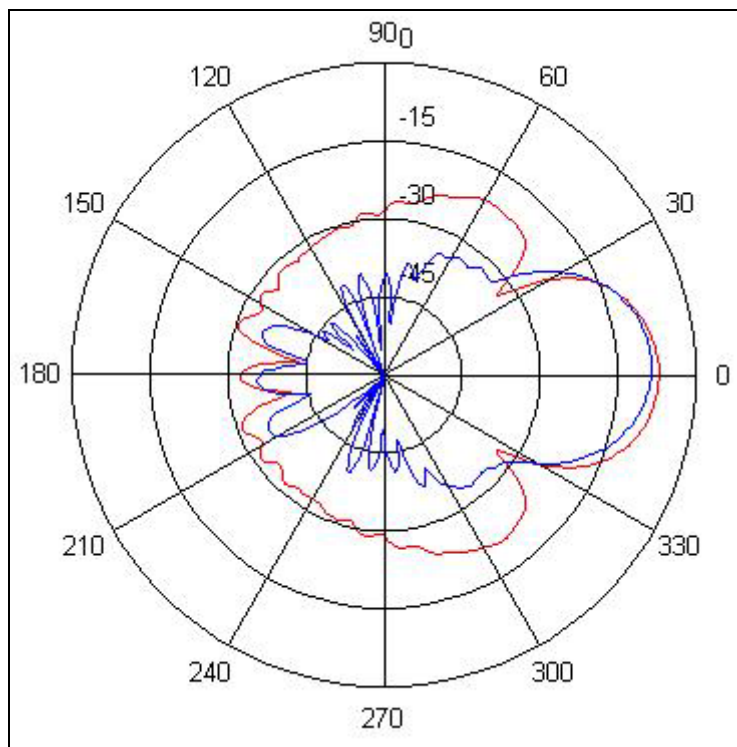


Figure 69. Pasternack Horn Antenna #1 Pattern at 9990MHz (E plane in red and H plane in blue).

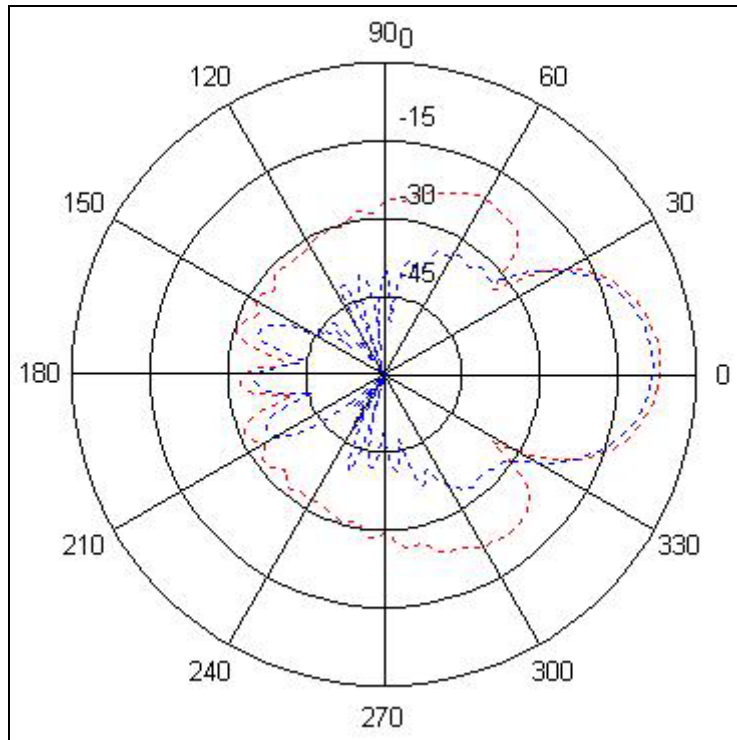


Figure 70. Pasternack Horn Antenna #2 Pattern at 9990MHz (E plane in red and H plane in blue).

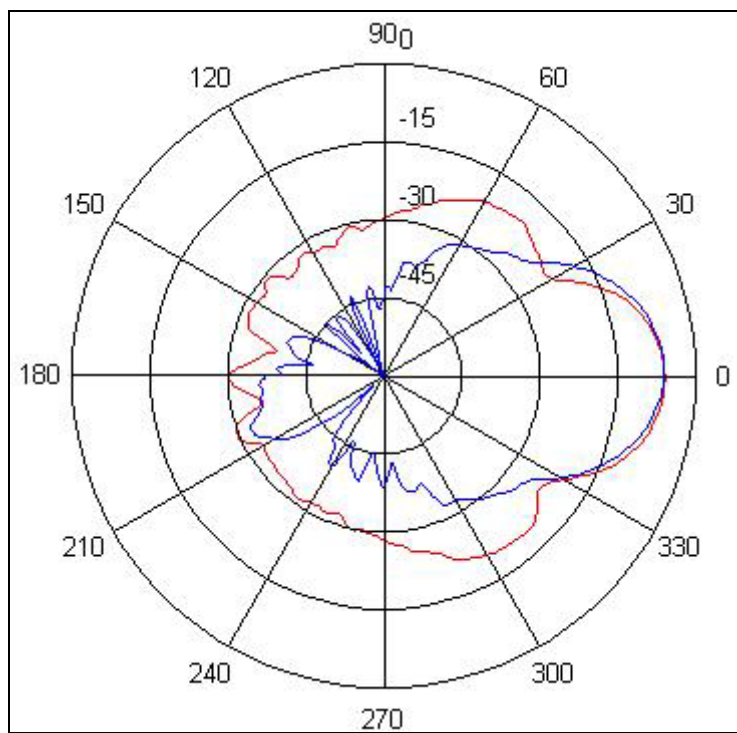


Figure 71. Standard Gain Horn Antenna Pattern at 9370MHz (E plane in red and H plane in blue).

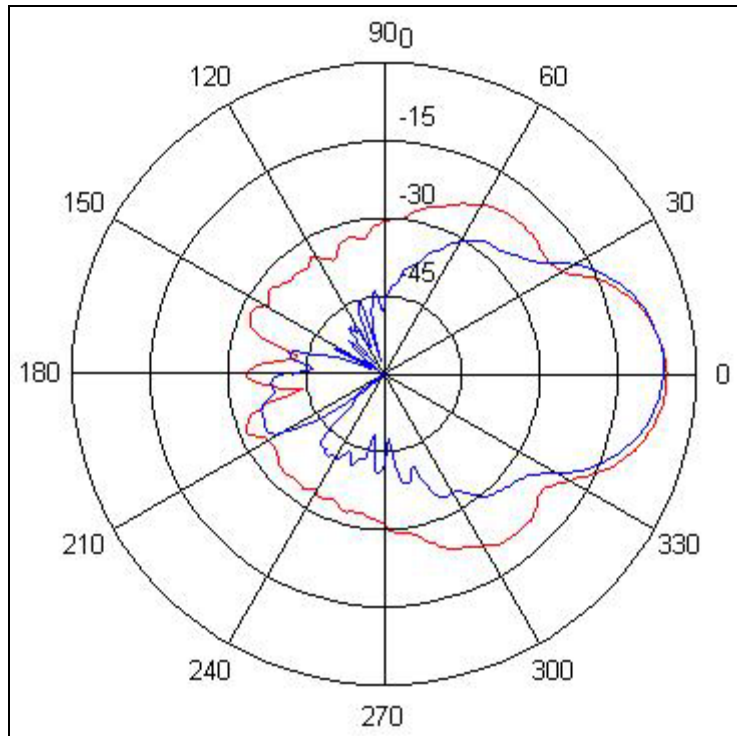


Figure 72. Standard Gain Horn Antenna Pattern at 9680MHz (E plane in red and H plane in blue).

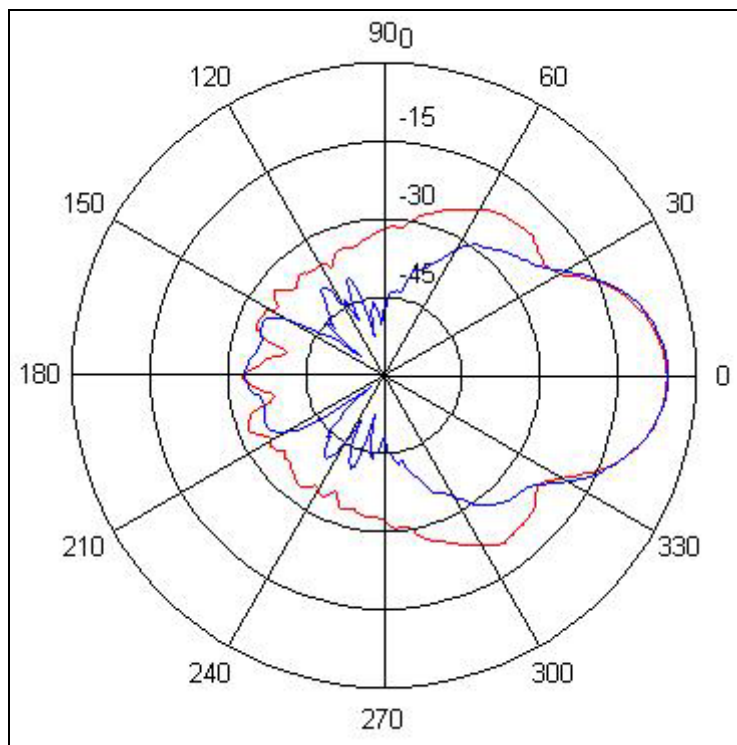


Figure 73. Standard Gain Horn Antenna Pattern at 9990MHz (E plane in red and H plane in blue).

C. MATLAB PLOTTING FILES

plotpatterns.m

```
polarDB(xbh9370H(:,1),xbh9370H(:,2),'r')  
polarDB(xbh9370V(:,1),xbh9370V(:,2),'b')
```

```
figure  
%% normalized ro to 0 not -15  
polarDB(ybh9370H(:,1),ybh9370H(:,2),'r:')  
figure  
polarDB(ybh9370V(:,1),ybh9370V(:,2),'b:')
```

```
figure  
polarDB(xbh9680H(:,1),xbh9680H(:,2),'r')  
polarDB(xbh9680V(:,1),xbh9680V(:,2),'b')
```

```
figure  
%% both normalized to 0  
polarDB(ybh9680H(:,1),ybh9680H(:,2),'r:')  
polarDB(ybh9680V(:,1),ybh9680V(:,2),'b:')
```

```
figure  
polarDB(xbh9990H(:,1),xbh9990H(:,2),'r')  
polarDB(xbh9990V(:,1),xbh9990V(:,2),'b')
```

```
figure  
polarDB(ybh9990H(:,1),ybh9990H(:,2),'r:')  
polarDB(ybh9990V(:,1),ybh9990V(:,2),'b:')
```

```
figure  
polarDB(sgh9370H(:,1),sgh9370H(:,2),'r-')  
polarDB(sgh9370V(:,1),sgh9370V(:,2),'b-')
```

```
figure  
polarDB(sgh9680H(:,1),sgh9680H(:,2),'r-')  
polarDB(sgh9680V(:,1),sgh9680V(:,2),'b-')
```

```
figure  
polarDB(sgh9990H(:,1),sgh9990H(:,2),'r-')  
polarDB(sgh9990V(:,1),sgh9990V(:,2),'b-')
```

plot_patterns2.m

%% -90 correction for 90 degree offset when patterns taken (-90 moves

%% boresight to 0 degrees)

polarDB(xpe9370H(:,1)-90,xpe9370H(:,2),'r')

polarDB(xpe9370V(:,1)-90,xpe9370V(:,2),'b')

figure

polarDB(ype9370H(:,1)-90,ype9370H(:,2),'r:')

polarDB(ype9370V(:,1)-90,ype9370V(:,2),'b:')

figure

polarDB(xpe9680H(:,1)-90,xpe9680H(:,2),'r')

polarDB(xpe9680V(:,1)-90,xpe9680V(:,2),'b')

figure

polarDB(ype9680H(:,1)-90,ype9680H(:,2),'r:')

polarDB(ype9680V(:,1)-90,ype9680V(:,2),'b:')

figure

polarDB(xpe9990H(:,1)-90,xpe9990H(:,2),'r')

polarDB(xpe9990V(:,1)-90,xpe9990V(:,2),'b')

figure

polarDB(ype9990H(:,1)-90,ype9990H(:,2),'r:')

polarDB(ype9990V(:,1)-90,ype9990V(:,2),'b:')

%%+6.5 correction for 6.5dB attenuator used in sgh measurement, not used

%%in pe measurements

figure

polarDB(sgh9370H(:,1),sgh9370H(:,2)+6.5,'r-')

polarDB(sgh9370V(:,1),sgh9370V(:,2)+6.5,'b-')

figure

polarDB(sgh9680H(:,1),sgh9680H(:,2)+6.5,'r-')

polarDB(sgh9680V(:,1),sgh9680V(:,2)+6.5,'b-')

figure

polarDB(sgh9990H(:,1),sgh9990H(:,2)+6.5,'r-')

polarDB(sgh9990V(:,1),sgh9990V(:,2)+6.5,'b-')

```
function polardb(ang,pat,line_style)
% NON-NORMALIZING VERSION THAT DOES NOT REQUIRE POLAR2
% take angle and dB data and generate polar plot
% angle data in ang(:) is degrees; dB data in pat(:)
if any(size(ang) ~= size(pat))
    error('THETA and RHO must be the same size.');
```

```
end
pmax=max(pat);
dynr=60; % dynamic range of dB scale
rticks=4; % number of rings in polar plot
dbstep=dynr/rticks; % dB spacing between rings -- must be integer
top=floor(pmax/dbstep)*dbstep+dbstep; % convenient outer ring dB value
theta=ang*pi/180;
% set a floor
for i=1:length(pat)
    if pat(i) < top-dynr, pat(i)=top-dynr; end
end
rho=pat+dynr-top;
hold on
% define a circle
    th = 0:pi/50:2*pi;
    xunit = cos(th);
    yunit = sin(th);

% now really force points on x/y axes to lie on them exactly
    inds = [1:(length(th)-1)/4:length(th)];
    xunits(inds(2:2:4)) = zeros(2,1);
    yunits(inds(1:2:5)) = zeros(3,1);
    rmax=dynr; rmin=0;
    rinc = (rmax-rmin)/rticks;
    for i=(rmin+rinc):rinc:rmax
        plot(xunit*i,yunit*i,'-','color','k','linewidth',1);
        text(0,i+rinc/10,[' ' num2str(i-dynr+top)],'verticalalignment','bottom' );
    end

% plot spokes
    th = (1:6)*2*pi/12;
    cst = cos(th); snt = sin(th);
    cs = [-cst; cst];
    sn = [-snt; snt];
    plot(rmax*cs,rmax*sn,'-','color','k','linewidth',1);

% annotate spokes in degrees
```

```

rt = 1.1*rmax;
for i = 1:max(size(th))

    text(rt*cst(i),rt*snt(i),int2str(i*30),'horizontalalignment','center' );
        if i == max(size(th))
            loc = int2str(0);
        else
            loc = int2str(180+i*30);
        end
        text(-rt*cst(i),-rt*snt(i),loc,'horizontalalignment','center' );
    end

% set view to 2-D
    view(0,90);
% set axis limits
    axis(rmax*[-1 1 -1.1 1.1]);

% transform data to Cartesian coordinates
xx = rho.*cos(theta);
yy = rho.*sin(theta);

% plot data on top of grid
    q = plot(xx,yy,line_style);
    hpol = q;
    axis('equal');axis('off');
    hold off

```

D. ABSOLUTE GAIN AND 3 DB BEAMWIDTH FOR X-BAND AND PASTERNAK HORN ANTENNAS (CALCULATIONS AND MEASUREMENTS)

Standard Gain Horn		Data from Manufacturer's Chart								
Frequency (GHz)		Gain (dB)								
9.37		15.66								
9.68		15.90								
9.99		16.15								
Standard Gain Horn (sgh)		Data Measured in Chamber								
Frequency (GHz)	Plane (E or H)	Location (Degrees from Boresight)	Gain (dB)							
9.37	E	-1	-12.43							
9.37	H	2	-12.61							
9.68	E	0	-12.07							
9.68	H	2	-12.65							
9.99	E	0	-12.05							
9.99	H	0*	-11.75							
*slight variation in setup										
X-band Horn 1 (xbh)		M=Measured, C=Calculated								
Frequency (GHz)	Plane (E or H)	Location (Degrees from Boresight)	Relative Gain (MAX Value, dB)	M	C	M	M	M	M	C
				Δ sgh (dB)	Absolute Gain (dB)	First -3dB Point (Loc, Deg) (Rel Gain, dB)	Second -3dB Point (Loc, Deg) (Rel Gain, dB)			3dB Beamwidth (Degrees)
9.37	E	2	-15.18	2.75	12.91	-15 -18.04	17 -18.08			32
9.37	H	3	-15.66	3.04	12.61	-21 -18.64	24 -18.62			45
9.68	E	3	-15.10	3.02	12.88	-14 -18.09	16 -18.03			30
9.68	H	2	-15.11	2.46	13.44	-19 -18.14	22 -18.10			41
9.99	E	0&1	-15.60	3.55	12.60	-14 -18.42	16 -18.56			30
9.99	H	1	-15.72	3.97	12.18	-18 -18.62	22 -18.73			40
X-Band Horn 2 (ybh)										
9.37	E	2	-14.71	2.28	13.38	-14 -17.43	17 -17.58			31
9.37	H	3	-15.02	2.41	13.25	-21 -18.02	24 -18.06			45
9.68	E	3	-14.89	2.82	13.08	-13 -17.81	17 -18.04			30
9.68	H	2	-14.80	2.15	13.75	-19 -17.93	22 -17.74			41
9.99	E	1	-15.12	3.06	13.09	-14 -18.09	16 -18.11			30
9.99	H	2	-15.34	3.59	12.56	-18 -18.38	22 -18.29			40

Table 8. Datafile for X-band Horn Antennas.

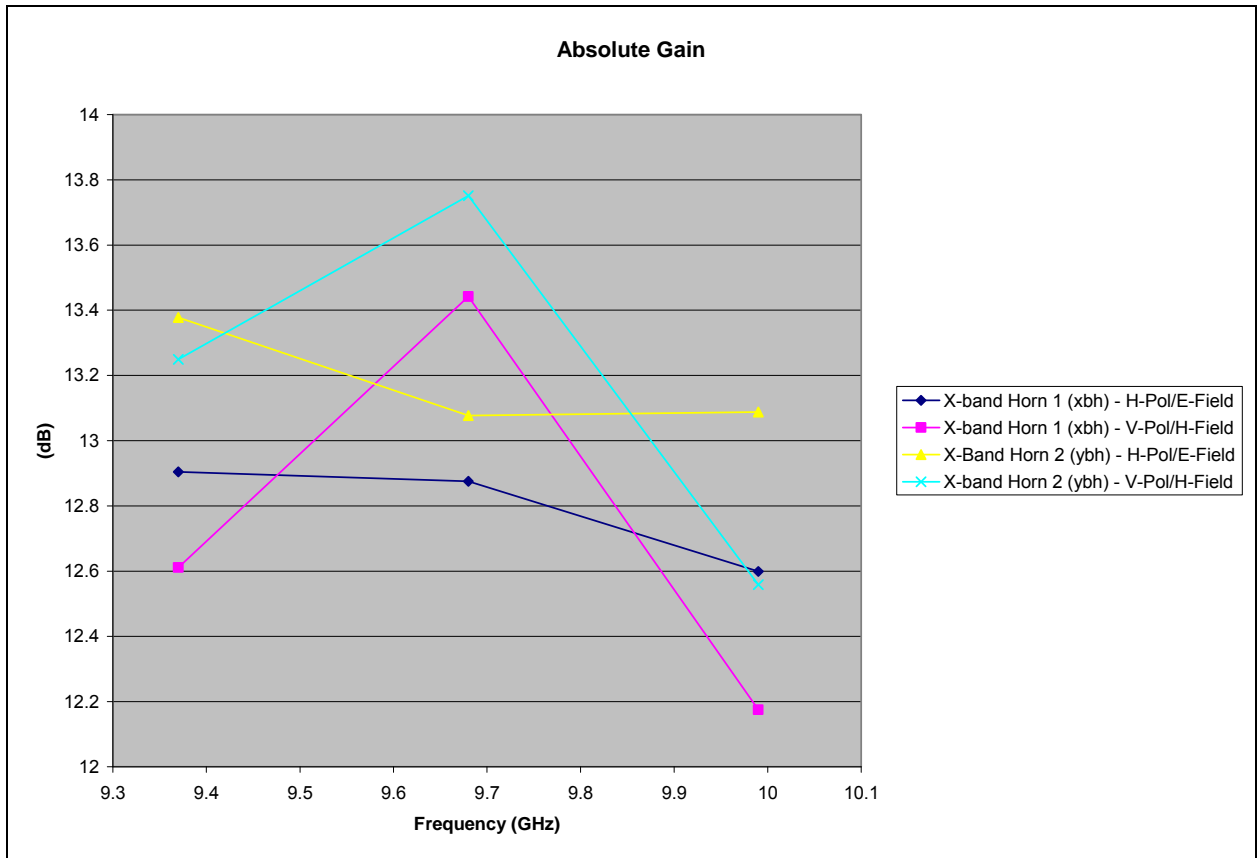


Figure 74. Plot of Absolute Gain for X-band Horn Antennas.

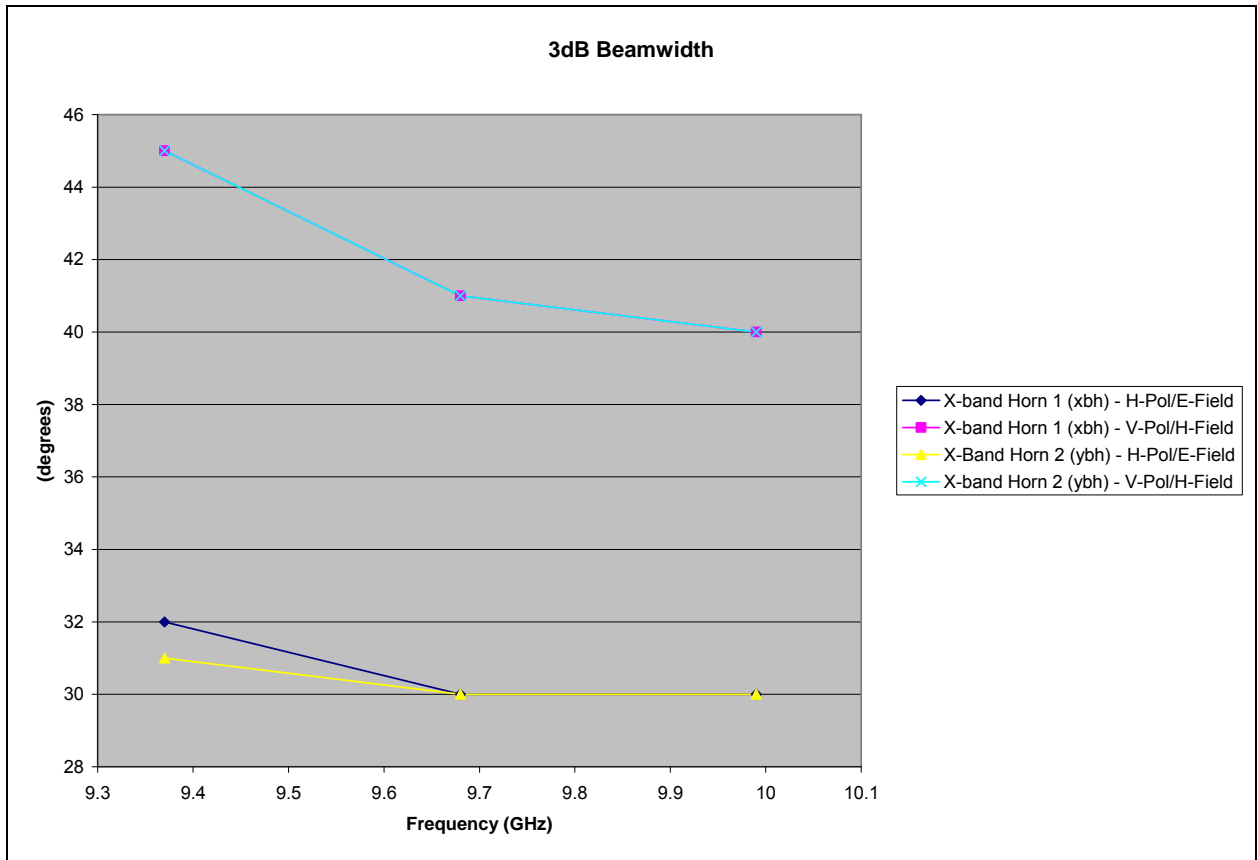


Figure 75. Plot of 3dB Beamwidth for X-band Horn Antennas.

Standard Gain Horn		Data from Manufacturer's Chart									
Frequency (GHz)		Gain (dB)									
9.37		15.66									
9.68		15.90									
9.99		16.15									
Standard Gain Horn (sgh)		Data Measured in Chamber [minus -6.5dB attenuator in line]									
Frequency (GHz)	Plane (E or H)	Location (Degrees from Boresight)	Gain (dB)								
9.37	E	-1	-5.93	-12.43							
9.37	H	2	-6.11	-12.61							
9.68	E	0	-5.57	-12.07							
9.68	H	2	-6.15	-12.65							
9.99	E	0	-5.55	-12.05							
9.99	H	0*	-5.25	-11.75							
*slight variation in setup											
Pasternack Horn 1 (1PE)		M=Measured, C=Calculated		M	C	C	M	M	M	M	C
Frequency (GHz)	Plane (E or H)	Location (Degrees from Boresight)	Relative Gain (MAX Value, dB)	Δ sgh (dB)	Absolute Gain (dB)	First -3dB Point (Loc, Deg)	(Rel Gain, dB)	Second -3dB Point (Loc, Deg)	(Rel Gain, dB)	3dB Beamwidth (Degrees)	
9.37	E	92	-7.24	1.31	14.35	76	-10.30	109	-10.32	33	
9.37	H	93	-8.85	2.74	12.91	77	-12.04	108	-12.10	31	
9.68	E	92	-6.87	1.30	14.60	77	-9.93	108	-9.91	31	
9.68	H	92	-8.16	2.01	13.89	79	-10.96	106	-10.96	27	
9.99	E	91	-7.02	1.47	14.68	76	-10.02	105	-10.19	29	
9.99	H	93	-8.43	3.18	12.97	78	-11.61	107	-11.57	29	
Pasternack Horn 2 (2PE)											
9.37	E	93	-7.38	1.45	14.20	77	-10.21	109	-10.30	32	
9.37	H	93	-8.86	2.74	12.91	78	-11.67	107	-11.64	29	
9.68	E	93	-6.71	1.14	14.76	77	-9.87	109	-9.92	32	
9.68	H	92&93	-8.07	1.92	13.98	79	-10.91	107	-11.24	28	
9.99	E	93	-6.85	1.29	14.86	78	-9.98	108	-10.19	30	
9.99	H	93	-8.17	2.92	13.23	79	-10.96	107	-11.27	28	

Table 9. Datafile for Pasternack Horn Antennas.

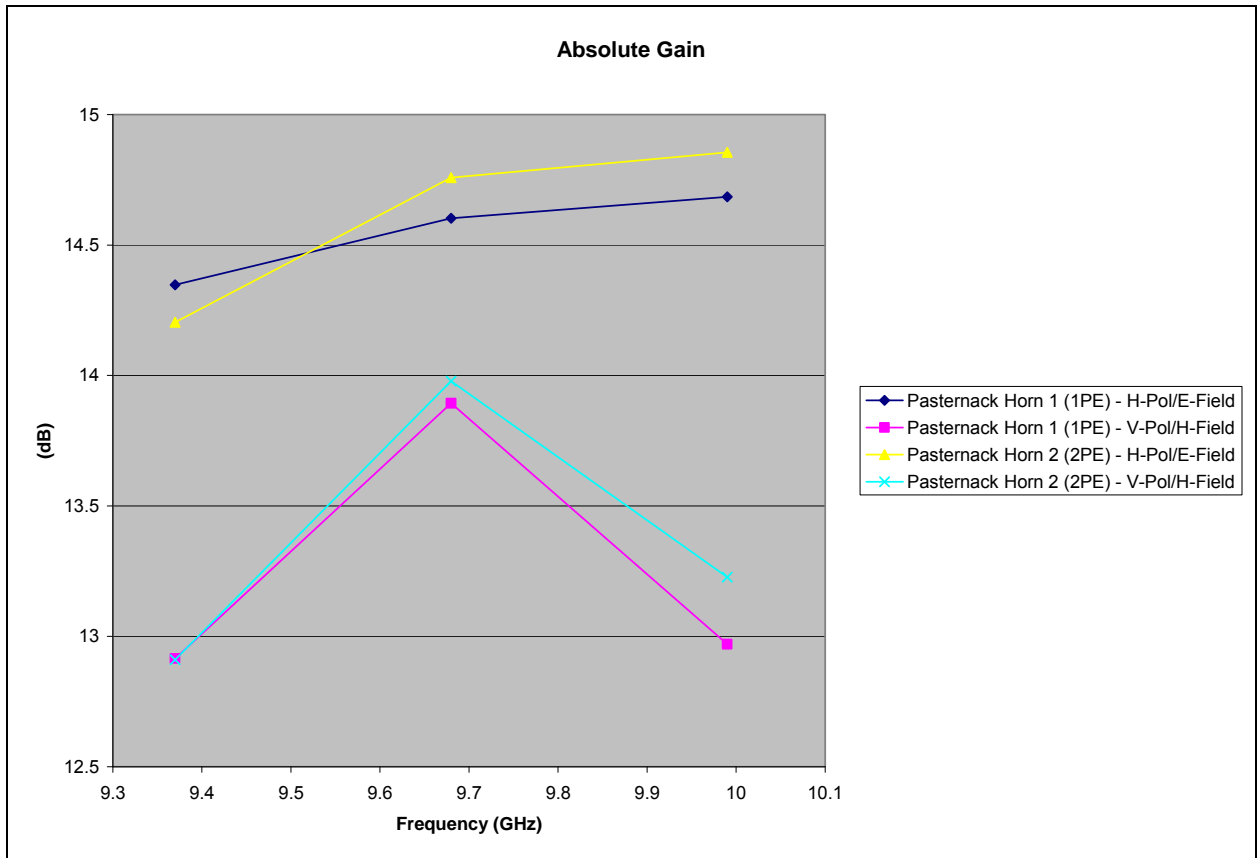


Figure 76. Plot of Absolute Gain for Pasternack Horn Antennas.

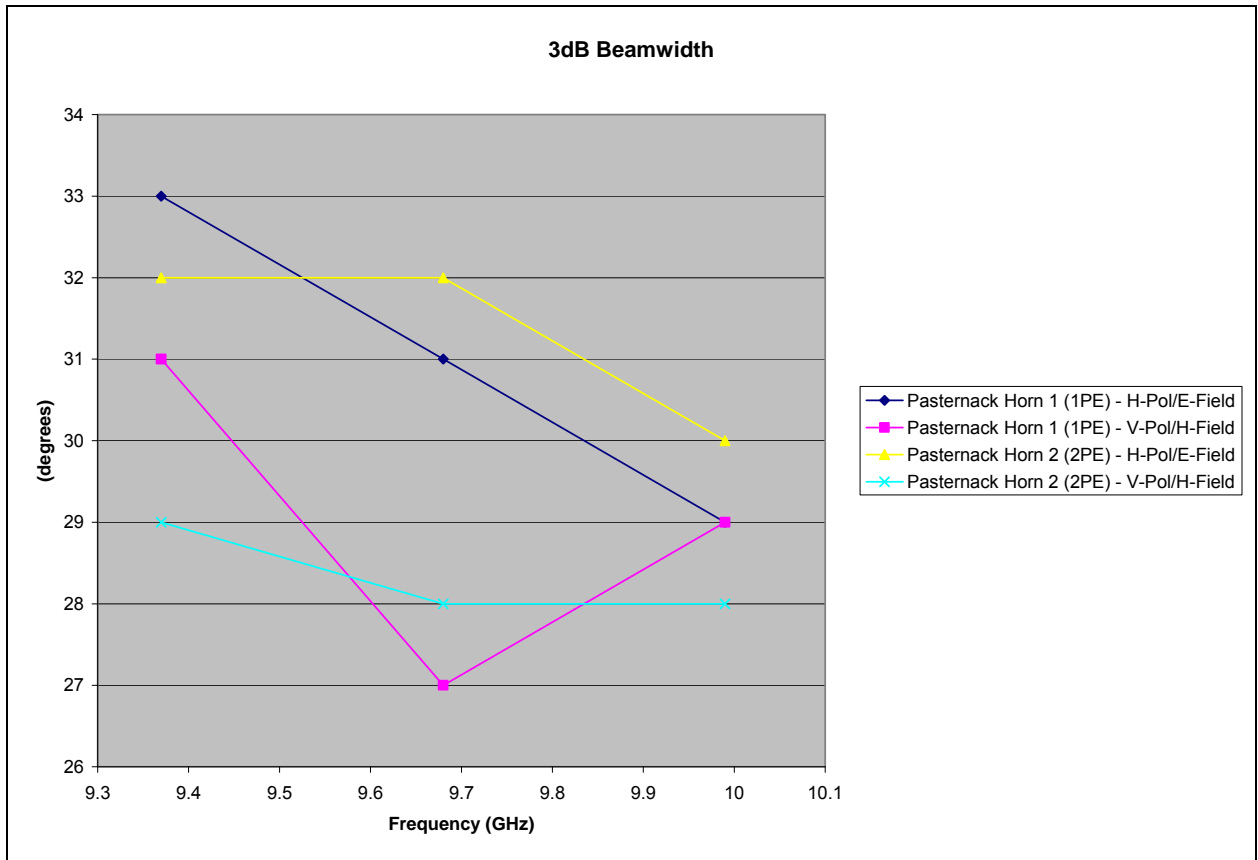


Figure 77. Plot of 3dB Beamwidth for Pasternack Horn Antennas.

E. EXPLANATION OF DATAFILE MEASUREMENTS AND CALCULATIONS

The first entry in both datafiles is the absolute gain of the reference horn antenna, the Narda standard gain horn antenna. These values were obtained from the Narda datasheet, page 5. See below for a replica of this graph with the look-up process annotated.

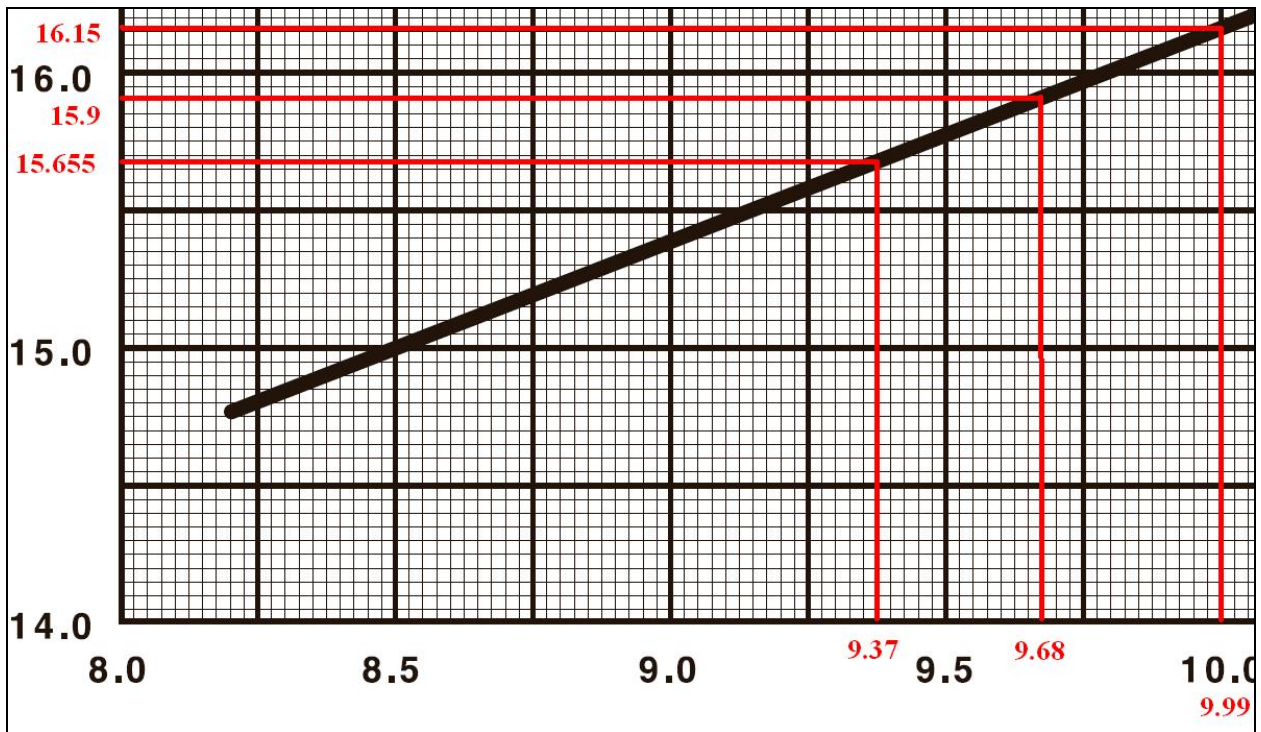


Figure 78. Narda Standard Gain Horn Absolute Gain Plot (zoomed to area of interest and annotated with values of interest).

The second entry in both datafiles is the measured power received when using the standard gain horn antenna during antenna testing as the antenna under test. In the Pasternack datafile these values have been adjusted by 6.5 dB because the measured values included an additional 6.5 dB of loss from an in-line attenuator that was required to prevent the power level from saturating the measurement device (Vector Network Analyzer or VNA).

The third entry in both datafiles is the measured power received when using either the X-band or Pasternack horn antenna during antenna testing as the antenna under test. The maximum relative amplitude as measured is listed. Then this value is subtracted from the corresponding standard gain horn measurement value to get a delta. Note the value is subtracted because the power values are in negative dBs and the X-band and Pasternack horn values were less than the standard gain horn values. This delta is then subtracted from the value of the absolute gain of the reference horn antenna obtained from the graph. Note the values are subtracted because the delta though positive is the

amount below in power. The result is the absolute gain for that antenna at the given frequency.

Then the value for the first measurement to exceed 3 dB below the maximum relative amplitude is listed along with its angle in degrees. This was done for both the first value above and below in angle of the maximum relative amplitude angle. These angle values were subtracted from one another to find the 3dB Beamwidth.

Example calculation from X-band Horn #1 at 9.37 GHz in the E plane (as described above):

Absolute Gain:

$$\begin{aligned}(-12.43115) - (-15.18115) &= 2.75 \text{ dB} \\ 15.655 - 2.75 &= 12.905 \text{ dB}\end{aligned}$$

3dB Beamwidth:

$$17 - (-15) = 32 \text{ dB}$$

F. ANTENNA ISOLATION TEST DATA

At 80 cm separation from each other oriented main beam parallel to each other both at horizontal polarization the isolation between the antennas was found to be -42 dB. At cross polarization (one horizontal and one vertical) the isolation was found to be -57 dB. At slant 45° degree polarization (parallel, then perpendicular) the isolation was found to be -47 dB. At twice the separation distance (160 cm), the isolation increased by 6 dB (to -48 dB from -42 dB for co-polarization horizontal). This demonstrated the drop-off from spreading loss alone (where twice the distance reduces power by a quarter). A distance of 6 ft (same as lumber length) was chosen for the antenna separation and mounting on the ACS. This was sufficient isolation to prevent regenerative feedback. In addition to this minimum antenna separation distance an RF isolator was used to make the ACS transmission path regenerative. There is a need for an RF isolator because all of the RF components are bidirectional. When the RF amplifier was used (as in the anechoic chamber testing) the isolator was not required, as an amplifier is a uni-directional device. If the signal path through the ACS is allowed to be bi-directional,

then the horns become radiators in a two element array with large electrical spacing. This results in a radiation pattern with numerous narrow lobes. This condition must be eliminated if the ACS radiation pattern is to be that of a single horn.

THIS PAGE INTENTIONALLY LEFT BLANK

APPENDIX G. ANECHOIC CHAMBER

This appendix provides information on the setup of the Naval Postgraduate School's anechoic chamber on the roof of Spanagel Hall. This is the anechoic chamber owned by the Electrical and Computer Engineering Department. This was the only anechoic chamber used in this thesis (to include Antenna Testing and Amplitude/Reflectivity Measurements).

Anechoic Chamber Calculations

Distance between horns - 19 ft. about 18.5 ft for the big horn

$$\text{Path loss @ 5.8GHz} = 10 \log_{10} \left(\frac{4\pi Rf}{c} \right)^2 = 63dB$$

General Friis Equation

$$P_r = P_t + G_t + G_r - L_p + \text{gains} - \text{losses}$$

In the chamber

$$P_r = P_t - 8.8dB_{line} + G_t - L_{path} + G_r - L_{variable\ att} - 1dB_{pad}$$

$$P_{ref} = P_t - 10dB_{coupler} - 20dB_{pad} - 8.8dB_{line} - 1dB_{pad}$$

The chamber measures $P_r - P_{ref}$ or the system loss.

Solving for P_t and substituting into the equation for P_r ,

after a little algebra, we find that:

$$G_r = \left(\underset{\text{measured value}}{P_r} - P_{ref} \right) - G_t + L_p + L_{\text{variable att}} - 30 \text{ dB}$$

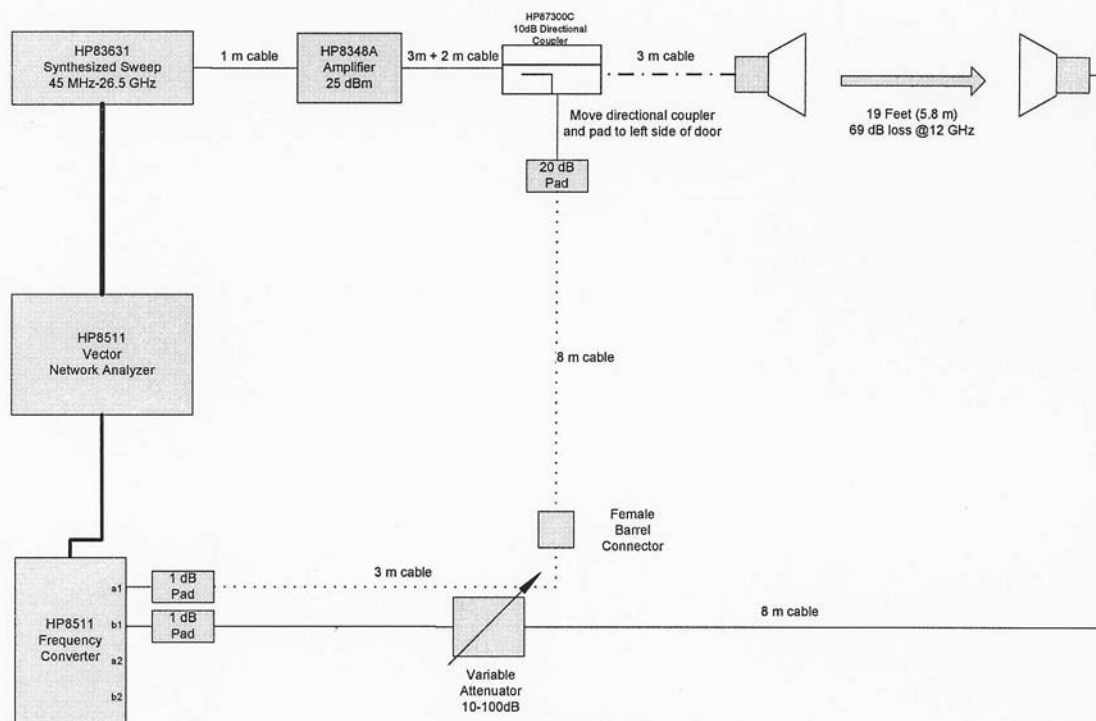
Planned configuration after repairs
March 2006

Figure 79. Anechoic Chamber Diagram.

APPENDIX H. COMPACTRIO

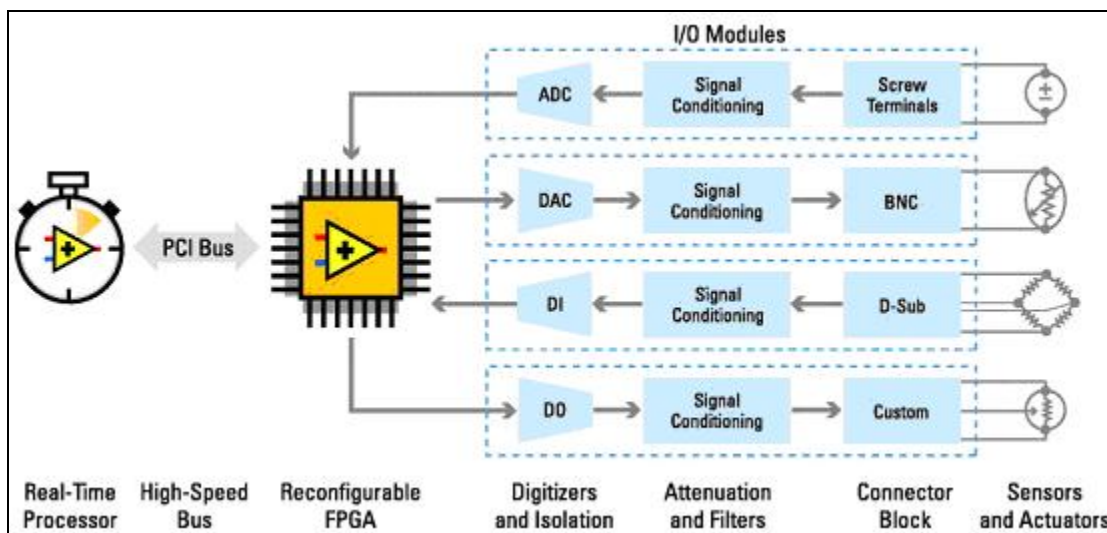


Figure 80. Figure of CompactRIO Software Architecture from ni.com.

A. COMPACTRIO REAL-TIME EMBEDDED CONTROLLER (NI CRIO-9004, 64/512 MEMORY)

This model embedded controller runs LabVIEW Real-Time with 64 MB of nonvolatile CompactFlash storage and 512 MB of DRAM memory, has a 195 MHz processor, and is equipped with a 10/100BaseT Ethernet port.

From the CompactRIO ADVISOR on the webpage for this device, <http://sine.ni.com/nips/cds/view/p/lang/en/nid/14155> “National Instruments CompactRIO real-time embedded controllers offer powerful stand-alone embedded execution for deterministic LabVIEW Real-Time applications. The NI CompactRIO controllers are designed for extreme ruggedness, reliability, and low power consumption, with dual 9 to 35 VDC supply inputs that deliver isolated power to the CompactRIO chassis/modules and a -40 to 70 °C operating temperature range. The NI cRIO-901x series controllers feature a 400 MHz industrial processor balancing low power consumption and powerful real-time floating-point signal analysis, control and logging. The cRIO-900x controllers feature a 200 MHz industrial processor for real-time analysis, control and logging.”



Figure 81. Picture of cRIO-9004 from ni.com.

CompactRIO Real-Time Embedded Controllers

NI cRIO-900x

- Small, rugged, high-reliability embedded real-time processor for intelligent stand-alone operation
- Executes powerful floating-point algorithms with deterministic real-time performance
- Low power consumption with dual DC supply inputs for redundancy
- 10/100BaseT Ethernet port with built-in LabVIEW remote panel Web server and FTP file sharing server
- RS232 serial port for peripheral devices

Operating System

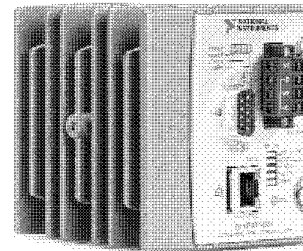
- LabVIEW Real-Time (ETS)

Development Environment

- LabVIEW Full or Professional Development System for Windows
- LabVIEW Reconfigurable I/O Software Development Kit (includes LabVIEW Real-Time and LabVIEW FPGA modules and developer toolkits)

Driver Software

- NI-RIO for reconfigurable embedded systems



Product	DRAM Memory (MB)	Internal Nonvolatile Storage (MB)	10/100BaseTX Ethernet Port	RS232 Serial Port	LEDs	DIP Switches	Power Supply Input Range	Power Consumption	Backup Power Input	Remote Panel Web Server	FTP Server
cRIO-9002	32	64	✓	✓	4	5	9 to 35 VDC	7 W max	✓	✓	✓
cRIO-9004	64	512	✓	✓	4	5	9 to 35 VDC	7 W max	✓	✓	✓

Table 1. cRIO-900x Selection Guide

Overview and Applications

National Instruments cRIO-900x real-time embedded controllers offer powerful stand-alone embedded execution for deterministic LabVIEW Real-Time applications. The NI cRIO-9002 includes 32 MB of DRAM memory and 64 MB of nonvolatile flash storage for file storage. The cRIO-9004 includes 64 MB of DRAM memory and 512 MB of nonvolatile flash storage for data-logging applications. Both controllers are designed for extreme ruggedness, reliability, and low power consumption with dual 9 to 35 VDC supply inputs that deliver isolated power to the CompactRIO chassis/modules and a -40 to 70 °C temperature range. A 195 MHz industrial processor balances low power consumption with powerful real-time floating-point signal processing and analysis capabilities for deterministic control loops exceeding 1 kHz.

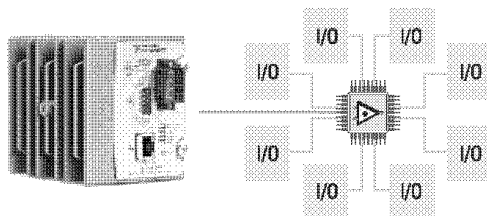


Figure 1. CompactRIO Hardware Architecture

System Configuration

The CompactRIO real-time controller connects to any 4- or 8-slot CompactRIO reconfigurable chassis. The user-defined FPGA circuitry in the chassis controls each I/O module and passes data to the controller through a local PCI bus, using built-in communication functions.

Embedded Software

You can synchronize embedded code execution to an FPGA-generated interrupt request (IRQ) or an internal millisecond real-time clock source. The LabVIEW Real-Time ETS OS provides reliability and simplifies the development of complete embedded applications that include time-critical control and acquisition loops in addition to lower-priority loops for postprocessing, data logging, and Ethernet/serial communication. Built-in elemental I/O functions such as the FPGA Read/Write function provide a communication interface to the highly optimized reconfigurable FPGA circuitry. Data values are read from the FPGA in integer format, and then converted to scaled engineering units in the controller.

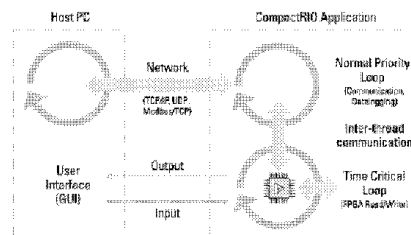


Figure 2. CompactRIO Software Architecture



Figure 82. Datasheet for CompactRIO Real-Time Embedded Controllers from ni.com.

B. COMPACTRIO RECONFIGURABLE EMBEDDED CHASSIS (NI CRIO-9101, 1M GATE 4-SLOT CHASSIS)

From the CompactRIO ADVISOR on the webpage for this device, <http://sine.ni.com/nips/cds/view/p/lang/en/nid/14154> “The National Instruments CompactRIO embedded chassis are the heart of the CompactRIO system because they contain the reconfigurable I/O (RIO) FPGA core. The RIO core has an individual connection to each I/O module and is programmed using easy to use elemental I/O functions to read or write signal information from each module. Because there is no shared communication bus between the RIO FPGA core and the I/O modules, input/output operations on each module can be precisely synchronized with 25 ns resolution. The RIO core can perform local integer-based signal processing and decision making and directly pass signals from one module to another.”

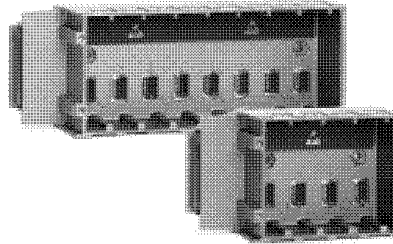


Figure 83. Picture of cRIO-9103 from ni.com.

CompactRIO Reconfigurable Chassis

NI cRIO-910x *NEW!*

- Design hardware using LabVIEW programming skills
- 4 or 8-slot chassis for any CompactRIO I/O modules
- 1 M or 3 M gate RIO FPGA core for normal or extended RIO processing power
- DIN-rail mounting, 19 in. rack mount, and panel mounting options
- NI CompactRIO Extreme Industrial Certifications and Ratings¹
- Program in easy-to-use LabVIEW FPGA graphical development environment to automatically synthesize an optimized high-performance electrical circuit implementation of your application
- RIO FPGA core executes LabVIEW control logic at rates up to 40 MS/s using single-cycle timed loops



Product	Module Slots	FPGA System Gates	RAM (KB)	Default Timebase (MHz)	Maximum Power Consumption (W)	Built-In Panel Mounting Holes
cRIO-9101	4	1 M	82	40	2.3	✓
cRIO-9102	8	1 M	82	40	2.3	✓
cRIO-9103	4	3 M	196	40	3	✓
cRIO-9104	8	3 M	196	40	3	✓

Overview and Applications

The National Instruments CompactRIO reconfigurable chassis are the heart of the CompactRIO system because they contain the reconfigurable I/O (RIO) core. The RIO FPGA core, which has an individual connection to each I/O module, is programmed with easy-to-use elemental I/O functions to read or write signal information from each module. Because there is no shared communication bus between the RIO FPGA core and the I/O modules, I/O operations on each module can be precisely synchronized with 25 ns resolution. The RIO core can perform local integer-based signal processing and decision-making and directly pass signals from one module to another.

The RIO core is also connected to the CompactRIO real-time controller through a local PCI bus interface. The real-time controller can retrieve data from any control or indicator on the front-panel of the RIO FPGA application through an easy-to-use FPGA Read/Write function. The RIO FPGA can also generate interrupt requests (IRQs) to synchronize the real-time software execution with the RIO FPGA. Typically, the real-time controller is used to convert the integer based I/O data to scaled floating-point numbers. In addition, the real-time controller typically performs single-point control, waveform analysis, data logging, and Ethernet/serial communication.

The reconfigurable chassis, real-time controller, and I/O modules combine to create a complete stand-alone embedded system. Application development consists of three steps:

1. Target the reconfigurable chassis to automatically detect the I/O modules and develop the RIO FPGA application,
2. Compile the RIO application to automatically synthesize an optimized high-performance electrical circuit implementation of your application,

3. Develop the real-time controller application to add floating-point control, signal processing, data logging, and communication

Key Features

- Create any local or multichassis timing, triggering, and synchronization scheme with 25 ns resolution
- Use multiple while loops to create a parallel processing application for high-performance signal processing or multirate control systems
- Built-in PID control functions for control system loop rates greater than 100 kHz
- Generate waveforms or implement nonlinear look-up tables (LUTs) using LabVIEW FPGA express VIs
- Integrate widely available third-party HDL cores using the LabVIEW FPGA Module HDL Node
- Enforce critical logic and interlocks in silicon hardware circuitry, or use the parallel RIO architecture to create dual, triple, or quadruple redundant systems

Visit ni.com/compactrio for example programs, application notes, and other developer tools.

For ordering information, see page 381.



For more information, see page 379.

¹See CompactRIO Overview on page 366 for details.

BUY ONLINE or CALL (866) 265-9891! Visit ni.com

373

CompactRIO
Reconfigurable Chassis

Figure 84. Datasheet for CompactRIO Reconfigurable Embedded Chassis from ni.com.

C. COMPACTRIO I/O MODULES FOR DIGITAL INPUT AND COUNTER/TIMER (NI 9401, 8 CH 5 V/TTL HIGH SPEED BIDIRECTIONAL DIGITAL I/O MODULE)

From the CompactRIO ADVISOR on the webpage for this device, <http://sine.ni.com/nips/cds/view/p/lang/en/nid/14168> “National Instruments CompactRIO digital input modules are compatible with any CompactRIO chassis and work with 5 V/TTL, industrial and universal logic levels and signals for direct connection to a wide array of devices such as industrial switches, encoders and transducers. Each module features an integrated connector junction box with a screw terminal or industrial D-Sub connector for flexible and low cost signal wiring. All modules feature the NI CompactRIO Extreme Industrial Certifications and Ratings. Each CompactRIO I/O module has a direct connection to the reconfigurable FPGA in CompactRIO systems. Using the LabVIEW FPGA module, users can configure and reconfigure all CompactRIO digital input modules to implement counter/timer, encoder, digital protocol, and/or static digital inputs.”

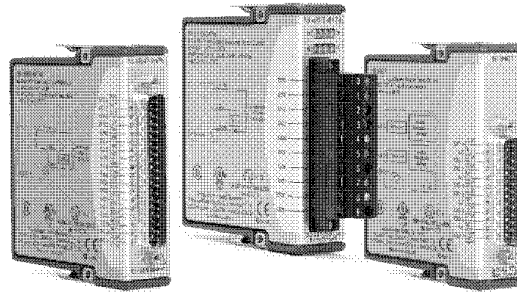


Figure 85. Picture of cRIO-9401 from ni.com.

C Series Digital Output and Relay Modules

NI 940x, NI 947x, NI 948x *NEW!*

- High- and low-speed high-voltage digital outputs (up to 60 V), 5 V/TTL, SPST (Form A) electromechanical relay outputs or solid-state relay outputs
- Up to 32 channels per module; up to 256 channels per 8-slot chassis
- Down to 100 ns output rate for ultrahigh-speed control, pulse-width modulation (PWM), or digital communication
- Isolation up to 2,300 V_{rms} (withstand), up to 250 V_{rms} (continuous)
- Externally powered with high current-switching capacity (up to 20 A per module) for direct control of a wide array of industrial actuators
- Short-circuit-proof outputs available to protect from damage caused by current surges



Compatibility		Logic	Channels	Sink/Source	I/O Delay Time	Signal Levels	Output Current per Channel	Isolation	Connector Options	
Product	CompactRIO/NI CompactDAQ									
NI 9401	✓	✓	5 V/TTL	8	Sink/Source	100 ns	5 V	2 mA	✓	D-Sub
NI 9403	✓	✓	5 V/TTL	32	Sink/Source	7 µs	5 V	2 mA	✓	D-Sub
NI 9472	✓	✓	High Voltage	8	Source	100 µs	6 to 30 V	750 mA	✓	Screw Terminal, D-Sub
NI 9474	✓	✓	High Voltage	8	Source	1 µs	5 to 30 V	1 A	✓	Screw Terminal
NI 9476	✓	✓	High Voltage	32	Source	500 µs	6 to 36 V	250 mA	✓	D-Sub
NI 9477	✓	✓	High Voltage	32	Sink	8 µs	5 to 60 V	625 mA	✓	D-Sub
NI 9481	✓	✓	Form A	4	Sink/Source	10 ms	60 VDC, 250 VAC	2 A (30 VDC)	✓	Screw Terminal
NI 9485	✓	✓	SSR	8	Sink/Source	8 ms	50 VDC, 30 VAC	750 mA	✓	Screw Terminal

Table 1. C Series Digital Output and Relay Module Selection Guide

Overview

High-performance digital output and switching modules for National Instruments CompactRIO embedded systems, R Series expansion chassis, and NI CompactDAQ systems provide extended voltage ranges and high current-switching capacity for direct control of a wide array of industrial and automotive actuators. Each module features an integrated connector junction box with screw-terminal or cable options for flexible, low-cost signal wiring. All modules feature the NI CompactRIO Extreme Industrial Certifications and Ratings.

System Compatibility

You can use NI C Series modules interchangeably in CompactRIO and NI CompactDAQ chassis. Many of the advanced timing features described apply only to CompactRIO reconfigurable I/O systems and not to NI CompactDAQ.

Advanced Features

When used in CompactRIO, C Series digital output modules connect directly to reconfigurable I/O (RIO) FPGA hardware to create high-performance embedded systems. The reconfigurable FPGA hardware within CompactRIO provides a variety of options for timing, triggering, synchronization, digital waveform generation, or digital communication. For instance, with CompactRIO you can implement a circuit to generate

pulse-width modulation (PWM) outputs for controlling motors, heaters, or fans, as well as perform pulse code modulation encoding (PCME) for wireless telemetry applications.

Key Features

- High-performance digital output switching for any CompactRIO embedded system, R Series expansion chassis, or NI CompactDAQ system
- Screw-terminal, strain relief, high-voltage, cable, solder-cup backshell, and other connectivity options
- Channel-to-earth ground double-isolation barrier for safety and noise immunity
- NI CompactRIO Extreme Industrial Certifications and Ratings

Visit ni.com/compactrio or ni.com/compactdaq for up-to-date information on module availability, example programs, application notes, and other developer tools.

Typical certifications – Actual specifications vary from product to product. Visit ni.com/certification for details.

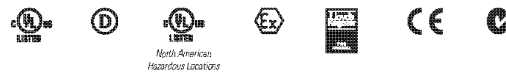


Figure 86. Datasheet for C Series Digital Output and Relay Modules from ni.com.

D. NI DEVELOPER SUITE WITH REAL-TIME AND FPGA SOFTWARE FOR COMPACTRIO

From the CompactRIO ADVISOR on the webpage for this software package, <http://sine.ni.com/nips/cds/view/p/lang/en/nid/14294> “The NI Developer Suite Core Package with the Real-Time Deployment and FPGA Deployment options include all of the tools you need for building a custom embedded system - LabVIEW FPGA for customizing hardware I/O in the user-configurable FPGA core and LabVIEW Real-Time for building deterministic and reliable real-time applications. The NI Developer Suite Core Package with the Real-Time Deployment and FPGA Deployment options also include a comprehensive set of LabVIEW add-on tools for algorithm development, real-time development analysis, Microsoft Office report generation, and database communication.”

Of particular note in this software package is the FPGA Deployment Option, which includes the LabVIEW FPGA Module and NI RIO. These are essential programming components to the LabVIEW software library used with the ACS. NI RIO is needed to communicate with the CompactRIO Chassis(FPGAs) and the LabVIEW FPGA module for programming commands that can be auto-compiled into VHDL for the CompactRIO Chassis(FPGAs).

APPENDIX I. LABVIEW FOR THE DIGITAL PHASE SHIFTER

How the digital phase shifter is controlled by code written in LabVIEW and run on the CRIO is explained here.

The LabVIEW Virtual Instruments (VIs) described here include: ManualControl, PhaseShifterControl, MasterControl, and SlaveControl. Together they provide three distinction functionalities in the development of the ACS's software. These are the main VIs. All VIs, including Block Diagram and Front Panel files for each, are included after the description of these main VIs. The VIs not described are test components only and not used with the ACS's current functionalities, although they did play a part in its past development and possibly future development and are included here for that purpose. Primarily they were used to test certain functions that were later incorporated into the main VIs or demonstrate alternative ways of implementing the same functionality as was incorporated into the main VIs as part of testing method efficiency. These VIs include: dataIO, fpgaRX_test, fpgaTX_test, NetworkRX_test, NetworkTX_test, and tDcalc. KNORR-CAL_project is an overall view of the LabVIEW project with all VIs and hardware indicated. The VI PSC6-bit is merely an example of how to modify the files for a different number of control bits. When the ACS was first developed a 6-bit digital phase shifter rather than an 8-bit digital phase shifter was used. The basic principle of this modification is to globally find and replace the number representing $2^{(\text{current number of bits})}$ with $2^{(\text{future number of bits})}$. For example, replace 255 (for 8-bit) with 63 (for 6-bit).

Observe the Block Diagram for each VI and follow along in the diagram left to right as the description explains the graphical code.

A. PHASESHIFTERCONTROL

First, the count is reset (initialized) to zero. Then, the time delay (tD) is read in to become the time between phase state changes. This is also referred to as 'ticks'. 1 tick = 1 bit change = 25 ns (the time of one 40MHz clock cycle). The count is checked so as to

not exceed the number of phase shifter bits (phase states). Here there are 8-bits or $2^8=256$ phase states. Since 0 is considered the first phase state, the count will increment through all 256 phase states and stop at 255.

If the Doppler shift is going to be an up Doppler shift (increase in frequency) the count proceeds unaltered, counting up. If the Doppler shift is to be a down Doppler shift (decrease in frequency) the count proceeds inverted, counting down. The integer value of the count is then converted into a Boolean value. For example, the integer value of 157 = 10011101. The Boolean value is then broken into each of its individual bits and routed to the corresponding Digital I/O (DIO) pin to apply or remove voltage from the appropriate phase shifter control pin. In this VI's current state, both DIO modules receive the same signal.

See Chapter on Future Work. Once the programmable attenuator is received, the second group of DIO pins will be assigned to control this device with dependent statistics. For independent statistics, a second PhaseShifterControl VI will need to be created(duplicated and renamed AttenuatorControl). The only difference between the original and its duplicate is that the duplicate DIOs will be deleted one from each VI so that each VI contains only one unique set of DIO assignments. For dependent (correlated) statistics the DIOs will be controlled from within the same VI in a synchronized time delay (tD).

Once the commands for the appropriate voltages have been sent, the count increments, and the process begins all over again. This process continues until one complete cycle through all the phase states is completed (one period of 2π). Then, the loop encounters an exit condition and the count is reset and the whole sequence begins again (the next period of 2π).

B. SLAVECONTROL

Paired with MasterControl provides automatic PhaseShifterControl to work with data read in from a file. The difference is that an array of integer values corresponding to the tD is first read and stored. Then, the individual time delay integer values are used to provide the appropriate phase shifter Doppler shift values as opposed to the manual entry

input by a user in the GUI of PhaseShifterControl. In addition, instead of a switch being flipped by a user in the GUI to decide up or down Doppler shift, the sign of the integer value is used. A negative sign is used to indicate a down shift and the absence of a negative sign (i.e. positive) to indicate an up shift. Zero indicates no Doppler shift. The process is then exactly the same as that implemented/programmed in PhaseShifterControl (See section above by the same name).

*NOTE: the number of Doppler frequencies cannot be automatically detected from the data file stored on the PC. The number of frequencies must be defined from within the VI. This allows the appropriate sized array to be created in the software even before it starts running. This is noted in the VI Front Panel (GUI) as well.

C. MASTERCONTROL

This VI reads in the value of the Doppler frequencies from a tab delaminated file (such as how the array of variables would be exported/saved from the Weather Signal Simulator in MATLAB). The numbers(frequencies) are read in as double floating point. numtDs is the number of Doppler frequencies read in. The Doppler frequencies (DF) are then used to calculate the Radial Velocity (Vr), Period (T), and Bit Delay (t) according to the following relations:

$$\text{Equation 1} \quad Vr = DF \times \frac{c}{RF \times 2} \text{ in meters per second}$$

$$\text{Equation 2} \quad T = \frac{1}{DF} \times 1000 \text{ in milliseconds}$$

$$\text{Equation 3} \quad t = \frac{T \cdot 10^6}{n \cdot 25} \text{ in 'ticks' (of 25ns)}$$

Where the RF Frequency (RF) is defined to be 9990000000Hz or 9.99GHz, the Speed of Light (c) is 299792458 m/s, and the number of Phase Steps (n) is 63 (for 6 bits).

However, since only integers (INT) can be passed to the FPGA, the doubles (DBL) are converted to integers and sent to the FPGA. The Period, DF, and Vr are then recalculated based on these 16-bit integer values. This is to show the user what actual values will be produced by the ACS. This only affects values stored in the data file which may have been truncated by the conversion. This is a potential software limitation.

However, this will not affect the calibration process, only “real world” weather simulation, because any variation from the input values that have been truncated are now recomputed and displayed to the user. The radar should be tested/calibrated to agree with these values, not the values output by the Weather Signal Simulator. This is a limitation of the calibrator’s software when interacting with the FPGA. Although values may be calculated accurately by the Weather Signal Simulator to agree with “real world” weather patterns, the calibrator cannot always reproduce these exact values. This is a hardware limitation due to the FPGA and seen in the software. In practice, this limitation is similar to other hardware limitations already discussed. See Hardware Limitations Section.

*NOTE: before executing the VI, the array size in SlaveControl must be defined to the number of Doppler frequencies intended to be read from the data file. This is not automatic. It cannot predetermine the number of entries. There is no “read until end of file.” See also SlaveControl NOTE.

*NOTE: the path on the PC to the data file must be entered into the VI. The data file must be a single row of tab delaminated Doppler frequency entries stored in a text file (.txt) where a negative sign indicates a down Doppler shift and no sign indicates an up Doppler shift. Do not use + signs.

_CODE	LabView Code (# indicates state change)
_UI	User Interface
	reads in data file containing Doppler Shift values input from
dataIO	Ulf Shroder's MATLAB weather simulator
fpgaRX_test	test file to send data read on laptop to fpga
fpgaTX_test	test file to receive data sent from laptop on fpga
KNORR-CAL_project	overall software view. LabView Project.
ManualControl	vi to manually control individual phase shifts. High or low
MasterControl	any one or combination of bits
NetworkRX_test	vi to automatically control phase shifts. Runs on laptop.
NetworkTX_test	test file to send data read on laptop to CRIO
PhaseShifterControl6-bit	test file to receive data sent from laptop on CRIO
PhaseShifterControl	only difference from PhaseShifterControl is 6-bit (63) test
SlaveControl	vs. 8-bit (255)
	fpga resident to control phaseshifter through a series of
	phase shifts
	version of PhaseShifterControl to work with MasterControl.
	LabVIEW computer for the mathematical relations between
	time delay tD, radial velocity, and Doppler frequency.
	MATLAB Script Node is used in MasterControl instead of
tDcalc	this.

Table 10. Table Summary of LabVIEW VIs.

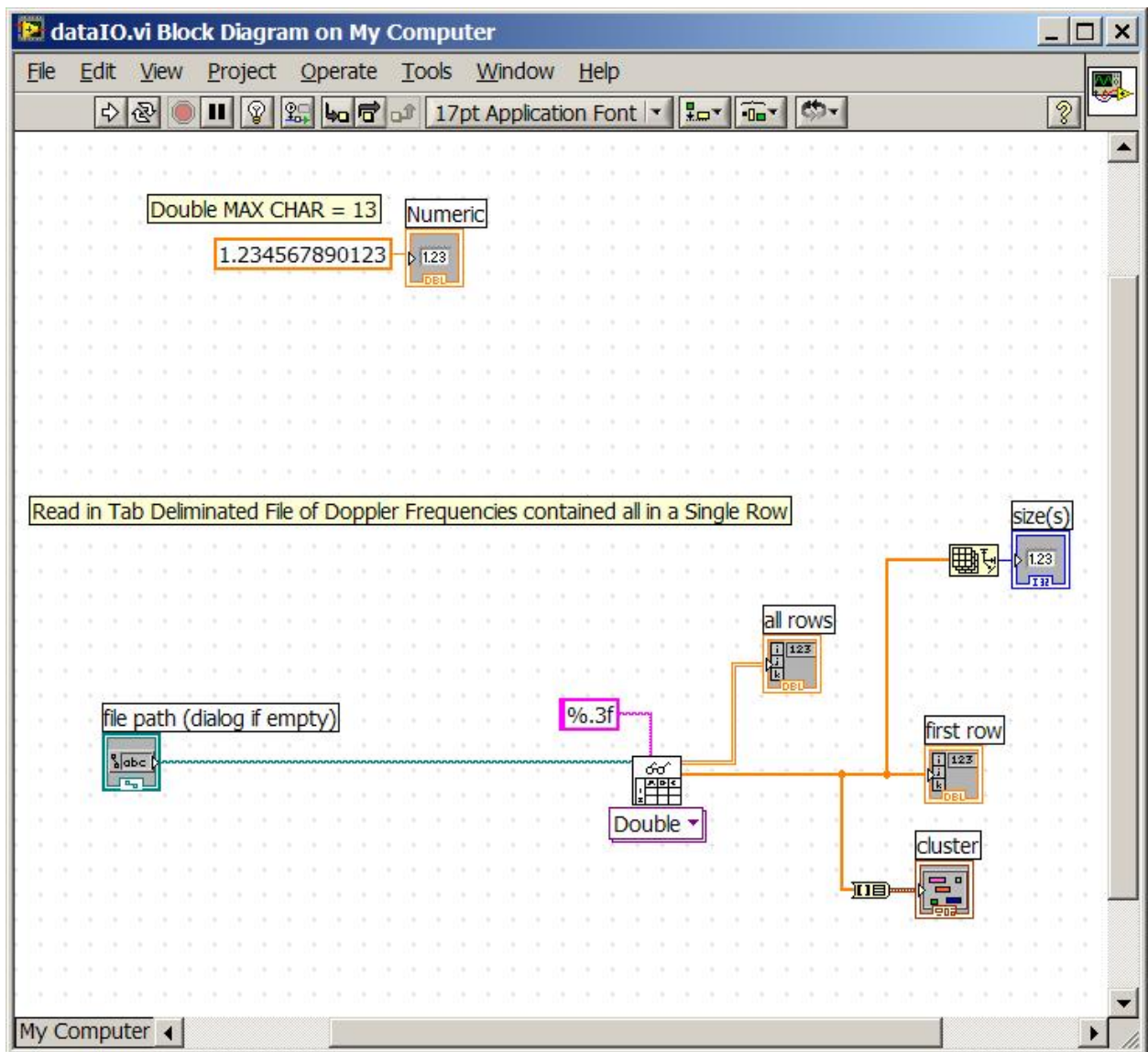


Figure 87. dataIO_CODE

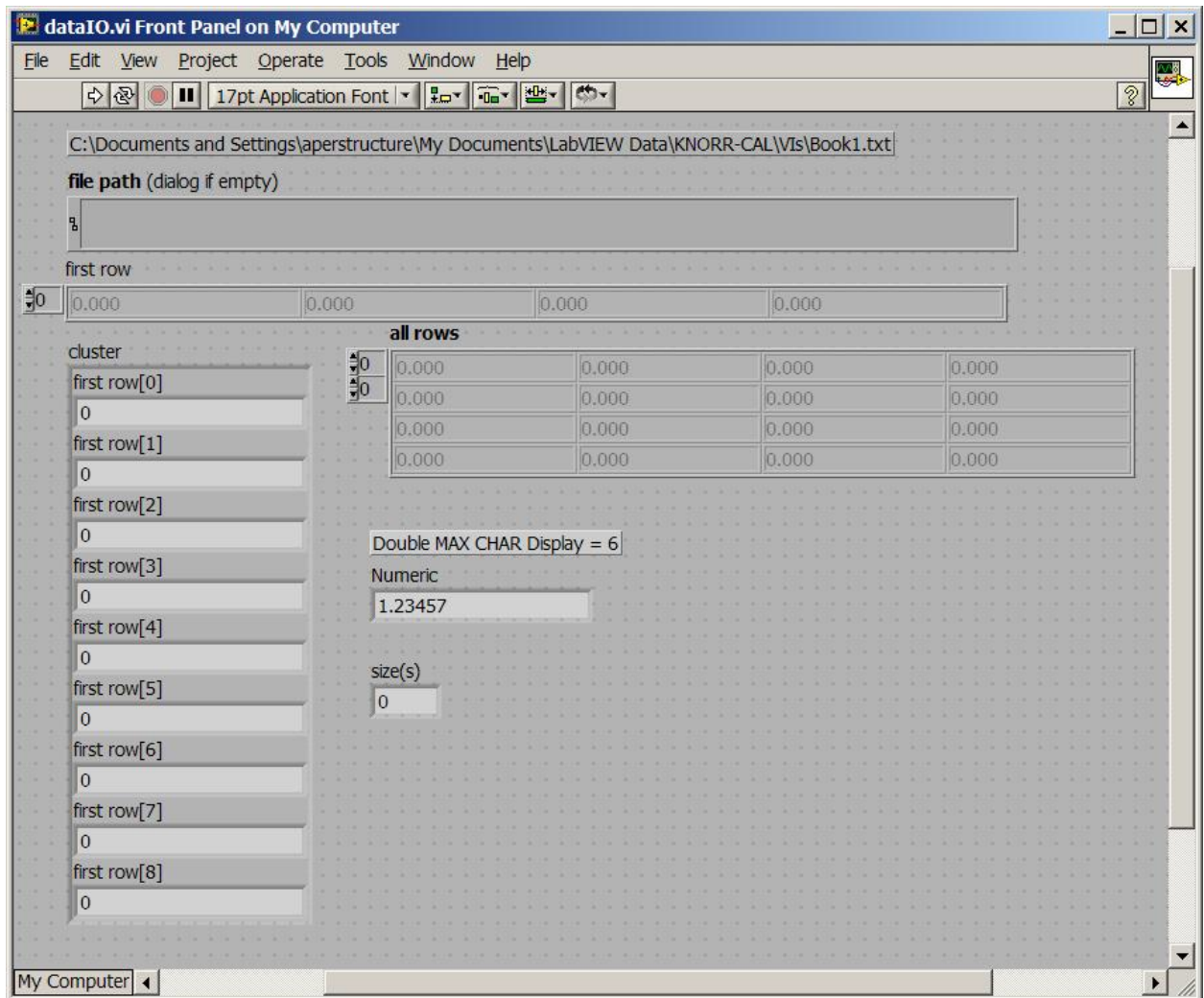


Figure 88. dataIO_UI

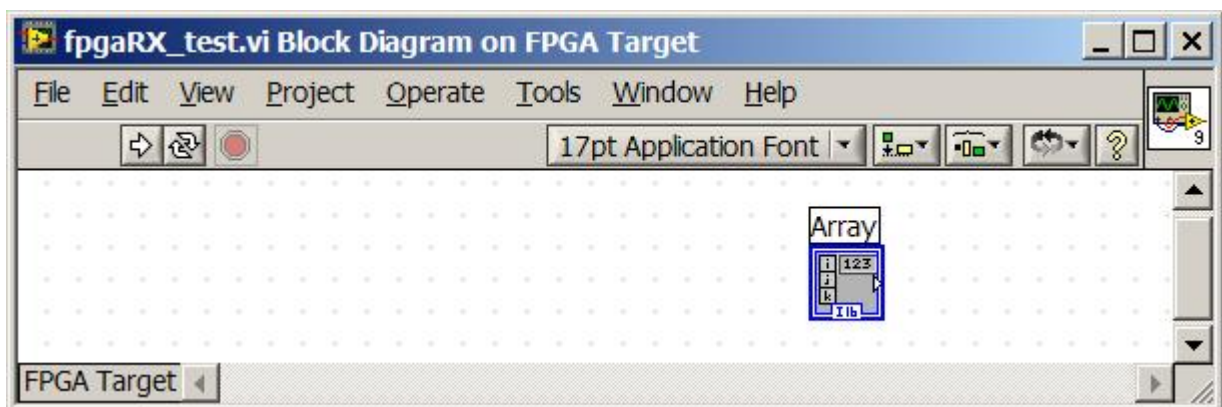


Figure 89. fpgaRX_test_CODE

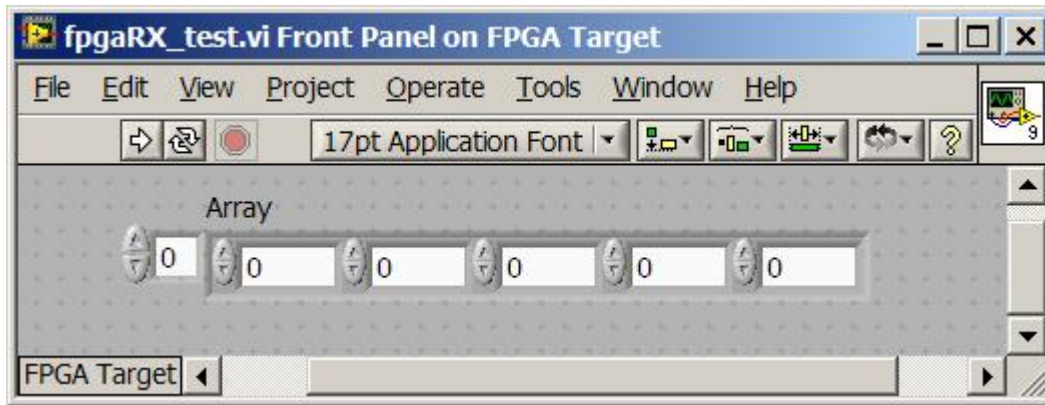


Figure 90. fpgaRX_test_UI

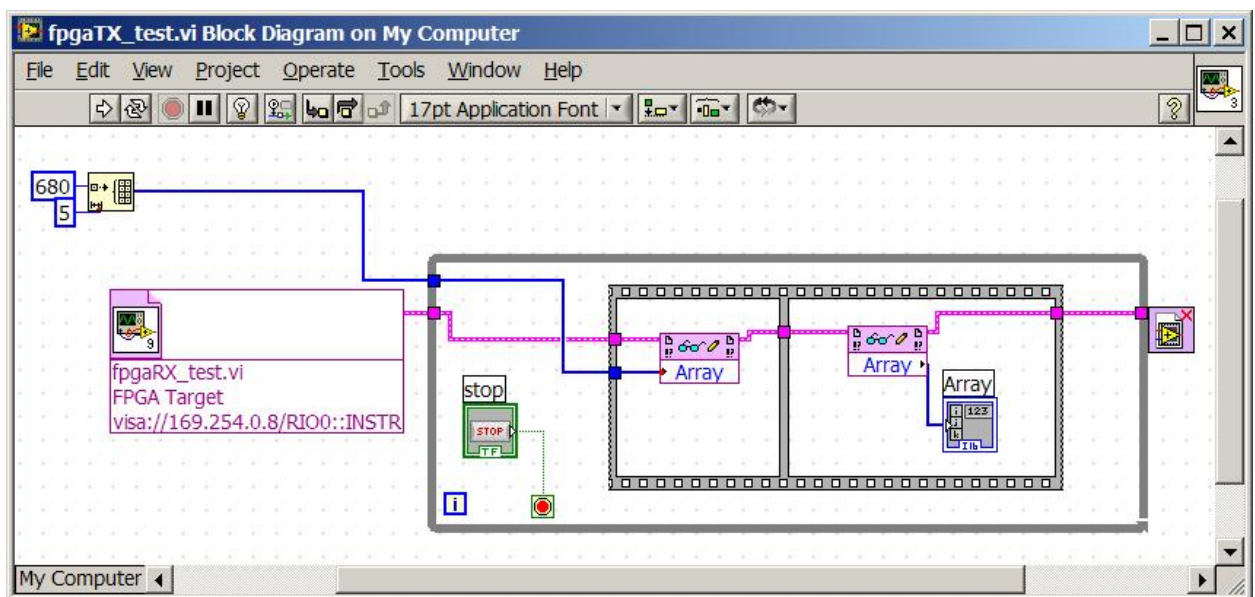


Figure 91. fpgaTX_test_CODE

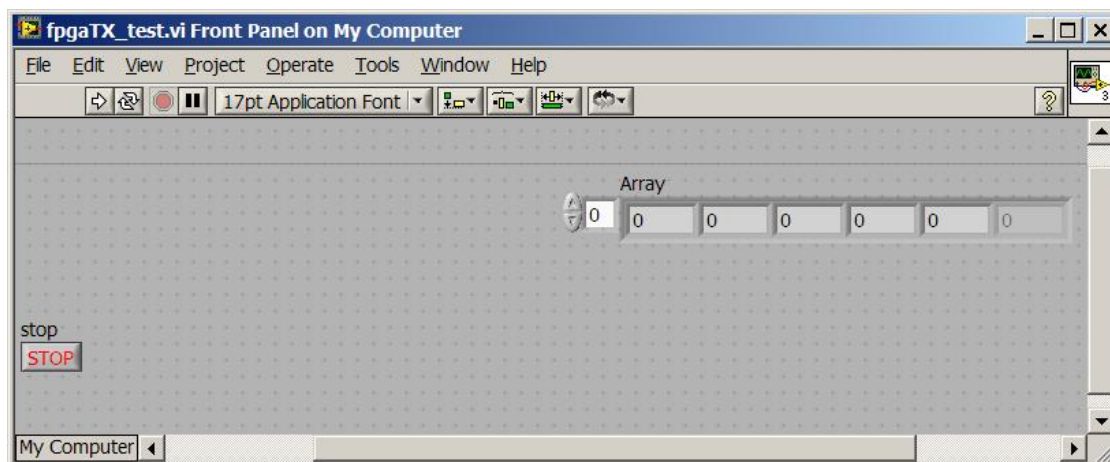


Figure 92. fpgaTX_test_UI

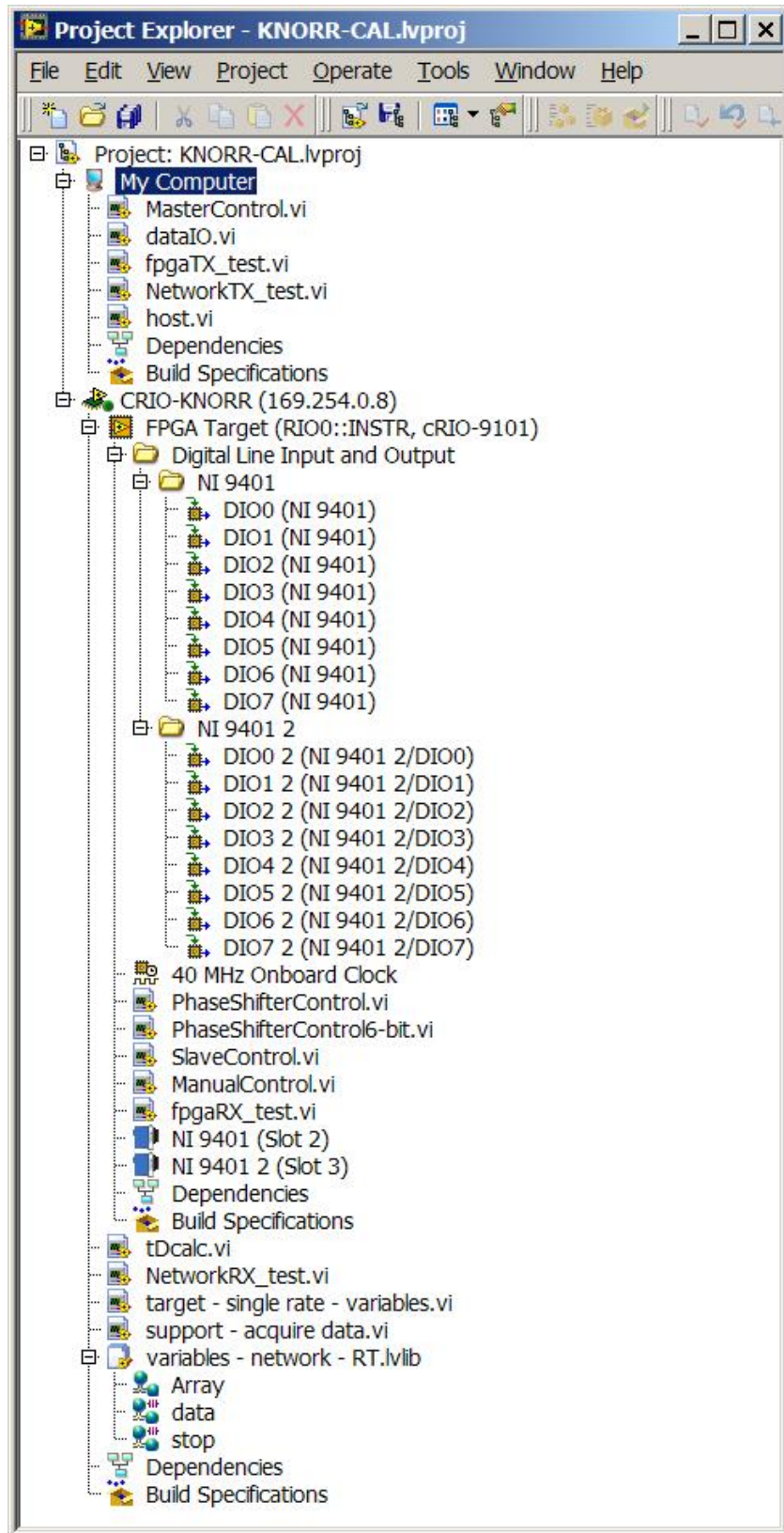


Figure 93. KNORR-CAL_project

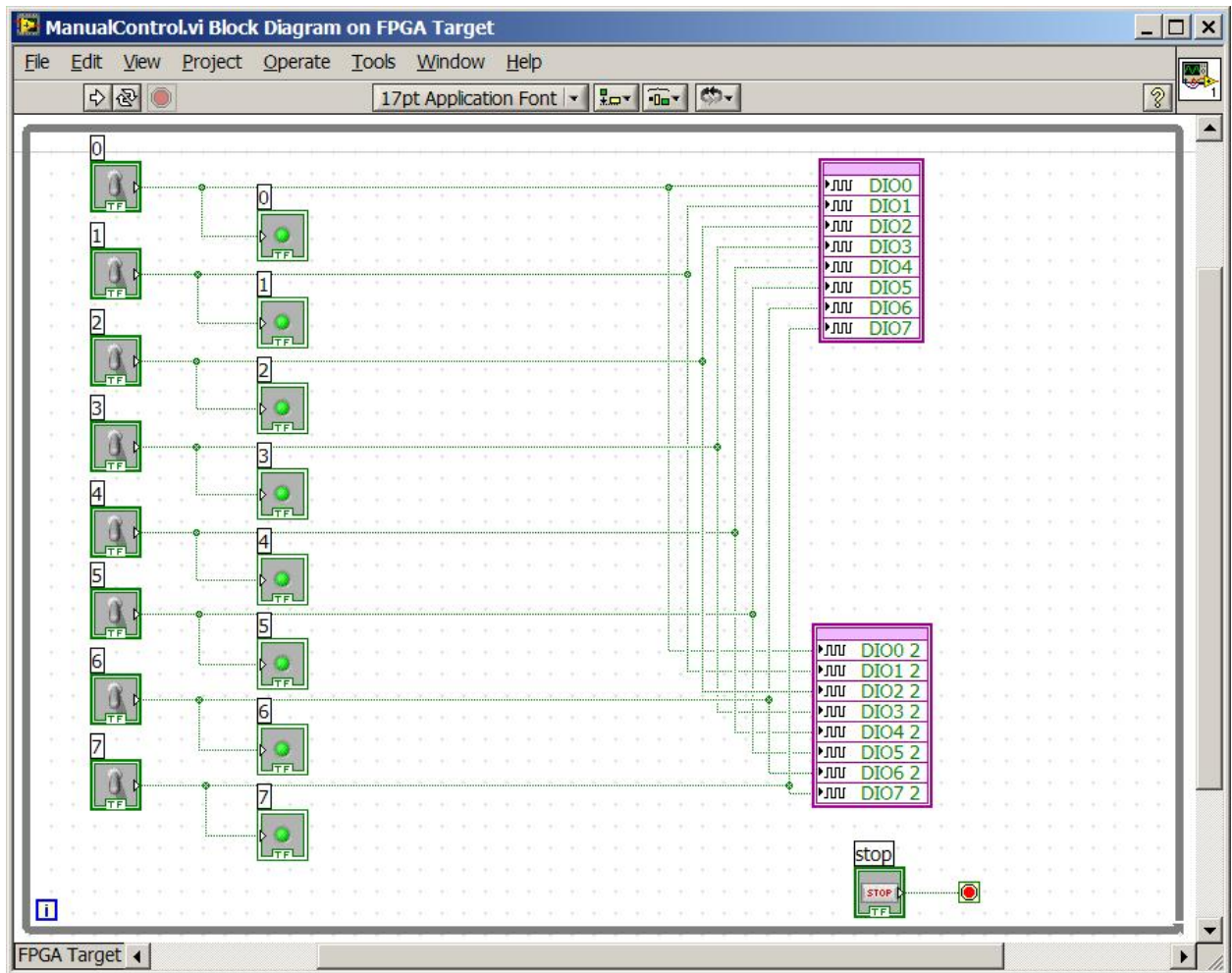


Figure 94. ManualControl_CODE

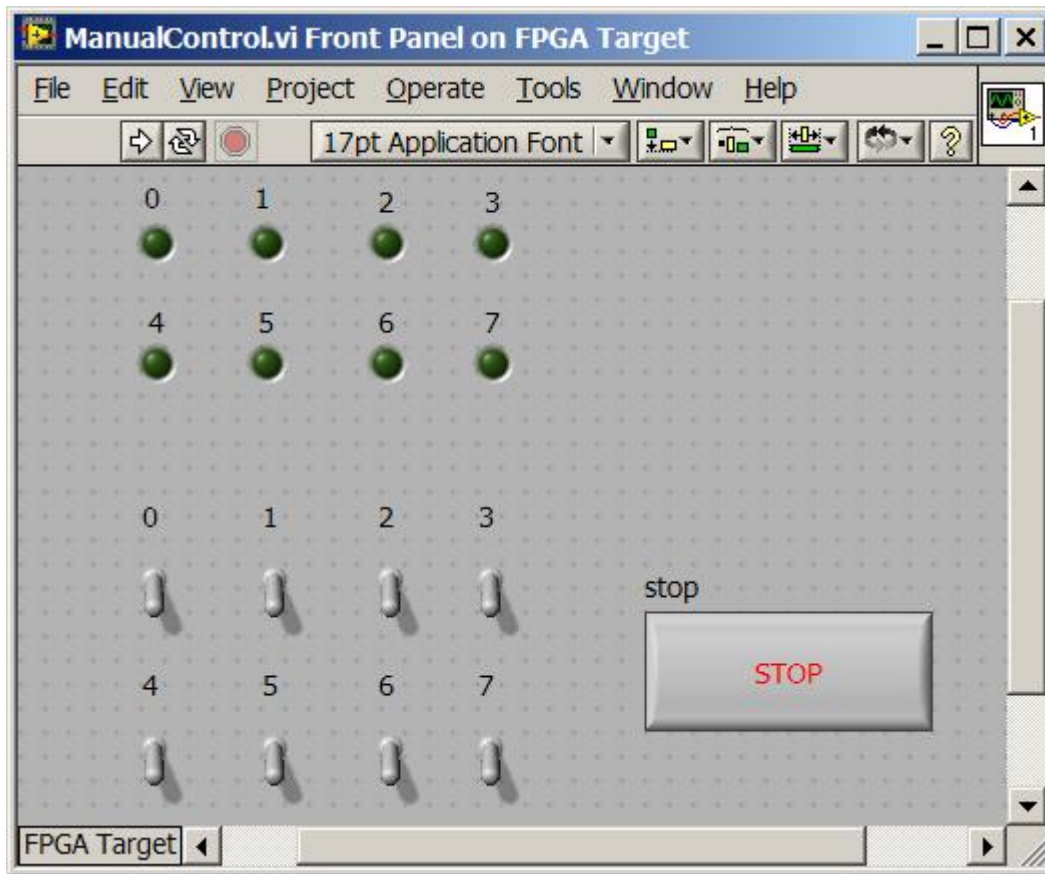


Figure 95. ManualControl_UI

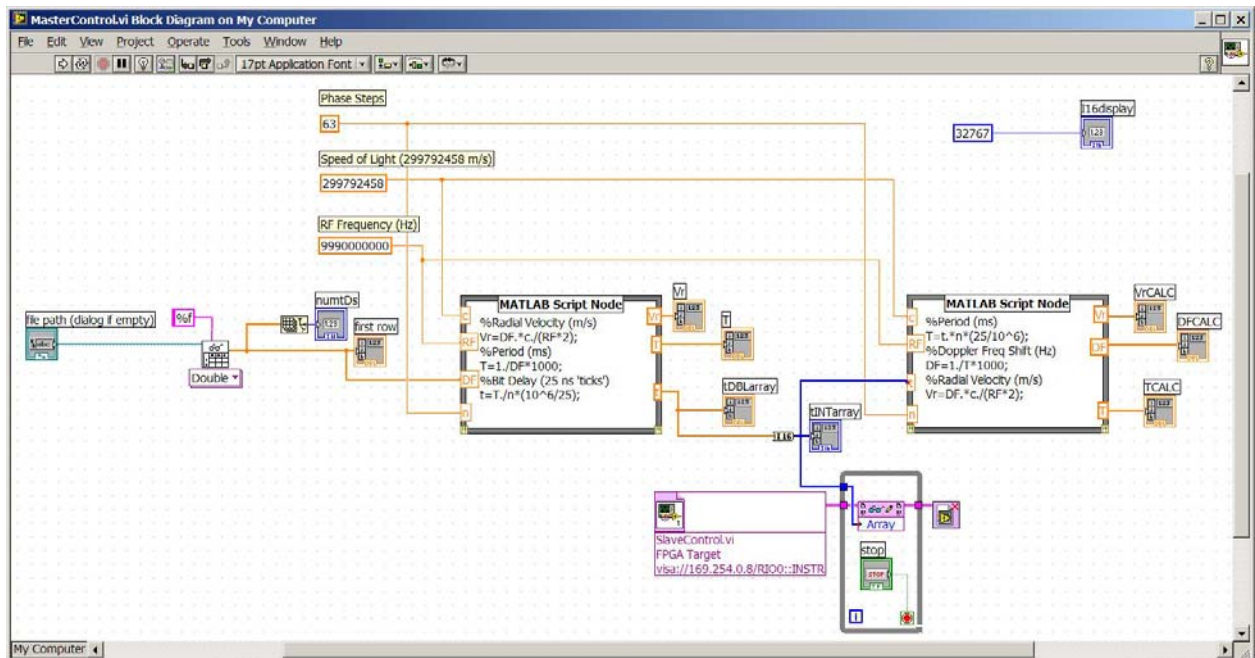


Figure 96. MasterControl_CODE

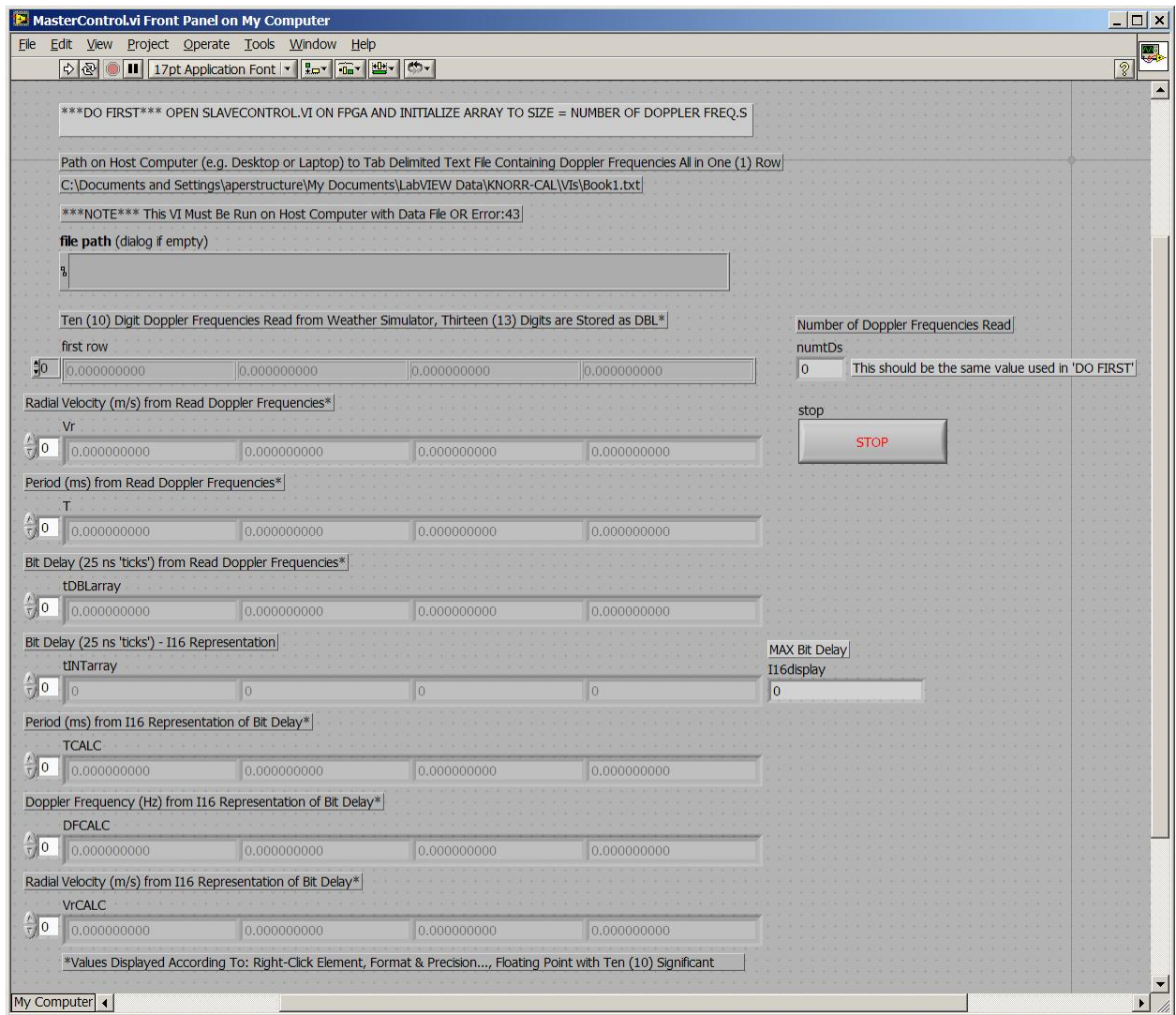


Figure 97. MasterControl_UI

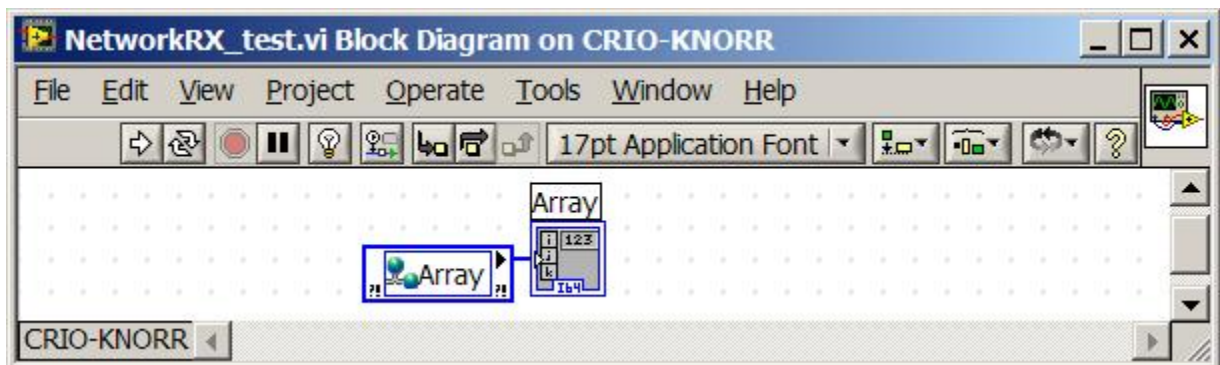


Figure 98. NetworkRX_test_CODE

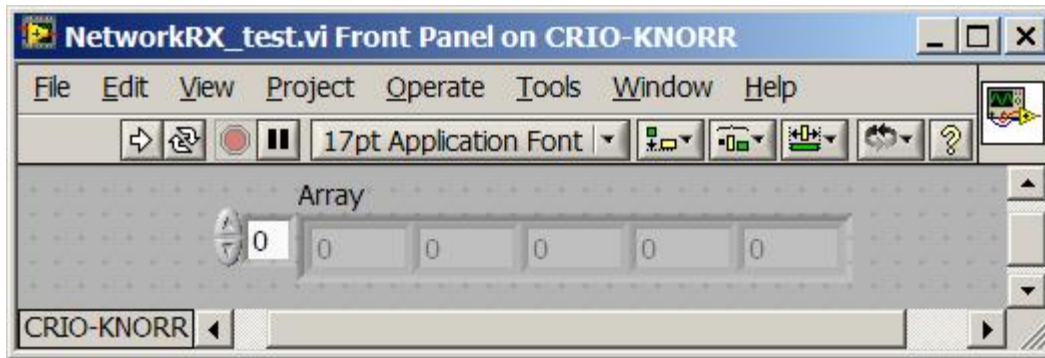


Figure 99. NetworkRX_test_UI

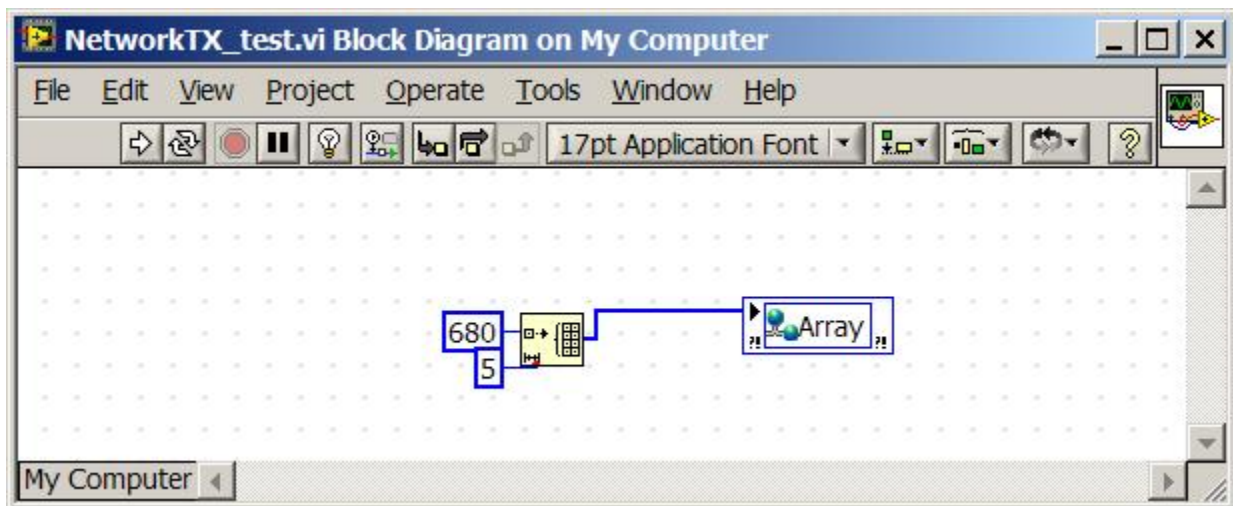
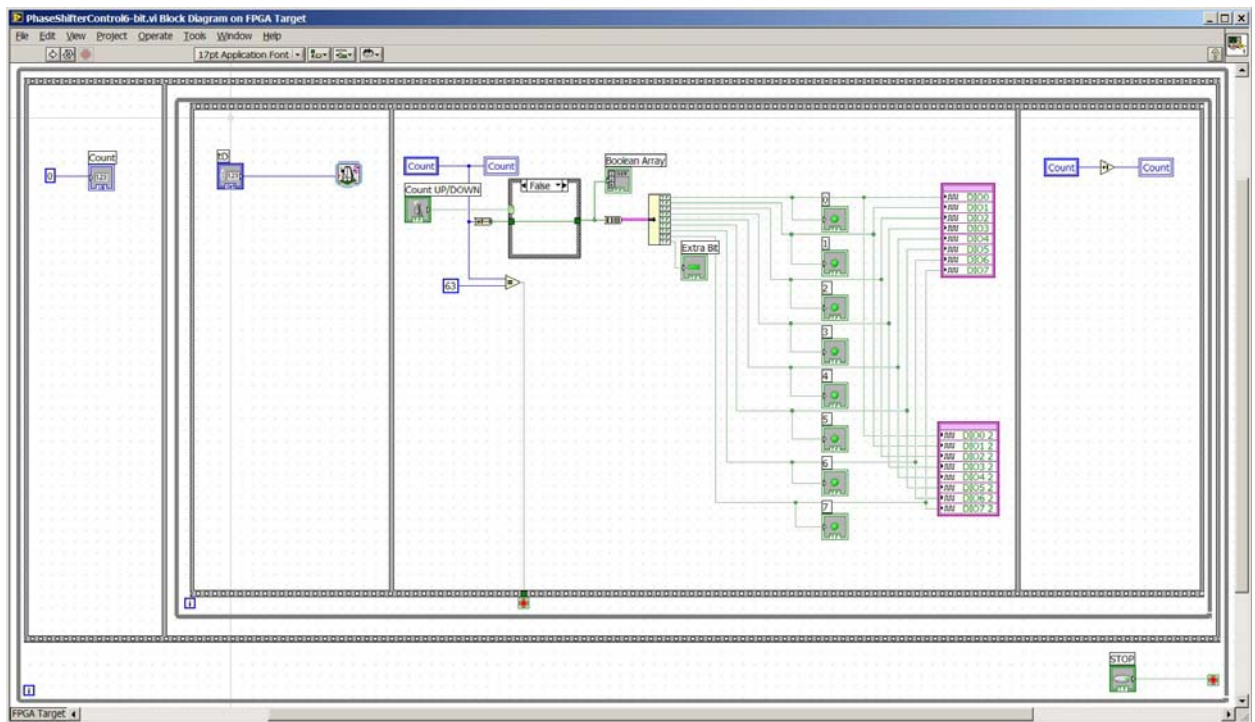
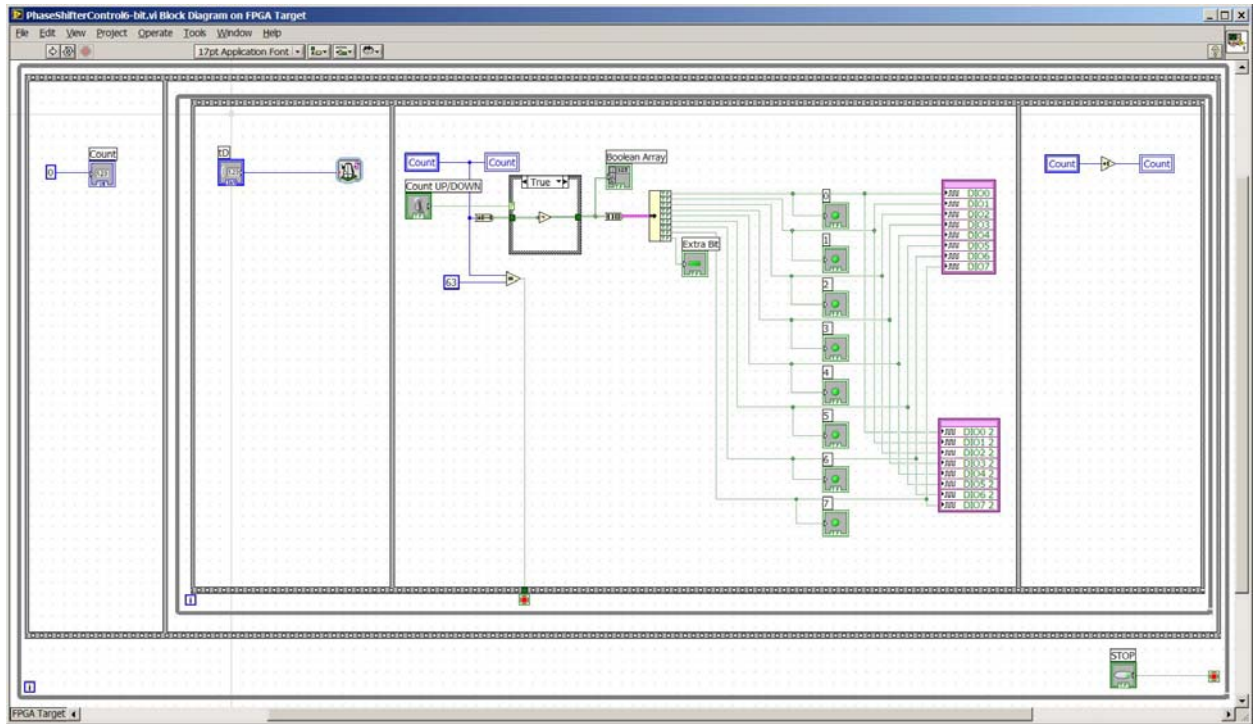


Figure 100. NetworkTX_test_CODE



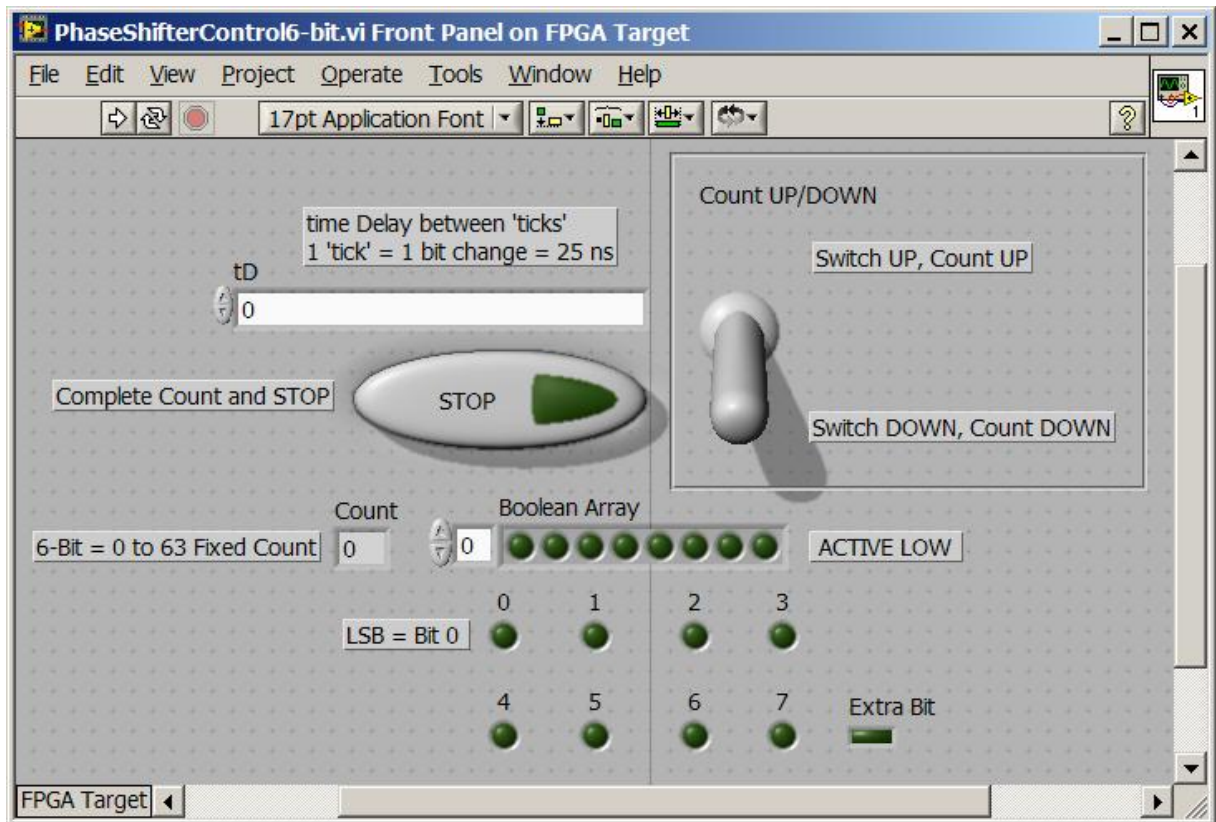


Figure 103. PhaseShifterControl6-bit_UI

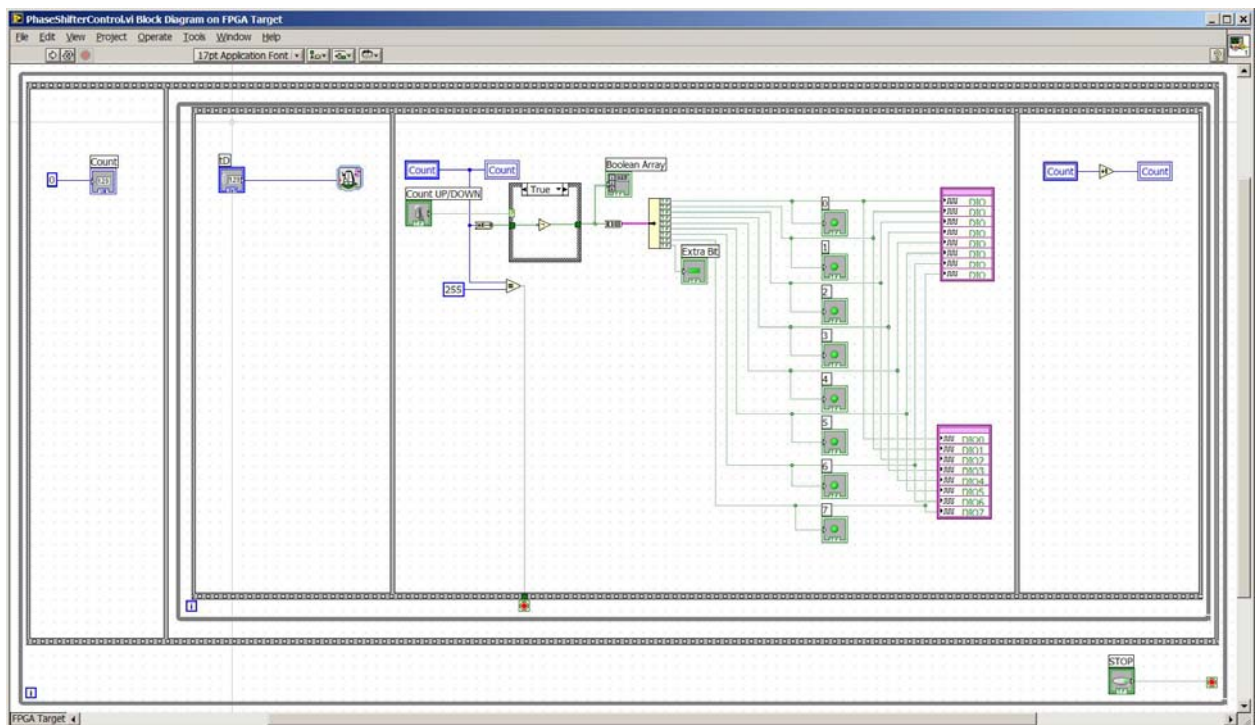


Figure 104. PhaseShifterControl_CODE1

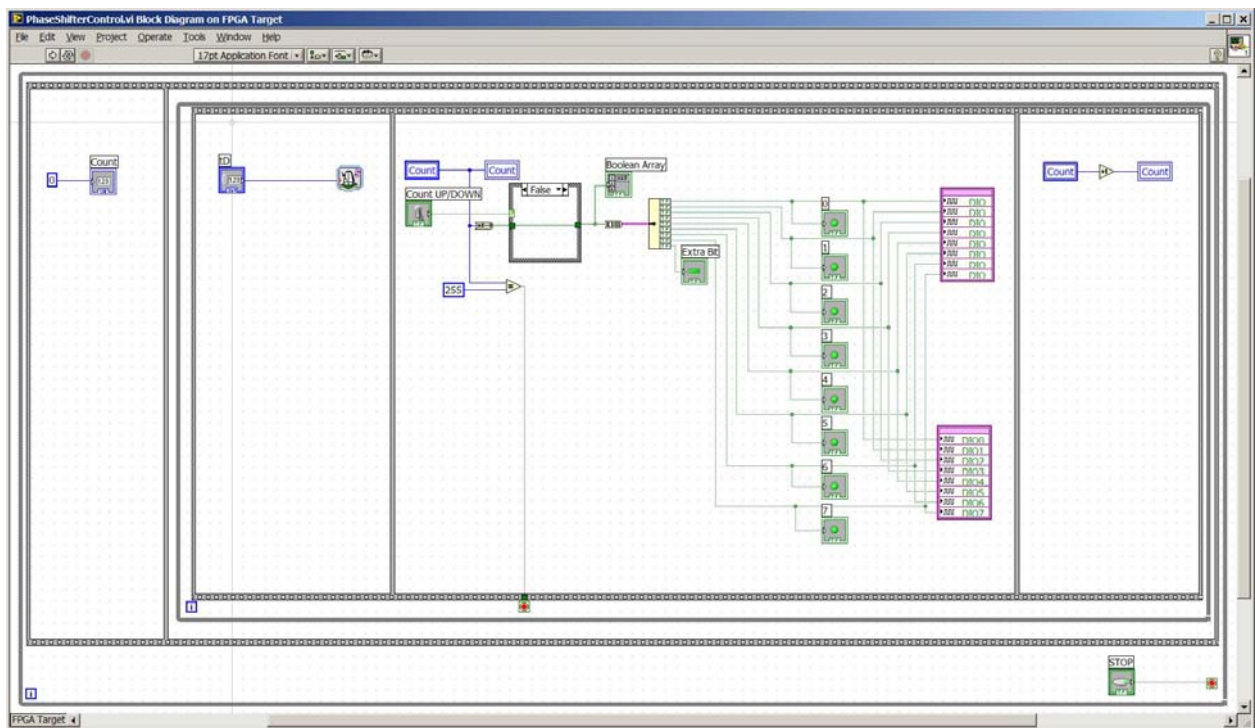


Figure 105. PhaseShifterControl_CODE2

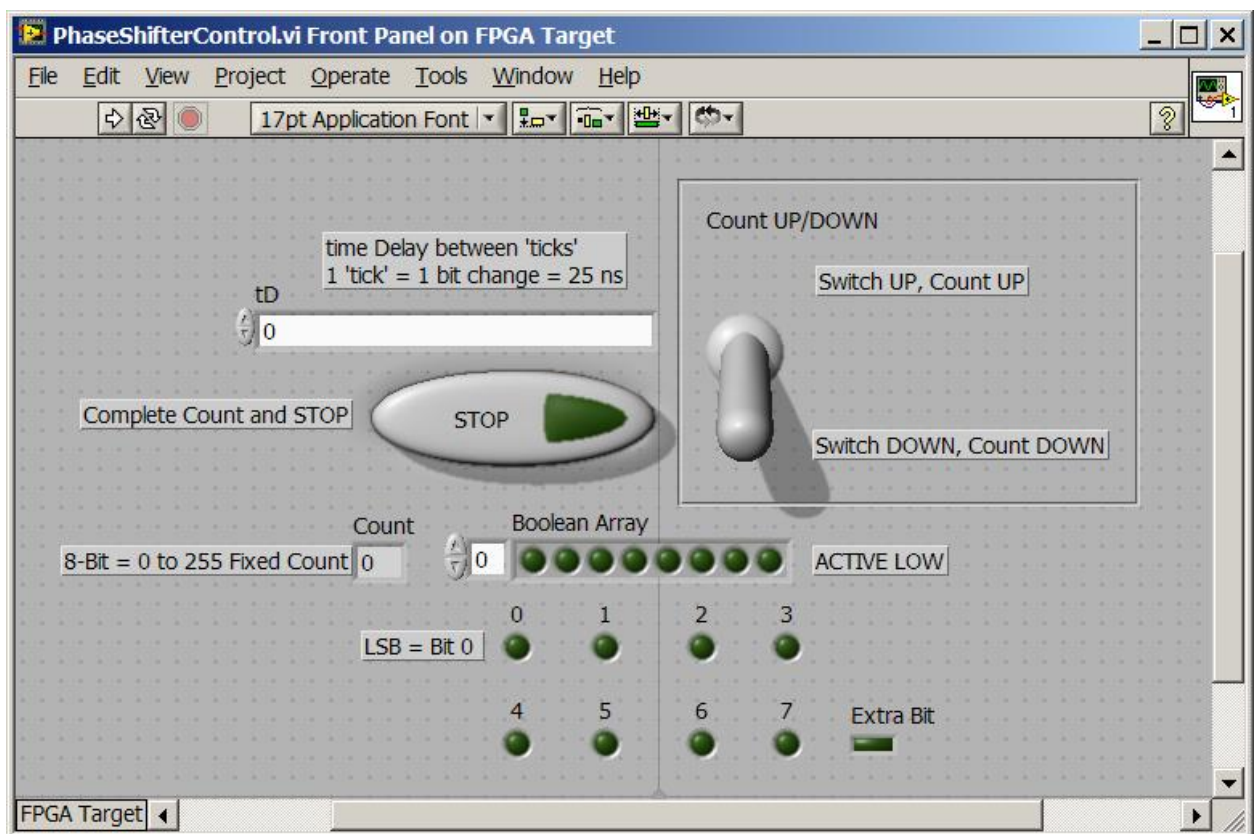


Figure 106. PhaseShifterControl_UI

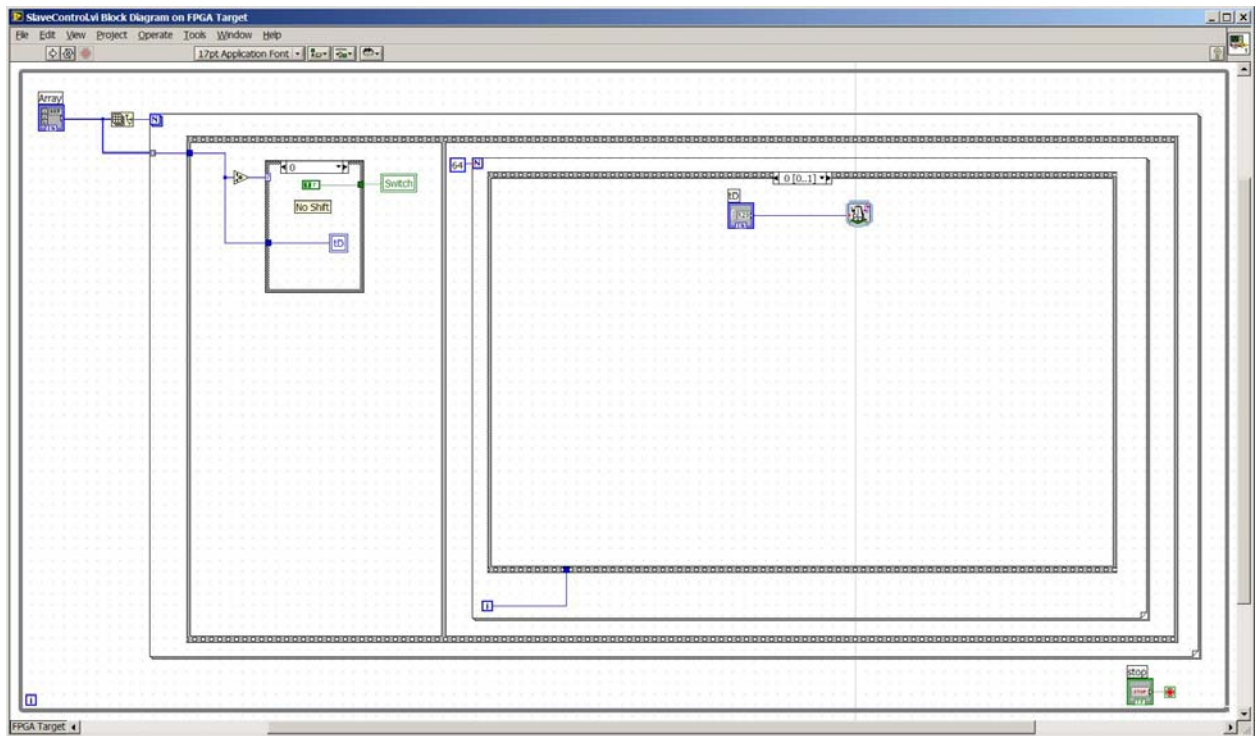


Figure 107. SlaveControl_CODE0

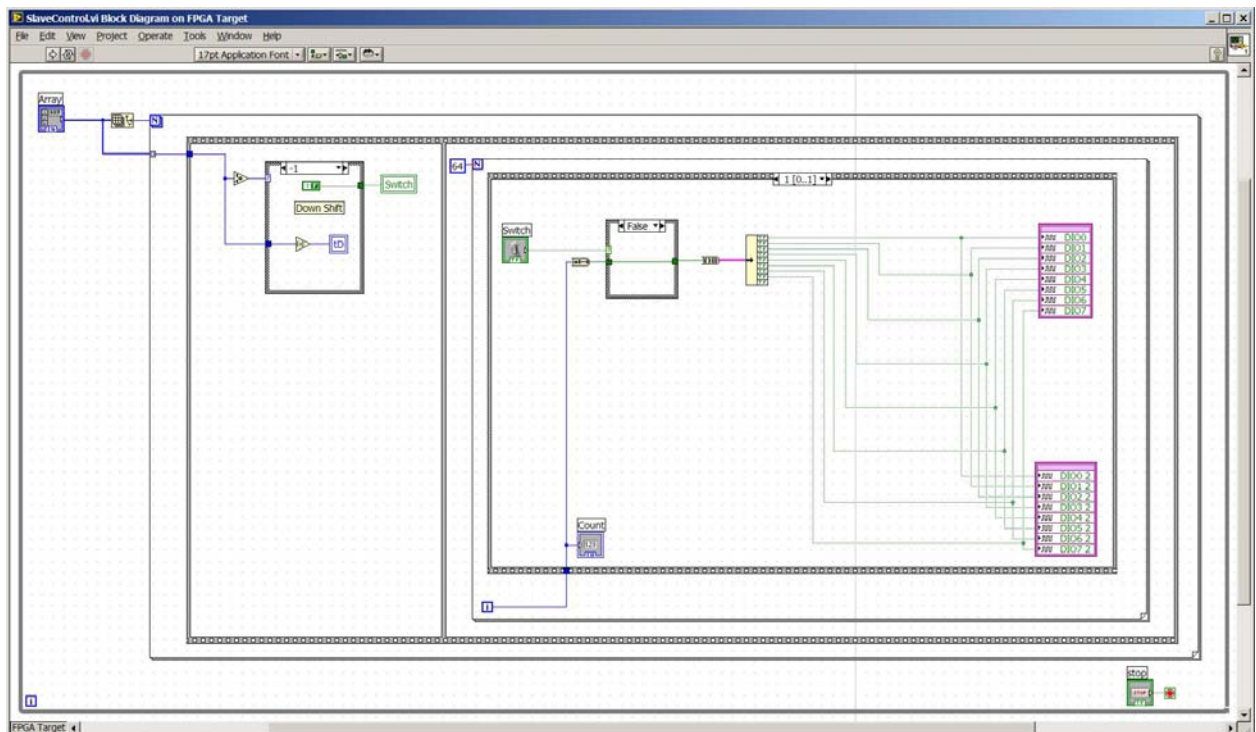


Figure 108. SlaveControl_CODE1

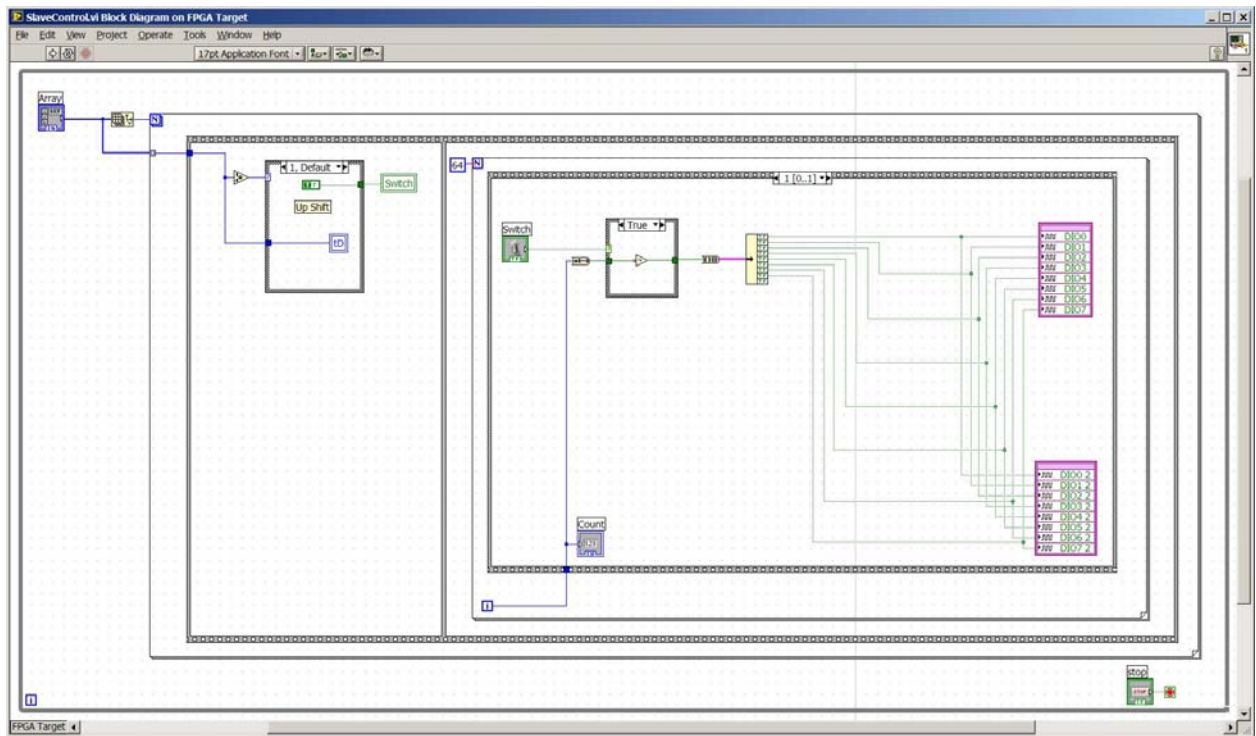


Figure 109. SlaveControl_CODE2

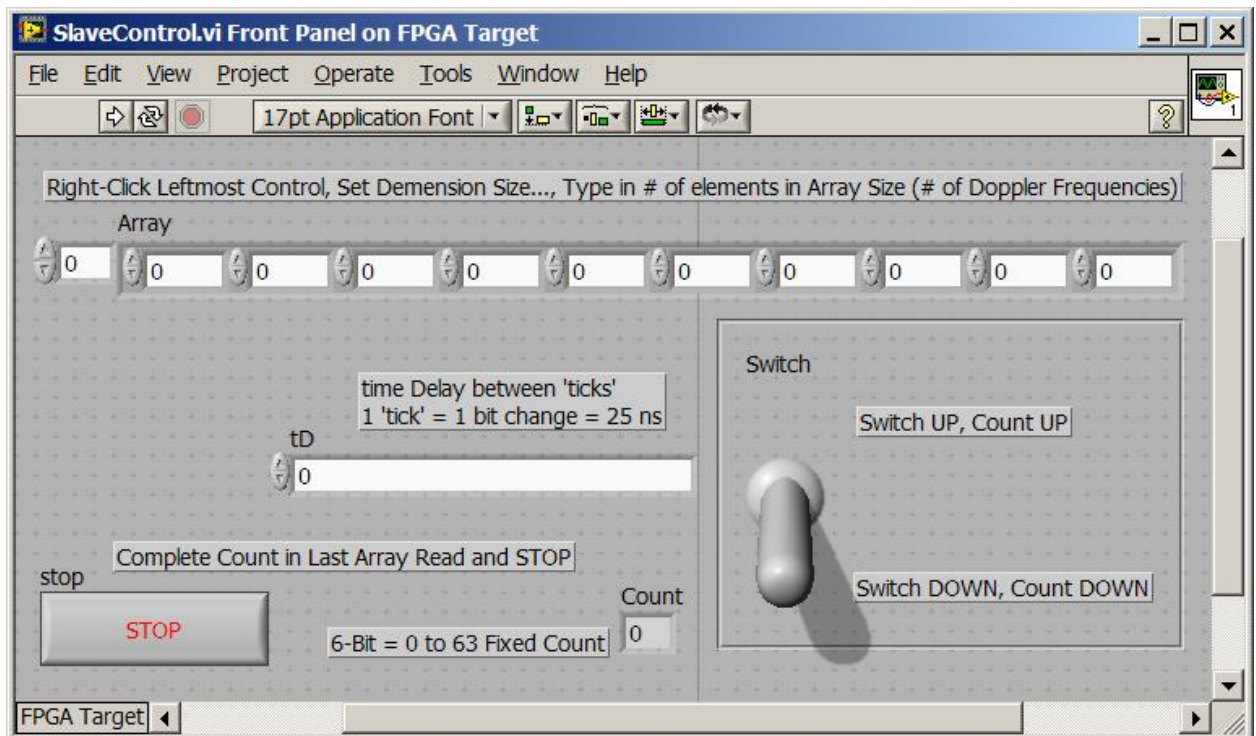


Figure 110. SlaveControl_UI

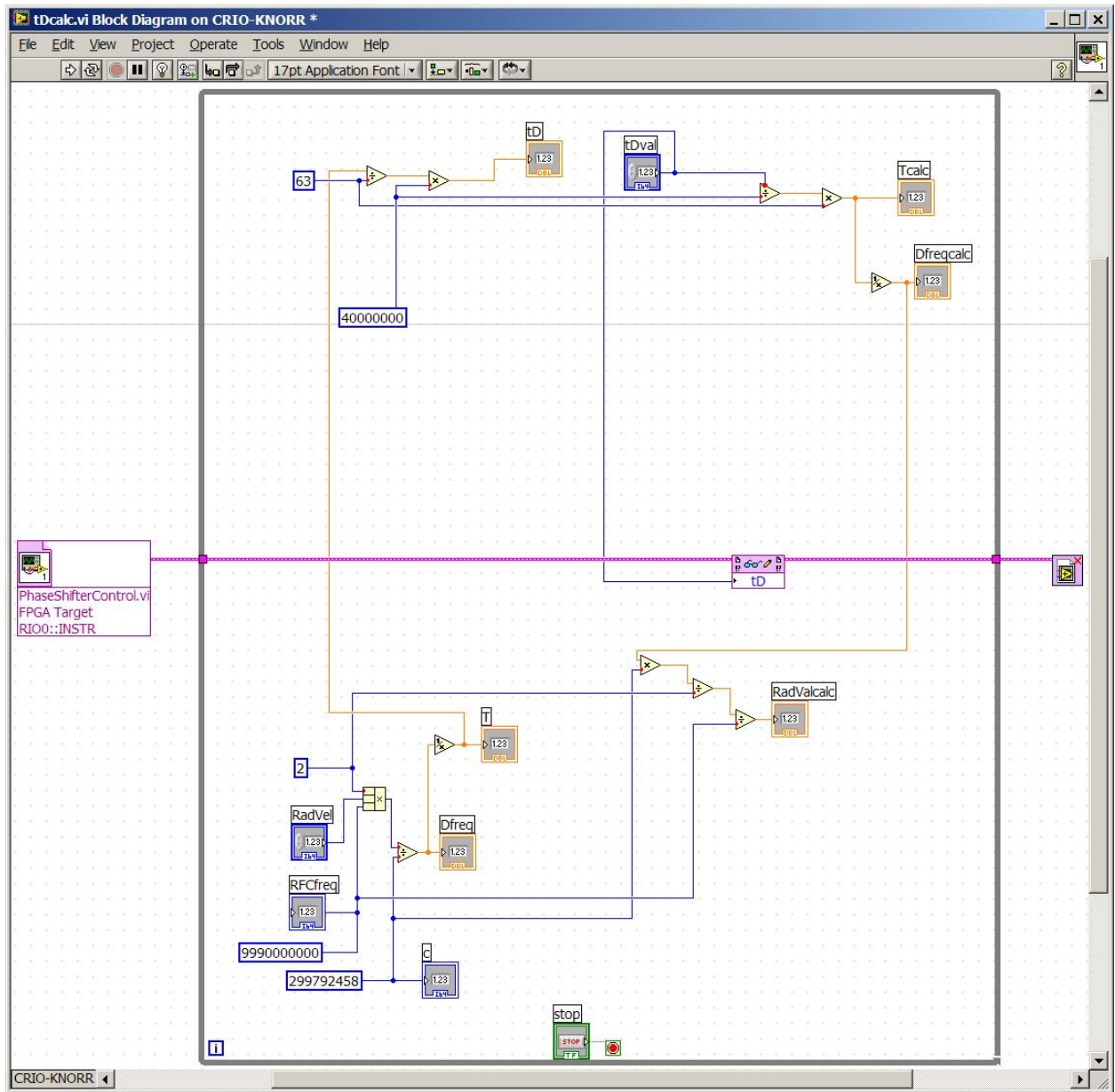


Figure 111. tDcalc_CODE

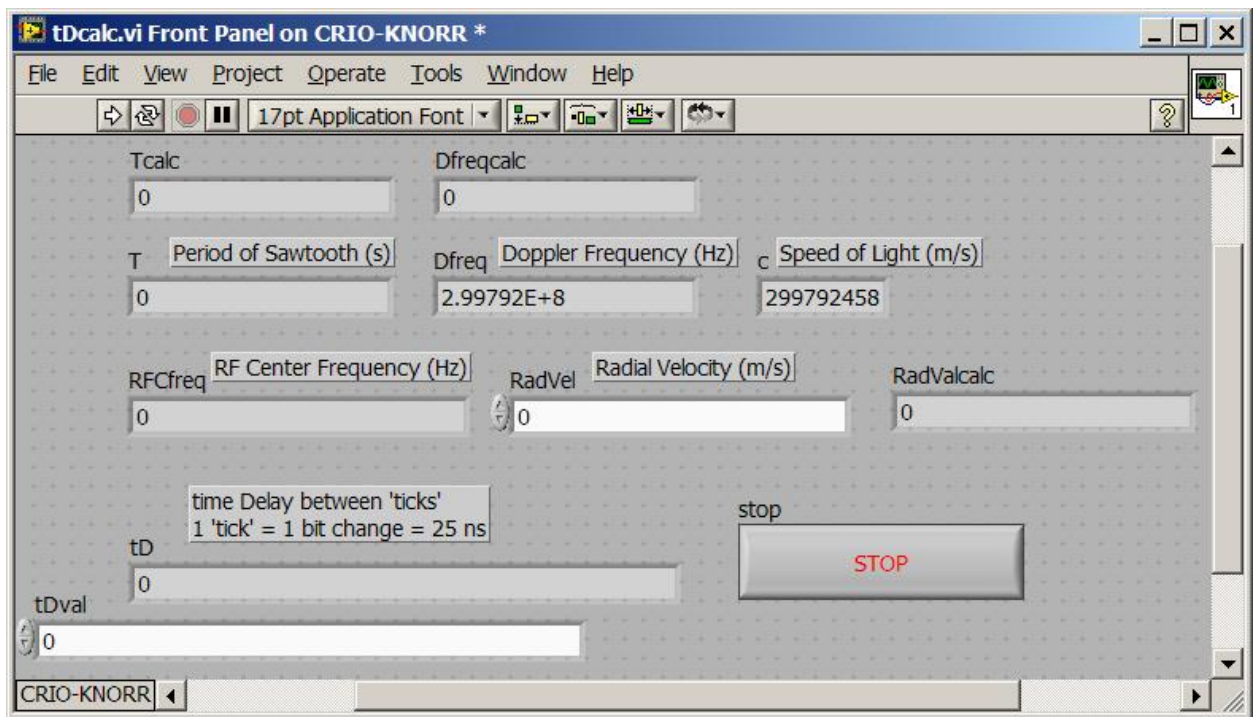


Figure 112. tDcalc_UI

LIST OF REFERENCES

- [1] Ulf P. Schroder, "Development of a Weather Radar Signal Simulator to Examine Sampling Rates and Scanning Schemes," *Naval Postgraduate School*, September 2005.
- [2] J.S. Marshall and W. Hitschfeld, "Interpretation of the Fluctuating Echo from Randomly Distributed Scatterers. Part I" *Canadian Journal of Physics*, Vol. 31, pp. 962-994, 1953.
- [3] Frank Pratte and Richard L. Ice, "External Radar Calibration Options Applicable to the WSR-88D Network" *Report on Special Project 20*, Norman, Oklahoma: Radar Operations Center Engineering Branch, 18 April 2005.
- [4] R.J. Doviak and D.S. Zrnić, *Doppler Radar and Weather Observations*, Second Edition, San Diego: Academic Press, 1993.
- [5] Jeffrey B. Knorr, "Weather Radar Equation Correction for Frequency Agile and Phased Array Radars" *IEEE Transactions on Aerospace and Electronic Systems*, pp. 1230-1238, July 2007.
- [6] Office of the Federal Coordinator for Meteorological Services and Supporting Research, "PartD – WSR-88D Unit Description and Operational Applications" *Federal Meteorological Handbook No. 11 – Doppler Radar Meteorological Observations (WSR-88D)*, Washington DC: U.S. Dept of Commerce/NOAA, February 2006.
- [7] J.R. Probert-Jones, "The Radar Equation in Meteorology," *Quarterly Journal of the Royal Meteorological Society*, Vol. 88, pp. 485-495, July 1962.
- [8] Ryzhkov, et al., *The Joint Polarization Experiment*, BAMS, pp. 809-823, June 2005.
- [9] Meng-Yoon Tan, "Serrodyning by means of a Digital Phase Shifter," *Naval Postgraduate School*, September 1989.
- [10] Raymond C. Cummings, "The Serrodyne Frequency Translator" *Proceedings of the IRE*, pp. 175-186, February 1957.
- [11] M.I. Skolnik, *Introduction to Radar Systems*, Second Edition, Boston: McGraw Hill, 2001.
- [12] *New Network Analyzer Methodologies in Antenna/RCS Measurements*, Agilent Technologies White Paper, literature number 5989-1937EN, November 2004.

THIS PAGE INTENTIONALLY LEFT BLANK

INITIAL DISTRIBUTION LIST

1. Defense Technical Information Center
Ft. Belvoir, Virginia
2. Dudley Knox Library
Naval Postgraduate School
Monterey, California
3. Professor Jeffrey B. Knorr
Chairman, Code EC
Department of Electrical and Computer Engineering
Naval Postgraduate School
Monterey, California
4. Professor Dan C. Boger
Chairman, Code IW
Department of Information Sciences
Naval Postgraduate School
Monterey, California
5. Terry E. Smith, Lt Col, USAF
Department of Information Sciences
Naval Postgraduate School
Monterey, California
6. Robert Broadston
Department of Electrical and Computer Engineering
Naval Postgraduate School
Monterey, California
7. Paul Buczynski
Department of Electrical and Computer Engineering
Naval Postgraduate School
Monterey, California
8. Professor David C. Jenn
Department of Electrical and Computer Engineering
Naval Postgraduate School
Monterey, California